UNIVERSITY OF TRENTO - Italy
Department of Civil, Environmental and Mechanical Engineering

Doctoral School in Civil, Environmental and Mechanical Engineering
Topic 3. Modelling and Simulation - 37th cycle 2021/2024

Doctoral Thesis - April 2026

Valeria Francesca Caspani

Advancing Bridge Health Monitoring through Satellite InSAR and Performance-Based System Design

Supervisors
Prof. Daniele Zonta, University of Trento, Italy

Alla mia famiglia

Acknowledgements

Here I would like to share a few personal considerations. The first thing that comes to mind is that I am grateful to have been able to begin this journey, and to have been able to complete it.

I owe this to Prof. Daniele Zonta, who several years ago saw something in me and pointed me toward a path that I would otherwise not have imagined I could pursue. Moreover, when after the first year of my PhD I decided to take up a work opportunity, he did not stand in my way; on the contrary, he allowed me to continue and complete this journey in a non-conventional way. For this I will always be grateful.

During these years, thanks to him I learned the importance of logical processes, which help organize thoughts and communicate them clearly. I also learned from him how to simplify problems that at first glance appear complex, and conversely not to treat seemingly simple problems superficially. I always came away from every discussion with something new; there was never a time when I did not feel enriched by it.

I would like to thank my family –mom, dad, and Giorgia– for always supporting me in doing whatever I wanted to do and in making whatever choices I wished to make, trusting me completely. I would also like to thank David for always truly believing in me and for always reminding me that I can do it, even when I sometimes feel lost or overwhelmed.

Finally, I would like to thank all my friends and colleagues, without naming them one by one–otherwise these acknowledgments would turn into a long list of names. The people who have been there for me know who they are, and they know that I am grateful to have them in my life.

Valeria

Ringraziamenti

Qui vorrei condividere alcune riflessioni personali. La prima cosa che mi viene in mente, è che sono grata di aver potuto iniziare, e di aver potuto finire questo percorso.

Questo lo devo al prof. Daniele Zonta, che alcuni anni fa ha visto in me qualcosa, e mi ha indicato una strada che altrimenti non avrei immaginato di poter percorrere. Inoltre, quando dopo il primo anno di dottorato ho voluto cogliere un'opportunità lavorativa, non mi ha ostacolata; al contrario, mi ha permesso di proseguire e portare a termine il percorso in maniera non convenzionale. Di questo gli sarò sempre grata.

Durante questi anni, grazie a lui ho imparato imparato l'importanza dei processi logici, che permettono di riordinare i pensieri e la loro comunicazione. Ho imparato da lui anche a semplificare problemi che sembrano a primo sguardo complessi, e viceversa a non trattare con superficialità problemi apparentemente semplici. Da ogni discussione ho portato a casa qualcosa, non c'è stata volta che non mi sia sentita arricchita.

Vorrei ringraziare la mia famiglia –mamma, papà e Giorgia– per avermi sempre supportato nel fare qualsiasi cosa volessi fare, e nel prendere qualsiasi scelta volessi prendere, dandomi piena fiducia. Vorrei ringraziare anche David, per credere sempre davvero in me e dirmi sempre che ce la posso fare, anche quando succede che mi senta persa o sopraffatta.

Infine, vorrei ringraziare tutti i miei amici/e e colleghi/e, senza nominarli uno ad uno, che altrimenti questi ringraziamenti diventano una lunga lista di nomi. Tanto, le persone che ci sono state per me lo sanno, e sanno che sono grata di averle nella mia vita.

Valeria

Abstract

Bridge infrastructure is a critical component of transportation networks, yet its management faces increasing challenges due to aging assets. Bridge Management Systems (BMS) aim to allocate resources efficiently by prioritizing repair and maintenance interventions based on structural condition assessment, which is usually derived from inspection reports. However, traditional condition ratings relying solely on visual inspections are often insufficient, as they lack quantitative evaluation of either mechanical properties of the structure, structural responses and applied loads. In this context, Structural Health Monitoring (SHM) offers a valuable opportunity for objective, timely and continuous assessment of structural performance. However, the high costs of permanent on-site SHM systems hinder their large-scale adoption, and the absence of standardized procedures for effective monitoring system design risks leading to inefficient use of resources through the installation of systems that provide useless information. As a result, SHM systems are currently usually installed only on a limited number of strategic or severely degraded bridges. Innovative techniques, algorithms and methods that enable network-scale and cost-effective monitoring therefore need to be explored and enhanced for potential integration in bridge management practice. This thesis proposes innovative solutions to overcome key obstacles to the widespread and systematic implementation of SHM in bridge management, by leveraging satellite SAR technology for device-free, large-scale, and inexpensive bridge monitoring, and a performance-based approach for monitoring system design. The main research contributions include: (i) an end-to-end application of satellite SAR technology to bridge monitoring, from the satellite data processing steps to the structural interpretation of results, advancing both the understanding and the practical applicability of SAR technology for infrastructure managers; (ii) a novel clustering algorithm for the automated classification of SAR-derived outputs, simplifying their rapid interpretation and enabling large-scale application of satellite monitoring; (iii) a closed-form expression for estimating the performance of SHM systems by predicting the structural state parameters uncertainty, which can be directly employed in the design of monitoring systems.

Contents

List of Figures

List of Tables

1. Overview

Structural Health Monitoring (SHM) has rapidly expanded over the past two decades, driven by tragic structural failures and the progressive deterioration of existing infrastructure [1, 2]. Despite remarkable advances and increasing application in both scientific research and engineering practice, several challenges remain in the systematic implementation of SHM and its integration into bridge management protocols [3, 4, 5]. In this doctoral thesis I aim to develop innovative methods and algorithms to support the standardization and network-scale deployment of SHM for infrastructure management, thereby enhancing its use and integration within Bridge Management Systems (BMS). The proposed approaches were validated through real case studies involving the bridge inventory managed by Autostrada del Brennero S.p.A.

The first contribution of this thesis consists in advancing the integration of spaceborne Synthetic Aperture Radar (SAR) technology into traditional bridge management practices. This is achieved by (i) presenting an application framework for analyzing road bridges by means of SAR data and (ii) providing a low-input algorithm for the automated post-processing of the outputs derived from SAR data analysis. The second contribution of this thesis concerns the advancement and standardization of monitoring system design. A user-friendly formulation for the evaluation of the effectiveness of a monitoring system during the design phase is proposed. This formulation targets the primary monitoring objectives for prestressed concrete bridges, and can be readily employed by infrastructure operators in the design of monitoring systems.

Noteworthily, during the development of this research, I worked full-time as a civil engineer at Autostrada del Brennero S.p.A., the A22 highway concessionaire. I was directly involved in the design of the Po Bridge monitoring system, which is currently being installed. I am currently developing a comprehensive database for the monitored bridges along the A22 highway and creating a python-based application for SHM data management and visualization. This platform is currently being tested on the SHM systems of the Colle Isarco and Micheletti viaducts, and will soon be extended to include the Po Bridge SHM system once the data are available.

This doctoral thesis is presented as a collection of published scientific articles. Specifically, this doctoral thesis collects four journal articles already published in international peer-reviewed journals. The first one is a literature review on Bridge Management Systems, the second and third focus on SAR satellite monitoring of bridges, and the fourth concerns the

design of monitoring systems. Here is the complete list of my scientific journal publications, presented in this thesis:

(J.1) Brighenti, F., **Caspani, V. F.**, Costa, G., Giordano, P. F., Limongelli, M. P., Zonta, D. (2024). Bridge management systems: A review on current practice in a digitizing world. Engineering Structures, 321, 118971, https://doi.org/10.1016/j.engstruct.2024.118971.

(J.2) Tonelli, D., **Caspani, V. F.**, Valentini, A., Rocca, A., Torboli, R., Vitti, A., Perissin, D., Zonta, D. (2023). Interpretation of bridge health monitoring data from satellite InSAR technology. Remote Sensing, 15(21), 5242, https://doi.org/10.3390/rs15215242.

(J.3) **Caspani, V.F.**, Tonelli, D., Bado, M.F., Rocca, A., Perissin, D., Zonta, D. (2025). Bridge monitoring with satellite InSAR technology and clustering algorithm. Measurement, 118939, https://doi.org/10.1016/j.measurement.2025.118939.

(J.4) **Caspani, V. F.**, Tonelli, D., Poli, F., Zonta, D. (2021). Designing a structural health monitoring system accounting for temperature compensation. Infrastructures, 7(1), 5, https://doi.org/10.3390/infrastructures7010005.

Whilst my primary focus was on the above topics, I also worked, jointly with my research group, on asset structural health assessment through visual inspections and non-destructive testing, with a contribution in two conference papers. In addition to these, other conference papers on my primary research topics have been published. The following are the main conference papers produced:

(C.1) Tonelli, D., Rossi, F., Luchetta, M., **Caspani, V.**, Zonta, D., Migliorino, P., ... & Ascari, G. (2021, March). Effectiveness of acoustic emission monitoring for in-service prestressed concrete bridges. In *Sensors and Smart Structures Technologies for Civil, Mechanical, and Aerospace Systems 2021* (Vol. 11591, pp. 178–192). SPIE.

(C.2) Tonelli, D., **Caspani, V. F.**, Zorzi, S., & Zonta, D. (2022, April). Designing monitoring systems for long-term structural response. In *Sensors and Smart Structures Technologies for Civil, Mechanical, and Aerospace Systems 2022* (Vol. 12046, pp. 184–192). SPIE.

(C.3) **Caspani, V.**, Tonelli, D., Poli, F., Zorzi, S., & Zonta, D. (2022, June). Pre-posterior analysis of temperature-compensated structural health monitoring data. In *European Workshop on Structural Health Monitoring* (pp. 318–326). Cham: Springer International Publishing.

(C.4) Poli, F., Bado, M.F., Possidente, L., Brighenti, F., **Caspani, V.F.**, & Zonta, D. (2022). Assessing the cost of subjectivity in reinforced concrete bridge inspections. In *Proceedings of the 6th fib Congress 2022*.

(C.5) **Caspani, V.F.**, Tonelli, D., Torboli, R., Zorzi, S., & Zonta, D. (2022). Remote monitoring of bridge displacements with satellite SAR technology. *8WCSCM*, Orlando (FL), USA.

(C.6) **Caspani, V. F.**, Tonelli, D., Rocca, A., Torboli, R., Vitti, A., & Zonta, D. (2023, April). Satellite InSAR technology for structural health monitoring of road bridges and the surrounding territory: a case study. In *Sensors and Smart Structures Technologies for Civil, Mechanical, and Aerospace Systems 2023* (Vol. 12486, pp. 293–302). SPIE.

1.1 Motivation

Bridges and viaducts play a vital role in the orderly functioning of modern society, contributing to its safety, comfort, and economic well-being. Effective management and maintenance of infrastructure are essential, given their progressive deterioration due to aging, increased traffic demands, environmental and geological phenomena, and the growing frequency of extreme weather events related to climate change [6].

In Europe, the first wave of highway construction began in the 1920s, followed by a major expansion in the 1960s [7, 8]. During this period, Italy carried out numerous large-scale infrastructure projects, including highways. As a consequence, today over half of Italy's highway bridges have exceeded their original design service life and often exhibit significant defects and signs of deterioration [9]. Many of these structures are nearing the point where they may no longer support the heaviest vehicles or meet adequate standards of durability and serviceability. However, the complete replacement of all these aging bridges is neither economically, logistically, nor environmentally feasible in the short term [10]. Therefore, infrastructure managers must keep assets in service while ensuring safety and functionality, which requires prioritizing maintenance activi-

ties and allocating financial resources through effective bridge management [11].

For example, the Brenner Highway "A22" was constructed between 1964 and 1974. It is a 314-km highway connecting the Brenner Pass with Bolzano, Trento, Verona, Mantua, and Modena, which established a strategic transport corridor between Italy and the rest of Europe via Austria, fostering social, economic, and cultural integration. The A22 highway includes 142 bridges–most made of reinforced concrete–146 overpasses, and 30 tunnels. The A22 infrastructure operators regularly check the condition of their bridge stock by means of periodic visual inspections, and upload the inspection reports to their BMS platform. For each bridge, they compile defect sheets and assign a condition rating. This process allows them to eventually prioritize maintenance for bridges showing defects or signs of deterioration. In essence, the BMS serves as a valuable inventory of the bridge stock and its condition based on visual inspections. Such traditional BMS approaches–centered around visual inspections–are widely used by infrastructure managers and highway concessionaires across the world [12, 13].

Yet, the traditional BMS approach of relying solely on visual inspection and on the evaluation of condition ratings of bridges for their structural upkeep management has proven insufficient, since it has significant limitations [14, 15]. Inspections may require traffic closures, are expensive especially for hardly accessible bridges, and cannot detect hidden defects such as corrosion or loss of prestress in cables [16]. Furthermore, they are subject to human interpretation and strongly depend on the expertise of inspectors [17]. Moreover, by focusing only on condition, key indicators of the structural state related to actions, response, environmental and geotechnical phenomena, and mechanical properties of the structure are overlooked [18]. Examples of key structural state parameters include long-term displacement, rotation, and deformation drifts, modal frequencies, post-tensioning force losses, corrosion rate, scour depth, joint aperture, etc. [19, 20, 21].

To enable the assessment of various types of structural state parameters, the last few decades have seen growing efforts to use and integrate innovative technologies and methods into bridge management frameworks [22, 23, 24, 25]. In 2007, Farrar et al. defined the combined use of such technologies and methods for structural state evaluation–commonly known as Structural Health Monitoring (SHM)–as *"the process of implementing a damage identification strategy (...) that involves the observation of a structure (...) to determine the current state of system health."* [26]. It should be noted that SHM is generally distinguished from non-destructive evaluation techniques (NDTs) by the fact that it exploits per-

manently acquiring sensor networks and does not take the structure of interest out of operation [27].

SHM allows continuous, objective, timely and accurate assessment of the structural state, potentially improving bridge management in terms of both maintenance planning economy and safety [27]. In recent years, in Italy as well as worldwide, the adoption of sensors for monitoring civil infrastructures has been further encouraged by guidelines for bridge monitoring and management and by national funding initiatives, leading to a growing interest in SHM among practitioners and infrastructure operators [28, 29].

However, SHM systems come with high costs. The higher the number of sensors and the better their accuracy, the higher the costs of permanent SHM systems–between 50-200k euros per bridge's span [30], and up to 2-3 million euros for a strategic multi-span bridge [31]. As a result, SHM is still typically limited to strategic or highly deteriorated structures. For example, on the A22 network, the Colle Isarco viaduct has served as a SHM pilot project, equipped between 2014 and 2016 with a multi-sensor system including topographic prisms, fiber optics, load cells, and temperature sensors. More recently, the design for an even more advanced SHM system has been completed for the Po River Bridge. Considering that in the near future, a significant amount of the infrastructure stock will exceed its design life, the number of assets that could benefit from permanent monitoring will also increase. Thus, cost-effective and network-scale SHM strategies are urgently needed.

In this context, it becomes essential to ensure that SHM systems themselves are effective, bringing useful information to the infrastructure operators [32]. In fact, SHM is only effective when it enables reliable identification of key state parameters with an appropriate level of confidence, thereby improving knowledge of the actual structural state [33]. This general rule should drive the design and installation of SHM systems for the assessment of relevant structural state parameters, based on the monitoring objectives defined for each structure and the needs of the asset manager. However, no specific regulations currently exist for the choice of technologies to use, and monitoring system design is often approached empirically [34]. This can result in the design and installation of inefficient SHM systems, leading to wasted or improperly used resources. A logical and rigorous procedure for monitoring system design and performance evaluation is therefore needed to support the cost-effective monitoring of an increasing number of bridges.

Building on the need for more scalable and cost-effective strategies, satellite remote monitoring offers a promising complementary solution to traditional contact-type monitoring. In particular, SAR technology

enables long-term monitoring over wide areas, capturing entire infrastructure networks without the need to install any sensors on-site. The cost of a single high-resolution archive image–suitable for infrastructure displacement analysis–can range from a few hundred to few thousand euros, depending on the product type, sensor, and size [35]. For example, the satellite imagery analyzed in this thesis is provided free of charge for research purposes, and costs 300€ per image for commercial use, covering areas of 40x40 km (COSMO-SkyMed Stripmap imagery). A set of images for monitoring a period of about 2 years costs approximately 10k€, while a set of images for monitoring a period of about 10 years costs around 70k€ [36, 37]–significantly less than installing traditional monitoring systems on multiple bridges along a roughly 40-km highway segment. The use of satellite SAR technology for SHM of bridges is a rapidly expanding field of research, with several areas that still require further development [38].

1.2 Problem Statement

The main research problems addressed in this thesis, previously introduced in Section 1.1, are presented below.

(1) **Limited studies on the use of SAR satellite technology for bridge monitoring and its integration in bridge management practices**: SAR technology offers significant potential for infrastructure monitoring, enabling the observation of large areas and structures without the need for on-site sensors. However, its use in SHM is still in the early stages, with several limitations yet to be overcome. Most civil engineers have limited familiarity with MT-InSAR data processing and often rely on pre-processed outputs provided by third-party analysts, without insight into critical data processing steps that can affect both accuracy and interpretation of the final results. Additionally, interpreting and classifying MT-InSAR derived results from a structural engineering perspective nowadays remains a challenging and time-consuming task – especially given the large number of Persistent Scatterers points (PS) that may be identified, depending on SAR dataset quality and coverage. These gaps need to be addressed to fully leverage MT-InSAR in SHM.

(2) **Lack of a standardized approaches for the design and performance evaluation of monitoring systems**: When monitoring a structure, the purpose is to identify a set of key parameters which are representative of its state. During the monitoring system de-

sign phase, these key parameters are defined. For the monitoring system to be effective, it must enable the identification of these parameters with sufficient confidence–i.e., within an acceptable level of uncertainty. However, predicting the uncertainty of the key parameters in the design phase, when no monitoring data is yet available, remains a challenge. The ability to estimate the expected performance of a monitoring system in terms of the accuracy of key state parameters is crucial both for infrastructure managers–who must allocate resources in advance–and for system designers–who must ensure the proposed solution meets performance requirements.

1.3 Objectives

The main objectives of this thesis, aimed at addressing the problems outlined in Section 1.2, are presented below:

(1) **Framework for MT-InSAR analysis of bridges and algorithm for automated post-processing of MT-InSAR outputs**: This thesis presents an end-to-end process for using MT-InSAR in the monitoring of road bridges in operational conditions. The process includes data acquisition, MT-InSAR data processing for PS displacement time series extraction, and the interpretation of the observed millimetric ground and bridge movements from a structural engineering standpoint. Furthermore, a novel, low-input clustering methodology is proposed for the automated classification of PS, sparing the need to individually check each PS one-by-one. This data-driven approach enables the rapid identification of PS distinct deformation patterns and their association with physical elements in the area. It is designed to be broadly applicable across different case studies and accessible to civil engineers with limited expertise in data science or InSAR processing. The methodology fosters efficient interpretation of MT-InSAR data and its potential integration into BMS frameworks.

(2) **Formulation to quantify the expected performance of monitoring systems, and its application to monitoring system design**: This thesis introduces a method for evaluating the effectiveness of a monitoring system in the design phase, before any data has been collected. It consists in a simple-to-use formulation that allows to calculate the expected uncertainty in key structural state parameters–specifically, long-term response trends–while accounting for temperature effects. The proposed approach repre-

sents a significant step forward in enabling broader adoption of SHM, as it provides infrastructure managers and engineers with a practical tool for designing monitoring solutions by quantifying their expected performance. The formulation was employed by the author and Autostrada del Brennero S.p.A infrastructure operators in the design of the multi-sensor SHM system for the Po River Bridge.

Through these objectives, this thesis aims to deliver practical and innovative solutions to real-world problems faced by infrastructure managers. The proposed methods are designed to enhance the effectiveness and efficiency of monitoring and managing critical infrastructure in a resource-constrained environment.

1.4 Methodology

The methodology adopted in this research to achieve the outlined objectives involved different steps.

First, a comprehensive review of Bridge Management Systems (BMS) was conducted to identify current practices, critical challenges, and emerging trends in bridge management (Chapter 5). Among other findings, this study provided insight into both the opportunities for enhancing bridge management through SHM, and the barriers that still hinder its systematic integration into practice. This study laid the foundation for the subsequent steps of my research, which aimed to address two critical challenges in bridge management through SHM: (i) the high costs associated with the installation of permanent on-site SHM systems at a network scale and management of large volumes of monitoring data; and (ii) the absence of standardized and consistent procedures for the design and performance evaluation of monitoring systems.

To address the need for large-scale and cost-effective SHM solutions, the use of satellite SAR technology for remote bridge monitoring was explored. First, a framework for analyzing SAR data and interpreting the outputs from a structural standpoint was developed. An application on the A22 Po River Bridge case study was carried out, starting from the raw SAR imagery dataset, and proceeding through the extraction and discussion of the results, including their correlation with environmental phenomena (Chapter 6). Then, a novel data-driven clustering algorithm for the automated classification of PS derived from MT-InSAR analysis was developed. The algorithm performs a one-step analysis that considers both the temporal and spatial domains of PS, allowing the identification of predominant PS time-series patterns and their association with

physical entities within the SAR image footprint area. This approach facilitates the rapid interpretation of large PS datasets and supports potential integration into BMS frameworks. The algorithm was tested on two case studies along the A22 highway: the Colle Isarco viaduct and the Po River bridge (Chapter 7).

Finally, a formulation to estimate the effectiveness of a monitoring system was developed. This formulation can be applied to the design of monitoring systems for long-term phenomena and explicitly accounts for temperature effects. It is particularly useful for the design of monitoring systems for prestressed concrete bridges, which are severely influenced by long-term phenomena (e.g. creep and shrinkage, prestress losses, ground movements) and by environmental temperature effects. It can be easily employed in the design phase, as it does not depend on the specific data acquired by the system itself. Specifically, the developed formulation allows estimating the expected uncertainty of long-term trend parameters (e.g. strain, rotation, displacement trend), enabling the evaluation of a tentative monitoring solution's effectiveness by verifying whether key state parameters can be identified with an adequate level of confidence. Validation was carried out on the A22 Colle Isarco viaduct case study by comparing the pre-posterior uncertainty estimate obtained through the proposed method to the actual uncertainty a posteriori derived from monitoring data (Chapter 8).

1.5 Outline

This thesis is organized in two parts (I and II) and in eight chapters, not including the present one. Part I, State of the art, contains three chapters and provides a brief state of the art on the research topics addressed in this thesis. Next, Part II, Publications, contains five chapters. The first four chapters contain the post-print of the four author's journal publications discussed in this thesis. The last chapter includes final considerations, limitations and possible future developments of this research. Finally, this thesis includes a brief appendix, where an additional discussion is presented to provide further insight on the main topics addressed in the research papers.

The present chapter (Chapter 1) introduces the work, outlining the motivation, problem statement, objectives, and methodology.

Chapter 2 provides a review of Bridge Management Systems, with particular emphasis on the role of Structural Health Monitoring in current practice. It draws on the author's comprehensive review, reported in Chapter 5.

Chapter 3 presents an overview of the theoretical background related

to SAR imagery and MT-InSAR processing. This chapter outlines the foundation and motivation for the studies presented in Chapters 6 and 7.

Chapter 4 describes the Performance-Based Monitoring System Design approach, highlighting its limitations and forming the basis for the study reported in Chapter 8.

Chapter 5 presents the article with title *"Bridge Management Systems: A Literature Review on Current Practice and Future Trends in a Digitizing World"*, which offers a comprehensive state-of-the-art review of BMS.

Chapter 6 and Chapter 7 focus on the application of MT-InSAR for SHM of bridges. These sections include the articles with titles *"Interpretation of Bridge Health Monitoring Data from Satellite InSAR Technology"* and *"Bridge Monitoring with Satellite InSAR Technology and Clustering Algorithm"*, respectively addressing the application of MT-InSAR for bridges monitoring and the development of a data-driven clustering algorithm for automatic classification of MT-InSAR outputs.

Chapter 8 includes the article with title *"Designing a Structural Health Monitoring System Accounting for Temperature Compensation"*, which introduces a formulation for the a pre-posteriori estimation of the uncertainty of long-term trend parameters. Such formulation can be employed for the design of monitoring systems.

Chapter 9 concludes the thesis with general insights, limitations and proposed future research directions.

Finally, some complementary considerations are presented as an appendix. Appendix A addresses the monitoring system design problem for a generic bridge, comparing the performance of on-site and remote satellite-based monitoring solutions. The analysis provides further insights into both the monitoring system design procedure and the cost-effectiveness of satellite monitoring.

Bibliography

[1] J. Brownjohn, "Structural health monitoring of civil infrastructure," *Philosophical Transactions of the Royal Society A: Mathematical, Physical and Engineering Sciences*, vol. 365, pp. 589–622, Feb. 2007. Number: 1851.

[2] C. R. Farrar and K. Worden, "An introduction to structural health monitoring," *Philosophical Transactions of the Royal Society A: Mathematical, Physical and Engineering Sciences*, vol. 365, pp. 303–315, Feb. 2007.

[3] P. Rizzo and A. Enshaeian, "Challenges in bridge health monitoring: A review," *Sensors*, vol. 21, no. 13, p. 4336, 2021.

[4] A. Aktan, F. N. Catbas, K. Grimmelsman, and C. Tsikos, "Issues in infrastructure health monitoring for management," *Journal of Engineering Mechanics*, vol. 126, no. 7, pp. 711–724, 2000.

[5] Z. Deng, M. Huang, N. Wan, and J. Zhang, "The current development of structural health monitoring for bridges: A review," *Buildings*, vol. 13, no. 6, p. 1360, 2023.

[6] F. Collins and F. Blin, *Ageing of Infrastructure: A Life-Cycle Approach*. CRC Press, 2018.

[7] B. B. für Straßenwesen, "Brückenstatistik," 2025.

[8] G. M. Calvi, M. Moratti, G. J. O'Reilly, N. Scattarreggia, R. Monteiro, D. Malomo, P. M. Calvi, and R. Pinho, "Once upon a time in italy: The tale of the morandi bridge," *Structural Engineering International*, vol. 29, no. 2, pp. 198–217, 2019.

[9] D. Zonta, R. Zandonini, and F. Bortot, "A reliability-based bridge management concept," *Structures & Infrastructure Engineering*, vol. 3, no. 3, pp. 215–235, 2007.

[10] D. M. Frangopol, K.-Y. Lin, and A. C. Estes, "Life-cycle cost design of deteriorating structures," *Journal of structural engineering*, vol. 123, no. 10, pp. 1390–1401, 1997.

[11] D. M. Frangopol and M. Liu, "Maintenance and management of civil infrastructure based on condition, safety, optimization, and life-cycle cost," *Structures and infrastructure systems*, pp. 96–108, 2019.

[12] F. Brighenti, V. F. Caspani, G. Costa, P. F. Giordano, M. P. Limongelli, and D. Zonta, "Bridge management systems: A review on current practice in a digitizing world," *Engineering structures*, vol. 321, p. 118971, 2024.

[13] Z. Mirzaei, B. T. Adey, L. Klatter, and J. S. Kong, "Overview of existing bridge management systems-report by the iabmas bridge management committee," in *6th International Conference on Bridge Maintenance, Safety and Management (IABMAS 2012)*, International Association for Bridge Maintenance And Safety (IABMAS), 2012.

[14] L. Quirk, J. Matos, J. Murphy, and V. Pakrashi, "Visual inspection and bridge management," *Structure and Infrastructure Engineering*, vol. 14, no. 3, pp. 320–332, 2018.

[15] H. Habeenzu, P. McGetrick, D. Hester, and S. Taylor, "Bridge management systems-a review of the state of the art and recommendations for future practice," *Bridge Maintenance, Safety, Management, Life-Cycle Sustainability and Innovations*, pp. 926–933, 2021.

[16] G. Puž, J. Radić, and D. Tenžera, "Visual inspection in evaluation of bridge condition," 2012.

[17] F. Poli, M. Bado, L. Possidente, F. Brighenti, V. Caspani, D. Zonta, *et al.*, "Assessing the cost of subjectivity in reinforced concrete bridge inspections," in *FIB SYMPOSIUM PROCEEDINGS*, pp. 2186–2195, fib. The International Federation for Structural Concrete, 2022.

[18] D. Agdas, J. A. Rice, J. R. Martinez, and I. R. Lasa, "Comparison of visual inspection and structural-health monitoring as bridge condition assessment methods," *Journal of Performance of Constructed Facilities*, vol. 30, no. 3, p. 04015049, 2016.

[19] M. F. Bado and J. R. Casas, "A review of recent distributed optical fiber sensors applications for civil engineering structural health monitoring," *Sensors*, vol. 21, no. 5, p. 1818, 2021.

[20] B. K. Oh, H. S. Park, and B. Glisic, "Time-dependent structural response estimation method for concrete structures using time information and convolutional neural networks," *Engineering Structures*, vol. 275, p. 115193, 2023.

[21] R. Cardoso, A. Cury, and F. Barbosa, "A robust methodology for modal parameters estimation applied to shm," *Mechanical Systems and Signal Processing*, vol. 95, pp. 24–41, 2017.

[22] J. Ko and Y. Q. Ni, "Technology developments in structural health monitoring of large-scale bridges," *Engineering structures*, vol. 27, no. 12, pp. 1715–1725, 2005.

[23] S. Hassani and U. Dackermann, "A systematic review of advanced sensor technologies for non-destructive testing and structural health monitoring," *Sensors*, vol. 23, no. 4, p. 2204, 2023.

[24] E. Figueiredo and J. Brownjohn, "Three decades of statistical pattern recognition paradigm for shm of bridges," *Structural Health Monitoring*, vol. 21, no. 6, pp. 3018–3054, 2022.

[25] S. Bianchi and F. Biondini, "Life-cycle assessment of deteriorating rc bridges using artificial neural networks," *Journal of Infrastructure Systems*, vol. 28, no. 2, p. 04022005, 2022.

[26] C. R. Farrar and K. Worden, "An introduction to structural health monitoring," *Philosophical Transactions of the Royal Society A: Mathematical, Physical and Engineering Sciences*, vol. 365, no. 1851, pp. 303–315, 2007.

[27] C. R. Farrar, N. Dervilis, and K. Worden, "The past, present and future of structural health monitoring: An overview of three ages," *Strain*, vol. 61, no. 1, p. e12495, 2025.

[28] I. Ministero delle Infrastrutture e dei Trasporti, Consiglio Superiore dei Lavori Pubblici: Roma, "Linee guida per la classificazione e gestione del rischio, la valutazione della sicurezza ed il monitoraggio dei ponti esistenti," tech. rep., Ministero delle Infrastrutture e dei Trasporti and Consiglio Superiore dei Lavori Pubblici, 2020.

[29] Highways England, "Cs 465 – management of post-tensioned concrete bridges. version 0. design manual for roads and bridges," technical report, National Highways, Birmingham, UK, 2020.

[30] D. Tonelli, V. F. Caspani, A. Valentini, A. Rocca, R. Torboli, A. Vitti, D. Perissin, and D. Zonta, "Interpretation of bridge health monitoring data from satellite insar technology," *Remote Sensing*, vol. 15, no. 21, p. 5242, 2023.

[31] Autostrada del Brennero S.p.A., "Verbale n. 22/2022," 2022.

[32] P. F. Giordano, S. Quqa, and M. P. Limongelli, "The value of monitoring a structural health monitoring system," *Structural safety*, vol. 100, p. 102280, 2023.

[33] V. F. Caspani, D. Tonelli, F. Poli, and D. Zonta, "Designing a structural health monitoring system accounting for temperature compensation," *Infrastructures*, vol. 7, no. 1, p. 5, 2021.

[34] C. Cappello, "Theory of decision based on structural health monitoring," 2017.

[35] SkyFi, "Skyfi imagery pricing," 2025.

[36] e-GEOS S.p.A., "Official price list — february 22nd 2021 (gd-com-21-003)," 2021.

[37] D. Amitrano, G. Di Martino, R. Guida, P. Iervolino, A. Iodice, M. N. Papa, D. Riccio, and G. Ruello, "Earth environmental monitoring using multi-temporal synthetic aperture radar: A critical review of selected applications," *Remote Sensing*, vol. 13, no. 4, p. 604, 2021.

[38] M. Lazecky, I. Hlavacova, M. Bakon, J. J. Sousa, D. Perissin, and G. Patricio, "Bridge displacements monitoring using space-borne x-band sar interferometry," *IEEE Journal of Selected Topics in Applied Earth Observations and Remote Sensing*, vol. 10, no. 1, pp. 205–210, 2016.

Part I

State of the art

2. Bridge Management Systems

In the first part of my research, a comprehensive review on Bridge Management Systems (BMS) was conducted to identify current practices, critical challenges, and emerging trends in bridge management. The review gives a historical perspective on the development of BMS and identifies four main modules of a complete BMS: data collection, diagnosis, prognosis, and decision making. By analysing these modules and their interconnections, the review highlights that current BMS practices still rely predominantly on visual inspections. However, the inherent limitations of inspections have led infrastructure operators to explore permanent SHM systems, which allow automated data collection and continuous updates on the structural state. Despite their potential, the systematic integration of SHM systems into bridge management practices still faces several challenges, including: (i) the high costs associated with the extensive deployment of permanent contact-type SHM systems at a network scale, and the need to manage and post-process vast amounts of monitoring data; and (ii) the lack of standardized, consistent, and harmonized procedures for the design of monitoring systems based on a quantitative evaluation of their performance and effectiveness.

This chapter provides a summary of the key findings from my literature review on BMS, *"Bridge management systems: A review on current practice in a digitizing world"*, with particular emphasis on the role of Structural Health Monitoring in current BMS practice, including recent advancements and persistent limitations. The full published manuscript is presented in Chapter 5.

2.1 BMS history and role

The effective management of transportation infrastructure is essential for ensuring safety, supporting economic growth, and maintaining international competitiveness. Bridges functionality can be compromised by ageing, increasing traffic demands, environmental exposure, and extreme events [1, 2]. Some forms of deterioration can be subtle and difficult to detect, yet they may lead to premature failure of critical components.

Many bridges were built during the major construction boom of the 1960s, particularly in Europe, and thus today exceed their design service life. According to the 2025 Infrastructure Report Card by the American Society of Civil Engineers (ASCE) [3], 45% of the 623,000 U.S. bridges are 50 years or older, 6.8% are in poor condition and 49.1% are in mediocre condition. The US Federal Highway Administration's

(FHWA) estimated bridge-related system rehabilitation needs at $191 billion. In Japan, around 40% of bridges are at least 50 years old [4]. In China, according to the Yearbook of China's Transportation, around 15% of bridges are in dangerous situation [5]. In Italy, it was estimated that 50.4% of the highway bridges are at least 50 years old [6].

Historical data show that between 1989 and 2000, hundreds of bridge failures have occurred in the United States, triggered by floods (about 53% of failures), collisions (about 20% of failures), design and construction flaws, or insufficient maintenance [7]. Recent decades have also seen numerous bridge failures with dramatic consequences in different nations [8], including the deadly collapse of the Morandi Bridge in Genoa, Italy, in 2018, with the loss of 43 people [9].

Replacing ageing structures at large scale is economically, logistically and environmentally unfeasible. Hence, infrastructure managers must find optimal strategies to keep the assets in service while ensuring safety and functionality [10]. The ultimate objective is to optimize budget allocation in a resource-costrained environment by maintenance planning and interventions prioritization based on structural condition assessment [11, 12]. Achieving this is only possible by relying on inspection programs and monitoring data to assess the bridges stocks deterioration level and structural performance in terms of durability, serviceability and reliability [13]. This paradigm forms the core of Bridge Management Systems (BMS), which were introduced to enhance maintenance efficiency, ensure safe operations, and optimize available economic resources.

BMS aim to provide a rational framework for data collection, structural state assessment, future deterioration prediction, and finally decision support on intervention prioritization and resource allocation [14]. Different countries and infrastructure managers have developed BMS that include codes, guidelines, and specific software programs applicable at both the individual bridge level (project-level) and the network level [15].

The development of BMS gained momentum after major failures such as the 1967 collapse of the Silver Bridge in the United States, which highlighted the need for systematic management practices. The first BMS softwares emerged in the 1970s–for example, Denmark's DANBRO– and were followed in the 1980s and 1990s by national platforms such as DISK in the Netherlands, BaTMan in Sweden, Pontis/BrM and Bridgit in the United States, KUBA in Switzerland, and other systems in Finland, Germany, France, and many other countries [14]. Over time, numerous road agencies and operators adopted, adapted or developed BMS software to meet their specific regulatory and operational conditions. In

[14], a list of the best-known software-based digital BMS in Europe and in the world is reported. Figure 2.1 reports a map of the BMS software employed worldwide.

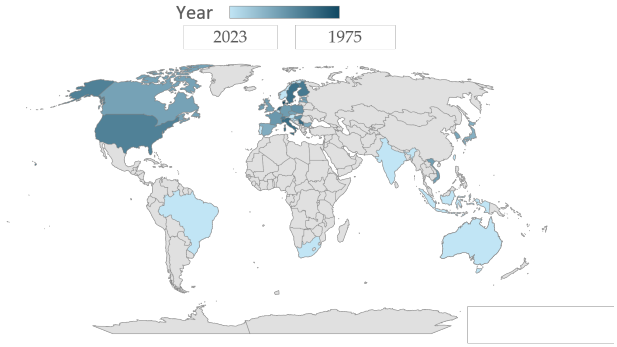

Year	Country	BMS name
1975	Denmark	DANBRO BMS
1977	Belgium	BDOA
1985	Netherlands	DISK
	Serbia	BPM
1986	Italy	Oracle, SQL Server
1987	Sweden	BaTMan
1990	Finland	The Finnish BMS (FBMS)
1991	Switzerland	KUBA
1992	USA	Pontis
1993	USA	Bridgit
1996	Hungary	Own System
1997	Poland	SMOK
1999	France	Own System
2000	Germany	Bauwerk Management System (GBMS)
2001	Poland	SZOK
	Vietnam	Bridgemann
	Ireland	Eirspan
	England	Oracle
	Estonia	Pontis
2002	Latvia	Lt Brutus
	Canada	Ontario BMS (OBMS)
	Czech Republic	IIS database + MS SQL Server
2003	Korea	Korea Road Maintenance Business System (KRBMS)
2004	Italy	Autonomous Province of Trento BMS (APTBMS)
	Bulgaria	Scanpoint-Freissinet
2005	Spain	SGP
2006	Japan	J-BMS, Regional Planning Institute of Osaka BMS (RPIBMS)
	Canada	EBMS, PEIBMMS
2008	Canada	Quebec BMB (QBMS)
2019	Croatia	Oracle 10.G
Nowsdays	Germany	BMS-Optimisation tools, SIB-Bauwerke
	Austria	BAUT
	UK	HiSMIS, SIMS, Cosmos, Exor
	Sweden	Safebro
	Finland	SIHA
	Denmark	COWI
	Portugal	GOA
	Canada	GMWT
	Brazil	SGO
	Australia	Bridge ASYST, MRWA, NSW
	Japan	MICHI
	Taiwan	T-BMS
	Italy	SAMOA, PerugiaBMS, Argo, Domus, Netkubed
	South Africa	Struman
	India	Bridgit
	Indonesia	Own system
	Norway	Brutus

Figure 2.1: Timeline of BMS softwares.

Despite significant progress and harmonization efforts [16], the adop-

tion and modernization of BMS remain uneven across countries and operators. Developing or maintaining a custom system often requires substantial financial investment and advanced digital capabilities, and many existing systems still need updates to fully exploit new data sources, particularly Structural Health Monitoring technologies.

2.2 BMS modules

To address diverse management objectives, a BMS must be flexible and incorporate different modules tailored to specific needs. Existing BMSs across countries and operators nowadays have different modules, and non-uniform definitions of BMS modules can be found in the literature [17, 18, 19].

However, some modules are common to all BMSs, namely the inventory module, i.e. the database of the bridge stock records, and the inspection module, which concerns the collection of structural condition data through visual inspections. Often, BMSs limit their scope to these modules.

Considering different approaches in literature, a uniform categorization of BMS modules into four main groups can be identified:

(1) **Data management**, which deals with the data regarding the stock inventory, including data collection, acquisition, transmission, and storage.

(2) **Diagnosis**, which aims to assess the condition of individual bridge components, single bridges, or infrastructure networks, based on the collected data.

(3) **Prognosis**, which gathers all the activities connected to the prediction of future bridge conditions.

(4) **Decision-making** to identify optimal management actions.

These four modules are strictly connected. Diagnosis and prognosis are carried out based on data collected on bridges and their components. Decision making depends on the results of diagnosis and prognosis and can also influence data management.

2.2.1 Data Management

Efficient data management plays a fundamental role in the effective implementation of a BMS. This process can be divided into four main stages: collection, acquisition, transmission, and storage. Data collection refers to obtaining information on the bridge through inspections or

SHM systems. While visual inspections allow identifying visible signs of deterioration, SHM systems enable gathering continuous, quantitative information on structural performance [20].

SHM systems are intended as the sets of sensing technologies that can be used to collect data on structural characteristics, including the structural response, for the purpose of estimating key parameters representative of the structural state [21]. An SHM system typically includes sensors, data acquisition and transmission modules, databases, and processing units for data analysis. A wide variety of contact-type sensors is available [22], including fiber-optic sensors, piezoelectric sensors, global navigation satellite system (GNSS) receivers, magnetostrictive sensors, and Microelectromechanical Systems (MEMS) [23]. Recent years have seen a surge of remote-sensing technologies, such as space-born satellite SAR [24].

In the acquisition phase, the gathered information is converted into a digital format suitable for processing and analysis. Subsequently, the data is transmitted to central databases via either wired or wireless communication channels. Robust storage solutions, such as cloud-based platforms, provide scalability and remote accessibility, allowing multiple users to simultaneously access and analyze the data.

2.2.2 Diagnosis

The diagnosis phase in BMS consists of assessing the condition of individual bridge components, entire bridges, or even infrastructure networks by using performance indicators (PIs). These indicators quantify the mechanical/physical properties and/or the level of structural degradation, which impact the ultimate capacity and serviceability of the structure [25, 26]. They can be derived both from inspection data and from SHM data.

Condition indicators at the bridge level (BCIs) are quantified by combining the condition rates of individual bridge components assigned during visual inspections [27]. Methods for their calculation include weighted average, qualitative, worst-conditioned component, and ratio-based approaches. BCIs alone cannot provide a clear structural safety judgment since no quantitative evaluation is done from either the resistance and the loading sides. On the other hand, nondestructive tests (NDTs) like ultrasonic testing, eddy current testing, and ground-penetrating radar, as well as destructive tests (DTs), involve controlled damage to evaluate material properties as key structural state parameters.

Key state parameters evaluated by means of SHM include a wide variety of options. They can be subdivided into main categories: dynamic (vibrational) and static parameters. They can identify a local response

or a global response of a structure. For instance, the strain drift is a static monitoring parameter, which provides information about the local structural response where the sensor is deployed [28]. In contrast, modal parameters are related to dynamic structural properties, and aim to assess the overall structural integrity [29]. A non exhaustive list of critical monitoring state parameters, with the corresponding physical quantity to be measured by means of the SHM system, is provided in Table 2.1.

Table 2.1: Key state parameters and observed quantities in SHM.

State parameter θ		**Observed quantity y**
Long-term strain trend $[\mu\varepsilon/year]$	$\dot{\varepsilon}$	Strain, temperature
Long-term displacement trend $[mm/year]$	$\dot{u}$	Displacement, temperature
Long-term rotation trend $[\mu rad/year]$	$\dot{\phi}$	Rotation, temperature
Instantaneous strain $\mu\varepsilon$	ε	Instantaneous strain
Scouring depth $[m]$	s	Scouring depth
Joint opening $[mm]$	a	Joint opening

State parameters provide information about the structural state and deterioration, usually with reference to their value in a baseline state. Otherwise, they can be directly correlated to the presence of damage by means of Damage Indicators (DIs) and compared to thresholds in order to classify the structural state.

In physics-based approaches, the value of the chosen key state parameter or DI is inferred by means of monitoring observations, which are related to the state parameter through an interpretation model.

Key state parameters and DIs should be sensitive to the specific phenomena to monitor, and they should be robust with respect to other sources of variability so that they would vary consistently only with the level of damage. Nevertheless, a critical problem for damage identification and structural state evaluation in SHM is the impact of operational and environmental effects on the quantities measured by sensors. Live loads as well as temperature changes (both daily and seasonal) can significantly influence the structural response and increase the uncertainty in the key parameters and DIs [30].

Overall, the implementation of PIs derived from SHM in BMS software is still at an early stage of development.

Finally, PIs related to structural reliability and risk can be identified. They include structural reliability and risk, cumulative probability of failure, survivor function, hazard rate function, structural redundancy, structural robustness, structural resilience, and load rating factor [31].

Other types of indicators are non-technical, such as economic, social, and environmental indicators, which complement technical indicators even though they are not systematically implemented in BMSs [32].

2.2.3 Prognosis

The prognosis module in BMS allows predicting the future states of bridges and their components by means of deterioration models, based on their current condition. BMSs predominantly employ two categories of deterioration models: deterministic or stochastic [33].

Deterministic models provide a single, definite solution for a given set of input parameters and model structures. The outcomes of these models are entirely determined by their inputs, assuming well-defined and predictable cause–effect relationships, without explicit consideration of uncertainty. For example, deterministic linear regression models describe deterioration as linearly dependent on time.

In contrast, stochastic models explicitly account for the inherent uncertainties involved in the deterioration process by incorporating random variables. Stochastic models can be broadly classified into two main approaches: state-based models, such as Markov Chain models, which describe deterioration as transitions between discrete condition states [34]; and time-based (or duration) models, which focus on the probabilistic estimation of the time taken for a component to deteriorate from one state to another, providing insights into the expected lifespans under varying conditions.

2.2.4 Decision Making

The decision-making module in BMS aims to optimize and prioritize maintenance activities identifying a priority ranking between different structures. It exploits the outputs from the diagnosis and prognosis modules.

Two primary approaches for decision-making can be employed in BMS: the top-down approach, which focuses on network-level optimization, considering the mutual relations and common features among bridges, minimizing the total costs of maintenance and delay of interventions, and maximizing the road network performance [35]; and the bottom-up approach, which concentrates on individual bridge maintenance optimization, establishing minimum performance standards and suitable intervention schedules for the bridge. The selection of the best approach generally depends on the size of the network and also on the optimization method employed.

Four different maintenance strategies are used in BMS, namely corrective, preventive, condition-based and predictive [36]. Corrective maintenance includes repairs or replacements of faulty components typically identified during inspections. Preventive maintenance consists of scheduled periodic activities aiming at reducing the risk of failure or severe

performance degradation of bridges. Condition-based maintenance uses data from diagnosis module (derived by means of visual inspections, tests, and SHM systems) to track deterioration and make decisions based on the current structural state. Predictive maintenance exploits prognosis module information to forecast future failures and to determine the optimal inspection and intervention scheduling.

Optimization methods adopted in BMSs consist mainly in single-objective optimization procedures to allocate resources and prioritize maintenance interventions, including priority index ranking and cost-benefit analyses. Priority index ranking approach evaluates and ranks interventions both at an element and at a network level, based PIs calculated in the diagnosis module [37]; cost-benefit analysis aims to identify the most economically advantageous maintenance strategy, considering life-cycle costs and incremental benefit analysis [38]. Societal, functional, and environmental aspects could be taken into account using multi-criteria [39].

2.3 Structural Health Monitoring advances in Bridge Management

The current practices in BMS are closely related to the methods adopted for data collection.

Nowadays, the management of bridge stocks still often relies solely on evaluating the BCIs based on visual inspections data, and visual inspections remain the most common method for data collection [40]. However, visual inspections come with notable drawbacks, including the subjectivity of results and challenges in accessing hidden structural components [13]. Moreover, condition ratings based on visual inspection overlook the quantitative assessment of the bridge performance in terms of key parameters representative of the structural state and deterioration level [31].

In recent decades, the limitations of traditional inspection methods have prompted infrastructure managers to adopt SHM systems, which enable automated data acquisition and continuous assessment of structural conditions [10]. Thus, in the data collection and structural state diagnosis context, bridge management will be increasingly based on integrated results of both SHM and visual inspections. Although key state parameters and DIs extracted from SHM data have been extensively investigated by the research community, their systematic integration into BMS frameworks requires notable regulation and standardization efforts [14].

Following the catastrophic collapse of the Morandi Bridge in Genoa

in 2018, Italy has made substantial investments in SHM systems for infrastructure [41]. ANAS, for instance, has launched a nationwide "Structural Health Monitoring Program" financed with 275 million euros [42]. From the research perspective, the FABRE national consortium supports advances in bridge monitoring and management [43], while the ReLUIS network actively contributes to developments in seismic and structural monitoring [44]. At both national and international level, various initiatives and organizations continue to promote knowledge exchange and innovation in SHM practices [45, 46].

Over the past few decades, several national guidelines have been published in different countries with the aim of standardizing SHM practices. Their objectives are to improve understanding of the SHM process, enhance awareness of its benefits, and establish consistent rules and protocols [47].

Among them, in Italy, the most relevant are the "Italian Guidelines for Structural Health Monitoring UNI/TR 11634:2016" [48] and the "Italian Guidelines for Risk Classification and Management, Safety Assessment and Monitoring of Existing Bridges" [49].

The first document provides general instructions for SHM system users, designers, and installation/maintenance operators, aligning with the international state of the art. It supports the conception, design, management, and use of SHM systems for civil infrastructure. It also defines a general logical procedure for SHM system design, starting from the definition of the monitoring objectives and the identification of the key state parameters, followed by the selection of the physical quantities to be measured, the preliminary configuration of the monitoring solution (sensor technology, system architecture, acquisition methods), and the selection of interpretation models. Finally, it includes the verification of the SHM system's accuracy requirements.

The second document focuses on the safety management of existing bridges, with the aim of preventing unacceptable levels of deterioration and reducing risk. It is structured into three main parts:

(1) inventory and risk classification of bridges;

(2) safety assessment;

(3) control and monitoring of existing bridges.

The guidelines adopt a multi-level approach consisting of six levels (from Level 0 to Level 5). The core of the methodology is Level 2, which involves the evaluation of the *Attention Classes* for each structure, based on the collected inventory and inspection data. For bridges assigned to

"High" or "Medium-High" Attention Classes, the installation of permanent or periodic SHM systems is required. The data collected by the systems must be analyzed to derive Performance Indicators (PIs). These PIs are then used to trigger threshold-based alerts, to develop degradation models and to update the Attention Class assigned to the bridge.

2.4 Current limitations

Despite the recent advances and development of SHM practices in bridge management, it is important to also acknowledge the current limitations of SHM systems and their systematic implementation within BMS.

First of all, there is no widely accepted procedure to demonstrate both the return on investment and the effectiveness of the performance of a SHM system. Nevertheless, an important research effort has been mounted over the past decade toward the quantification of the return on investment in an SHM system, for instance through the VoI from Bayesian decision theory. The VoI can be compared with the cost of the SHM system to establish if the SHM should be adopted: if the VoI is higher than the corresponding cost, the SHM should be installed [50].

One of the greatest limitation to the extensive employment of SHM technology consists in the lack of rules regarding the choices of technologies to use and, in general, the procedure to follow for monitoring system design. The Italian Guidelines for Structural Health Monitoring [48] propose a logical procedure for performance-based monitoring system design. However, further effort is needed for supporting its practical implementation by defining formulations for the calculation of the main involved quantities (i.e., the monitoring demand and capacity) [51].

The cost for extensive on-site SHM instrumentation can range significantly, limiting SHM application to strategically important or most degraded bridges of a stock. Moreover, on-site permanently installed SHM systems degrade in time and require continuous maintenance, making it difficult to distinguish between anomalous data caused by out-of-service systems, malfunctioning sensors, or actual structural damage [52]. To overcome such limitations, network-scale device-free SHM approaches are gaining popularity to address scalability issues characterizing classic contact-based SHM approaches. Among these, spaceborne InSAR technology has emerged as a powerful solution to remotely monitor long-term phenomena, providing velocity maps and millimeter-level time series of displacements [53, 54]. Nevertheless, the application of InSAR technology for infrastructure monitoring is still relatively new, and requires significant research efforts for interpretation and integration within BMS frameworks. Furthermore, network-scale SHM appli-

cation implies the collection of huge amounts of data that have to be adequately managed and post-processed, highlighting the need for low-input, speedy and accessible analysis approaches.

In conclusion, it is also important to specify that SHM systems should not be considered as a replacement of visual inspections, but rather as an integration. The combination of visual inspection data with SHM data can enhance the understanding of the behavior of the bridge and allow experts from different locations to virtually inspect the bridge for final assessment. SHM techniques – especially the vibration-based ones – are generally not sensible to superficial and small damages, which instead can be directly detected by visual inspections. Moreover, the lack of experts proficient in the proper analysis of SHM processes still leads to a preference among managers for more familiar data collection methods, such as visual inspections [55].

3. Multi-Temporal Interferometric Synthetic Aperture Radar technology

In Chapter 2, recent advancements in Structural Health Monitoring (SHM) within bridge management practices were discussed. Since the last few decades, bridge management is increasingly relying on SHM data rather than solely on visual inspection data [56]. Monitoring infrastructure through permanently installed sensors has repeatedly demonstrated its value in providing accurate and timely information on the state of bridges, allowing to overcome several critical limitations of traditional visual inspection methods for data collection and structural condition assessment [57].

Despite their advantages, contact-type SHM systems still present critical limitations. As highlighted in Chapter 2, a major constraint lies in the high cost of SHM instrumentation, which restricts its application mainly to strategically important bridges. Additionally, these systems are subject to progressive degradation over time, requiring continuous maintenance and causing reliability issues [58].

To address these challenges, recent years have witnessed growing interest in device-free remote sensing technologies, such as Synthetic Aperture Radar (SAR).

This Chapter provides an overview of the most relevant theoretical background related to SAR imagery and the MT-InSAR processing steps. This widely adopted technique, which enables the extraction of highly accurate ground deformation measurements from SAR imagery, was employed in this thesis, particularly in the studies presented in Chapters 6 and 7. The purpose of this Chapter is to outline the fundamental concepts underlying the use of MT-InSAR, with particular reference to its application in bridge monitoring, while avoiding extensive technical details and derivations that are available in specialized reference texts. For further technical details on SAR Interferometry and SAR data processing, readers are referred to [53, 59, 60, 61]. Finally, this Chapter also highlights the main current challenges and limitations hindering the widespread application of MT-InSAR for infrastructure monitoring, including the issues addressed in my research work presented in Chapters 6 and 7.

Some sections of this chapter include material and descriptions drawn from my publications, *"Interpretation of Bridge Health Monitoring Data from Satellite InSAR Technology"* and *"Bridge Monitoring with Satellite InSAR Technology and Clustering Algorithm"*, reported in Chapters 6

and 7 of this thesis.

3.1 Basic SAR principles

Synthetic Aperture Radar (SAR) is an active remote sensing system that acquires data by transmitting microwave pulses towards the Earth's surface and recording the backscattered returns. It operates within the invisible portion of the electromagnetic spectrum, with wavelengths ranging from millimeters to meters. The SAR sensor on the satellite emits the pulse, and after it is emitted there is an "echo window" period where the SAR sensor collects the backscattered echoes and stores the received signals.

Current spaceborne SAR sensors typically operate in three wavelength bands: L-band (24 cm), C-band (5.6 cm), and X-band (3.1 cm). Unlike optical imaging systems, which rely on visible light waves, SAR can penetrate clouds and precipitation, and can operate both day and night, regardless of solar illumination. This makes it a powerful technology for providing high-resolution, all-weather imaging with global coverage.

SAR satellites follow near-polar orbits, meaning they travel in a North–South direction from pole to pole around the Earth. During the ascending pass, the satellite moves northward along one side of the planet, while during the descending pass, it travels southward along the opposite side.

SAR systems have a side-looking imaging geometry, meaning that the sensor is looking sideways with respect to the flight direction. Figure 3.1 illustrates the typical SAR imaging geometry. The satellite orbit direction is called Azimuth. The Nadir is the point on the earth surface directly below the satellite sensor as it progresses along its line of flight (vertical projection). The width of the acquired image is known as the swath width, whereas the image length depends on the duration for which the radar remains active. Depending on the SAR acquisition mode, the swath width can vary from 30 km to 500 km. The satellite viewing direction is defined as the Line of Sight (LoS), and has an inclination, θ, of 20 to 50 relative to the vertical (Nadir) [62].

The satellite revisit time is the time between any two acquisitions of the same location, including those from adjacent orbital paths with some overlap. The satellite repeat pass is the time interval between two acquisitions of the same location by a satellite, where the satellite follows the same orbital path. Revisit time or repeat pass determine the temporal baseline, i.e. the time difference between two radar acquisitions of the same area.

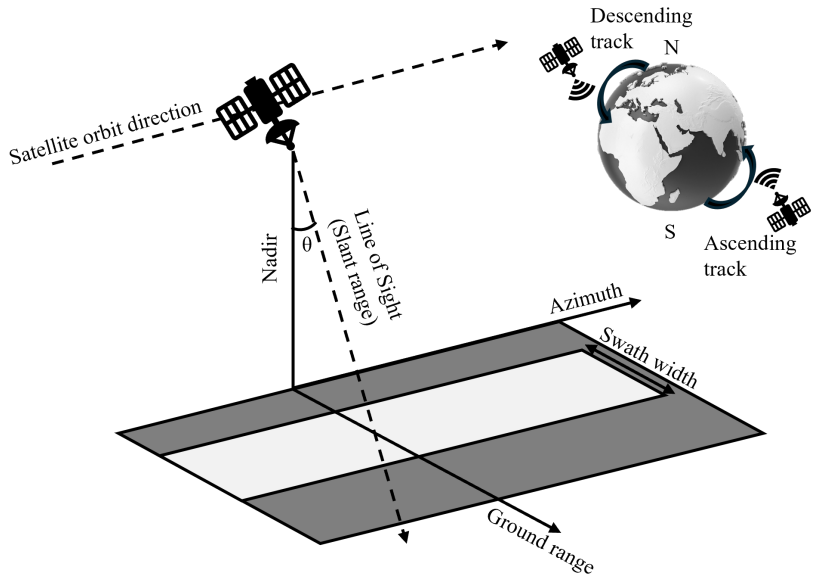

Figure 3.1: Side-looking acquisition geometry of SAR satellites and ascending and descending orbits.

The satellite position over the same area at two distinct times is never perfectly identical, and the spatial separation between two antenna positions when acquiring data is defined as the spatial baseline. The projection of the baseline along the direction perpendicular to the satellite LoS is the perpendicular baseline.

A SAR signal is a sinusoidal wave with a period of 2π radians, which contains amplitude and phase information and has a specific wavelength. SAR imaging is the production of a digital SAR image that is made up of a two dimensional matrix formed by columns and rows of 'pixels'. The two dimensions of the matrix correspond to the Range direction and the Azimuth direction. The pixels are also known as 'resolution cells' and are associated with an area on the earth's surface (the size of the resolution cell varies with each satellite, depending on the wavelength and bandwidth of the transmitted signal [63]). The value in each pixel comes from the received radar reflections and is complex in nature, with the real and imaginary parts of this complex value representing amplitude and phase values respectively. Detailed information about SAR image formation can be found in [64].

3.2 InSAR

SAR Interferometry (InSAR) exploits the phase information of a pair of SAR images acquired at different times over the same area to detect motion of targets on the ground within the observed area [65, 66]. When features on the ground move, the distance between the sensor on the satellite and the earth's surface changes, thereby producing a corresponding change in measured signal phase. The principle of InSAR is to evaluate the changes in measured phase values that occur between two repeat passes of the satellite (and therefore image acquisitions), and use them to quantify ground movement in the direction of the satellite LoS. Images acquired from the same flight track at different times are usually used (along-track interferometry).

In the InSAR technique, an interferogram is produced by crossmultiplying two SAR images acquired over the same area, pixel by pixel. Through this operation, the common backscattered phase within each resolution cell is removed, leaving a residual phase component that reflects the differential path delay of the signal between the two acquisitions. Consequently, an interferogram is a complex image in which each pixel encodes the phase difference between the two SAR observations at the same ground location, ranging from -π to +π radians. This phase variation appears in the image as a series of interferometric fringes, represented in Figure 3.2b as repeating colour cycles.

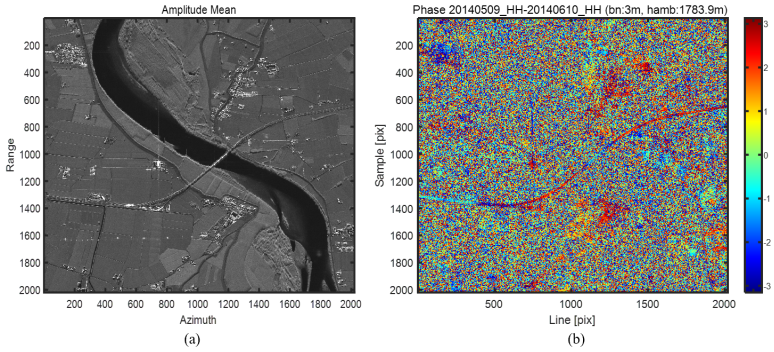

Figure 3.2: (a) SAR image of the Po River Bridge site. (b) Interferogram generated by two radar images acquired over the Po River Bridge site.

The process of along-track SAR interferometry was first explained by Gabriel et al. [67]. The phase information ϕ of one image is directly proportional to the two-way travel distance $2r$ between the radar sensor and the target P, and inversely proportional to the wavelength λ of the

signal (Equation 3.1):

$$\phi = \frac{2\pi}{\lambda} \cdot 2r = \frac{4\pi}{\lambda} r \tag{3.1}$$

Let us assume that the observed ground target moves from point P at time t_0 to point P' at time $t_1 = t_0 + \Delta t$ along the satellite Line of Sight (LoS), resulting in a change in the radar signal path length between the two acquisitions, denoted as Δr. The corresponding phase variation, $\Delta\phi$, between the two temporally separated acquisitions can be expressed as in Equation 3.2:

$$\Delta\phi = \frac{4\pi}{\lambda} \Delta r \tag{3.2}$$

Figure 3.3 provides a schematic representation of along-track interferometry geometry (images taken on the same satellite flight track), using the symbols introduced in the text above.

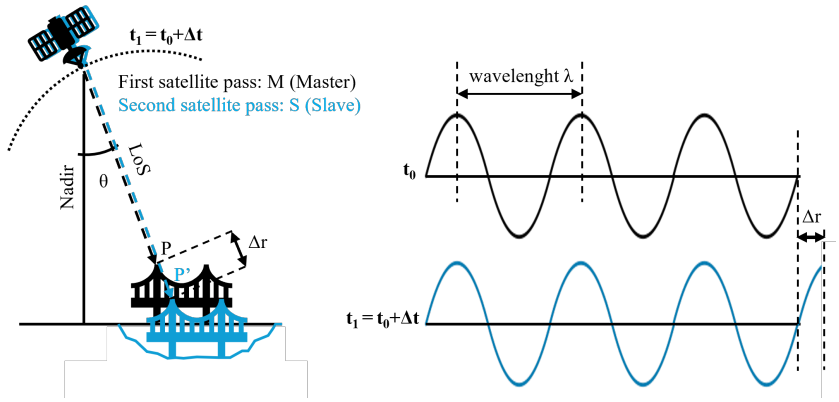

Figure 3.3: Schematic representation of InSAR monitoring of bridge deformations.

In practice, however, the problem is more complex than the idealized case described above. The interferometric phase $\Delta\phi$ does not only capture the displacement of the observed target ($\Delta\phi_{def}$), but also includes several additional contributions: the flat-earth component $\Delta\phi_{earth}$, the topographic component $\Delta\phi_{topo}$, the atmospheric delay $\Delta\phi_{atm}$, and a noise term $\Delta\phi_{noise}$:

$$\Delta\phi = \Delta\phi_{def} + \Delta\phi_{earth} + \Delta\phi_{topo} + \Delta\phi_{atm} + \Delta\phi_{noise} \tag{3.3}$$

The components $\Delta\phi_{earth}$ and $\Delta\phi_{topo}$ arise from differences in the apparent Earth curvature and local topography between two SAR acquisitions of the same area, due to the slightly different satellite positions with respect to its nominal orbit when revisiting the scene.

The atmospheric phase component $\Delta\phi_{atm}$ reflects signal delay caused mainly by differences in atmospheric conditions, i.e. water vapor content, between the two acquisition times.

Finally, the noise component $\Delta\phi_{noise}$ accounts for phase variations possibly introduced by spatial and temporal decorrelations of the radar signal, co-registration inaccuracies, orbital errors, changes in soil moisture, and residual errors related to the imperfect estimation of the other phase components.

To evaluate the actual displacement signal component, all additional phase contributions in Equation 3.3 must be estimated and removed. The terms $\Delta\phi_{earth}$ and $\Delta\phi_{topo}$ are usually removed by using precise orbital information and a Digital Elevation Model (DEM) of the study area. However, when only a pair of SAR images is used to generate a single interferogram, it is challenging to correct atmospheric effects and eventual signal decorrelations.

Multi-interferogram approaches –namely, Multi-Temporal (MT)-InSAR techniques– allow all these undesired components to be modelled and thus removed, thereby improving the accuracy in the estimation of the target deformation phase. This concept is discussed in greater detail in the following section (Section 3.3).

3.3 MT-InSAR

In Section 3.2, InSAR technique for extracting ground deformation from the signal measured by SAR sensors was described. This technique involves comparing a pair of SAR images and allows for measuring target displacements with centimeter-level accuracy [53]. However, when monitoring infrastructure, the observed deformations can be even smaller– in the order of a few millimeters–depending on the type of phenomenon causing the movement, and therefore higher accuracy is required.

InSAR technique can be further enhanced to achieve millimeter-level sensitivity by analysing long series of SAR images using a set of advanced signal processing methods, known as Multi-Temporal InSAR (MT-InSAR) [68]. As a result, data acquired by SAR satellites can be effectively used to monitor not only ground movements but also tiny displacement of structures, dams, buildings, bridges and more [69].

In MT-InSAR approaches, multiple interferograms are generated by comparing image pairs sequentially until the entire stack of images has been processed. This allows for the analysis of the temporal evolution of the signal in the observed area, thereby enabling the separation of ground motion from atmospheric disturbances and reducing decorrelation effects.

In most MT-InSAR applications, a linear model of ground motion is typically assumed, but nonlinear models can also be employed [70]. In addition, seasonal thermal expansion effects can be modelled and estimated within the MT-InSAR processing framework. This is possible because multiple SAR acquisitions collected on different days over the same area can capture seasonal variations in environmental conditions while remaining unaffected by diurnal temperature and humidity changes, as SAR satellites are programmed to pass over the same area at a fixed local time in Coordinated Universal Time (UTC) [71].

MT-InSAR encompasses various methods such as Small Baseline Subset (SBAS), Persistent Scatterer InSAR (PSInSAR), Quasi-PS, Iterative Persistent Terrain Analysis (IPTA), SqueeSAR, Persistent Scatterer – Distributed Scatterer (PS-DS). Among those, the most established for obtaining high-accuracy results is undoubtedly the approach introduced by Ferretti et al., namely the Persistent Scatterer InSAR (PSInSAR) [54]. This approach only processes a subset of image pixels corresponding to highly reflective ground targets that maintain stable backscattering over time, therefore referred to as Persistent Scatterers (PS). Throughout this thesis, the term MT-InSAR will specifically refer to this technique.

Thanks to their geometry and dielectric characteristics, man-made structures such as bridges, buildings, monuments, and metallic elements, as well as natural outcrops like exposed rocks, represent ideal PS candidates. Conversely, targets subjected to significant variability or producing weak radar returns, such as vegetation and water bodies, typically do not generate PS. In urban areas, the density of PS can range from several thousands to tens of thousands per km^2, while in non-urban environments PS can still be abundant along infrastructures such as viaducts, roads, and railways [72]. These targets are characterised by strong radar reflections, which dominate over weaker scatterers within the same pixel, for instance vegetation or water.

The main crucial steps involved in MT-InSAR workflow are the following:

(1) **Connection graph**. The combination pairs of SAR images used to generate the interferograms is defined. The interferograms to be generated are based on the relationships established in this step by means of the connection graph (Figure 3.4). The master image of the dataset is selected. It is the barycentre of the connection graph and minimises the temporal and normal baselines, reducing the temporal and spatial decorrelation between images. The master image is the reference image to which all other (slave) images are co-registered and relative to which displacements are measured.

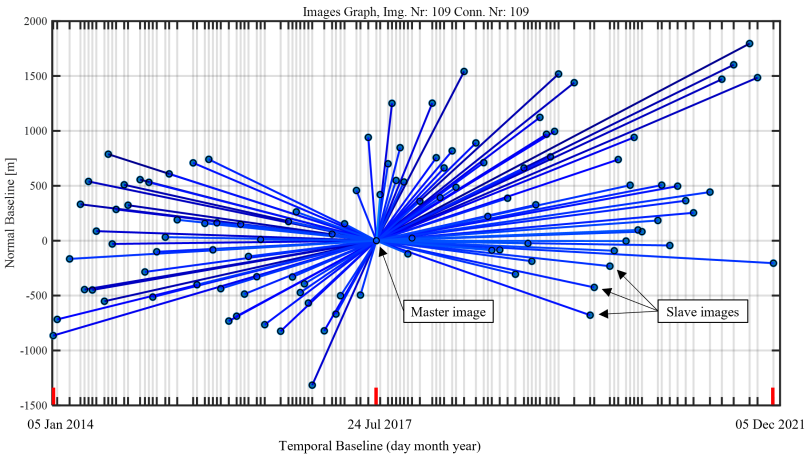

Figure 3.4: Example connection graph with red marks highlighting dates of first, master, and last images.

(2) **Coregistration**. The SAR images are coregistered, meaning that they are spatially aligned using the amplitude values within the SAR image pixel. The quality of the interferograms is higher when the images are correctly aligned, reducing $\Delta\phi_{earth}$ (Equation 3.3).

(3) **Interferogram generation**. Interferograms are generated to measure the phase difference between SAR images (master-slave pairs). The result is a pattern of fringes containing the information on the relative phase changes between the two images (Figure 3.2b). Each cycle of colour represents an interferometric phase cycle (modulo 2π, range from $-\pi$ to $+\pi$).

(4) **Topographic phase removal**. The topographic phase term $\Delta\phi_{topo}$ (Equation 3.3) must be removed to isolate $\Delta\phi_{def}$. In order to do so, the topographic phase is derived from another data source, i.e. a Digital Elevation Model (DEM).

(5) **Atmospheric-phase removal**. The atmospheric phase component of each image is primarily due to the water vapor content in the troposphere which the SAR has to pass through and varies from image to image (and also within a single image). The removal of $\Delta\phi_{atm}$ is critical because the atmospheric phase contribution is one of the primary sources of error in InSAR data. An initial selection of pixels related to potential candidate targets (the PS) is processed by connecting them in a spatial graph and estimating the main parameters affecting the interferometric phase along the con-

nections (namely, deformation velocity, thermal expansion, and height of the targets). After this estimation, the residual phase signal is used to estimate and remove the Atmospheric Phase Screen (APS) contribution from the original SAR images [73].

(6) **Geocoding and Persistent Scatterer Selection**. Once the APS phase contribution is removed from the images, a higher number of pixels can be analysed with the MT-InSAR algorithm to derive the parameters with respect to a common reference point (RP)–a specific PS used to anchor the estimated deformation time series. The RP is selected based on high temporal coherence and limited deformation over time. After estimating the parameters, PS can be filtered based on a limit temporal coherence value (usually 0.6 or 0.7). The temporal coherence is a quality metric of the extracted displacement time series with respect to the model used and ranges from 0 (low quality) to 1 (high quality). Finally, deformation time-series can be extracted for every PS based on the filtered phase data, and the selected PS points are mapped onto commonly used earth coordinates (Figure 3.5).

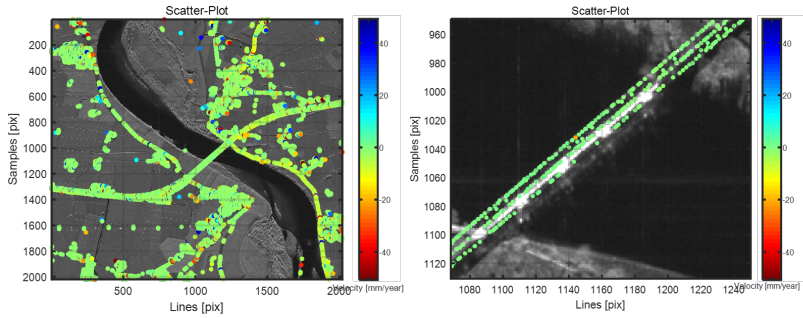

Figure 3.5: Example of (a) map of PSs selected by means of MT-InSAR analysis over the area of the Po River Bridge; (b) focus on the PSs on the bridge.

The final outcomes of MT-InSAR analysis include, for each identified PS: the deformation time-series; the average velocity of deformation time-series; the geospatial information (geographic coordinates, elevation); the temporal coherence.

Displacements are relative in time and space. In time, they are relative to the date of the master image; in space, they are relative to the displacement of the common RP. Note that deformations mean displacements along the satellite LoS. A negative deformation means that the PS

moves away from the satellite, while a positive deformation means that the PS moves towards the satellite.

The quality and reliability of MT-InSAR measurements is commonly expressed through the temporal coherence parameter, ζ_{PS} (Equation 3.4):

$$\zeta_{PS} = \left| \frac{1}{N} \sum_{n=1}^{N} e^{i(\Delta\phi_n - \Delta\psi_n)} \right| \tag{3.4}$$

where N is the number of images used in the processing, $\Delta\phi_n$ is the measured interferometric phase of the n$^{\text{th}}$ image, and $\Delta\psi_n$ corresponds to the modelled interferometric phase of the same image, obtained from the estimated parameters of the MT-InSAR analysis. The temporal coherence ranges from 0 to 1; higher values indicate greater consistency between observations and the adopted phase model, and therefore correspond to more accurate and reliable displacement estimates.

3.4 Accuracy of MT-InSAR derived displacements

The capability of MT-InSAR to reach a millimetre scale accuracy accuracy on single deformation measurements depends on the data quality and the joint use of processing parameters and methodologies. Indeed, the accuracy of MT-InSAR results is inherently affected by several sources of uncertainty related to both the SAR data and the MT-InSAR processing chain.

The technological parameters that affect the quality of MT-InSAR results include the wavelength and bandwidth of the SAR signal (decreasing from L-band, wavelength $\approx$ 23 cm, to C-band, wavelength $\approx$ 5.5 cm, and to X-band, wavelength $\approx$ 3.1 cm), the revisit time, the total observation period, the spatial resolution, and the orbital tube.

The deformations and deformation rates accuracy is higher for small wavelengths, high spatial resolution (small pixels dimension in Range and Azimuth directions), short revisit times and long monitoring periods (high number of acquisitions) [63, 73]. The height elevation measure, which impacts on the product geocoding (i.e. on the final geo-location precision of the PS), depends also on the orbital tube size. The density of measurable PS targets on the ground is mainly influenced by the spatial resolution: high-resolution data lead to a significant increase in the detectable number of stable PS.

In general, the X-band missions provide the best performance in terms of accuracy, especially for limited observation time spans. The use of small wavelengths (X-band) is particularly necessary in applications measuring small displacement variations, such as infrastructure moni-

toring, allowing to capture variations in the order of a few millimetres between satellite acquisitions.

Primary sources of error that arise in the MT-InSAR processing chain, which may lead to noisy or biased results, include:

- **phase ambiguity**, when the phase unwrapping process does not occur correctly due to signal amplitude exceeding the 2π phase variation range between successive satellite passes;
- **temporal decorrelation**, caused by changes in surface properties between acquisitions, which can degrade coherence and reduce the number of reliable PS;
- **atmospheric phase delay**, where uncorrected atmospheric signals introduce phase shifts unrelated to ground motion;
- **topographic phase removal**, where inaccuracies in the DEM can introduce biases in both displacement estimates and geolocation;
- **baseline estimation**, where incorrect estimation of the baseline between image pairs can affect phase computation and PS selection.

The potential for MT-InSAR technique to provide submillimetric measurement accuracy has previously been demonstrated.

Field experiments have verified the accuracy of MT-InSAR measurements, confirming the capability of MT-InSAR to reach millimetre-scale accuracy [74, 75]. Ferretti et al. [68] designed an experiment using two dihedral reflectors which were moved a few millimetres between SAR acquisitions, and found that the standard deviation between InSAR measurements and ground truth was 0.75 mm in the vertical direction, and 0.58 mm in the horizontal direction.

Moreover, several authors have assessed the accuracy of MT-InSAR measurements through real case studies, by comparing SAR-derived data with ground-based observations obtained using other surveying and measurement techniques, such as topographic monitoring systems and GNSS. These studies demonstrate that the standard deviations between X-band MT-InSAR displacement measurements and on-site measurements is typically in the range of 1–3 mm [76], [77].

3.5 SAR missions and datasets

Since the early ’90s, hundreds of SAR satellites have been orbiting the Earth, providing weather-independent imagery of the Earth with different radar frequencies and wavelength, resolutions, acquisition modes and revisit times. Some of these satellites are no longer active, but have pro-

vided extensive data archives that remain valuable for investigating past deformation processes and historical analysis.

Figure 3.6 presents an up-to-date overview –to the best of the author's knowledge– of the main past, current, and upcoming satellite SAR missions, specifying for each sensor the operating frequency band, the revisit time, and the spatial resolution.

Ongoing SAR missions include COSMO-SkyMed, TerraSAR-X, Sentinel-1, and many others. These second generation missions can achieve meter-scale spatial resolutions with revisit times of only a few days [78].

Latest satellite missions, such as ICEYE and Capella, along with future scheduled missions, will soon be able to deliver data at sub-meter resolution and with revisit times on the order of hours, enabling the potential for near real-time monitoring with SAR technology [79].

This research makes use of X-band data (3.1cm in wavelength), as these satellites collect SAR images with a higher accuracy than L-band or C-band satellites. Specifically, I analysed satellite images acquired by the COSMO-SkyMed mission operated by the Italian Space Agency (ASI) in the Stripmap HIMAGE swath mode, with a spatial resolution of 3x3 m, covering large regions of 40x40 km within a single satellite scene.

This high-resolution imagery is provided free of charge to the scientific community for research purposes upon submission of a scientific proposal, while most X-band missions are commercial satellite constellations, and so imagery must be either purchased from the provider or granted for academic research use.

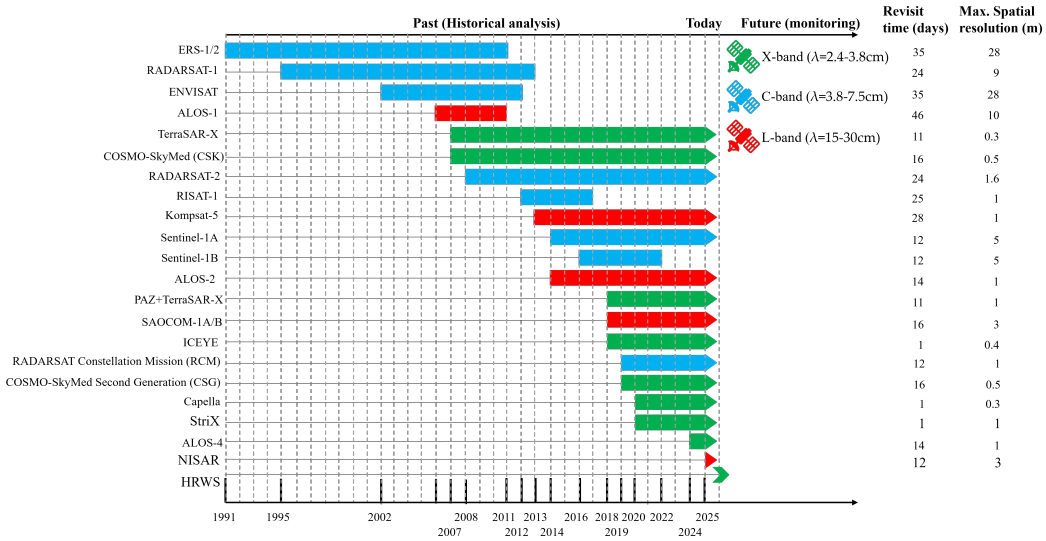

Figure 3.6: Timeline of past, present and future SAR missions between 1991 and 2025, and their main features.

3.6 Applications of InSAR to bridge monitoring

InSAR has emerged as a powerful tool for monitoring subsidence, uplifting, and landslides on a large scale. Among recent research contributions, Yu et al. [80] applied MT-InSAR combined with principal component analysis (PCA) to analyse long-term surface deformations in the Liaohe oilfield. Ghaderpour et al. [81, 82] used InSAR time-series to monitor slow-moving landslides in Central Italy and to investigate the impact of river flow and climate variations on ground deformation in an industrial area of the Sacco River Valley.

In recent years, the research community has also started to investigate the possibility of using InSAR technology for monitoring the response of civil structure and infrastructure.

As far as buildings are concerned, visual inspection campaigns were conducted in [83] to confirm the reliability of satellite technology in determining differential movements that would decrease serviceability, and the negative effects of the subsidence phenomenon have been observed in [84]. The reliability of structural monitoring of dams through InSAR technology was studied by Di Martire et al. [85], even though it was carried out by first-generation sensors (ENVISAT) with low spatial/temporal resolution. However, this study encouraged monitoring dams with higher spatial resolution sensors, as in the case of [86]. InSAR has also been used for monitoring ground surface movements following the con-

struction of underground tunnels. Two applications are reported by Barla et al. [87]: the first emphasises the integration between InSAR monitoring and traditional monitoring; the second studies the temporal evolutions of settlements along a landslide slope hosting two tunnels using Multi-Temporal InSAR. Regarding roads and railways, the possibility of large-scale monitoring of these structures through InSAR is demonstrated in [88]. Similarly, Macchiarulo et al. [89] presented a completely automated monitoring solution for road networks, highlighting possible damages or unexpected displacements.

Delving into the published studies on bridge monitoring using InSAR technology, Selvakumaran et al. [90] extracted important information regarding the effects of bridge scour. Through the analysis of historical series, the authors observed unexpected behaviour of the pier affected by scour already one month before its collapse. Selvakumaran et al. [91] also combined InSAR with traditional instrumentation, including total stations and sensors installed on the bridge, for the monitoring of Waterloo Bridge. DePrekel et al. [92] studied the progressive displacement of some bridges in California (USA), observing how these movements were not attributable to structural defects but were caused by subsidence phenomena resulting from the continuous water pumping from the surrounding aquifers. Milillo et al. [93] demonstrated that it was possible to measure past anomalous deformations of the Morandi Bridge (Italy)–which collapsed in 2018–using archived InSAR images, highlighting a continuous increase in the relative deformation between the pier and the deck of this bridge since 2015. Another interesting study, published by Cusson et al. [24], utilises satellite monitoring as an early warning tool for unexpected displacements.

Recent studies highlighted the potential of satellite data to accurately detect long-term displacement trends and to complement traditional structural monitoring systems [94, 95]. An attempt to reconstruct the two-dimensional displacement field was conducted by Farneti et al. [96], acquiring displacement information from both ascending and descending geometry for the Albiano-Magra viaduct, which collapsed in 2020. In this direction, Giordano et al. proposed an approach for the quantification and reductions of uncertainties in InSAR-derived displacement measurements accounting for spatial and temporal resampling [97]. Quqa et al. [98] developed a regional-scale methodology to detect anomalies across multiple bridges using InSAR displacements and environmental data.

The number of scientific publications focusing on InSAR-based SHM of civil infrastructure is increasing exponentially, as well as the special sessions on this topic in international conferences.

3.7 Current limitations

Although numerous recent studies have demonstrated the great potential of MT-InSAR for monitoring infrastructure assets, its routine and operational use still faces several obstacles. This section discusses the main challenges that currently hinder the widespread adoption of MT-InSAR as a tool for structural monitoring. These challenges can be broadly divided into two categories: (i) technological constraints related to SAR sensors, data, and the MT-InSAR processing chain, and (ii) practical and operational issues that limit the integration of MT-InSAR into everyday bridge management procedures and frameworks adopted by infrastructure managers. The main challenges belonging to the first category are discussed in 3.7.1, 3.7.2,3.7.3, and 3.7.4. The main challenges belonging to the second category are discussed in 3.7.5 and 3.7.6.

In my research work, particularly in the studies presented in Chapters 6 and 7, I mainly focus on proposing solutions to the second category of challenges, while remaining mindful of the first, which are essential considerations when employing MT-InSAR for SHM applications.

3.7.1 Availability and location of PS

Regarding the technological limitations, one of the primary constraints of MT-InSAR concerns the availability and spatial distribution of PS within a study area. In fact, the location and number of PS are not known prior to performing the MT-InSAR analysis [99]. This represents a significant drawback for structural monitoring applications, where it is essential to identify relevant PS and associate them with specific structural elements or other physical features on the ground in order to effectively assess the structural behaviour. The availability of PS mainly depends on the stable reflectivity of the targets on the ground over time. Because of their geometry and materials, bridges, roads and buildings often produce a large number of PS. Nevertheless, in certain situations, the long-term stability of the radar backscatter from these structures can deteriorate, resulting in a partial or total loss of PS. This may occur due to factors such as snow cover, flooding, maintenance activities, or excessive structural displacements [100]. Another key factor influencing PS availability is the sensor's spatial resolution. When using low-resolution SAR imagery–meaning large pixels dimensions–multiple reflectors may fall within the same pixel, which can significantly reduce the number of identifiable PS. This limitation is particularly relevant for monitoring small-scale structures such as short-span bridges, where the resulting PS density may be insufficient for reliable structural state assessment [101].

3.7.2 One-dimensional viewing geometry

Another important limitation of SAR measurements lies in their one-dimensional viewing geometry. Specifically, SAR sensors can only measure the target's displacements projection along the direction of the satellite LoS, rather than its full three-dimensional motion. Thus, data acquired from a single viewing geometry cannot fully capture the actual magnitude and direction of the real target deformation, and LoS displacements generally underestimate the actual motion [102]. Due to the generally low values of the incidence angle of SAR satellites (around $\theta \approx 30°C$), MT-InSAR is mostly sensitive to vertical displacements rather than horizontal displacements. In addition, since SAR satellites travel north-south along near-polar orbits, they are insensitive to north-south movements, which are always perpendicular to the LoS. As a result, north–south-oriented structures are disadvantaged, as their longitudinal motion cannot be retrieved from SAR data.

To avoid misunderstanding, incorrect interpretation, or oversimplification of SAR-derived displacements, the analysis and interpretation of MT-InSAR data should always take into account the expected structural motion, the possible loads and actions affecting the structure, the topography and features of the area surrounding the structure within the SAR image, and the geometry and orientation of the observed structure [103].

In some cases, such prior considerations about the expected kinematic can be used to make assumptions regarding the direction of the structural deformation, thus simplifying the mathematical formulations for the extraction of displacements along the main directions of the structural elements (e.g. vertical, transverse, longitudinal) from LoS measurements. For example, possible different assumptions on the expected structural movements, depending on the acting loads and on the static scheme, may be: (a) exclusively vertical displacements; (b) exclusively horizontal displacements; (c) exclusively longitudinal displacements. The schematic representation of such assumptions and their corresponding mathematical formulations for deriving structural displacements from LoS measurements are illustrated in Figure (see Figure 3.7).

When no simplifying assumptions can be made regarding the direction of the expected structural displacements, such as those illustrated in Figure 3.7, the limitation of one-directional LoS measurements could be in theory overcome by combining InSAR images acquired from opposite viewing geometries (i.e., ascending and descending). By processing both ascending and descending datasets covering the same area over the same time span, it is possible to derive the vertical (up–down) and horizontal (east–west) components of deformation, thereby reconstructing

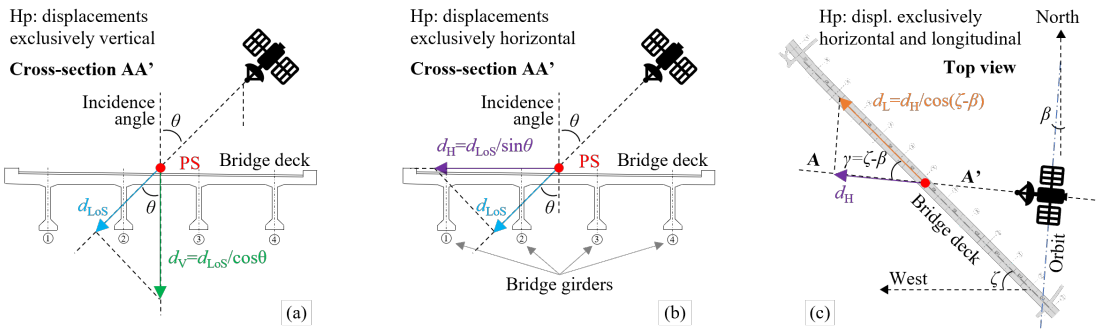

Figure 3.7: Projection of bridge displacements measured along the LoS (d_{LoS}) onto different directions based on assumptions.

the three-dimensional motion without requiring any assumptions [104]. Indeed, the extracted descending and ascending LoS measurements can be used to solve the system of Equations 3.5, 3.6 for the calculation of up-down and east-west displacements:

$$d_{east-west} = \frac{1}{2}\left(\frac{d_{LoS,desc}}{sin(\theta_{desc})} - \frac{d_{LoS,asc}}{sin(\theta_{asc})}\right) \tag{3.5}$$

$$d_{up-down} = \frac{1}{2}\left(\frac{d_{LoS,desc}}{cos(\theta_{desc})} + \frac{d_{LoS,asc}}{cos(\theta_{asc})}\right) \tag{3.6}$$

However, this approach presents significant drawbacks. The PS points identified in the ascending and descending datasets are not necessarily the same and may differ in geolocation [105]. Moreover, satellites with ascending and descending orbits pass over the same area at different times of the day, a few days apart from each other, acquiring measurements affected by different temperature and environmental conditions [106]. As a consequence, to combine datasets from different viewing geometries, pixels in each dataset need to be interpolated both in space and time. Such spatial and temporal resampling inevitably introduces considerable uncertainty into final estimates of structural displacements reconstructed from InSAR data [97], limiting the applicability of this strategy.

3.7.3 Phase unwrapping problem

To continue, one of the most critical technological limitations of InSAR lies in the phase unwrapping problem. Owing to the periodic nature of the radar phase, MT-InSAR observations are inherently ambiguous, as the measured phase is wrapped within the interval from $-\pi$ to $+\pi$. When, for two acquisitions compared during MT-InSAR processing, the

differential deformation phase exceeds this range, the deformation cannot be estimated unambiguously. The problem of resolving such phase ambiguity is called phase unwrapping. Without careful treatment of this issue, large or rapid structural deformations may not be properly detected [107]. Furthermore, substantial displacements can cause decorrelation and a consequent loss of temporal coherence, particularly over long observation periods or in areas undergoing significant surface changes. The limit of π on the differential phases corresponds to a maximum differential deformation of $\lambda/4$ over two consecutive SAR acquisitions (Equation 3.2). Thus, using an X-band SAR sensor with a wavelength of 31mm limits the movements that in theory can be unambiguously defined to 7.75mm between acquisitions.

Due to phase ambiguity, not only the movements that can be measured between two satellite acquisitions, but also the deformation rate that can be estimated by means of multiple images are limited. The maximum detectable velocity depends on the assumption of a deformation model. For example, for a linear model, Equation 3.2 can be written as in Equation 3.7 [108]:

$$\Delta\phi = \frac{4\pi}{\lambda}\Delta r = \frac{4\pi}{\lambda}\Delta T \cdot D \tag{3.7}$$

where D represents the average displacement rate between the first and last acquisition, and ΔT denotes the satellite repeat interval. Accordingly, the maximum deformation rate for a linear model can be written as in Equation 3.8:

$$D = \frac{\lambda/4}{\Delta T} \tag{3.8}$$

Under this assumption, considering for example the COSMO-SkyMed mission specifics (repeat interval of 16 days and wavelength of 3.1cm) the maximum differential deformation rate measurable using a X-band SAR sensor is 17.7cm/year.

3.7.4 Geometric distorsions

Finally, one last significant technological constraint concerns the geometry of SAR data acquisition. The three-dimensional space captured by the satellite is projected onto a two-dimensional radar coordinate system defined by slant range and azimuth. This projection can introduce different types of geometric distortions, including layover, foreshortening, and shadowing [60]. These issues can sometimes be mitigated by using datasets acquired from different looking orbits, as areas that are obscured or shadowed in one geometry (e.g., ascending pass) may become visible in the other (e.g., descending pass).

3.7.5 Cross-domain expertise and studies

Regarding operational limitations hindering the application of InSAR for SHM purposes by infrastructure operators, a critical aspect consists in the need for specialised processing skills for the extraction of deformations from series of SAR images. This remains a barrier preventing the widespread adoption of MT-InSAR data within the civil engineering industry [103].

However, while a consolidated knowledge and experience in MT-InSAR technology and data processing is crucial to secure reliable results, a deep knowledge of the processes governing structural deformation is also fundamental to correctly interpret MT-InSAR measurements for structural monitoring applications. Expertise in SAR signal processing and expertise in structural assessment usually belong to distinct professional paths (i.e., radar data analysts and civil engineers), making it difficult to find experts or technicians with interdisciplinary knowledge spanning both fields.

As a consequence of such separated expertise, nowadays, most current research works on MT-InSAR applications for SHM can be divided into two categories. The first addresses the estimation of displacement time series of PSs identified on the civil infrastructure, focusing on the InSAR data processing technique and the mathematical aspects of the algorithms exploited, without giving any interpretation of data from the structural standpoint (e.g., kinematic behaviour of the structure, structural response to loads, identification of abnormal variation in extracted time series possibly related to structural damages or evolving degradation). The second addresses the interpretation of the PS displacement time-series relying on ready-to-use processed MT-InSAR results, paying little or no attention to measurement accuracy or the possibility that some patterns visible in the time-series were related to the parameters employed and choices taken in the data analysis. It is important to cover this gap by addressing both MT-InSAR processing steps and engineering interpretation of results for bridges. This lies the motivation for my research study presented in Chapter 6.

3.7.6 Large volume of data

Finally, a critical limitation to the widespread of MT-InSAR for SHM of bridges and its incorporation in BMS frameworks consists in the need for time-consuming analyses in order to extract meaningful structural information from the large amount of data generated by MT-InSAR [89].

The number of PS extracted by means of MT-InSAR can potentially be quite high (thousands of PS), depending on the size and quality of

the SAR dataset imagery. The higher their number, the denser is the information on the deformation field of the area of interest. However, the higher their number, the longer the time required by the data analyst to discriminate PS located on the structure to be monitored, and to analyse and compare their displacement time-series with those of the surrounding PS.

To overcome this problem and support the integration of MT-InSAR in BMS, there is the need for automated methods that reduce the user effort to extract and interpret information from large MT-InSAR datasets. This forms the basis for my research study presented in Chapter 7.

4. Performance-Based Monitoring System Design

In Chapter 2, recent advancements in Structural Health Monitoring (SHM) within bridge management practices were discussed. Since the last few decades, bridge management is increasingly relying on SHM data rather than solely on visual inspection data [56]. Monitoring infrastructure through permanently installed sensors has repeatedly demonstrated its value in providing accurate and timely information on the state of bridges, allowing to overcome several critical limitations of traditional visual inspection methods for data collection and structural condition assessment [57].

Despite the growing interest in SHM, encouraged by recent guidelines [49, 48], several challenges still prevent its effective use and integration into bridge management practice. As highlighted in Chapter 2, one of the main limitations hindering the systematic implementation of SHM lies in the lack of clearly defined and standardised approaches for the design of monitoring systems. Therefore, further developments in this direction are required.

In the literature, most studies on monitoring system design focus on the problem of optimal sensor placement, addressing the allocation of sensors in few optimal locations, particularly in vibration-based monitoring applications [109]. Papadimitriou et al. [110] proposed a method based on the minimization of information entropy, defined as the parameter that quantifies the uncertainty of a random variable. Udwadia [111] proposed a method based on the maximization of the Fisher information matrix norm. Fedorov and Hackl proposed the individuation of the optimal sensor configuration in the one that minimizes the coefficients of the variance and covariance matrix [112]. More recently, Wei et al. proposed an optimal sensor placement strategy which accounts for both modal parameter identification uncertainties and possible structural changes [113]. Generally, in all of these problems, the optimal choice of sensors configuration is based on the minimization of a value representing the uncertainty, maximizing the information gain [114]. For comprehensive and up-to-date reviews of optimal sensor placement techniques for bridge monitoring and different optimization criteria, the reader can refer to [115, 116].

On the other hand, recognising that the primary purpose of SHM is to support decision-making, several approaches for evaluating the convenience of monitoring systems based on the principles of Expected Utility Theory (EUT) and Value of Information (VoI) have been formalised over the past decades by various authors [117, 118]. Indeed, in the SHM

context, the VoI represents the a priori difference between the expected costs before and after acquiring monitoring information, i.e. the monetary amount saved each time the operator consults the monitoring system [119]. These concepts can be applied to the monitoring system design problem: a monitoring system is considered economically convenient, and therefore worth installing, if its VoI exceeds the disutility, which corresponds to the cost of the monitoring system itself.

The VoI concept was originally introduced by Lindley [114] and later formalised by Raiffa and Schlaifer [120] and DeGroot [121]. Recent contributions have extended the VoI framework to account for many aspects relevant to SHM applications. For instance, recent studies have investigated how sensor data quality issues, including measurement drift and other sources of errors, affect the value of monitoring information [122, 123]. Makhoul et al. have explored a decision-making process for bridge management based on the Value of Information Quality Assessment [124]. The VoI framework has also been applied to quantify the economic benefit of SHM information for specific hazard scenarios, such as bridges exposed to flood-induced scour [125].

To summarise, when deciding whether to install a tentative monitoring system, two key aspects should be taken into account: (i) whether the information provided by the system sufficiently improves the manager's knowledge of the structural state, and (ii) whether this information leads to economic benefits that outweigh the system's cost by enabling informed, cost-effective decisions. The definition of these crucial aspects lays the foundation for the Performance-Based Monitoring System Design method, first formulated in [51].

The rationale and key steps of the Performance-Based Monitoring System Design approach are summarised in this Chapter. This approach is fully consistent with the monitoring design prescriptions proposed by the recent Italian Guidelines for Structural Health Monitoring (UNI/TR 11634:2016) [48]. The aim of this Chapter is to present the method's main principles and underlying logic, without delving into the detailed mathematical formulations of the general concepts on which the method is based, such as probability theory, Bayesian inference, EUT, and VoI. Readers may refer to appropriate sources for a deeper understanding of these topics: Bayesian logic and probability theory have been extensively studied and applied to problems of inference under uncertain conditions [126, 127], while a comprehensive review on information value and decision analysis in SHM is provided in [128]. Finally, this chapter also outlines the limitations of the Performance-Based Monitoring System Design method, as well as the critical aspects that require further research to enable its widespread adoption by engineers and practitioners

in the daily design of monitoring systems, including the issue addressed in my research work presented in Chapter 8.

4.1 Rationale of the approach

SHM systems aim to provide useful information to structural managers to increase their level of knowledge on the structural condition and allow them to make better decisions on the structure management, by integrating this information within a BMS or Decision Support System (DSS). However, SHM systems components such as sensors and reading units for the acquisition of information on the structure behaviour come with a cost, and the effectiveness of data is not guaranteed due to the uncertainties involved in the process of evaluating the structural state.

Engineers typically approach monitoring design differently from structural design. In designing a structure, a civil engineer follows a well-established rational procedure codified by standards. In contrast, when an engineer designs a monitoring system, the approach is often heuristic with performance evaluation based on experience or common sense, rather than on quantitative analysis. Nevertheless, in logical terms, the processes of monitoring design and structural design are equivalent, and their analogies are summarized in Table 4.1.

Table 4.1: Analogy between structural design and monitoring system design.

	Semi-probabilistic structural design	**Performance-based monitoring design**
Scope	Structural stability	Knowledge of structural state parameters with appropriate confidence
Design target	Design loads A	State parameters θ
Tentative solution	Materials, geometry, static scheme	Sensors types, layout, specifications (accuracy, frequency, range)
Demand	Effects of design loads S	Limit uncertainty in the knowledge of structural state parameters $\bar{\sigma}^2_{\theta\|y}$
Model	Relationship between material properties and structural capacity	Relationship between monitoring observations and state parameters
Capacity	Resistance (maximum effects of loads before failure) R	Expected uncertainty of the structural state parameters $\sigma^2_{\theta,pp}$
Limit state	$S < R$	$\bar{\sigma}^2_{\theta\|y} > \sigma^2_{\theta,pp} \rightarrow \frac{1}{\bar{\sigma}^2_{\theta\|y}} < \frac{1}{\sigma^2_{\theta,pp}}$
Performance metric	Safety factor $= \frac{R}{S}$	Effectiveness index $= \frac{\bar{\sigma}^2_{\theta\|y}}{\sigma^2_{\theta,pp}}$

Before commenting and further explaining the content of 4.1, let us define the basic concepts of sensor, key state parameter, observations, and model:

- Sensor: any device which functions as a source of information [129];

- Observations $\mathbf{y}$: physical quantities observed by the monitoring system, usually organized in a vector.
- Key State Parameter θ: a parameter quantifying the state of the structure, such as the physical/mechanical properties, structural response, loads, or damage level. It can be specified by a discrete variable or a class (for example, damaged/undamaged), by continuous parameters (for example, the Young modulus of concrete, the opening of a crack), or by a combination of the two. Examples of common structural state parameters in bridges monitoring are provided in Table 2.1.
- Model $f(\theta)$: the way we assume the observations are correlated to the state parameters.

In structural design, the scope is to ensure that the structure can withstand the design actions with an appropriate safety margin. Once the tentative design solution and design loads are identified, the process consists in the following phases: the analysis of the design loads effects on structural elements to obtain the demand, the evaluation of structural capacity by means of mechanical models, and finally the comparison between demand and capacity to verify if the limit state is satisfied.

Analogously, the design of an SHM system aims to ensure that the information acquired can sufficiently reduce the uncertainty associated with the assessment of key structural state parameters.

The process requires the definition of specific monitoring objectives depending on the type of information to be obtained, leading to the identification of relevant state parameters. Each state parameter is associated with a maximum acceptable uncertainty in its estimation. These requirements constitute the monitoring demand. Then, the designer must identify a tentative technical solution for measuring the physical quantities needed to derive the state parameters. This solution must be compatible with available technologies and comply with the budgetary constraints set by the infrastructure operator. Based on a model describing the relationship between state parameters and monitoring measurements, the process continues with the calculation of the expected uncertainty of the key state parameters. This value represents the monitoring capacity, i.e. the expected performance of the system evaluated before installing it.

The design is satisfactory if the monitoring capacity obtained with the tentative sensor technology to be employed is equal or better than the monitoring demand. The verification of this condition enables the selection of the most appropriate and effective SHM system for the case under consideration.

The above described methodology is called Performance-Based Mon-

itoring System Design, and is the counterpart of semi-probabilistic structural design [51]. Its steps are summarised in the flowchart in Figure 4.1, resembling the procedure prescribed for monitoring system design by the Italian Guidelines for Structural Health Monitoring (UNI/TR 11634:2016) [48].

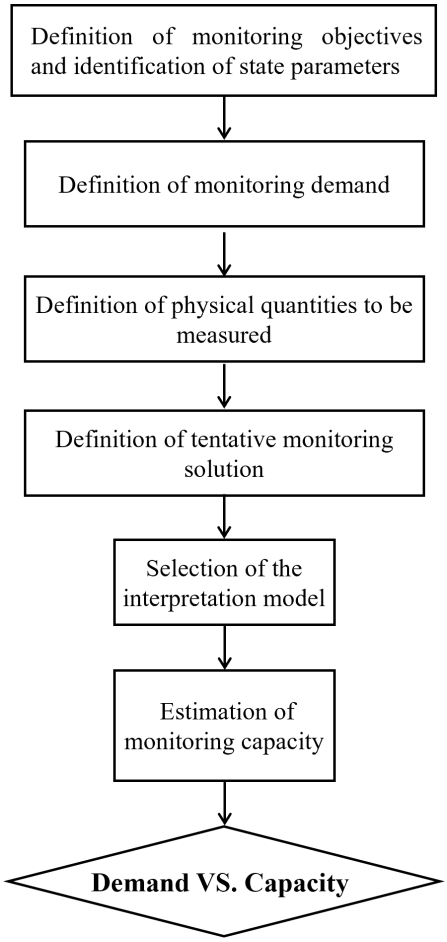

Figure 4.1: Performance-Based monitoring system design procedure.

4.2 Monitoring capacity

The monitoring capacity $\sigma^2_{\theta,pp}$ is the uncertainty in the identification of the key state parameter θ of a structure based on the observations provided by the monitoring system.

In general, the state of a structure is identified by a set of discrete variables, continuous parameters, or a combination of both. For clarity,

in this Chapter we assume that the key state parameter is defined by a single continuous parameter θ. In this case, SHM aims to estimate the posterior probability $p(\theta|\boldsymbol{y})$ of the structural state θ based on a set of observations $\boldsymbol{y}$. The logical inference process to obtain the posterior probability distribution of θ given the observations $\boldsymbol{y}$ is mathematically encoded in Bayes' rule [130]:

$$p(\theta|\boldsymbol{y}) = \frac{p(\boldsymbol{y}|\theta) \cdot p(\theta)}{p(\boldsymbol{y})} \tag{4.1}$$

Where $p(\boldsymbol{y}|\theta)$ is the likelihood function expressing the probability of observing the data $\boldsymbol{y}$ given the state θ, $p(\theta)$ is the prior distribution of parameter θ, and $p(\boldsymbol{y})$ is the evidence.

Equation 4.1 defines a probability density function in the joint space of the parameter θ and the observations $\boldsymbol{y}$. The maximum a posteriori (MAP) $\mu_{\theta|\boldsymbol{y}}$ and variance $\sigma^2_{\theta|\boldsymbol{y}}$ can be estimated through Equations 4.2 and 4.3, which are both functions of the observations $\boldsymbol{y}$:

$$\mu_{\theta|\boldsymbol{y}} = \int_{\mathcal{D}_\theta} \frac{p(\boldsymbol{y}|\theta) \cdot p(\theta) \cdot \theta \; d\theta}{p(\boldsymbol{y})} \tag{4.2}$$

$$\sigma^2_{\theta|\boldsymbol{y}} = \int_{\mathcal{D}_\theta} \frac{p(\boldsymbol{y}|\theta) \cdot p(\theta) \cdot (\theta - \mu_{\theta|\boldsymbol{y}}(\boldsymbol{y}))^2 \; d\theta}{p(\boldsymbol{y})} \tag{4.3}$$

The variance $\sigma^2_{\theta|\boldsymbol{y}}$ is the monitoring capacity because it represents the uncertainty in the estimation of the state parameter θ based on the monitoring observations $\boldsymbol{y}$. When the monitoring observations $\boldsymbol{y}$ are available, this quantity can be calculated directly. However, in the monitoring design phase, monitoring capacity must be estimated before observations even exist, since the system has not yet been installed to collect such data. Therefore, we must infer a priori the value $\sigma^2_{\theta|\boldsymbol{y}}$ of the posterior distribution $p(\theta|\boldsymbol{y})$, assuming that some data $\boldsymbol{y}$ will be acquired, even though they are not yet available. This analysis is known as prior estimation of the posterior or *pre-posterior analysis*.

The Bayesian pre-posterior analysis (PP) for the calculation of the expected monitoring capacity $\sigma^2_{\theta,pp}$ is a simulation *a priori* of Bayesian inference *a posteriori* [131, 120]. Since the posterior distribution $p(\theta|\boldsymbol{y})$ is a function of the observations $\boldsymbol{y}$, and thus also the variance $\sigma^2_{\theta|\boldsymbol{y}}$, and since $\boldsymbol{y}$ is a vector of random variables affected by uncertainty, $\sigma^2_{\theta|\boldsymbol{y}}$ cannot be determined deterministically before monitoring takes place. Instead, we can make an uncertain prediction of such value based on prior information. The quantity we can compute is an expected monitoring

capacity–the pre-posterior variance of the structural state–based on the prior distribution $p(\boldsymbol{y})$.

To obtain the prior distribution $p(\boldsymbol{y})$, the designer must know:

(1) a model $\tilde{\boldsymbol{y}} = f(\theta)$ relating the observed quantities $\boldsymbol{y}$ to the state parameter θ;

(2) the distribution of the residuals $\boldsymbol{z} = \tilde{\boldsymbol{y}} - \boldsymbol{y}$, i.e. the difference between the statistically independent observations $\boldsymbol{y}$ and the nominal value of the model $\tilde{\boldsymbol{y}}$ –which include sensor noise, sensor bias and model uncertainties;

(3) the prior distribution $p(\theta)$ of the state parameter θ.

Once that the distribution $p(\boldsymbol{y})$ is available, the expected monitoring capacity $\sigma^2_{\theta,pp}$ can be calculated as:

$$\sigma^2_{\theta,pp} = \mathrm{E}\left[\sigma^2_{\theta|\boldsymbol{y}}(\boldsymbol{y})\right] = \int_{\mathcal{D}_\theta,\boldsymbol{y}} p(\boldsymbol{y}|\theta) \cdot p(\theta) \cdot (\theta - \mu_{\theta|\boldsymbol{y}}(\boldsymbol{y}))^2 \, d\theta \quad (4.4)$$

In practice, the quantity $\sigma^2_{\theta,pp}$ represents the expected variance of the structural state estimation after monitoring is performed, i.e. the pre-posterior variance. Note that it is independent of any monitoring observation; therefore, it is in fact an a priori quantity.

The monitoring capacity can be estimated analytically or numerically.

When the prior probability distribution of the state parameters $p(\theta)$ and the likelihood function $p(\boldsymbol{y}|\theta)$ are Gaussian, and the inverse function of the model $\tilde{\boldsymbol{y}} = f(\theta)$ exists and is approximately linear in the region where $p(\boldsymbol{y})$ is significant (around $\tilde{\mu}_{\boldsymbol{y}}$), the monitoring capacity can be estimated analytically through uncertainty propagation [132], without numerical algorithms. An example of such calculation for a simple monitoring design problem with a single state parameter θ and a single observation y has been reported in [51].

In more complex cases–when the model is a nonlinear numerical function of multiple state parameters and multiple observations–it is often not possible to invert the model to obtain an analytical expression for each state parameter based on the model outputs. In these situations, uncertainty propagation cannot be used to estimate the monitoring capacity. A possible solution is to perform a Monte Carlo simulation [133, 134]. Markov chain Monte Carlo (MCMC) methods are approximate inference methods based on stochastic numerical sampling from probability distributions. These methods allow the numerical estimation of mean and

covariance of a collection of samples drawn from arbitrary probability distributions. Therefore, Monte Carlo methods can estimate the monitoring capacity in cases with severely nonlinear models or non-Gaussian priors and likelihoods. However, MCMC methods are computationally intensive and are mainly used for small-scale problems [127].

4.3 Monitoring demand

The monitoring demand $\bar{\sigma}^2_{\theta|y}$ is the limit maximum acceptable uncertainty for the determination of the structural state key parameters. It is an upper-limit value that a monitoring designer needs to ensure is not exceeded when exploiting the observations from a tentative monitoring system for the evaluation of key monitoring state parameters. In general, its value depends on the problem to be tackled. Since SHM should help a manager in the identification of key structural state parameters, each accuracy requirement depends on the specific state parameters to be identified by means of the designed system, e.g. 0.1 mm for joint aperture, 1 mm/year for deflection rate, 1 Hz for modal frequency. Many infrastructure operators have an idea of the accuracy in the structural state parameter they want to obtain, so that usually the monitoring demand can be estimated based on experience or common sense, and not on formal prediction of advantages and disadvantages.

Nevertheless, given that monitoring design can be formulated as a decision problem –where the choice of a particular monitoring solution should be driven by its VoI (i.e., the costs of the equipment and its operation versus the benefits resulting from information-based management)– the definition of the monitoring demand should be based on the concept of Value of monitoring Information (VoI). Indeed, defining the monitoring demand based on VoI ensures that if a monitoring system meets such demand, it provides an economic benefit in terms of structural management that is higher than the costs incurred for its installation.

According to Raiffa and Schlaifer [120], this decision problem is solved by maximizing the Expected Net Gain of Sampling (ENGS), i.e., in our problem, the economic measure of the quality of the monitoring information accounting for both the value of information and the costs of the monitoring. ENGS can be written as in Equation 4.5:

$$\begin{aligned}\text{ENGS}(\xi) = &\int_{\mathcal{D}_{\boldsymbol{y}}} \left[\max_a \int_{\mathcal{D}_\theta} u(z + z_{\text{SHM},\xi}|\theta) \cdot p_\xi(\theta|\boldsymbol{y}) \cdot d\theta \right] \cdot p_\xi(\boldsymbol{y}) \cdot d\boldsymbol{y} \\ &- \max_a \int_{\mathcal{D}_\theta} u(z|\theta) \cdot p(\theta) \cdot d\theta \end{aligned} \tag{4.5}$$

where:

- ξ is a hyperparameter representing the tentative monitoring solution;
- a represents the set of management actions that the operator can carry out in response to the state of the bridge;
- z are the monetary outcomes corresponding to the set of actions a;
- z_{SHM} is the cost of the monitoring system;
- u is the utility function;
- θ is the state parameter of the monitoring;
- $\boldsymbol{y}$ are the monitoring observations;

The second term of 4.5 is the expected utility that the designer would get choosing not to install any monitoring system, therefore it does not depend on the monitoring system concept ξ. On the other hand, the tentative monitoring solution ξ affects the first term of 4.5. If the designer chooses to install the monitoring system represented by ξ, each outcome after the installation is increased by the cost of such system $z_{\text{SHM},\xi}$. Moreover, the choice of a monitoring system ξ will influence the probability distributions $p_\xi(\theta|\boldsymbol{y})$ and $p_\xi(\boldsymbol{y})$: the higher the accuracy of the monitoring system in the acquisition of the measurements, the lower the uncertainties in $p_\xi(\theta|\boldsymbol{y})$ and $p_\xi(\boldsymbol{y})$.

Thus, the optimal configuration of the monitoring system is the one that maximises ENGS:

$$\xi^* = \underset{\xi}{\operatorname{argmax}} \left\{ \text{ENGS}(\xi) \right\}. \tag{4.6}$$

And the limit for which a tentative monitoring system ξ is financially convenient is:

$$ENGS(\xi) = 0 \tag{4.7}$$

Let us assume that the state of the structure is represented by a single state parameter θ whose posterior distribution is normal, $p(\theta, \sigma^2_{\theta|\boldsymbol{y}}|\boldsymbol{y}) = N(\mu_{\theta|\boldsymbol{y}}, \sigma^2_{\theta|\boldsymbol{y}})$, with mean vector $\mu_{\theta|\boldsymbol{y}}$ and variance $\sigma^2_{\theta|\boldsymbol{y}}$. Let us also assume that the cost of monitoring $z_{\text{SHM}}(\sigma^2_{\theta|\boldsymbol{y}})$ can be defined as a monotonically decreasing function of the variance of the posterior distribution $\sigma^2_{\theta|\boldsymbol{y}}$. It is reasonable because monitoring solutions that are less accurate are usually cheaper. Then, we can define the monitoring demand $\bar{\sigma}^2_{\theta|y}$ as the value of expected variance for which the ENGS is zero, satisfying Equation 4.7:

$$\bar{\sigma}^2_{\theta|y} = E\left[\sigma^2_{\theta|\boldsymbol{y}}\right] : \int_{\mathcal{D}_{\boldsymbol{y}}} \left[\max_a \int_{\mathcal{D}_\theta} u(z + z_{\text{SHM}}(\sigma^2_{\theta|\boldsymbol{y}})|\theta) \cdot p(\theta, \sigma^2_{\theta|\boldsymbol{y}}|\boldsymbol{y}) \cdot d\theta\right] \cdot p(\boldsymbol{y}, \sigma^2_{\theta|\boldsymbol{y}}) \cdot d\boldsymbol{y} - \max_a \int_{\mathcal{D}_\theta} u(z|\theta) \cdot p(\theta) \cdot d\theta = 0 \tag{4.8}$$

Such calculation of the ENGS requires the monitoring designer to know the probability and the outcomes of each possible realization of the state θ. The evaluation of the involved probability distributions can require complex probabilistic models and significant analytical or numerical effort (as discussed in Section 4.2). The calculation of the outcomes, i.e. the financial consequences, should take into account both the direct and the indirect costs related to the realization of each structural state, including the losses due to casualties, road user costs, and the impact of the structural behaviour on the society and the environment [135]. Estimating these costs is challenging because it requires a priori knowledge or data from different scenarios involving similar structures, as well as financial calculations that are not always familiar to structural engineers. These difficulties undermine the feasibility of a VoI-based estimation of the monitoring demand in typical real-world situations.

In structural design, design standards such as Eurocode 0 (EN 1990) and NTC2018, are based on a semi-probabilistic approach that prescribes the structural loads and does not require the structural designer to know probability values or costs. Based on the idea that Performance-Based Monitoring Design represents the counterpart of the semi-probabilistic structural design performed every day by practitioners, a straightforward procedure is needed for the evaluation of the monitoring demand. For this reason, it was suggested to calculate the VoI-based monitoring demand for family of structure types and for the most important key state parameters, and then include the results of such extensive analysis in monitoring design codes [136].

4.4 Monitoring effectiveness check

In 4.2 and 4.3, the key concepts regarding the calculation of expected monitoring capacity and monitoring demand for Performance-Based Monitoring System Design were summarized.

Finally, three logical rules to check a tentative monitoring system effectiveness can be formalized by answering the questions:

(1) Do I really need a monitoring system?

(2) Does the monitoring system improve my knowledge on the structural state?

(3) Does the monitoring system match the requirements?

Regarding (1), a monitoring system is necessary when the uncertainty in the estimation of the structural state a priori σ^2_θ is higher than the maximum acceptable error, i.e. the demand $\bar{\sigma}^2_{\theta|\boldsymbol{y}}$. In this case, the infrastructure operator cannot infer the structural state with enough accuracy to manage the bridge properly, and thus monitoring observation may be needed to improve their knowledge.

Regarding (2), a monitoring system is informative if the pre-posterior uncertainty $\sigma^2_{\theta,pp}$ in the estimation of the structural state is lower than its value a priori σ^2_θ. In this case, the designer expects that monitoring data will indeed improve the manager's knowledge about the structural state, providing information about the parameters of interest.

Finally, regarding (3), a monitoring system is effective when the expected error in the estimation of the structural state based on monitoring observation, i.e. the capacity $\sigma^2_{\theta,pp}$ is lower than the maximum acceptable error, i.e. the demand $\bar{\sigma}^2_{\theta|\boldsymbol{y}}$. This last rule is of course the most important because it represents the final check for the tentative monitoring system solution, as the counterpart of the structural design check (demand versus capacity).

To sum up the three logical rules read as follows:

$$\begin{cases} \bar{\sigma}^2_{\theta|\boldsymbol{y}} \leq \sigma^2_\theta \\ \sigma^2_{\theta,pp} \leq \sigma^2_\theta \\ \sigma^2_{\theta,pp} \leq \bar{\sigma}^2_{\theta|\boldsymbol{y}} \end{cases} \tag{4.9}$$

It should be noted that the three conditions in Equation 4.9 are not independent. In particular, if conditions (1) and (3) are satisfied, condition (2) is implicitly satisfied. Nevertheless, their separation helps clarify the logical steps involved in assessing whether monitoring is (1) needed, (2) informative, and (3) ultimately effective.

A great advantage of the Performance-Based Monitoring System Design method is that both the monitoring demand $\bar{\sigma}^2_{\theta|\boldsymbol{y}}$, the expected monitoring capacity $\sigma^2_{\theta,pp}$, and the prior variance σ^2_θ are expressed in engineering units, which can be easily handled and interpreted by practitioners.

4.5 Current limitations

In this Chapter, Performance-Based Monitoring System Design approach was presented. Such approach has been proposed as a straightforward procedure for everyday monitoring design practice, representing the counterpart of the semi-probabilistic structural design.

The main limitation to the actual implementation of this approach consists in the definition of the monitoring demand based on the concept of VoI. VoI requires the calculation of expected utilities and outcomes, to marginalize the difference between the expected utilities a posteriori and a priori on the possible outcomes of monitoring. Thus, to compute it, complete knowledge of the probabilistic models of the SHM framework is required, as well as prior knowledge of the operator's management strategies and the relative possible consequences.

However, resources allocated to the design of monitoring systems are often limited. Moreover, the choice of management actions and the quantification of their consequences is often highly uncertain and affected by the subjectivity of operators. Therefore, the complexity of the VoI makes it difficult to define a VoI-based monitoring demand for everyday monitoring design procedures to apply in most practical cases.

To avoid this problem, it was suggested to calculate the VoI-based monitoring demand for family of structure types and for the most important key state parameters, and then include the results of such extensive analysis in monitoring design codes [136]. In this way, the monitoring demand can be prescribed by monitoring system design codes, similar to the structural design codes that prescribe the load requirements for semi-probabilistic structural design. Until further developments in this direction are reached, the monitoring demand can be determined empirically on the basis of the monitoring objectives, the structural characteristics of the asset, the operational context, available technology and the manager's needs. Typically, the limit acceptable uncertainty is set as a fraction (e.g.: $1\% - 10\%$) of the prior value of the structural state parameter [51].

On the other hand, the calculation of the monitoring capacity is based on the uncertainties that affect the evaluation of the state parameter a posteriori, depending on monitoring observations. Like in structural design, the calculation of the monitoring capacity is the only task that should be left to practitioners. But how can they do that in practice, in the design phase, before even installing the system, when monitoring observations are not yet available?

A simple example of evaluation of the monitoring capacity in a pre-posteriori framework is presented in [51], assuming a single observation y and a single state parameter θ. This application allows estimating the capacity of a monitoring system for the evaluation of stay cable tensioning force (state parameter θ) from first vibration frequency measurement (observation y), by means of uncertainty propagation.

However, it is not always feasible for practitioners and civil engineers to use probabilistic analytical or numerical methods for the evalu-

ation of the pre-posterior uncertainty of the monitoring key parameters –i.e., the monitoring capacity– particularly for multiple parameters and observations problems, due to increase in complexity and computational effort.

Further research effort is needed to address the evaluation of the pre-posterior uncertainty for the most common monitoring objectives and key state parameters in SHM. Some cases may require accounting for multiple parameter models, as well as multiple observations. There is the need for simple-to-use closed form expressions for monitoring system design, to be used by infrastructure operators in everyday practice. This issue is addressed in my research work presented in Chapter 8.

Bibliography

[1] F. Collins and F. Blin, *Ageing of Infrastructure: A Life-Cycle Approach*. CRC Press, 2018.

[2] I. G. Ganiev, Z. Muradov, *et al.*, "Global issue of ageing reinforced concrete bridge infrastructure," *Technical Science Integrated Research*, vol. 1, no. 3, pp. 3–9, 2025.

[3] A. S. of Civil Engineers (ASCE), "Report card for america's infrastructure 2025: A comprehensive assessment of america's infrastructure," 2025. Accessed: 2025-11-15.

[4] T. Ministry of Land, Infrastructure and T. of Japan, "White paper on land, infrastructure, transport, and tourism in japan 2019," 2019.

[5] B. Pang, P. Yang, Y. Wang, A. Kendall, H. Xie, and Y. Zhang, "Life cycle environmental impact assessment of a bridge with different strengthening schemes," *The International Journal of Life Cycle Assessment*, vol. 20, no. 9, pp. 1300–1311, 2015.

[6] D. Tonelli, F. Rossi, F. Brighenti, A. Verzobio, A. Bonelli, and D. Zonta, "Prestressed concrete bridge tested to failure: the alveo vecchio viaduct case study," *Journal of Civil Structural Health Monitoring*, vol. 13, no. 4, pp. 873–899, 2023.

[7] B. Wolmuth and J. Surtees, "Crowd-related failure of bridges," in *Proceedings of the Institution of Civil Engineers-Civil Engineering*, vol. 156, pp. 116–123, Thomas Telford Ltd, 2003.

[8] G. Zhang, Y. Liu, J. Liu, S. Lan, and J. Yang, "Causes and statistical characteristics of bridge failures: A review," *Journal of traffic and transportation engineering (English edition)*, vol. 9, no. 3, pp. 388–406, 2022.

[9] G. M. Calvi, M. Moratti, G. J. O'Reilly, N. Scattarreggia, R. Monteiro, D. Malomo, P. M. Calvi, and R. Pinho, "Once upon a time in italy: The tale of the morandi bridge," *Structural Engineering International*, vol. 29, no. 2, pp. 198–217, 2019.

[10] M. F. Bado and J. R. Casas, "A review of recent distributed optical fiber sensors applications for civil engineering structural health monitoring," *Sensors*, vol. 21, no. 5, p. 1818, 2021.

[11] R. Denysiuk, J. Fernandes, J. C. Matos, L. C. Neves, and U. Berardinelli, "A computational framework for infrastructure asset maintenance scheduling," *Structural engineering international*, vol. 26, no. 2, pp. 94–102, 2016.

[12] D. M. Frangopol, "Life-cycle performance, management, and optimisation of structural systems under uncertainty: accomplishments and challenges 1," *Structure and infrastructure Engineering*, vol. 7, no. 6, pp. 389–413, 2011.

[13] F. Poli, M. F. Bado, A. Verzobio, and D. Zonta, "Bridge structural safety assessment: a novel solution to uncertainty in the inspection practice," *Structure and Infrastructure Engineering*, vol. 21, no. 3, pp. 421–435, 2025.

[14] F. Brighenti, V. F. Caspani, G. Costa, P. F. Giordano, M. P. Limongelli, and D. Zonta, "Bridge management systems: A review on current practice in a digitizing world," *Engineering structures*, vol. 321, p. 118971, 2024.

[15] P. Vassie and C. Arya, "Bridge management," in *ICE Manual of Bridge Engineering: Second Edition*, pp. 591–613, ICE Publishing, 2008.

[16] R. Woodward, D. Cullington, A. Daly, P. Vassie, P. Haardt, R. Kashner, R. Astudillo, C. Velando, B. Godart, C. Cremona, *et al.*, "Bridge management in europe (brime)-deliverable d14-final report," 2001.

[17] M. Pregnolato, "Bridge safety is not for granted–a novel approach to bridge management," *Engineering Structures*, vol. 196, p. 109193, 2019.

[18] C. Pellegrino, A. Pipinato, and C. Modena, "A simplified management procedure for bridge network maintenance," *Structure and Infrastructure Engineering*, vol. 7, no. 5, pp. 341–351, 2011.

[19] J. Lauridsen, J. Bjerrum, N. H. Andersen, and B. Lassen, "Creating a bridge management system," *Structural engineering international*, vol. 8, no. 3, pp. 216–220, 1998.

[20] D. Agdas, J. A. Rice, J. R. Martinez, and I. R. Lasa, "Comparison of visual inspection and structural-health monitoring as bridge condition assessment methods," *Journal of Performance of Constructed Facilities*, vol. 30, no. 3, p. 04015049, 2016.

[21] C. R. Farrar and K. Worden, "An introduction to structural health monitoring," *Philosophical Transactions of the Royal Society A: Mathematical, Physical and Engineering Sciences*, vol. 365, no. 1851, pp. 303–315, 2007.

[22] M. Abdulkarem, K. Samsudin, F. Z. Rokhani, and M. F. A Rasid, "Wireless sensor network for structural health monitoring: A contemporary review of technologies, challenges, and future direction," *Structural health monitoring*, vol. 19, no. 3, pp. 693–735, 2020.

[23] Z. He, W. Li, H. Salehi, H. Zhang, H. Zhou, and P. Jiao, "Integrated structural health monitoring in bridge engineering," *Automation in construction*, vol. 136, p. 104168, 2022.

[24] D. Cusson, C. Rossi, and I. F. Ozkan, "Early warning system for the detection of unexpected bridge displacements from radar satellite data," *Journal of Civil Structural Health Monitoring*, vol. 11, no. 1, pp. 189–204, 2021.

[25] D. Inaudi, "Long-term static structural health monitoring," in *Structures Congress 2010*, pp. 566–577, 2010.

[26] C.-C. Comisu, N. Taranu, G. Boaca, and M.-C. Scutaru, "Structural health monitoring system of bridges," *Procedia engineering*, vol. 199, pp. 2054–2059, 2017.

[27] C. Iacovino, Z. I. Turksezer, P. F. Giordano, and M. P. Limongelli, "A survey of bridge condition rating systems," in *International Conference of the European Association on Quality Control of Bridges and Structures*, pp. 14–22, Springer, 2021.

[28] H. Abdel-Jaber and B. Glisic, "Monitoring of long-term prestress losses in prestressed concrete structures using fiber optic sensors," *Structural Health Monitoring*, vol. 18, no. 1, pp. 254–269, 2019.

[29] M. Limongelli, "Frequency response function interpolation for damage detection under changing environment," *Mechanical Systems and Signal Processing*, vol. 24, no. 8, pp. 2898–2913, 2010.

[30] V. F. Caspani, D. Tonelli, F. Poli, and D. Zonta, "Designing a structural health monitoring system accounting for temperature compensation," *Infrastructures*, vol. 7, no. 1, p. 5, 2021.

[31] M. A. Zanini, F. Faleschini, and J. R. Casas, "State-of-research on performance indicators for bridge quality control and management," *Frontiers in built environment*, vol. 5, p. 22, 2019.

[32] A. Strauss, K. Bergmeister, A. M. Ivanković, and J. C. e Matos, "Applied and research based performance indicator database for highway bridges across europe," *Life-cycle of engineering systems: Emphasis on sustainable civil infrastructure*, pp. 1503–1510, 2016.

[33] A. F. Shahraki, O. P. Yadav, and H. Liao, "A review on degradation modelling and its engineering applications," *International Journal of Performability Engineering*, vol. 13, no. 3, p. 299, 2017.

[34] H. Mohseni, S. Setunge, G. Zhang, and R. Wakefield, "Markov process for deterioration modeling and asset management of community buildings," *Journal of Construction Engineering and Management*, vol. 143, no. 6, p. 04017003, 2017.

[35] P. Bocchini and D. M. Frangopol, "Connectivity-based optimal scheduling for maintenance of bridge networks," *Journal of Engineering Mechanics*, vol. 139, no. 6, pp. 760–769, 2013.

[36] A. Strauss, A. Orcesi, A. Lampropoulos, B. Briseghella, D. M. Frangopol, H. S. Sousa, J. Casas, J. C. Matos, K. Schellenberg, M. Valenzuela, *et al.*, "Iabse survey of implemented decision-making models used by public and private owners/operators of road-and railway infrastructures," *Structural Engineering International*, vol. 34, no. 1, pp. 87–96, 2024.

[37] D. Zonta, R. Zandonini, and F. Bortot, "A reliability-based bridge management concept," *Structures & Infrastructure Engineering*, vol. 3, no. 3, pp. 215–235, 2007.

[38] S. Sabatino, D. M. Frangopol, and Y. Dong, "Life cycle utility-informed maintenance planning based on lifetime functions: Optimum balancing of cost, failure consequences and performance benefit," *Structure and Infrastructure Engineering*, vol. 12, no. 7, pp. 830–847, 2016.

[39] G. Kabir, R. Sadiq, and S. Tesfamariam, "A review of multi-criteria decision-making methods for infrastructure management," *Structure and infrastructure engineering*, vol. 10, no. 9, pp. 1176–1210, 2014.

[40] S. B. Chase, Y. Adu-Gyamfi, A. Aktan, E. Minaie, *et al.*, "Synthesis of national and international methodologies used for bridge health indices," 2016.

[41] P. G. Malerba, "Bridge vulnerabilities and collapses: the italian experience," *Structure and Infrastructure Engineering*, vol. 20, no. 7-8, pp. 976–1001, 2024.

[42] ANAS, "Monitoraggi di ponti e viadotti tramite sensori," n.d. [Online].

[43] Consorzio Fabre, "Consorzio fabre," n.d. [Online].

[44] Consorzio della Rete dei Laboratori Universitari di Ingegneria Sismica e Strutturale (RELUIS), "Reluis," n.d. [Online].

[45] COST TU1402, "Quantifying the value of structural health monitoring," n.d. [Online].

[46] International Association for Experimental Vibration Analysis for Civil Engineering Structures (EVACES IA), "Evaces ia," n.d. [Online].

[47] M. P. Limongelli, "Standardization of structural performance monitoring: existing documents and open questions," in *IABSE Symposium. Prague 2022*, pp. 1–7, 2022.

[48] U. E. I. di Normazione, "Uni/tr 11634:2016. guidelines for structural health monitoring," tech. rep., Ente Italiano di Normazione (UNI), Milano, Italy, 2016. Technical Report.

[49] I. Ministero delle Infrastrutture e dei Trasporti, Consiglio Superiore dei Lavori Pubblici: Roma, "Linee guida per la classificazione e gestione del rischio, la valutazione della sicurezza ed il monitoraggio dei ponti esistenti," tech. rep., Ministero delle Infrastrutture e dei Trasporti and Consiglio Superiore dei Lavori Pubblici, 2020.

[50] D. Zonta, B. Glisic, and S. Adriaenssens, "Value of information: impact of monitoring on decision-making," *Structural Control and Health Monitoring*, vol. 21, no. 7, pp. 1043–1056, 2014.

[51] D. Tonelli, C. Cappello, and D. Zonta, "Performance-based design of structural health monitoring systems," in *European Workshop on Structural Health Monitoring*, pp. 238–247, Springer, 2020.

[52] P. F. Giordano, S. Quqa, and M. P. Limongelli, "The value of monitoring a structural health monitoring system," *Structural safety*, vol. 100, p. 102280, 2023.

[53] D. Perissin, "Interferometric sar multitemporal processing: Techniques and applications," in *Multitemporal Remote Sensing: Methods and Applications*, pp. 145–176, Springer, 2016.

[54] A. Ferretti, C. Prati, and F. Rocca, "Permanent scatterers in sar interferometry," *IEEE Transactions on geoscience and remote sensing*, vol. 39, no. 1, pp. 8–20, 2002.

[55] B. Glisic, D. Inaudi, and N. Casanova, "Shm process as perceived through 350 projects," in *Smart Sensor Phenomena, Technology, Networks, and Systems 2010*, vol. 7648, pp. 174–187, SPIE, 2010.

[56] P. C. Chang, A. Flatau, and S.-C. Liu, "Health monitoring of civil infrastructure," *Structural health monitoring*, vol. 2, no. 3, pp. 257–267, 2003.

[57] A. Kamariotis, E. Chatzi, and D. Straub, "A framework for quantifying the value of vibration-based structural health monitoring," *Mechanical Systems and Signal Processing*, vol. 184, p. 109708, 2023.

[58] L. Iannacone, P. Francesco Giordano, P. Gardoni, and M. Pina Limongelli, "Quantifying the value of information from inspecting and monitoring engineering systems subject to gradual and shock deterioration," *Structural health monitoring*, vol. 21, no. 1, pp. 72–89, 2022.

[59] R. Bamler and P. Hartl, "Synthetic aperture radar interferometry," *Inverse problems*, vol. 14, no. 4, p. R1, 1998.

[60] R. F. Hanssen, *Radar interferometry: data interpretation and error analysis*. Springer, 2001.

[61] A. Ferretti, A. Monti-Guarnieri, C. Prati, F. Rocca, and D. Massonet, *InSAR principles-guidelines for SAR interferometry processing and interpretation*, vol. 19. 2007.

[62] A. Moreira, P. Prats-Iraola, M. Younis, G. Krieger, I. Hajnsek, and K. P. Papathanassiou, "A tutorial on synthetic aperture radar," *IEEE Geoscience and remote sensing magazine*, vol. 1, no. 1, pp. 6–43, 2013.

[63] F. Bovenga, A. Belmonte, A. Refice, G. Pasquariello, R. Nutricato, D. O. Nitti, and M. T. Chiaradia, "Performance analysis of satellite missions for multi-temporal sar interferometry," *Sensors*, vol. 18, no. 5, p. 1359, 2018.

[64] R. Bamler and B. Schättler, "Sar data acquisition and image formation," *Geocoding: ERS-1 SAR Data and Systems, Wichmann-Verlag*, pp. 53–102, 1993.

[65] P. A. Rosen, S. Hensley, I. R. Joughin, F. K. Li, S. N. Madsen, E. Rodriguez, and R. M. Goldstein, "Synthetic aperture radar interferometry," *Proceedings of the IEEE*, vol. 88, no. 3, pp. 333–382, 2002.

[66] D. Massonnet and K. L. Feigl, "Radar interferometry and its application to changes in the earth's surface," *Reviews of geophysics*, vol. 36, no. 4, pp. 441–500, 1998.

[67] A. K. Gabriel, R. M. Goldstein, and H. A. Zebker, "Mapping small elevation changes over large areas: Differential radar interferometry," *Journal of Geophysical Research: Solid Earth*, vol. 94, no. B7, pp. 9183–9191, 1989.

[68] A. Ferretti, G. Savio, R. Barzaghi, A. Borghi, S. Musazzi, F. Novali, C. Prati, and F. Rocca, "Submillimeter accuracy of insar time series: Experimental validation," *IEEE Transactions on Geoscience and Remote Sensing*, vol. 45, no. 5, pp. 1142–1153, 2007.

[69] D. Perissin and A. Ferretti, "Urban-target recognition by means of repeated spaceborne sar images," *IEEE Transactions on Geoscience and Remote Sensing*, vol. 45, no. 12, pp. 4043–4058, 2007.

[70] U. G. Sefercik, M. Gorken, and M. Nazar, "Analysis of coherence between linear and cubic sbas displacement models in deformation monitoring," *The International Archives of the Photogrammetry, Remote Sensing and Spatial Information Sciences*, vol. 48, pp. 259–264, 2025.

[71] O. Monserrat, M. Crosetto, M. Cuevas, and B. Crippa, "The thermal expansion component of persistent scatterer interferometry observations," *IEEE Geoscience and Remote Sensing Letters*, vol. 8, no. 5, pp. 864–868, 2011.

[72] P. Milillo, G. Giardina, M. J. DeJong, D. Perissin, and G. Milillo, "Multi-temporal insar structural damage assessment: The london crossrail case study," *Remote Sensing*, vol. 10, no. 2, p. 287, 2018.

[73] D. Perissin, "Geometric processing: Active sensor modeling and calibration (sar)," 2018.

[74] P. Marinkovic, G. Ketelaar, F. van Leijen, and R. Hanssen, "Insar quality control: Analysis of five years of corner reflector time series," in *Proceedings of the Fringe 2007 Workshop (ESA SP-649), Frascati, Italy*, pp. 26–30, 2007.

[75] G. Quin and P. Loreaux, "Submillimeter accuracy of multipass corner reflector monitoring by ps technique," *IEEE Transactions on Geoscience and Remote Sensing*, vol. 51, no. 3, pp. 1775–1783, 2012.

[76] D. Tonelli, A. Valentini, A. Rocca, S. Zorzi, A. Lotti, and D. Zonta, "Uncertainty quantification of satellite insar-monitoring of bridges: a case study," *ce/papers*, vol. 6, no. 5, pp. 900–906, 2023.

[77] A. Alonso-Díaz, D. Roque, M. Solla, and J. N. Lima, "Comparative analysis of mt-insar algorithms supported by gnss data and corner reflectors: Assessing performance and accuracy," *Procedia Computer Science*, vol. 239, pp. 1460–1466, 2024.

[78] M. Bonano, M. Manunta, A. Pepe, L. Paglia, and R. Lanari, "From previous c-band to new x-band sar systems: Assessment of the dinsar mapping improvement for deformation time-series retrieval in urban areas," *IEEE Transactions on Geoscience and Remote Sensing*, vol. 51, no. 4, pp. 1973–1984, 2013.

[79] V. Ignatenko, P. Laurila, A. Radius, L. Lamentowski, O. Antropov, and D. Muff, "Iceye microsatellite sar constellation status update: Evaluation of first commercial imaging modes," in *IGARSS 2020-2020 IEEE International Geoscience and Remote Sensing Symposium*, pp. 3581–3584, IEEE, 2020.

[80] B. Yu, T. Niu, J. Zhao, D. Ma, G. Liu, X. Wang, K. Dai, and Y. Gu, "Deformation monitoring and primary driving factor analysis in the coastal area of liaohe oilfield utilizing mt-insar and pca," *PFG–Journal of Photogrammetry, Remote Sensing and Geoinformation Science*, vol. 92, no. 3, pp. 213–234, 2024.

[81] E. Ghaderpour, C. Masciulli, M. Zocchi, F. Bozzano, G. Scarascia Mugnozza, and P. Mazzanti, "Estimating reactivation times and velocities of slow-moving landslides via ps-insar and their relationship with precipitation in central italy," *Remote Sensing*, vol. 16, no. 16, p. 3055, 2024.

[82] E. Ghaderpour, P. Mazzanti, F. Bozzano, and G. S. Mugnozza, "Ground deformation monitoring via ps-insar time series: An industrial zone in sacco river valley, central italy," *Remote Sensing Applications: Society and Environment*, vol. 34, p. 101191, 2024.

[83] S. Bianchini, F. Pratesi, T. Nolesini, and N. Casagli, "Building deformation assessment by means of persistent scatterer interferometry analysis on a landslide-affected area: the volterra (italy) case study," *Remote sensing*, vol. 7, no. 4, pp. 4678–4701, 2015.

[84] V. Cerchiello, G. Tessari, E. Velterop, P. Riccardi, M. Defilippi, and P. Pasquali, "Building damage risk by modeling interferometric time series," *IEEE Geoscience and Remote Sensing Letters*, vol. 14, no. 4, pp. 509–513, 2017.

[85] D. Di Martire, R. Iglesias, D. Monells, G. Centolanza, S. Sica, M. Ramondini, L. Pagano, J. J. Mallorquí, and D. Calcaterra, "Comparison between differential sar interferometry and ground measurements data in the displacement monitoring of the earth-dam of conza della campania (italy)," *Remote sensing of environment*, vol. 148, pp. 58–69, 2014.

[86] P. Milillo, D. Perissin, J. T. Salzer, P. Lundgren, G. Lacava, G. Milillo, and C. Serio, "Monitoring dam structural health from space: Insights from novel insar techniques and multi-parametric modeling applied to the pertusillo dam basilicata, italy," *International journal of applied earth observation and geoinformation*, vol. 52, pp. 221–229, 2016.

[87] G. Barla, A. Tamburini, S. Del Conte, and C. Giannico, "Insar monitoring of tunnel induced ground movements," *Geomechanics and Tunnelling*, vol. 9, no. 1, pp. 15–22, 2016.

[88] L. Chang, R. P. Dollevoet, and R. F. Hanssen, "Nationwide railway monitoring using satellite sar interferometry," *IEEE Journal of Selected Topics in Applied Earth Observations and Remote Sensing*, vol. 10, no. 2, pp. 596–604, 2016.

[89] V. Macchiarulo, P. Milillo, C. Blenkinsopp, and G. Giardina, "Monitoring deformations of infrastructure networks: A fully automated gis integration and analysis of insar time-series," *Structural Health Monitoring*, vol. 21, no. 4, pp. 1849–1878, 2022.

[90] S. Selvakumaran, S. Plank, C. Geiß, C. Rossi, and C. Middleton, "Remote monitoring to predict bridge scour failure using interferometric synthetic aperture radar (insar) stacking techniques," *International journal of applied earth observation and geoinformation*, vol. 73, pp. 463–470, 2018.

[91] S. Selvakumaran, C. Rossi, A. Marinoni, G. Webb, J. Bennetts, E. Barton, S. Plank, and C. Middleton, "Combined insar and terrestrial structural monitoring of bridges," *IEEE Transactions on Geoscience and Remote Sensing*, vol. 58, no. 10, pp. 7141–7153, 2020.

[92] K. DePrekel, E. H. Bouali, and T. Oommen, "Monitoring the impact of groundwater pumping on infrastructure using geographic information system (gis) and persistent scatterer interferometry (psi)," *Infrastructures*, vol. 3, no. 4, p. 57, 2018.

[93] P. Milillo, G. Giardina, D. Perissin, G. Milillo, A. Coletta, and C. Terranova, "Pre-collapse space geodetic observations of critical infrastructure: The morandi bridge, genoa, italy," *Remote Sensing*, vol. 11, no. 12, p. 1403, 2019.

[94] D. Tonelli, M. Zini, L. Simeoni, A. Rocca, D. Perissin, and D. Zonta, "Integrating satellite insar and topographic data for long-term displacement monitoring of bridge crossing slow-moving landslides," *Structural Control and Health Monitoring*, vol. 2025, no. 1, p. 2106133, 2025.

[95] P. F. Giordano, M. Kwapisz, A. Miano, R. Liuzzo, A. Vorwagner, M. P. Limongelli, A. Prota, and M. Ralbovsky, "Monitoring of a multi-span prestressed concrete bridge using satellite interferometric data and comparison with on-site sensor results," *Structural Concrete*, vol. 26, no. 5, pp. 5430–5453, 2025.

[96] E. Farneti, N. Cavalagli, M. Costantini, F. Trillo, F. Minati, I. Venanzi, and F. Ubertini, "A method for structural monitoring of multispan bridges using satellite insar data with uncertainty quantification and its pre-collapse application to the albiano-magra bridge in italy," *Structural Health Monitoring*, vol. 22, no. 1, pp. 353–371, 2023.

[97] P. F. Giordano, A. Kamariotis, G. Giardina, E. Chatzi, and M. P. Limongelli, "Uncertainty propagation in satellite insar data analysis for structural health monitoring," *Automation in Construction*, vol. 177, p. 106371, 2025.

[98] S. Quqa, A. Palermo, F. Ubertini, and A. Marzani, "Regional-scale bridge condition monitoring using insar displacements and environmental data," *Structural Health Monitoring*, vol. 24, no. 4, pp. 2271–2291, 2025.

[99] M. Crosetto, O. Monserrat, M. Cuevas-González, N. Devanthéry, and B. Crippa, "Persistent scatterer interferometry: A review," *ISPRS Journal of Photogrammetry and Remote Sensing*, vol. 115, pp. 78–89, 2016.

[100] D. Perissin and T. Wang, "Repeat-pass sar interferometry with partially coherent targets," *IEEE Transactions on Geoscience and Remote Sensing*, vol. 50, no. 1, pp. 271–280, 2011.

[101] G. Giardina, P. Milillo, M. J. DeJong, D. Perissin, and G. Milillo, "Evaluation of insar monitoring data for post-tunnelling settlement damage assessment," *Structural Control and Health Monitoring*, vol. 26, no. 2, p. e2285, 2019.

[102] J. Hu, Z. Li, X. Ding, J. Zhu, L. Zhang, and Q. Sun, "Resolving three-dimensional surface displacements from insar measurements: A review," *Earth-Science Reviews*, vol. 133, pp. 1–17, 2014.

[103] V. Macchiarulo, P. Milillo, C. Blenkinsopp, C. Reale, and G. Giardina, "Multi-temporal insar for transport infrastructure monitoring: recent trends and challenges," in *Proceedings of the Institution of Civil Engineers-Bridge Engineering*, vol. 176, pp. 92–117, Thomas Telford Ltd, 2023.

[104] T. J. Wright, B. E. Parsons, and Z. Lu, "Toward mapping surface deformation in three dimensions using insar," *Geophysical Research Letters*, vol. 31, no. 1, 2004.

[105] S. Gernhardt, X. Cong, M. Eineder, S. Hinz, and R. Bamler, "Geometrical fusion of multitrack ps point clouds," *IEEE Geoscience and Remote Sensing Letters*, vol. 9, no. 1, pp. 38–42, 2011.

[106] E. Hoppe, B. Bruckno, E. Campbell, S. Acton, A. Vaccari, M. Stuecheli, A. Bohane, G. Falorni, and J. Morgan, "Transporta-

tion infrastructure monitoring using satellite remote sensing," *Materials and Infrastructures 1*, vol. 5, pp. 185–198, 2016.

[107] H. Yu, Y. Lan, Z. Yuan, J. Xu, and H. Lee, "Phase unwrapping in insar: A review," *IEEE Geoscience and Remote Sensing Magazine*, vol. 7, no. 1, pp. 40–58, 2019.

[108] B. M. Kampes, *Radar interferometry: persistent scatterer technique*. Springer, 2006.

[109] M. Meo and G. Zumpano, "On the optimal sensor placement techniques for a bridge structure," *Engineering Structures*, vol. 27, pp. 1488–1497, Aug. 2005.

[110] C. Papadimitriou, J. L. Beck, and S.-K. Au, "Entropy-based optimal sensor location for structural model updating," *Journal of Vibration and Control*, vol. 6, no. 5, pp. 781–800, 2000.

[111] F. E. Udwadia, "Methodology for optimum sensor locations for parameter identification in dynamic systems," *Journal of engineering mechanics*, vol. 120, no. 2, pp. 368–390, 1994.

[112] V. V. Fedorov and P. Hackl, "Optimal experimental design: spatial sampling," *Calcutta Statistical Association Bulletin*, vol. 44, no. 1-2, pp. 57–82, 1994.

[113] J.-Y. Wei, F.-L. Zhang, W. Xiang, and G.-Q. Gong, "Optimal sensor placement strategy considering bayesian identification uncertainty and state change in bridge health monitoring," *ASCE-ASME Journal of Risk and Uncertainty in Engineering Systems, Part A: Civil Engineering*, vol. 12, no. 1, p. 04025108, 2026.

[114] D. V. Lindley, "On a measure of the information provided by an experiment," *The Annals of Mathematical Statistics*, vol. 27, no. 4, pp. 986–1005, 1956. Publisher: Institute of Mathematical Statistics.

[115] S. Hassani and U. Dackermann, "A systematic review of optimization algorithms for structural health monitoring and optimal sensor placement," *Sensors*, vol. 23, no. 6, p. 3293, 2023.

[116] Z. Sun, M. Mahmoodian, A. Sidiq, S. Jayasinghe, F. Shahrivar, and S. Setunge, "Optimal sensor placement for structural health monitoring: a comprehensive review," *Journal of Sensor and Actuator Networks*, vol. 14, no. 2, p. 22, 2025.

[117] D. Zonta, B. Glisic, and S. Adriaenssens, "Value of information: impact of monitoring on decision-making," *Structural Control and Health Monitoring*, vol. 21, pp. 1043–1056, July 2014. Number: 7.

[118] P. F. Giordano, L. J. Prendergast, and M. P. Limongelli, "A framework for assessing the value of information for health monitoring of scoured bridges," *Journal of Civil Structural Health Monitoring*, vol. 10, pp. 485–496, July 2020. Number: 3.

[119] M. Pozzi and A. Der Kiureghian, "Assessing the value of information for long-term structural health monitoring," (San Diego, California, USA), p. 79842W, Mar. 2011.

[120] H. Raiffa and R. Schlaifer, *Applied statistical decision theory*. Studies in managerial economics, Boston: Div. of Research, Graduate School of Business Administration, Harvard Univ, 1961.

[121] M. H. Degroot, "Changes in utility as information," *Theory and Decision*, vol. 17, no. 3, p. 287, 1984. Publisher: Kluwer Academic Publishers.

[122] P. F. Giordano, S. Quqa, and M. P. Limongelli, "Value of information analysis accounting for data quality," in *Sensors and Smart Structures Technologies for Civil, Mechanical, and Aerospace Systems 2023*, vol. 12486, pp. 235–245, SPIE, 2023.

[123] P. Giordano, M. Limongelli, *et al.*, "Value of information analysis accounting for sensor data quality: focus on drift," in *Latin American Workshop on Structural Health Monitoring (LATAM-SHM2023)*, pp. 1–9, 2024.

[124] N. Makhoul and M. P. Limongelli, "Integration of information quality assessment in bridge resilience management," in *Life-Cycle of Structures and Infrastructure Systems*, pp. 1653–1660, CRC Press, 2023.

[125] P. F. Giordano, L. J. Prendergast, and M. P. Limongelli, "Quantifying the value of shm information for bridges under flood-induced scour," *Structure and Infrastructure Engineering*, vol. 19, no. 11, pp. 1616–1632, 2023.

[126] E. T. Jaynes, *Probability theory: The logic of science*. Cambridge university press, 2003.

[127] C. M. Bishop and N. M. Nasrabadi, *Pattern recognition and machine learning*, vol. 4. Springer, 2006.

[128] S. Thöns, C. Caprani, M. H. Faber, D. M. Frangopol, P. Gardoni, P. F. Giordano, D. Honfi, L. Iannacone, M. S. Khan, J. Köhler, S. Kim, N. De Koker, M. P. Limongelli, S. Miraglia, J. S. Nielsen, M. Pandey, and C. Viljoen, "On information value and decision analyses," *Structural Safety*, vol. 113, p. 102481, Mar. 2025.

[129] D. L. Hall and S. A. McMullen, *Mathematical techniques in multisensor data fusion*. Artech House, 2004.

[130] D. Sivia and J. Skilling, *Data analysis: a Bayesian tutorial*. OUP Oxford, 2006.

[131] M. H. Faber, "On the treatment of uncertainties and probabilities in engineering decision analysis," *Journal of Offshore Mechanics and Arctic Engineering*, vol. 127, no. 3, pp. 243–248, 2005.

[132] I. Farrance and R. Frenkel, "Uncertainty of measurement: a review of the rules for calculating uncertainty components through functional relationships," *The Clinical Biochemist Reviews*, vol. 33, no. 2, p. 49, 2012.

[133] J. L. Beck and S.-K. Au, "Bayesian updating of structural models and reliability using markov chain monte carlo simulation," *Journal of engineering mechanics*, vol. 128, no. 4, pp. 380–391, 2002.

[134] D. P. Kroese and R. Y. Rubinstein, "Monte carlo methods," *Wiley Interdisciplinary Reviews: Computational Statistics*, vol. 4, no. 1, pp. 48–58, 2012.

[135] M. H. Faber and M. A. Maes, "Issues in societal optimal engineering decision making," *Structure and Infrastructure Engineering*, vol. 4, no. 5, pp. 335–351, 2008.

[136] C. Cappello, "Theory of decision based on structural health monitoring," 2017.

Part II

Publications

5. Bridge management systems: A review on current practice in a digitizing world

This chapter contains the post-print of

> Brighenti, F., **Caspani, V. F.**, Costa, G., Giordano, P. F., Limongelli, M. P., Zonta, D. (2024). Bridge management systems: A review on current practice in a digitizing world. *Engineering Structures*, 321, 118971, https://doi.org/10.1016/j.engstruct.2024.118971.

as published in the Journal *Engineering Structures*, differing only from the published article in terms of layout, formatting, and notation.

Abstract

Bridges are subject to a plethora of deterioration phenomena, such as corrosion, fatigue, and damaging events (e.g., truck impacts and earthquakes) that can affect their performance and compromise functionality and safety. These challenges, along with the expansion of physical infrastructures and limited economic resources, underscore the need for effective management systems to enhance the efficiency of maintenance activities. To address this need, bridge operators have developed Bridge Management Systems (BMSs), which assist in ensuring safe operations while optimizing budget allocation and intervention strategies. Existing state-of-the-art studies on BMSs, dating back several years, primarily focus on specific aspects of BMSs and do not provide exhaustive insight into the implemented processes. Consequently, a comprehensive analysis of the entire process is currently lacking. This review organizes and discusses the key features of existing BMSs and introduces a novel definition of BMS modules–data management, diagnosis, prognosis, and decision-making–where consensus is currently lacking. The paper covers the historical and current practices of the most common BMSs, outlining the main principles of each phase along with their critical aspects and future trends.

Keywords:
Bridge management system; Digitalization; Automation; Inspection; Structural health monitoring; Digital twin; Decision making; Life-cycle analysis.

Glossary

In this section, the authors provide a brief glossary of the notation and the mathematical entities involved in the present paper.

BMS	Bridge Management System
IT	Information Technology
BrIM	Bridge Information Modelling
NDTs	Non-Destructive Tests
DTs	Destructive Tests
SHM	Structural Health Monitoring
ECT	Eddy Cutting Testing
AE	Acoustic Emission
MFL	Magnetic Flux Leakage
VoI	Value of Information
ROI	Return On Investment
MEMS	Microelectromechanical Systems
DIC	Digital Image Correlation
WSN	Wireless Sensor Networks
IoT	Internet of Things
PI	Performance Indicator
BCI	Bridge Condition Indicator
DI	Damage Indicator
LCC	Life-Cycle Cost
FE	Finite Element
TP	True Positives
TN	True Negatives
FP	False Positives
FN	False Negatives
PDF	Probability Density Function
ROC	Receiver Operating Characteristic
EUT	Expected Utility Theory
CS	Condition State
AR	Augmented Reality
AI	Artificial Intelligence
CNN	Convolutional Neural Networks
RNN	Recurrent Neural Networks
LSTM	Long Short-Term Memory
GRU	Gated Recurrent Unit
GAN	Generative Adversarial Networks
UAV	Unmanned Air Vehicle
LiDAR	Light Detection and Ranging

VR	Virtual Reality
ISHM	Indirect SHM
InSAR	Interferometric Synthetic Aperture Radar
FRC	Fiber Reinforced Composites
UHPFRC	Ultra-high Performance Fiber Reinforced Concrete
FRCM	Fiber Reinforced Cementitious Mortar
EB	Externally Bonded
NSM	Near Surface Mounted
MOOP	Multi-Objective Optimization Problem
MCDM	Multi-Criteria Decision-Making

5.1 Introduction

The rapid expansion of transportation infrastructure and the continuous advancements in technology have significantly transformed the landscape of bridge management [1]. As transportation networks grow more complex and the volume of collected data generated increases, there is a heightened demand for automated systems that can effectively manage and utilize this information for optimal bridge maintenance and decision-making [2, 3].

Nevertheless, effective bridge management goes beyond addressing immediate maintenance needs; it also encompasses ensuring the long-term safety and cost-effectiveness of these critical assets [4]. Consequently, authorities and infrastructure managers are increasingly focused on developing and implementing policies that promote the sustainable operation of bridges throughout their entire life-cycle –from initial design to eventual replacement [5].

In response to these demands, Bridge Management Systems (BMSs) have been developed in the last decades. A BMS can encompass a compilation of codes and guidelines, as well as a specific software program. Typically, BMSs incorporate both elements, with the software serving as a digital implementation of the standards established over the years. BMSs can be utilized at two distinct levels: the individual bridge level and the network level. [6]. Recently, thanks to the developments in Information Technology (IT), BMSs benefit from information systems such as Bridge Information Modelling (BrIM) and Digital Twins [7, 8]. All these aspects facilitate bridge management in a digitalizing world while meeting quality and performance standards [9].

Nevertheless, developing a custom BMS is a long-term commitment that involves the most advanced informatics skills, and high costs in terms of time, resources, and funds, both for initial development and

subsequent maintenance due to the need for continuous and periodic updates.

This paper provides an updated and complete overview of the current state of the art of BMSs, with the fundamental goal of reviewing current procedures and identifying areas of further research and improvements. As discussed in the following section, despite the importance of the topic, the majority of state-of-the-art studies on BMSs are dated between 2000 and 2014. Post-2014, documents have predominantly focused on specific aspects of BMSs, often targeting a limited cluster of countries. In this work, the available literature, including state-of-the-art studies on this topic, is analyzed and the history and current practice of BMSs are presented. Despite considerable advancements in the field, there remains a lack of consensus on a standardized definition for these modules. Thus, based on a comprehensive review of the literature and the analysis of practices from numerous countries, this study proposes a novel definition for the modules of BMSs. The main techniques used in BMSs for data collection, acquisition, transmission, and storage are discussed. The current practices for condition assessment within a BMS framework are analyzed. The paper also identifies and analyses the principal deterioration models as well as decision ort tools adopted in existing BMSs. The procedures of very few infrastructure operators are publicly reported due to copyright reasons as well as the confidentiality of budget management. One such operator is the Autonomous Province of Trento with the BMS APTBMS, whose documents have been thoroughly analyzed in this paper as an illustrative example. Future trends in BMSs are discussed, followed by general conclusions that summarize the study's findings.

5.2 BMSs in the current literature

While the topic of BMS is recognized as an important aspect of bridge management, there is a notable scarcity of comprehensive studies dedicated to BMSs. However, there are a few noteworthy exceptions that merit discussion.

At the beginning of 2000, the European project "Bridge Management Europe" (BRIME) undertook the development of an overarching framework for an ideal BMS tailored to the European road network. This envisioned BMS aimed to facilitate rational bridge stock management, optimizing budgets while ensuring adequate structural performance. The final report [10] focused on a sample of 10 BMSs and identified six key modules. McGee et al. [11] conducted an analysis of 11 BMSs from various locations worldwide and compared them with BMSs in Australia and

New Zealand. In addition to outlining the architecture of the reviewed BMSs, the study offers insights into the two fundamental approaches that govern bridge management: the top-down and bottom-up approaches. Furthermore, the report highlights potential future directions for BMS development, addressing emerging challenges and offering recommendations for advancements in the field. The International Association for Bridge Maintenance and Safety (IABMAS) compiled a comprehensive report on BMSs in 2008, gathering information from BMSs worldwide. Subsequently, the report was updated in 2010, 2012, and 2014 to ensure its relevance and incorporate new developments in the field of bridge management. The most recent version of the report [12] gathers data from 25 BMSs in 18 countries through questionnaires. The report provides an overview of global practices in BMSs, offering insights into their design, functionalities, and implementation approaches.

To the best of the authors' knowledge, no comprehensive state-of-the-art review on BMSs has been published in the past decade.

Nevertheless, numerous papers address specific aspects of BMSs. In December 2023, a preliminary literature review was carried out using the Scopus database using the keyword "Bridge Management Systems", which produced 844 results. Figure 5.1 reports the number of publications on the topic per year.

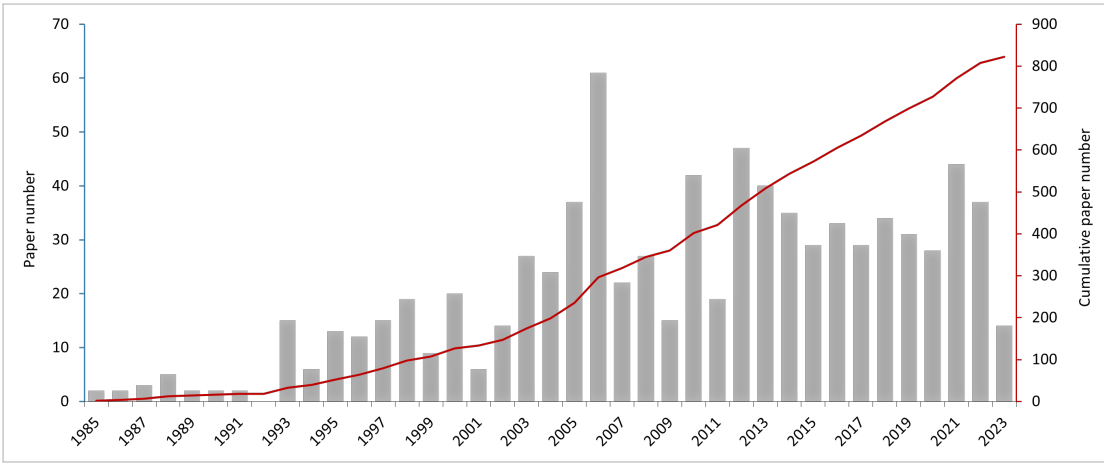

Figure 5.1: Publications on BMSs.

The first publications in the field date back to 1985 and the scientific interest in the topic has had an increasing trend over the years with a significant peak in 2006, due to the large number of papers on BMS published in [13].

A "network visualization diagram" is created through VOSviewer

software to highlight the most common keywords associated with BMSs, see Figure 5.2. The different colors suggest the clusters of the words that are reported together in the analyzed documents. The concepts of "maintenance", "inspection", "deterioration", "life-cycle costs" and "optimization" are often studied in relation to BMSs. However, they are not generally integrated. These aspects are analyzed in the following sections.

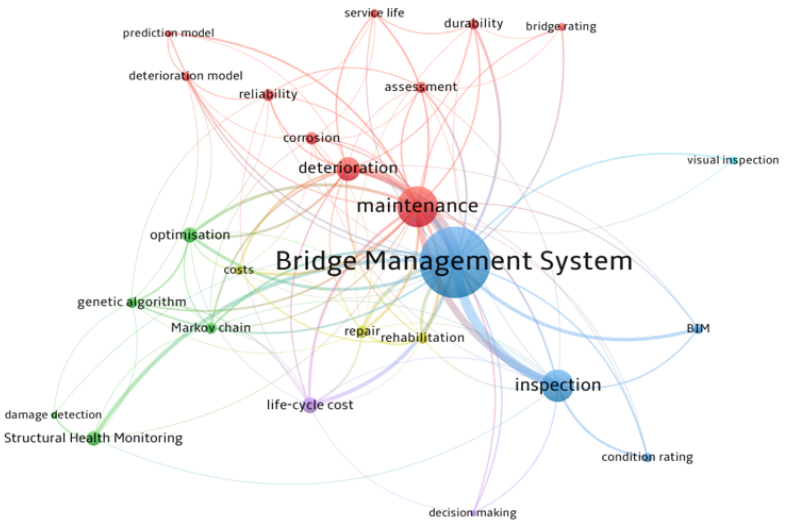

Figure 5.2: Network visualization diagram related to the BMS literature.

5.3 BMSs in the world: history and current practice

The development of BMSs was initially fostered by tragedies such as the collapse of the Silver Bridge on December 15th, 1967, in the US. According to the authors' knowledge, the first developed BMS software is the Danish DANBRO BMS which was released in 1975 to support and implement the increasingly comprehensive and restrictive management regulations. Later, the BMS DISK was developed in the Netherlands in 1985, and it is still used along with the TISBO Infrastructure Maintenance Management System, a BMS that integrates inspection registration and maintenance management. In 1985, Serbia introduced a BMS, called BPM, with a system of prioritization that is still used nowadays [14]. Italy started using Oracle and SQL Server in 1986. Nowadays, in Italy, several BMSs exist, among which the Autonomous Province of Trento BMS (APTBMS) was developed in 2004 by Zonta et al. [15]. This BMS introduces reliability concepts for bridge management and in-

cludes sections for condition state evaluation based on visual inspections, safety assessment, and prioritization. Several Italian infrastructure operators are currently working on their own BMS, such as Autostrade per l'Italia (Argo), Rete Ferroviaria Italiana (DOMUS) and Autovie Venete (Netkubed).

In 1987, Sweden implemented the software Bridge and Tunnel Management System (BaTMan). At the beginning of the 90s', several BMSs were created, such as the Finnish BMS (FBMS) in 1990, the KUBA BMS of Switzerland in 1991, and the well-known Pontis [16] and Bridgit [17] in the US, respectively in 1992 and 1993. Pontis was developed for the FHWA and became an AASHTO product renamed BrM in 1994 [18]. Although Pontis is the most well-known and widespread BMS in the US, other BMSs have been developed both by individual states [19, 20, 21, 22] and at the Federal level [23, 24] in recent years. In the late 90s', Hungary started using BMS software in 1996, France in 1999, and in 1997 Poland implemented SMOK which was then followed by the software SZOK in 2001.

Between 2000 and 2001, Germany created the Bauwerk Management System or SIB-Bauwerke (GBMS). In 2001, numerous countries developed their own BMS, namely Vietnam with Bridgeman, Ireland with Eirspan which was developed using DANBRO as a starting point, and England with Oracle. In the same year, Estonia started using Pontis. The following year, in 2002, Latvia implemented LT Brutus, Canada the Ontario BMS (OBMS), and the Czech Republic the IIS database +MS SQL Server. Later on, in 2003, Korea started using the Korea Road Maintenance Business System (KRBMS) [12], and between 2004 and 2005, Bulgaria developed Scanpoint-Freissinet, which was integrated in 2009 with a prioritization system. In 2005, Spain developed SPG. In 2006, Japan released the Regional Planning Institute of Osaka BMS (RPIBMS) [18, 25]. During the same year, two more Canadian BMSs were implemented, namely EBMS and PEIBMMS, followed by Quebec BMS (QBMS), in 2008. More recently, between 2019 and 2020, Croatia also developed a BMS, called Oracle 10.G. Nowadays, within a single country, different road operators or administration entities might have their own management systems, due to the differences in bridge management practices [12]. These systems are usually developed internally by the operators, sometimes by consulting private companies. Other BMSs are BAUT (Austria), SIMS (United Kingdom) [26], SAMOA (Italy), and GOA (Portugal) [12], GNWT (Canada) [12], SGO (Brazil), BridgeASYST, MRWA and NSW(Australia) [12], MICHI (Japan) [12], T-BMS (Taiwan) [18, 27], Slovenia BMS (Slovenia) [28], HiBris and Hanke-Shira (Finland) and Lagora (France) [29] and the North Carolina's BMS

NCDOT [11].

5.4 The general architecture of a BMS

To effectively address diverse management objectives, BMSs must be adaptable and include various modules tailored to specific needs. The design of BMSs can vary significantly depending on the country or the requirements of the operator. In the context of the BRIME project [10], key requirements for a BMS were identified, along with essential modules, see Figure 5.3.

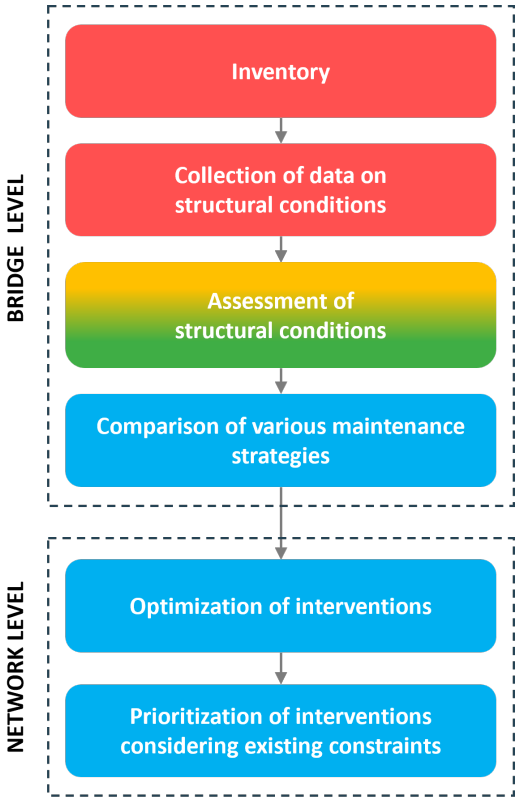

Figure 5.3: BMS modules according to BRIME [10].

The first four modules pertain to individual structures, covering (1) the inventory (database), (2) the collection of data on structural conditions, (3) the assessment of structural conditions, and (4) the comparison of different maintenance strategies. The remaining modules relate to the bridge network, encompassing (5) the optimization of interventions, and (6) the prioritization of interventions considering existing constraints.

Specifically, modules (1) and (2) are concerned with data management (in red), while module (3) pertains to both diagnosing the structural state and predicting future conditions (the yellow indicates diagnosis whereas the green indicates prognosis). Modules (4), (5) and (6) are focused on decision-making (in blue) regarding individual structures and the bridge portfolio.

Nevertheless, non-uniform definitions of BMS modules can be found in the literature (see Table 5.2). For instance, Lauridsen et al. [30] defined BMS components as: 1) Interrelated activities for handling bridges, 2) Set of codes and guidelines, 3) Organization to manage and carry out previous activities, 4) Database holding data resulting from previous activities, and 5) Set of computer tools for processing the data. Zonta et al. [15] detailed sections within the APTBMS as: 1) Database, 2) Inspection and evaluation module, 3) Maintenance degradation reliability and cost module, and 4) Decision tools module. Pellegrino et al. [31] considered: 1) Bridge Database, 2) Inspection System, 3) Structural capacity evaluation, 4) Lifetime prediction of the future condition of the structure, and 5) Cost evaluation system. Pregnolato [32] identified modules as: 1) Inventory, 2) Inspection, 3) Repair and Rehabilitation, and 4) Optimization.

Table 5.2: BMS modules according to different authors.

Lauridsen et al.[30]	BRIME[10]	APTBMS[15]	Pellegrino et al.[31]	Pregnolato[32]
Interrelated activities for handling bridges	Inventory	Database	Bridge Database	Inventory
Set of codes and guidelines	Collection of data on structural conditions	Inspection and evaluation	Inspection System	Inspection
Organization to manage and carry out previous activities	Assessment of structural conditions	Maintenance degradation reliability and cost	Structural capacity evaluation	Repair and Rehabilitation
Database holding data resulting from previous activities	Comparison of various maintenance strategies	Decision tools	Lifetime prediction of the future condition of the structure	Optimization
Set of computer tools for processing the data	Optimization of interventions		Cost evaluation system	
	Prioritization of interventions considering existing constraints			

The inventory module and inspection module are always present, though they may be referred to by different names, establishing them as fundamental components of BMSs. Often, BMSs limit their scope to these modules, guiding decisions based on engineering judgment. Discrepancies across the literature also emerge in modules dedicated to condition assessment and decision-making. Consequently, there is a pressing need to establish standardized categories. Defining uniform BMS modules is important for several reasons. A standardized definition ensures a common understanding within the industry, promoting clear communication among researchers, practitioners, and policymakers. Uniform definitions also facilitate comparisons and benchmarking across different BMSs, promoting best practices and continuous improvement. Furthermore, standardized modules provide a foundation for the development of interoperable and compatible BMSs. This interoperability is increasingly important in an era where data exchange and integration between different systems are vital for comprehensive and efficient bridge

management. Hence, in this paper, BMS modules are defined as follows:

(1) *Data management*, dealing with data about bridges and the status of their components;

(2) *Diagnosis*, consisting of condition rating and deteriorating assessment;

(3) *Prognosis*, gathering all the activities connected to the prediction of future bridge conditions;

(4) *Decision-making* identifying optimal management actions.

The proposed four modules are interconnected, as shown in Figure 5.4. Diagnosis and prognosis rely on data pertaining to bridges and their components, while decision-making is influenced by the outcomes of diagnosis and prognosis and can also impact data management. The subsequent sections present and examine these four modules in detail.

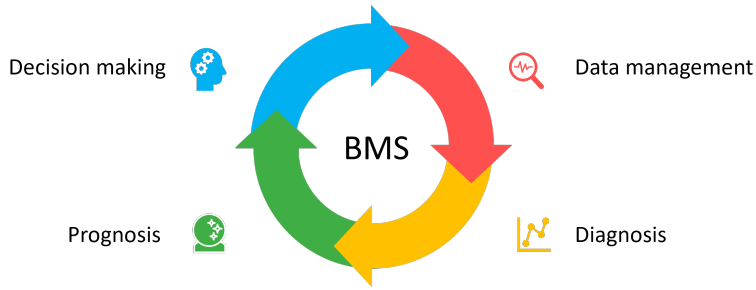

Figure 5.4: Modules of a BMS.

5.5 Data management

Data management encompasses four stages, namely data collection, acquisition, transmission, and storage. The collection phase involves gathering data pertaining to the bridge inventory, such as observations or signals. Two primary approaches have emerged for data collection: inspections –including visual inspections, Non-Destructive Tests (NDTs), and Destructive Tests (DTs)– and Structural Health Monitoring (SHM). The acquisition phase entails converting the collected data into a computer-readable format. Data transmission refers to the process of sending data to computing networks or electronic devices. Lastly, the storage phase involves saving and recording the data. These four phases are illustrated in Figure 5.5. In the subsequent sections, these phases are discussed with

reference to inspections and SHM. Visual inspections provide a direct, qualitative assessment of visible damage and structural conditions, while NDT and DT techniques offer quantitative data on material properties and hidden defects. Instead, SHM can reveal trends and anomalies that might not be apparent through inspections alone, serving as a valuable complement to inspections, particularly in critical or complex structures [33]. Inspections and SHM should not be seen as replacements but as complementary processes that allow operators to achieve a comprehensive understanding of a bridge's condition.

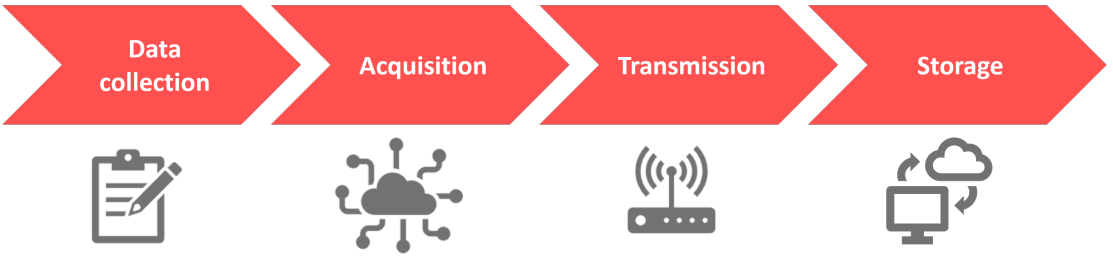

Figure 5.5: Phases of data management.

5.5.1 Inspection data management

Inspection methods involve technicians who assess structural and non-structural anomalies [34]. Different types of inspection exist with varying levels of detail based on their scope and frequency, such as inventory, routine, in-depth, and special inspections [35]. Inventory inspections provide baseline condition assessment when the bridge is first constructed or added to the management system. Routine inspections, conducted at regular intervals, ensure ongoing monitoring of the bridge's condition. In-depth inspections are more detailed and may involve accessing hard-to-reach areas to closely examine specific components. Special inspections are carried out in response to specific events, such as after a natural disaster or a vehicle impact, to assess any resulting damage [36].

Extensive research and documentation exist on inspection methods, see, e.g., [35, 37]. Due to the importance of inspections in current practice, they are typically regulated by codes and guidelines at the national or regional level. However, operators typically have the flexibility to adopt internal procedures as long as they align with overarching regula-

tions. Table 5.3 shows some examples of inspection codes and guidelines. In addition to the description of the procedures and of the instrumentation to use, these documents generally specify the requirements that must be met in terms of inspection competencies and expertise depending on the type of inspection.

Table 5.3: Inspection codes and guidelines.

Country	Regulation
US	American Association of State Highway and Transportation Officials, The Manual for Bridge Evaluation[24] Federal Highway Administration (FHWA), Bridge Inspector's Reference Manual[36]
	Massachusetts Department of Transportation, Bridge Inspection Handbook - Field Inspection, Data Collecting, Report Writing and Report Review[21]
	New York State Dept. of Transportation Office of Structures, Bridge Inspection Manual[22]
	Iowa Office of Bridges and Structures, Bridge Maintenance Manual[20]
Canada	Ontario Ministry of Transportation, Ontario Structure Inspection Manual[38]
	Alberta Transportation (AT), Bridge inspection and maintenance system: BIM Level 1 inspection manual. Version 4[39]
UK	Highway England, Requirements for Inspection and Management of Bridges, BD 62/94 and BD63/94[40]
Norway	Norwegian Public Roads Administration, Handbook for Bridge Inspection Part I[41]
China	Ministry of Transport of the People's Republic of China, Standards for Quality inspection and verification of highways.[42]
Australia	Main Roads Western Australia, Detailed Visual Bridge Inspection Guidelines[43].
Italy	Consiglio Superiore dei Lavori Pubblici, Linee Guida per la classificazione e gestione del rischio, la valutazione della sicurezza ed il monitoraggio dei ponti esistenti[44]
Spain	Ministerio de Fomento, Guia para la realizaciòn de inspecciones principales de obras de paso en la Red de Carreteras de Estado[45]
Ireland	Transport Infrastructure Ireland, EIRSPAN bridge management system principal inspection manual[46]

While inspections are widely used and remain a cornerstone of bridge condition assessment, they come with several limitations. Accessing certain areas of a bridge, such as underwater pier foundations or bridge soffits on long-span bridges, can be challenging and often requires specialized equipment like bridge inspection trucks, boats, and drones. These logistical challenges can also necessitate traffic interruptions or restrictions, leading to additional costs and inconvenience. The periodic nature of inspections, typically scheduled at regular intervals or triggered by specific events, means they do not offer early warning signals for the occurrence of damage, limiting their effectiveness in proactive maintenance. Additionally, the costs associated with inspections can be substantial, particularly for bridges that are difficult to access.

Inspection data collection

Procedures for bridge data collection include visual surveys, NDTs, and DTs. Visual inspections are a fundamental component of bridge management, typically carried out by trained technicians. The scope of these inspections varies based on the inspection type; for example, routine inspections may focus only on accessible elements, while more detailed inspections might include hard-to-reach areas. The primary purpose of visual inspections is to detect visible signs of deterioration, such as cracks, corrosion, spalling, and deformation, and to document these findings for further analysis [47]. Furthermore, visual inspections allow for the detection of a variety of issues beyond structural integrity, including hydraulic phenomena (e.g., presence of scour or debris accumulation on piers in water) and geotechnical phenomena (e.g., initiation of landslides). These aspects have been stressed by e.g., the recent Italian Guidelines for bridges [44] which suggest a multi-risk assessment of bridges based on archive data and visual inspections.

Visual inspections involve several steps. Inspectors use checklists and standardized forms to ensure consistency and comprehensiveness in their assessments. They often use tools such as binoculars, cameras, and drones to enhance their ability to inspect inaccessible areas [48]. Findings are recorded, often using digital platforms that facilitate data storage, analysis, and sharing among stakeholders. Visual inspections remain indispensable despite advancements in technology, as they provide a direct and immediate evaluation of a bridge's condition. Nevertheless, they are inherently subjective, as the outcomes can vary based on the skills and expertise of individual inspectors. This subjectivity can lead to inconsistencies, especially when inspection codes and guidelines lack clarity on how to assign judgments to specific defects. Furthermore, visual inspections face challenges in identifying hidden defects.

In turn, NDTs can identify defects in structural elements that are not visible such as internal flaws and delamination. Ultrasonic testing, Eddy Cutting Testing (ECT), Acoustic Emission (AE), and Magnetic Flux Leakage (MFL) testing can be used to detect corrosion and fatigue on steel components [49, 50, 51]. Specifically, ultrasonic testing uses high-frequency sound waves to detect internal defects, such as flaws and irregularities, and measure material properties, like changes in microstructural or mechanical properties. ECT utilizes electromagnetic induction to detect surface or subsurface defects in conductive materials. AE techniques monitor the release of elastic stress waves from localized sources (such as cracks or other discontinuities) when a material deforms under stress. MFL testing detects corrosion, breaks, pitting, and breaks by inducing a magnetic field to the component and evaluating leakage in

the material from its flux path. Further, NDTs such as impact echo and ground penetrating radar can detect corrosion in reinforced concrete. Impact echo is an ultrasonic method that is able to detect defects by measuring the velocity of propagation of elastic waves [52]. Ground-penetrating radar employs radar pulses to image subsurface anomalies. Thermography utilizes infrared imaging to detect variations in temperature that indicate potential defects like delamination, fatigue crack propagation, or moisture intrusion [53].

DTs involve controlled damage to a part of the bridge to evaluate its properties and performance [53]. Material properties might differ from design values. Also, as bridges age, uncertainties related to the structure increase due to deterioration mechanisms and real-life conditions. Therefore, reliable prediction of bridge capacity and behavior often requires DTs of material samples for calibrating models and evaluating the performance of existing bridges [54, 55]. Common DTs include core drillings to extract material samples for analysis, cutting and removing portions of the structure for detailed examination, chemical testing to assess material composition and degradation, and accelerated aging tests to simulate long-term wear and environmental impacts [56].

Acquisition, transmission, and storage of inspection data

Inspections generate a variety of data types. In consideration of visual inspections, outputs include photographs, videos, sketches, and written reports that describe observed conditions and defects. NDTs and DTs of material specimens generate another layer of critical data for bridge assessments. The acquisition of NDT and DT data involves using specialized equipment to collect measurements, that are then converted into digital formats for analysis. These data need to be collected, transmitted, and stored for effective use in BMSs [57].

The results of inspections are typically collected in a database, either by the operator who performed the inspection or by the technical office based on the submitted inspection record, in paper format, or through the interfaces of the software. To this end, smartphones and tablets have been rapidly developing in the inspection field in recent years. Smartphones, which embed a mini personal computer integrated with sensors, operating systems, and communication systems, proved to be an effective tool for data acquisition and particularly for the improvement of inspection both in terms of immediacy and accuracy [58, 59].

Transmission of inspection data can rely on wireless communication technologies and cellular networks to transfer images and videos to central databases. In the case of high-resolution and complex outputs, a stable internet connection is essential to prevent data loss and ensure

accuracy. Both for visual inspection and NDT and DT data, the storage solution must accommodate the large file sizes and diverse formats generated during inspections. Cloud-based storage systems offer scalability and remote access, allowing multiple users to view and analyze data concurrently [60]. These systems also support robust data management practices, including version control, metadata tagging, and secure access protocols, ensuring that inspection data remains organized and easily retrievable. Storage systems must also ensure data security and integrity, supporting features like encryption, blockchains, backup, and recovery protocols [61, 62]. Smartphones allow not only for direct cloud communication with databases but also the ability to associate increasingly high-quality photographs with inspection judgments in an immediate way thanks to the possibility of having BMS software on the field. Similarly, the use of drones connected to BMS software for inspections is also gaining popularity [63]. Field software, particularly when connected to the BrIM of the structures, can offer significant advantages. The possibility of updating in real-time the condition of the structure brings significant savings in terms of time for acquisition, transmission, and storage [64].

The acquisition of inspection data can be enhanced with digital tools that allow inspectors to annotate images, create 3D models, and integrate findings into centralized databases. Advanced software platforms facilitate real-time data entry during inspections, enabling inspectors to upload images and notes directly from the field using mobile devices, in order to process and analyze findings in an immediate way facilitating quick identification of critical issues [65]. The rapid digitization of inspection data not only streamlines the documentation process but also ensures that critical information is promptly available for analysis [66].

5.5.2 SHM data management

In recent decades, the limitations of inspections have driven operators to explore SHM systems, which automate data collection and provide continuous updates on structural conditions. National and international initiatives and organizations have played a crucial role in advancing SHM technologies and practices, promoting best practices and collaborative research across countries, and underscoring the global impact and potential of SHM advancements. Associations such as the International Society for Structural Health Monitoring of Intelligent Infrastructure (ISHMII) [67] and the International Association for Experimental Vibration Analysis for Civil Engineering Structures (EVACES IA) [68], foster research about SHM. Furthermore, numerous international conferences bring together researchers and practitioners periodically, such as SMAR

[69], EVACES [70], EWSHM [71], IWSHM [72], IOMAC [73], EUROSTRUCT [74], IABMAS [75], and EURODYN [76]. As for research projects, it is worth mentioning the COST Action TU1402, active from 2014 to 2019, which involved representatives from academia, industry, infrastructure owners, operators, and authorities. Its primary objective was to advance the management of structures and infrastructure systems through optimized SHM systems based on the Value of Information (VoI) [77, 78].

Following the tragic collapse of the Morandi bridge in Genoa in 2018 [79], Italy has made significant investments in bridge instrumentation with monitoring systems. For instance, ANAS, the operator of most Italian roads, has launched a "Structural Health Monitoring Program" funded with 275 million euros [80, 81]. From the academic point of view, the Italian national FABRE consortium exemplifies collaborative scientific endeavors aimed at enhancing bridge management and monitoring practices [82]. Additionally, the ReLUIS (Rete dei Laboratori Universitari di Ingegneria Sismica e Strutturale) network focuses on seismic engineering and structural monitoring, contributing significantly to the development of SHM practices in Italy [83].

Nevertheless, it is important to acknowledge the current limitations of SHM. First, SHM techniques – especially the vibration-based ones – are generally not sensible to superficial and small damages, which instead can be directly detected by visual inspections. Also, SHM systems degrade in time and require continuous maintenance, making it difficult to distinguish between anomalous data caused by out-of-service systems, malfunctioning sensors, or actual structural damage [84]. There is no widely accepted procedure to demonstrate the Return On Investment (ROI) in an SHM system, which represents maybe the greatest limitation to the extensive employment of SHM technology [78]. Additionally, permanent SHM systems collect huge amounts of data that have to be adequately managed and post-processed, and there are no general rules regarding the choices of technologies to use. Another significant barrier is the shortage of experts proficient in the proper analysis of SHM processes [85]. This lack of expertise leads to a preference among managers for more familiar data collection methods, such as visual inspections.

To address these challenges, several guidelines have been published starting from 2001 with the aim of standardizing SHM practices. The objective is to enhance understanding and knowledge of the SHM process, highlight its value, and develop rules and protocols [86]. These documents also provide recommendations for data processing in structural diagnosis applications. Figure 5.6 illustrates a chronological compilation of significant documents. It showcases the purpose of SHM as defined

in each specific document, indicating a current trend of integrating SHM data into BMSs.

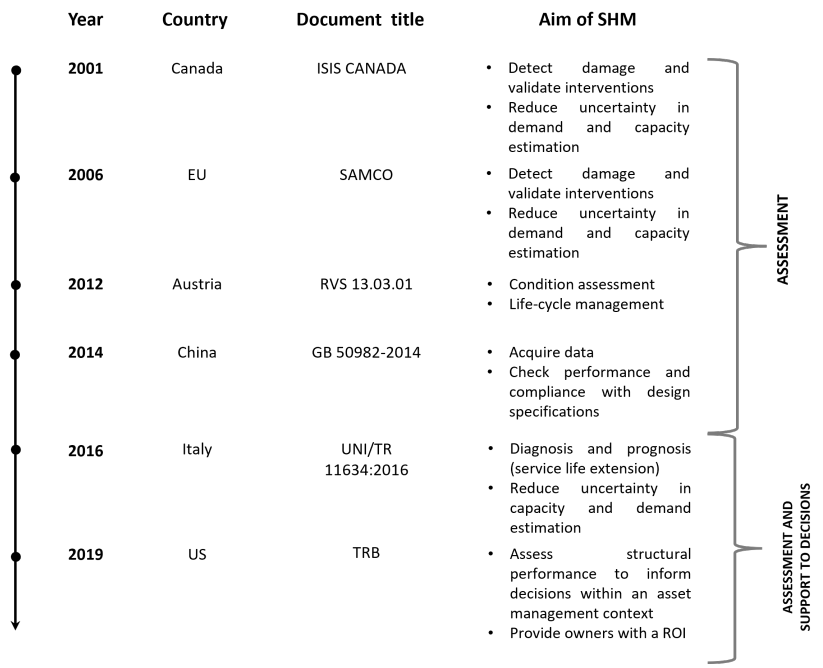

Figure 5.6: Documents for the standardization of SHM.

SHM data collection

SHM systems consist of several components, including sensors, data acquisition devices, data transmission systems, databases for storage, and processing units for analysis and modeling [87]. This hardware converts physical measurements into damage-sensitive features, providing insights into structural health over time. A wide range of sensors has been introduced over the last decades [88]. Widely used sensing technologies in SHM include contact sensors such as fiber optics, piezoelectric sensors, global navigation satellite systems, and magnetostrictive sensors [89]. Microelectromechanical Systems (MEMS) sensors are gaining widespread popularity [90, 91] due to their reliability, efficiency, and compact size, making them highly suitable for a wide range of applications [92].

Sensors have been exploited to measure different types of quantities relating not only to structural behavior but also to external actions and environmental factors. Figure 5.7 shows a non-exhaustive list of monitorable parameters in SHM.

SHM strategies are typically categorized as local or global approaches.

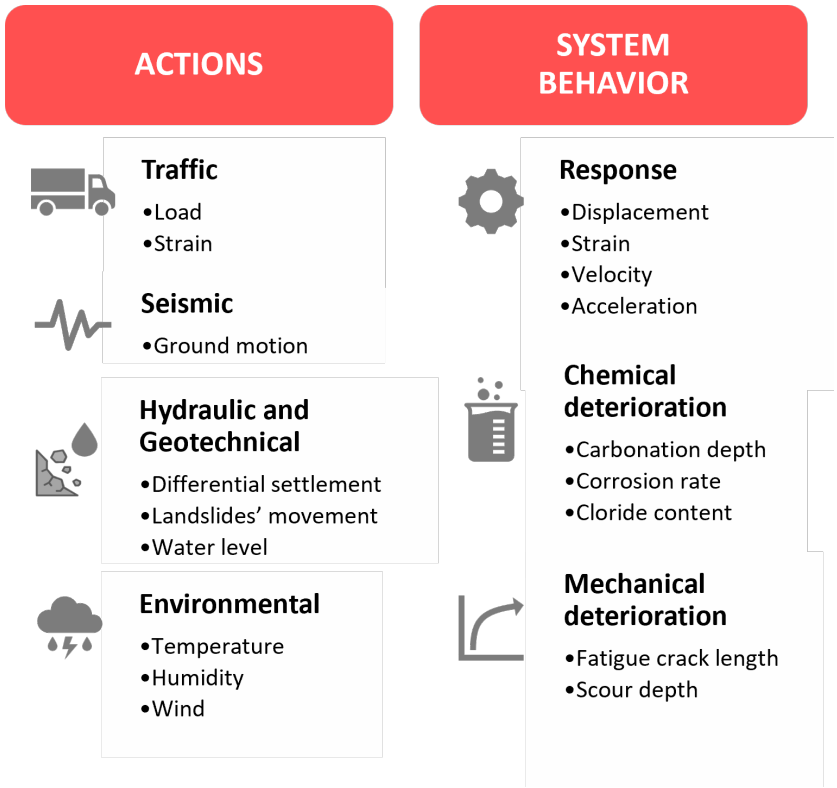

Figure 5.7: Non exhaustive list of SHM monitorable parameters.

Local SHM provides detailed information about specific locations within the structure where sensors are deployed [93, 94], often focusing on monitoring slow-varying parameters such as pier tilt and strain. In contrast, global SHM focuses on dynamic structural properties such as modal parameters to assess overall structural integrity, even without sensors positioned directly at potential damage sites [95, 96].

Critical phenomena such as corrosion, fatigue, and scour, in principle, can be identified by both local and global monitoring systems.

Recent advancements in local fatigue crack and corrosion detection include the development of high-sensitivity vibration and acoustic emission sensors [97], as well as large-area strain sensing technologies [98] and ultrasonic guided waves [99]. On a global scale, tracking modal parameters from acceleration records, such as natural frequencies, can also be effective in identifying corrosion and fatigue cracks, particularly when these phenomena cause significant changes in structural stiffness [100, 101]. Data acquisition methods can be combined with signal processing algorithms and machine learning techniques for damage iden-

tification, facilitating timely interventions. Ongoing research focuses for example, on refining fatigue and corrosion models through neural-network [102, 103] as opposed to more classical analytical probabilistic formulations [104].

Digital Image Correlation (DIC) has shown promising results as an advanced technique for detecting and quantifying both in-plane and out-of-plane fatigue cracks, which are common in steel bridge components [105, 106]. As a noncontact, vision-based sensing technology, DIC tracks the surface deformation of materials by analyzing changes in a speckle pattern applied to the structure's surface. This method is particularly advantageous for inspecting fatigue-prone regions because it provides high-resolution, real-time data on crack initiation and growth without the need for direct physical contact or extensive on-site monitoring.

Scour is considered one of the major causes of bridge failure world-wide [107]. A variety of sensors have been developed to monitor scour occurrence and progression [108], such as float-out devices, radar and sound-based systems, and buried rod systems. These technologies are based on the detection of changes in scour hole depth and therefore are able to provide information about specific locations. Alternatively, Vibration-based SHM systems have become increasingly popular in recent years. These systems monitor changes in the natural frequency of a bridge structure caused by scour, which affects the structural boundary conditions and consequently the global modal behavior [109].

Acquisition, transmission, and storage of SHM data

The process of acquisition, transmission, and storage of SHM data is generally digitalized and automated. When the sensor receives an input, an acquisition system converts an analog signal into a digital one by an analog-to-digital converter, to make the signal readable by a computer [110]. Despite future direction aims at the employment of sensors that do not necessarily require converters, e.g., most of the aforementioned MEMS sensors, the great majority of sensors on the market still employ acquisition systems that include these elements. An acquisition system generally consists of three main elements: sensors, signal conditioning circuits, and the aforementioned analog-to-digital converter. When a sensor converts a physical phenomenon into an electrical signal, the data often requires signal conditioning to be useful for SHM. This process may involve filtering to remove noise, buffering to stabilize the signal, amplification to enhance weak signals, and potentially compensations or linearization to correct for any distortions or non-linearities, depending on the quality and characteristics of the original signal.

Regarding transmission, traditional SHM systems are mainly wired-

based. Wired systems transmit data through coaxial wires to process them afterward with the system [110, 111]. Lately, there has been great progress in wireless-based solutions [112, 113]. Wireless Sensor Networks (WSN) often consist of many sensor nodes, connected with sensors, which contact each other via a wireless network and send data directly toward the base station [88]. The newest mobile communication technology, 5G, has introduced innovative network paradigms capable of offering an unprecedented level of reliability, low latency, higher connectivity, and higher data rates [114].

Given the escalating data acquisition rates in emerging technologies, the volume of data and the available memory are critical parameters for data storage, especially in long-term monitoring. Internet of Things (IoT) systems and cloud-based architectures have become prevalent due to their numerous advantages [115, 116]. These benefits include large data flow and storage capacities without the significant physical footprint of traditional solid storage, as well as the capability for wireless communication with remotely connected devices, such as sensors, smartphones, and tablets. The goal is to store data files in a more compact form while retaining sufficient information for future use, processing, and analysis, aided by increasingly performant databases.

5.6 Diagnosis

The objective of the diagnosis module is to evaluate the condition of individual bridge components, single bridges, or infrastructure networks. This requires the identification of appropriate Performance Indicators (PIs), thresholds, or goals at various levels (component, system, and network). The research community has made significant strides in this field in recent years. For instance, the COST TU 1406 Action has played a key role in developing a guideline for quality control plans in roadway bridges, with a focus on standardizing and harmonizing PIs, thresholds, and goals across different countries [117, 118]. The following sections describe methodologies and approaches for assessing bridge conditions via PIs.

5.6.1 Performance Indicators

Different types of PIs exist to address and describe different aspects concerning the structure of interest. In general terms, PIs can be classified into technical PIs and non-technical PIs [119], see Figure 5.8. At different levels, decision-making is then guided by the integration of both types of PIs [118].

Technical PIs capture the mechanical properties and/or the degrada-

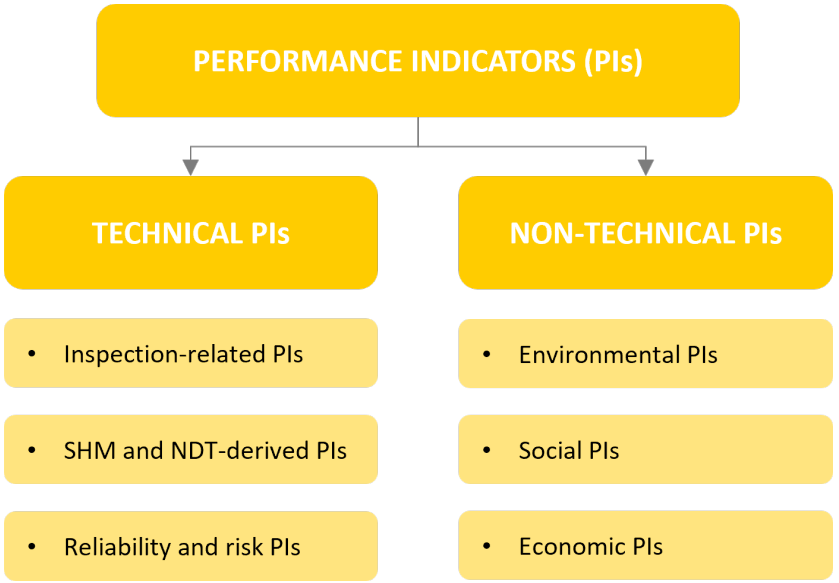

Figure 5.8: Classification of performance indicators.

tion of structures and can characterize their ultimate capacity as well as serviceability conditions. Additionally, technical PIs can also encompass aspects related to the surrounding conditions of the structure, addressing e.g., geotechnical, and hydraulic aspects.

Herein, technical PIs are classified into (i) PIs based on the results of inspections (including visual inspections and tests), (ii) PIs obtained from SHM, and (iii) PIs dealing with structural reliability and risk.

Bridge Condition Indicators (BCIs) are quantified by combining the condition rates of individual bridge components assigned during visual inspections [120]. The evaluation of the BCI for a stock of bridges can lead to a priority repair ranking within the network [29, 121]. BCIs are commonly used in practice by road agencies and their computation is implemented in BMSs worldwide, although the quantification methods can differ. Nevertheless, often the optimum repair or rehabilitation strategy is not obvious based only on such information. BCIs alone cannot provide a clear structural safety judgment since no quantitative evaluation is done from both the resistance and the loading sides.

Different types of key state parameters (or damage-sensitive features) can be extracted from SHM data according to the type of sensors, the type of structure, and the goal of the monitoring. In general, an SHM-derived PI that can be correlated to the presence of damage is defined as Damage Indicator or Index (DI) [122]. Overall, the implementation of DIs in BMS software is still at an early stage of development.

More recently, the interest in PIs taking into account reliability and risk considerations has increased [117]. They include structural reliability and risk, cumulative probability of failure, survivor function, hazard rate function, structural redundancy, structural robustness, structural resilience, and load rating factor [119, 123, 124]. Reliability is an important PIs, which is linked to the probability of failure for a bridge component with respect to a given limit state function, considering both load and resistance characteristics [2, 125, 126]. It is often used to forecast structure performance over time: combining the reliability of different failure modes with a deterioration model, a reliability profile for the observed bridge can be obtained [127]. However, reliability by itself does not enable accounting for the consequences related to failure which in turn may be a decisive factor in prioritizing maintenance interventions, especially under budget constraints. Risk provides a more comprehensive assessment by considering both the probability and consequences of potential failures [128].

Economic, social, and environmental indicators complement technical integrators [119] even though they are not systematically implemented in BMSs [117]. Non-technical PIs include economic, social, and sustainability PIs.

Economic PIs relate to construction and maintenance costs. One of the most important economic indicators is the Life-Cycle Cost (LCC), which consists of the sum of all costs related to a bridge during its service life, e.g., reconstruction costs, inspection costs, preventive maintenance costs, repair costs, out-of-service costs, user costs [129, 130, 131]. At the component level, a widely used economic indicator is the ratio between the total cost of repairing individual damages and the price of a new component. Components with a ratio exceeding 1.0 are typically recommended for replacement [118]. The APTBMS (Italy) [15] includes the calculation of a cost indicator, which is directly used for the priority ranking of the stock.

Social PIs are related to road users' satisfaction and safety to assess the social performance of a bridge. They encompass factors such as increased travel times for users.

Sustainability PIs characterize the environmental impact of a structure in the course of its life-cycle. They consider aspects such as cumulative energy demand during a bridge life-cycle, the use of renewable or non-renewable resources, durability, solid waste production, and the emissions measured in kg of CO_2 equivalents [119].

5.6.2 Condition assessment using technical indicators

Technical indicators play a crucial role in BMSs by providing quantifiable measures of structural damage and its severity. The first part of this section addresses technical performance indicators derived from inspection results, which are extensively utilized in BMSs worldwide. The second part focuses on technical performance indicators obtained from SHM data.

Condition assessment based on BCIs

BCIs are generally calculated based on the condition ratings of structural components and, in some cases, the service provided by the bridge (i.e., the importance of the bridge within the network). Four main approaches for the evaluation of the BCI are identified [120, 132], as follows:

- **Weighted average approach**. The BCI is estimated by combining condition ratings of all individual bridge components weighted by the importance of the component in terms of functionality and safety, by the gravity of the damages identified during the inspection, or by the bridge's importance within the network.
- **Qualitative approach**. The BCI is assigned based on numeric rating scales (e.g.,1-5) and linguistic expressions such as excellent, good, fair, and poor, based on the condition state and importance of the investigated components.
- **Worst-conditioned component approach**. The BCI corresponds to the rating of the component in the worst condition.
- **Ratio-based approach**. The BCI is assigned based on the ratio of the current condition to the condition of the structure when it is new.

Table 5.4 reports, for each condition rating approach, examples of BMS software adopting that particular approach and the country in which the BMS has been implemented.

In general, BCIs provide a rating of the bridge condition and generally enables owners and operators to rank the interventions within the bridge inventory. Ranking procedures are suitable for implementation in BMS frameworks since they can be easily linked with recommendations about follow-up actions, maintenance and rehabilitation plans, and costs [133].

Numerous frameworks have been proposed for BCI evaluation, addressing both gradual deterioration [119, 134, 135] and the effects of natural hazards [136, 137]. Some studies employ probabilistic approaches to account for uncertainties in BCI evaluations, particularly through visual inspections, investigating the link between the probability of dam-

Table 5.4: BCI in existing BMSs.

Condition rating approach	BMS	Country
Weighted average approach	HiBris, Hanke-Siha	Finland
	SMIS	UK
	STRUMAN	South Africa
Qualitative approach	LAGORA	France
	BaTMan	Sweden
Qualitative approach	LAGORA	France
Worst conditioned component approach	SIB-Bauwerke	Germany
	APTBMS	Italy
Ratio-based approach	Pontis/BrM	US

age detection and condition ratings [131, 138]. Fuzzy logic tools [139], evidential reasoning approaches [140], and machine learning [141] were explored to enhance the accuracy and reliability of bridge condition assessments.

Condition assessment based on SHM

Traditionally, four levels of damage identification are contemplated [142], namely: damage detection (i.e., identify or not the presence of damage), damage localization (i.e., find the location of damage), damage assessment (i.e., quantify the level of damage), and prognosis (i.e., forecast the evolution of damage).

Key structural state parameters or damage-sensitive features often do not provide information about damage by themselves, unless with reference to their value in a baseline state. This calls for the need to define the DI, which might not have a clear and direct physical meaning but allows for expressing variations of state parameters with respect to the baseline. The extraction of DIs can be performed based on two different approaches: physics-based, and data-based.

The physics-based approach utilizes the inverse problem technique to deduce the state of a structure based on the selected DI. Inverse problems involve inferring the values of the chosen DI and other related parameters that describe the system using measured data obtained from monitoring. The interpretation models establish the connection between the DI under investigation, which represents the state of the structure, and the observations from monitoring. These models can take the form of analytical or numerical functions, such as Finite Element (FE) models. Model updating techniques are crucial in physics-based approaches and are employed to refine and improve the accuracy of the models [143].

The data-based (or data-driven) approach uses a variety of algorithms to learn structural behavior from collected data. This approach does not rely on the use of a predefined physical interpretation model. Differ-

ent machine learning algorithms have been developed and used to distinguish patterns in SHM data [144, 145]. The common final goal of machine learning algorithms is the extraction of DIs from monitoring data and the detection of outliers lying at an abnormal distance from the population of the damage-sensitive feature.

Ideally, the DIs should be sensitive to the specific phenomena to monitor, and they should be robust with respect to other sources of variability so that they would vary consistently only with the level of damage. Nevertheless, a critical problem for damage identification in SHM is the impact of operational and environmental effects on the quantities measured by sensors and, in turn, DIs. Live loads as well as temperature changes (both daily and seasonal) can significantly influence the structural response and increase the uncertainty in the detection of damage [51, 146]. Environmental effects can hide the presence of damage or be misinterpreted and result in a false indication of damage and must therefore be removed. Such an issue is common to both physics-based and data-based approaches.

Damage indicators are typically compared to predefined thresholds in order to classify the structural condition. The choice of a specific threshold is closely linked to the uncertainty inherent in the damage detection process. The selected threshold needs to strike a balance: it must be strict enough to prevent false identification of damage due to uncertainty, while still allowing for the identification of outliers caused by structural damage.

In the simplest scenario, the classification of structural conditions based on the DI value involves two possibilities: damaged and undamaged, constituting a binary classification. When comparing the DI with a particular threshold, there are four possible outcomes: True Positives (TP), True Negatives (TN), False Positives (FP), and False Negatives (FN). To determine the probabilities associated with these outcomes, the Probability Density Function (PDF) of the damage indicator in both undamaged and damaged conditions can be considered, as depicted in Fig. 5.9.

Analyzing these PDFs provides a means to assess the likelihood of different outcomes when comparing the DI value with a specific threshold. In binary classification problems, the choice of a threshold should be based on the minimization of the odds of false damage detection (false positives and false negatives). A statistical tool that enables the evaluation of the desired results (true positives and negatives) and unwanted results (false positives and negatives) is the Receiver Operating Characteristic (ROC) curve. A ROC curve is a graphical tool that allows for quantifying the performance of classifiers, varying the threshold posi-

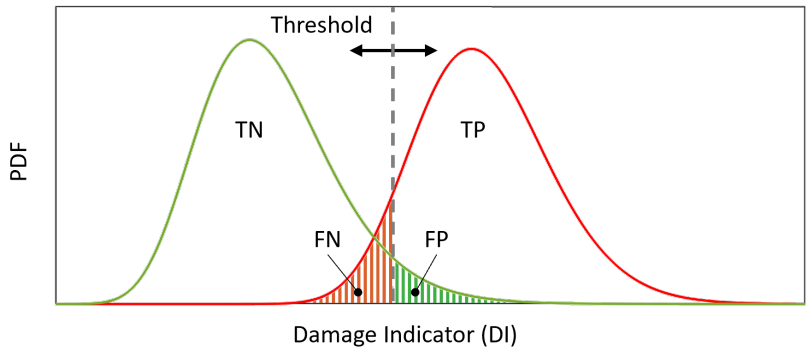

Figure 5.9: Binary classification of damage indicators.

tion, and statistically evaluating the erroneous predictions related to false detection [147].

In most cases, however, it is not convenient to decide among thresholds based solely on ROC curves (i.e., based on true positive-false positive pairs). In decision problems, possible different consequences and expected costs related to the different outcomes should be considered. This problem has been tackled using the principles of the Expected Utility Theory (EUT) [148, 149].

5.7 Prognosis

The prognosis module relies on deterioration models and incorporates information about the current conditions of bridges and their components to forecast their future states. The diverse characteristics of bridge components–varying in importance, size, age, position, and material–coupled with their exposure to various loading and environmental conditions, result in a significant variability in the rate of deterioration among these components. The literature on degradation models spans various applications, addressing both structural and nonstructural components, different materials, degradation mechanisms, and environmental factors [150].

However, the literature provides limited details on the implementation of deterioration models in existing BMSs, which hinders the expansion of this section. Following a thorough examination, information about twenty BMSs was found and is reported in Table 5.5. These BMSs predominantly incorporate two types of deterioration models: stochastic and deterministic. BaTMan, Slovenia BMS, STRUMAN, and NCDOT BMS, utilize deterministic deterioration models. However, the majority

of BMSs, including APTBMS, Bridgit, KUBA, Ontario BMS, Pontis, and BAUT, use stochastic deterioration models.

Table 5.5: Deterioration models used in BMSs.

BMS name	Country	Deterioration Model
AASHTOWare	United States of America	Stochastic[12]
APTBMS	Sweden	Deterministic: Regression[151]
BAUT	Austria	Stochastic: Markov chains[152]
Bridgit	United States of America	Stochastic: Markov Chain[11]
Disk	Netherlands	Stochastic[12]
EBMS	United States of America	Stochastic: Markov Chain[12]
Florida DOT	United States of America	Stochastic: Semi-Markov Chain[153, 154]
GNWT	Canada	Stochastic: Markov Chain[12]
KRMBS	Korea	Stochastic[12]
KUBA	Switzerland	Stochastic: Markov Chains[156]
Lat Brutus	Latvia	Stochastic[12]
NCDOT BMS	United States of America	Deterministic: Regression[11]
NSW	Australia	Stochastic[12]
Ontario BMS	United States of America	Stochastic: Markov Chain[11]
PEI BMS	Canada	Stochastic: Markov Chain[12]
Pontis	United States of America	Stochastic: Markov Chain[11]
QBMS	Canada	Stochastic: Markov Chain[12]
RPIBMS	Japan	Stochastic[12]
Slovenia BMS	Slovenia	Deterministic: Regressio[28]
STRUMAN	South Africa	Deterministic: Regression[155]

Subsequent sections introducing these types of deterioration models do not aim to explain them, as models adopted in existing BMSs are well-established and widely known. Readers are directed to the provided reference for further details [154, 156].

The limited knowledge regarding the prognosis module remains a key focal point in this study, providing an avenue for discussing crucial aspects and future directions within the dedicated sections.

5.7.1 Deterministic models

Deterministic models provide a single, definite solution for a given set of model parameters and inputs. Essentially, the outcomes of deterministic models are entirely determined by their inputs and the model's structure devoid of any consideration for uncertainty. These models assume well-defined and predictable cause-and-effect relationships.

Among deterministic models, regression models find application in BMSs. They can be either linear or non-linear depending on the type of function used to fit the data. Linear regression models, consisting of first-order functions, describe the deterioration process as linearly dependent on time. Instead, nonlinear regression models utilize nonlinear functions, such as multiple-order polynomial functions. These models can be more

accurate in long-term predictions than linear ones [11].

According to Table 5.5, regression models are applied into the Swedish BaTMan [152], the NCDOT BMS [11], the Slovenia BMS [28], and the South African STRUMAN [155].

In particular, NCDOT BMS [11] employs linear regression models, allowing, for instance, the prediction of material condition ratings by assuming a constant traffic load over time and regular maintenance.

The recent Slovenia BMS [28] implements piece-wise linear functions to approximate the deterioration state of bridge components. Such deterioration model accounts for material characteristics (reinforced concrete, steel, or stone), year of construction (before or after 1995, year of implementation of the current design code), and damage degree (negligible, low average, high, or severe). The inclusion of these parameters in the definition of the linear functions was determined by analyzing 25 years of recorded inspection data and has proven to be accurate in short/medium-term predictions.

Similarly, the deterioration model adopted in STRUMAN consists of a piece-wise linear function. In addition to the parameters considered by the Slovenia BMS, it accounts for traffic volume as well as environmental and climatic factors [155].

The Swedish BaTMan system differs from other BMSs by not implementing linear regression models at the level of bridge components. Instead, it forecasts the evolution of network performance [12]. The evaluation of bridge component deterioration is left to the judgment of expert engineers [152].

Deterministic models are used in BMSs because of their simplicity and practicality. The main disadvantages include neglecting the stochastic nature of bridge deterioration and the need to recalibrate the deterioration model when new data are acquired.

5.7.2 Stochastic models

Stochastic models are essential tools for predicting the deterioration of bridge components, incorporating inherent uncertainties through the use of random variables. These models diverge into two primary approaches: state-based models, exemplified by Markov Chain models, and time-based models, also known as duration models [154].

Markov Chain models represent a fundamental state-based approach to deterioration modeling within BMSs. These models operate under the assumption of the memoryless property, where future states depend solely on the current state and not on the historical condition of the component. They describe the progression of bridge condition states over discrete time intervals using fixed transition probabilities organized into

transition matrices. Markov Chain models can be either time-homogeneous, with constant transition probabilities (the transition matrix is thereby defined as stationary), or time-inhomogeneous, where these probabilities vary over time based on external factors such as environmental changes or maintenance interventions. Expert opinions, bridge type, current condition, environmental factors, and historical maintenance data inform the determination of these transition probabilities [157]. The simplicity and ability to integrate expert knowledge make Markov Chain models popular in BMS applications, such as the implementation detailed in the APTBMS.

Time-based or duration models offer an alternative stochastic approach to deterioration prediction, focusing on the time a bridge component remains in a particular condition state. These models utilize statistical distributions such as Weibull or Gamma to describe the variability in the duration until the component transits to a new condition state. Unlike Markov Chain models that emphasize discrete states and transitions, duration models provide insights into the expected lifespan of components under varying conditions. Factors influencing duration models include environmental conditions, structural design, and the effectiveness of maintenance and rehabilitation efforts.

An example of a stochastic deterioration model that integrates a duration model is documented in the Florida DOT BMS [153]. In this model, the likelihood of a structure maintaining its initial condition state is characterized using a Weibull survival function, while transitions between subsequent condition states are governed by a Markov Chain. This combined approach is known as Semi-Markov chain model, offering a nuanced depiction of deterioration over time.

Stochastic deterioration models represent an active research area in academia as evidenced by recent studies [158].

However, there are some critical aspects to consider when using these models. First, the assumptions underlying Markov chain models are hardly satisfied in practice. For instance, it is often difficult to estimate accurately the probabilities of transition between different states of the structure due to the lack of reliable data. Additionally, most common deterioration models are not always reliable, especially for bridges that have been subjected to unusual or extreme loading conditions or that have experienced environmental or geological hazards. Current deterioration models can grasp generalized deterioration processes at the bridge component level. However, the failure of a component is often due to localized deterioration phenomena. This fact represents a limitation to the application of deterioration models and must be taken into account when performing maintenance schedules [159].

5.8 Decision-making

Bridge management accounts for three different scales, namely: network, element, and component scale. The network scale refers to a set of bridges sharing some common characteristics, e.g., position, static scheme, and length. The element scale focuses on an individual bridge whereas the component scale encompasses both structural components (e.g., deck, girders, piers) and non-structural components (e.g., road accessories, road surfaces, drainage systems) of individual bridges.

At the level of single bridges, an important aspect of bridge management relates to the optimization of maintenance activities at the component level. Maintenance corresponds to the sequence of actions to be taken to preserve the initial performance of a bridge and maximize life expectancy [160]. Still, managers usually handle large portfolios of bridges and account for unavoidable constraints in economic, material, and personnel resources. For this reason, managers need to prioritize maintenance activities identifying a priority ranking between different structures. Two primary approaches for decision-making are identified: the top-down approach, which focuses on network-level optimization, and the bottom-up approach, which concentrates on individual bridge maintenance optimization. The selection of the best approach generally depends on the size of the network and also on the optimization method employed.

5.8.1 Maintenance Strategies

Four different maintenance strategies exist, namely corrective, preventive, condition-based, and predictive maintenance, each with different characteristics and increasing complexity [160, 161, 162], see Figure 5.10.

The corrective (or reactive) maintenance strategy includes the set of actions that are performed to repair or replace faulty components and equipment. These failures are typically identified during routine inspections. Interventions can be carried out immediately after the detection of failure or deferred in time, in the case the failure does not significantly affect the bridge functionality. The corrective strategy is implemented in case the costs sustained for downtime and repair are lower than the investment required for a scheduled maintenance program or data collection. This strategy is generally considered cost-effective for non-structural bridge components.

Preventive strategies imply periodic activities performed on predetermined schedules or according to prescribed rules (e.g., use-based), aiming at reducing the risk of failure or severe performance degrada-

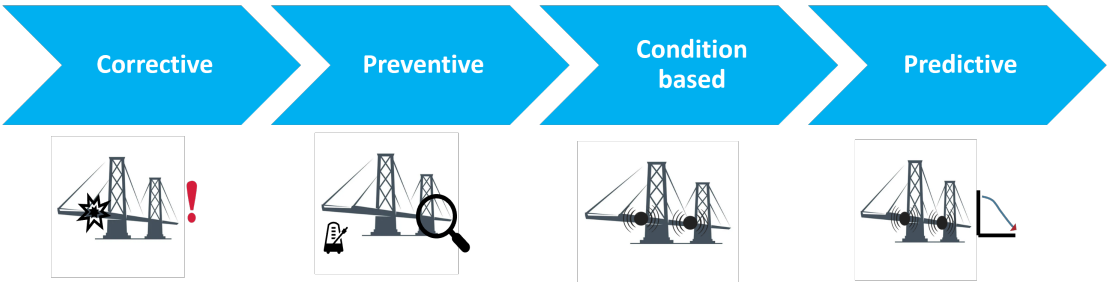

Figure 5.10: Maintenance strategies.

tion of bridges. Preventive strategies can be applied both for structural and non-structural bridge components. For example, APTBMS utilizes a preventive maintenance strategy for certain categories of bridge components, such as components positioned on the road planes (joints, road slabs, etc.) and accessories (guardrails, etc.) with a time frame of one year [151]. Similarly, STRUMAN implements preventive plans for non-structural bridge components such as drainage systems [155].

Condition-based maintenance uses new data from visual inspections, tests, and SHM systems to identify and track deterioration. It follows specific condition criteria, e.g., reliability thresholds, to decide when maintenance is needed. This method cuts long-term maintenance costs, reducing the chances of major failures. Condition-based maintenance strategies are used for instance, by DANBRO, MRWA, and Bridgeman BMSs, which do not include a prognosis module for maintenance optimization [12].

Predictive maintenance exploits information about deterioration models to assess current conditions and forecast future failures before they occur. This strategy is used to determine the optimal inspection and intervention scheduling and prevent system failures.

Predictive maintenance involves utilizing inspection, test, and SHM data coupled with deterioration models to forecast bridge failures before they occur. By monitoring key parameters and analyzing trends, predictive maintenance enables timely interventions and minimizes downtime. Predictive maintenance strategies are implemented by several BMSs, such as APTBMS, KUBA, and BatMan, as reported in [12].

5.8.2 The Top-down and the Bottom-up approaches

The literature traditionally distinguishes two main approaches to deal with bridge management optimization, namely the Top-down and the Bottom-up approaches [11], see Figure 5.11.

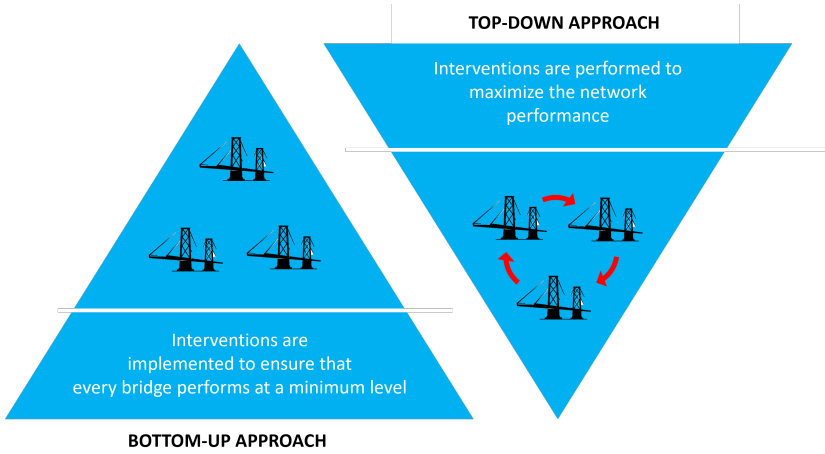

Figure 5.11: The Bottom-up and the Top-down approaches for bridge management.

The top-down approach operates at the network level considering the mutual relations and common features among bridges. This approach includes the optimization of the network maintenance planning, minimizing the total costs of maintenance and delay of interventions, and maximizing the road network performance [163]. The network topology and network roles are analyzed to find relations and determine the most critical bridges that, if closed, would result in the highest indirect costs (social and environmental). The identification of bridge clusters with similar properties allows for more efficient planning of inspections and interventions [1]. However, applying the top-down approach to large networks becomes computationally challenging due to the need to assess network relations and clusters in the road network.

The bottom-up approach focuses on identifying the optimal maintenance strategy for an individual bridge. This approach establishes minimum performance standards for the bridge and determines the most suitable inspections and intervention schedule. However, unlike the top-down approach, the bottom-up approach does not consider the role of the bridge within the network. As a result, the bottom-up approach potentially results in adverse traffic conditions and a lack of coordination in implementing maintenance activities among neighboring bridges [11].

The US Pontis [16] and Ontario BMS [164], the South African STRUMAN [155], and the Slovenian BMS [28], implement a top-down approach in the planning of interventions. STRUMAN provides a ranking of the bridge at the network level based on the indirect consequences of the loss of functionality taking into consideration the relevant average daily traffic [155]. The US Bridgit and the US NCDOT [1] implement a bottom-up approach prioritizing maintenance activities based upon a minimum bridge condition standard and within the budget. Information about budget optimization approaches used in current BMSs is shown in Table 5.6.

Table 5.6: Budget optimization approaches in BMSs.

BMS name	Country	Budget optimization approach
Autonomous Province of Trento BMS (APTBMS)	Italy	Top-down[151]
Bridgit	United States of America	Bottom-up[11]
DANBRO	Denmark	Top-down[165]
KUBA	Switzerland	Bottom-up[166]
North Caroline Department of Transportation (NCDOT BMS)	United States of America	Bottom-up[11]
Ontario BMS	United States of America	Top-down[164]
Pontis	United States of America	Top-down[16]
Slovenia BMS	Slovenia	Top-down[28]
STRUMAN	South African	Top-down[155]

5.8.3 Optimization methods

Optimization methods adopted in existing BMSs include single-objective optimization procedures to allocate resources and prioritize maintenance interventions [167]. Specifically, BMSs implement two main optimization methods: priority index ranking and cost-benefit analyses [12].

The calculation of a priority index is a rather simple approach the majority of BMSs adopt to evaluate and rank interventions both at an element and at a network level. At the element level, priority indexes can be used to compare different interventions and select the optimal one. At a network level, priority indexes can be used to prioritize interventions among different bridges [15]. As anticipated in the diagnosis section, both technical and non-technical PIs can be used for decision-making. For instance, reliability and risk PIs can be used in prioritizing repair and maintenance interventions. Cerema in France and more recently the Ministry of Transportation of Italy developed multilevel assessment procedures with increasing complexity for network scale risk management for bridge portfolios. Both procedures are characterized

by a multi-level approach that begins with a qualitative risk assessment of the entire bridge portfolio and concludes with a detailed analysis of fewer critical bridges. Specifically, the Italian guidelines address multiple types of hazards, including earthquakes, landslides, structural issues, and hydraulic actions. In contrast, the French guidelines are divided into different volumes, each focusing on a single hazard. Maintenance interventions are ordered by a priority ranking and implemented consequently according to budget constraints.

BMSs typically integrate a cost model. The descriptions of the most common interventions on the numerous bridge components are standardized into BMSs (in terms of cost, time, and effect) and utilized in the maintenance optimization [12]. The APTBMS [151] utilizes a priority index both to compare different alternatives (repair or substitute) and to prioritize interventions within the network. This is detailed in the next section.

Life-cycle cost analysis is typically employed in BMSs to assess different intervention strategies. The optimal strategy is determined based on the life-cycle cost minimization considering either the bridge or the network. Life-cycle cost analysis at the bridge or the network level is implemented in numerous BMSs such as the Austrian BAUT, the Swiss KUBA BMS, the US Pontis, Ontario, and Bridgit BMS. These BMSs use a standardized forecast model that considers the costs of the bridge through its entire life span (from construction to demolition) accounting for interventions, development of future budgets for inspections and interventions and cost transparency through the life-cycle of the structure. An example of life cost analysis can be found in the Austrian national guidelines for bridge management [168].

Furthermore, KUBA BMS, Pontis, and Slovenia BMS implement an incremental cost-benefit analysis aiming to determine the margin by which one option is more convenient than another [16, 166]. An incremental cost analysis considers increasing budgets from zero to the maximum constraint. For each budget, a different set of interventions and activities can be afforded, and the resulting benefits quantified. The lowest cost-benefit ratio indicates the most economically advantageous maintenance strategy. The restriction imposed by the limited budget influences the final choice of maintenance activities to be executed in a predefined time frame [16, 169]. The Slovenia BMS does not consider the entire service life of the structure in the incremental benefit analysis, but only the period for which the maintenance strategy is adopted and implemented [28].

One of the main issues in single-objective optimization procedures is that they disregard economic, societal, functional, and environmental

aspects. These aspects could be taken into account using multi-criteria optimization methods [161]. Despite the extensive research on this matter, as far as the authors' knowledge, there is not yet literature relevance that BMSs incorporate multi-criteria optimization processes [170]. A discussion on multi-criteria optimization and other future directions is reported in the dedicated section of this paper.

5.9 Illustrative case study: The APTBMS

In 2004, the Autonomous Province of Trento in Italy implemented a BMS called APTBMS, based on reliability concepts. This system aimed to evaluate the condition and safety of its extensive inventory of approximately 950 bridges. The development of APTBMS was a collaborative effort involving the Autonomous Province of Trento, the University of Trento, and specialists in database and web design. The system is fully web-based and interactive, and its development was carried out incrementally, with calibration and adjustments made as needed. It is continuously maintained and transparent to users [151].

The APTBMS is composed of various components tailored to specific functions, including data management, safety assessment, priority indexing, cost evaluation, and decision-making. Each component consists of a package of procedures and operational tools, which can be computer-based or paper-based. The BMS encompasses modules at the system level, focusing on individual bridges, and modules at the network level, which pertain to the entire bridge inventory. The system-level modules contain inventory data for each bridge, information on the condition of individual bridge components as well as the entire bridge, and safety and structural reliability evaluations for each bridge. On the other hand, the network-level module includes information relevant to the entire inventory, such as the intervention price list and cost model.

The subsequent sections analyze these components and organize them within the four modules of BMS presented in this paper.

5.9.1 Data management

Within the framework of the APTBMS, data acquisition relies on visual inspections. The inventory data encompasses details about bridge identification, location, construction, and retrofitting. The primary objective of the inspection system is to gather information regarding the inventory and condition of each bridge, which is achieved through five types of inspections: inventory, superficial, regular routine, in-depth routine, and special inspections. To facilitate data management, each bridge is divided into Structural Units, such as decks, piles, and abutments.

These units represent conceptual entities defined by shared attributes like length, material, typology, and spatial location. The database is populated with information obtained from documentation and direct analysis of each bridge. Inspectors and evaluators carry out manual data entry, encompassing inspections and safety evaluations. During inventory inspections, the inspector verifies the conformity of the design documents with the actual constructed state. Superficial inspections are carried out annually. They consist of a brief visual examination aimed at detecting defects of a certain severity. Regular routine inspections are conducted every three years. Their objective is the periodic control of structures and the collection of data related to the degradation of individual components. In-depth routine inspections are carried out every six years. In-depth main inspection differs from the regular routine inspection only in terms of the inspection approach, as it requires close-range examination and the use of appropriate equipment such as mobile platforms or scaffolding. Special inspections, on the other hand, are triggered by specific events, such as the inability to evaluate an element during routine inspections or the detection of structural anomalies that pose safety risks.

5.9.2 Diagnosis

After storing the inspection information in the database, the bridge inventory is assessed at the component, system, and network levels. At the component level, inspectors assign Condition States (CSs) based on the results of visual inspections contained in evaluation sheets. The CS of a component is ranked using an indicator ranging from 1 (indicating good condition) to a variable maximum between 3 and 5 (indicating poor condition), depending on the type of component being assessed. The component level CSs are divided in 5 different groups depending on the type of structure they belong to: deck components (e.g. slab and joints), main superstructure components (i.e., beams, arches and vaults), main substructure components (i.e., piers, abutments), secondary components (i.e., secondary beams, bracings), and accessory components (e.g., parapets and guardrails) [151].

At the structure level, different indicators are defined in APTBMS. The most important indicator, resulting directly from the component level CSs assigned by means of visual inspections, is the bridge condition state CS_{bridge} which provides an overall assessment of the bridge, offering an immediate and comprehensive judgment on both its components and the bridge as a whole. It consists of a numerical value ranging from 1 (very good conditions) to 5 (very bad conditions). The procedure for the calculation of the CS_{bridge} consists of four steps, starting from

the CSs collected at the component level [151].

First, a condition state CS_N is calculated for each component of the bridge. CS_N is normalized with respect to the maximum CS value for that component (CS_{max} ranges from 3 to 5 depending on the component) and to the maximum value of the bridge condition state CS_{bridge}, which is set equal to 5. See Equation 5.1.

$$CS_N = \left[\frac{(CS-1)}{(CS_{\text{max}}-1)} \cdot (CS_{bridge}-1) \right] + 1 \tag{5.1}$$

Second, each bridge component is categorized into five groups (deck components, main superstructure components, main substructure components, secondary components and accessory components) and a maximum normalized condition state $CS_{NMax}^{type,i}$ is calculated for each group type i as shown in Equation 5.2.

$$CS_{NMax}^{type,i} = max\{CS_{Ni}^{type,i}; ...; CS_{Nn}^{type,i}\} \qquad i = 1, ..., 5 \tag{5.2}$$

Third, two weights are assigned to each group i: Table 5.7 reports the weight values $\%^i$ that describe the importance of the group type i in the evaluation of the overall substructure and superstructure condition states.

Table 5.7: Weight values for the estimation of the bridge condition index in APTBMS.

Type group i	**Weight value for the Substructure** CS	**Weight value for the Superstructure** CS
1 - deck	25%	25%
2 - main superstructure elements	0%	70%
3 - main substructure elements	70%	0%
4 - secondary elements	5%	5%
5 - accessory elements	0%	0%

Thus, the coefficients $CS_{superstructure}$ and $CS_{substructure}$ are calculated as in 5.3, 5.4:

$$CS_{superstructure} = \sum_{1}^{5} CS_{NMax}^{i} \cdot \%_{superstructure}^{i} \tag{5.3}$$

$$CS_{substructure} = \sum_{1}^{5} CS_{NMax}^{i} \cdot \%_{substructure}^{i} \tag{5.4}$$

Finally, the condition state of the bridge CS_{bridge} is calculated as the maximum value between the conditions state coefficients of the superstructure and the substructure.

$$CS_{bridge} = max\{CS_{superstructure}; CS_{substructure}\} \quad (5.5)$$

Other indicators defined in the APTBMS, such as the reliability index, the probability of failure, and the critical loads multiplier, are evaluated only in specific cases, e.g., when the condition state of a structure raises concern about structural safety [151].

At the network level, the priority index is calculated to rank the interventions on the bridge inventory. Its calculation requires the definition of deterioration models, maintenance models, and cost models. It serves as a decision support tool for the manager who employs the APTBMS. The subsequent sections focus on these aspects in more detail.

5.9.3 Prognosis

The evolution of the CS of bridge components is predicted through a Markov Chain algorithm. By incorporating factors such as loading time, environmental effects, and the quality of construction and maintenance, the algorithm provides a systematic approach to forecasting the condition of bridge components. The algorithm utilizes a transition matrix, which captures the probabilities of transitioning from one condition state to another. This matrix considers the various factors affecting the deterioration of bridge components and their impact on the condition state. By analyzing the transition matrix, it becomes possible to estimate the probability of a component belonging to a specific condition state at a given time.

Figure 5.12 represents the estimation of the probability distribution of the condition states over time. It provides a graphical representation of how the condition of bridge components is expected to change as time progresses.

Additionally, the impact of interventions on the CS is measured using a secondary transition matrix, which enables the estimation of the probability of a component improving its condition state when a maintenance action is implemented. The model encompasses various types of interventions, including preventive maintenance, retrofitting, and reconstruction actions.

5.9.4 Decision support tool

The APTBMS incorporates a decision support tool to prioritize interventions across the bridge network. In the prognosis phase, the tool estimates the probability of a specific bridge component being in a particular CS. To further evaluate the structural integrity, a capacity function is defined, allowing for the calculation of the cumulative probability of failure $P_X(t_L)$ at time t_L, based on the CS of its components.

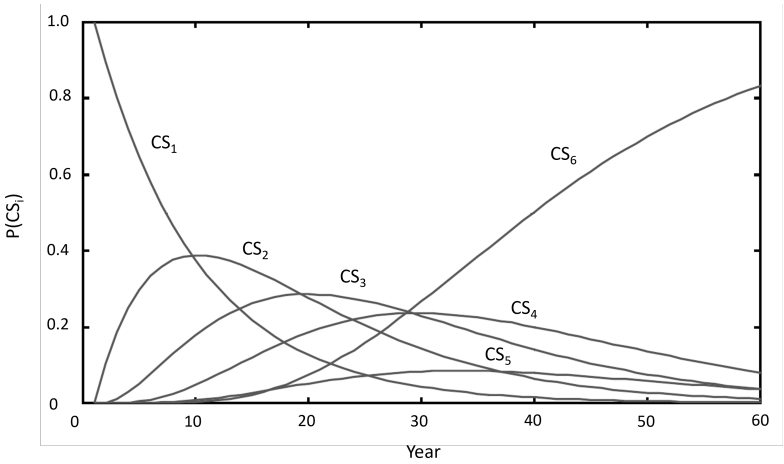

Figure 5.12: Probability of being in a condition state vs time. Adapted from [151].

The Decision support tool relies on the calculation of a priority index to determine the importance of interventions, which is defined as follows:

$$\alpha = \frac{P_X(t_L) - P_{X|a}(t_L)}{\Delta C} \tag{5.6}$$

where, $P_X(t_L)$ represents the probability of an unacceptable event X occurring during the period (0, t_L) if no action a (such as preventive maintenance, renovation, or reconstruction) is taken; $P_{X|a}(t_L)$ represents the probability of the same event X occurring if the action a is performed; ΔC denotes the cost difference between implementing action a and doing nothing. An example of the application of the APTBMS prioritization is reported in [171].

The assessment of unacceptability for a particular event depends on the stakeholders involved and could pertain to the collapse of the structure or the loss of functionality and traffic safety.

For each bridge and each potential action, a priority index is calculated. The highest index indicates the most favorable action to implement on the respective bridge. To prioritize interventions across the network, the priority indexes of each bridge in the portfolio are ordered, and a top-down approach is employed.

5.10 Future direction

Over the last decades, bridge management has experienced significant changes toward digitalization. The digital twin paradigm is becoming

increasingly popular among researchers and bridge managers. A digital twin is the digital reconstruction of a real-life asset (the physical twin). It can include a numerical model of the bridge (e.g., finite element model), a building information model, and a deterioration model and can be updated whenever new information is acquired. A digital twin aims to provide feedback in "what-if" simulations to predict asset performance and evaluate risks [172, 173]. In this way, critical phases and potential risks connected to the operation of these assets can be assessed and avoided or tackled before the criticality occurs. Design and construction parameters, environmental conditions, and loading history can be attributed to the digital twin and contribute to the prediction of the future condition state of the structure. A key feature of digital twins is the continuous updating of the virtual model which progressively and automatically evolves with the physical asset.

Digital twins provide components assessment and deterioration prediction for specific disruptive scenarios. The simulation of a deterioration phenomenon and the subsequent insurgence of damages on the structure can provide a guide in inspection SHM data analysis, prognosis, and scheduling aiding emergency protocols. Nevertheless, their practical application for civil engineering systems is in its infancy and is limited mainly due to the computation and resource burden [174].

In order to counteract these limits, surrogate models are increasingly utilized. Surrogate models aim to simplify the description of complex structures and deterioration phenomena thereby enabling fast analyses and simulations. Surrogate models can be based on several approaches, such as response surface models [175], Kriging models [159], high polynomial functions [175], and Artificial Neural Networks [176, 177, 178]. Surrogate models can be continuously updated by collected SHM data allowing for real-time condition assessment [175].

In the data collection context, bridge management will be increasingly based on integrated results of both SHM and visual inspections. Bridge inspection is already progressively relying on cutting-edge technologies [60]. Smartphones and tablets are being complemented with Augmented Reality (AR) to control drones equipped with advanced sensors, which can access hard-to-reach areas, capturing detailed visual and thermal images for centralized analysis [113]. These techniques can enhance visual inspections by overlaying digital information onto physical structures, and by allowing for the detection and localization of early-stage defects [179]. Artificial Intelligence (AI) is increasingly expected to play a crucial role in detecting, recognizing, and quantifying surface damage on bridge components. Specifically, Convolutional Neural Networks (CNNs) are typically utilized [180]. Qualitative damage classes

can be defined [181] and crack width and length can be measured [182]. A digital shadow of the bridge is created by the collected digital clouds and detailed surface damage information can be integrated [183]. Lately, Recurrent Neural Networks (RNN), such as Long Short-Term Memory (LSTM), and Gated Recurrent Unit (GRU), and Generative Adversarial Networks (GAN) are finding great interest in the research community [184]. Further, Unmanned Air Vehicle (UAV), photogrammetry and LiDAR (Light Detection and Ranging) can be used for Virtual Reality (VR) applications. The integration of advanced technologies (such as VR, AR, AI, and IoT) to create an immersive and interactive virtual environment for bridge management is referred to as "Metaverse" [185]. For example, in some applications, interactive digital representations of physical bridges are created and associated with SHM data. The combination of visual data with SHM data can potentially enhance the understanding of the dynamic behavior of the bridge and allow experts from different locations to virtually inspect the bridge for final assessment [186].

Network-scale SHM approaches are gaining popularity to address scalability issues characterizing classic contact-based SHM approaches including indirect SHM, satellite-based InSAR monitoring, and Transfer learning.

Indirect or "drive-by" SHM (ISHM) gathers data from sensors in moving vehicles, significantly cutting instrumentation costs for bridge managers. Issues in ISHM relate to modeling vehicle-bridge interaction, road roughness, and complex time-varying loading patterns [187]. Crowdsourced strategies have been developed involving drivers using their smartphones to collect data while crossing bridges [59].

Satellite-based Monitoring uses Interferometric Synthetic Aperture Radar (InSAR) data for bridge monitoring, eliminating the need for on-site sensors. InSAR focuses on static monitoring, providing velocity maps and millimeter-level time series of displacements. It allows for continuous, non-intrusive monitoring, even in difficult environments, and offers historical data for trend analysis and proactive maintenance [188]. Additionally, remote monitoring has proven to be effective in studying large-scale or local geotechnical and hydraulic phenomena, such as scour, subsidence, and landslides [189, 190, 191].

Transfer-Learning Strategies, also known as "population-based" SHM, enhance knowledge about structures with limited or unavailable data by leveraging information from similar structures. This method involves assessing similarities between bridges and transferring knowledge about structural anomalies observed in some bridges to others within the monitored population [192].

These advancements streamline the documentation process, by en-

abling real-time cloud communication and high-quality data capture, which enhances immediacy and accuracy during inspections [193]. To this end, efficient data storage solutions are crucial, given the large file sizes and diverse formats involved. Enhanced cloud-based systems are now at the forefront of innovation, offering scalability, remote access, and robust data management, including version control, metadata tagging, blockchains, and secure protocols to maintain data integrity [61, 62, 63].

To foster the development of SHM systems, an important research effort has been mounted over the past decade toward the quantification of the return on investment in an SHM system, for instance through the VoI from Bayesian decision theory. The VoI can be compared with the cost of the SHM system to establish if the SHM should be adopted: if the VoI is higher than the corresponding cost, the SHM should be installed [194, 195, 187, 196].

In the prognosis context, to overcome the shortcomings of Markov Chain and regression deterioration models, reliability-based mechanistic deterioration models were proposed to be applied in the next generation of BMSs. Corrosion and fatigue represent the two main degradation phenomena affecting the durability of steel and concrete bridges. The fatigue life of steel, reinforced concrete, and prestressed concrete components is significantly affected by corrosion as it reduces the available cross-section and fosters the creation of pits acting as stress concentrators and crack initiators. Thus, deterioration models consider both phenomena [197, 198], also considering changing traffic loads [199, 200]. Further, the use of DTs and surrogate models to predict components' fatigue life facilitates inspecting/monitoring planning and maintenance optimization [201].

Although substantial research has been dedicated to in-plane stress-induced fatigue in welded details, distortion-induced fatigue–caused by out-of-plane deformation–has not been adequately addressed in current codes and regulations, despite its significant impact on structural integrity [202]. Addressing this gap is crucial for enhancing fatigue design and life evaluation for steel girder bridges. Distortion-induced fatigue typically manifests in the web gaps of steel girders, where differential deflections between adjacent girders or components result in out-of-plane bending stresses [203]. Stress concentrations can lead to the initiation and propagation of fatigue cracks, particularly in the web gap areas of skewed or curved bridges [202]. To address the gaps in understanding and predicting distortion-induced fatigue, numerical simulation techniques have emerged as powerful tools [202, 204, 205, 206, 207]. The digital simulations offer high efficiency and broad applicability, making it a promising direction for the future development of fatigue research in

steel bridges.

As for the decision-making module, the set of intervention options should integrate the latest developments in reinforcement and maintenance technologies. Forefront advancements for the reinforcement and maintenance technologies include Fiber Reinforced Composites (FRC), such as Ultra-high Performance Fiber Reinforced Concrete (UHPFRC), Fiber Reinforced Cementitious Mortar (FRCM), Externally Bonded (EB) techniques, Near Surface Mounted (NSM) techniques, and anchorage systems [208, 209].

Fatigue cracking represents a critical challenge for the safety and longevity of steel bridges. To address these issues, effective reinforcement methods are essential to ensure structural integrity and extend the service life of these structures. These methods can be broadly categorized into hot reinforcement and cold reinforcement techniques [207]. Hot reinforcement methods involve techniques that typically introduce significant tensile residual stresses or create new fatigue-prone details. For example, welding is a common hot reinforcement approach where new steel plates are welded directly to cracked areas or existing welded connections are reworked [210]. In contrast, cold reinforcement methods aim to avoid introducing additional tensile residual stresses or creating new fatigue-prone details. Techniques such as drilling stop-holes at crack tips [211, 212], bolting steel angles to cracked regions [213], and bonding steel plates using adhesives fall into this category [214, 215]. Research has demonstrated that cold reinforcement methods can significantly enhance fatigue performance.

Although only a few examples of optimization methods in BMSs are documented in the literature, bridge management optimization constitutes an active research field. BMS decision support systems take into consideration different parameters when determining optimal management strategies. Current research focuses on the identification of the most significative parameters and on the definition of a Multi-Objective Optimization Problem (MOOP), which could be integrated into the next BMS generation. The MOOP can be solved by considering the weighted sum of single objective optimization problems [216] or adopting some advanced resolution methods, such as Multi-Criteria Decision-Making (MCDM), grid searching, and genetic algorithms [217, 218]. MCDM includes a wide number of analytical frameworks to perform such optimizations accounting for multiple and often contrasting objectives, such as maximum reliability, minimum cost, minimum environmental impact, minimum impact on users, and maximum network functionality, by proposing a trade-off among them. Further, several European Projects, such as IM-SAFE and BRIDGITISE, aim to investigate a common decision-

making flow for optimized and digitalized bridge management [219, 220].

The topic of transportation network resilience has been recently discussed by several authors aiming to describe the ability of transportation systems to respond, react, and recover from adverse events such as earthquakes, floods, climate change, and cyber-attacks [173, 221]. Further, national guidelines, such as the Italian Guidelines for bridges [44], report the necessity to identify bridges of significant importance within a road network and perform resilience analyses to evaluate the consequences of a possible interruption of the bridge operation on the socio-economic context.

5.11 Conclusions

The need for efficient management of existing bridges has become increasingly pressing in recent years. BMSs have emerged as a powerful tool for managing infrastructure assets, with significant advancements in associated technologies in recent years. This paper provides a comprehensive overview of the current state of the art of BMSs, including a historical perspective on the development of BMS software and the definition of the four main modules of a complete BMS: data collection, diagnosis, prognosis, and decision making.

While BMSs have shown great potential in managing infrastructure assets, there are still several limitations that need to be addressed. The current practices in bridge diagnosis and prognosis are closely related to the methods adopted for data collection. Visual inspections remain the most common method for data collection; however, they come with notable drawbacks, including the subjectivity of results and challenges in accessing hidden structural components. New technologies, such as SHM and drone inspections, have emerged as promising additions to overcome these limitations.

In terms of bridge diagnosis, condition ratings based on data collected through visual inspections is the main tool for assessing structural conditions. Although damage indicators extracted from SHM data have been extensively investigated by the research community, their systematic integration into BMS frameworks requires further research and standardization efforts.

In the prognosis phase, most of the analyzed BMSs utilize Markov chains and deterministic methods to forecast the future state of a structure. While these traditional methods have been widely implemented, they have several limitations, including their reliance on simplifying assumptions and potential inaccuracies in predicting complex deterioration

processes. As a result, there is increasing interest in novel approaches that combine artificial intelligence techniques with physical modeling. These hybrid methods, which are actively being explored in the literature, promise to address the shortcomings of traditional methods by offering better predictions of structural conditions.

Finally, even though several decision-making tools have been reported in the literature, most BMSs hardly implement them yet. Current approaches rely on prioritization of interventions based on priority indices that take into account both the structural conditions and the costs associated with different remedial actions. There is a need for further research to improve decision-making processes, and BMSs will likely become more sophisticated in this aspect in the future.

In summary, the four modules of BMSs have undergone significant changes toward digitalization and automation, and innovative technologies, such as digital twins, are expected to enhance innovation in bridge management and lead to more sustainable, safer, and cheaper transportation infrastructure. The overview provided in this paper has demonstrated the significant progress in BMSs in recent years, but there is still a long way to go to achieve optimal, all-around management of infrastructure assets.

Bibliography

[1] C. Wu, P. Wu, J. Wang, R. Jiang, M. Chen, and X. Wang, "Critical review of data-driven decision-making in bridge operation and maintenance," *Structure and infrastructure engineering*, vol. 18, no. 1, pp. 47–70, 2021.

[2] D. M. Frangopol, J. S. Kong, and E. S. Gharaibeh, "Reliability-based life-cycle management of highway bridges," *Journal of computing in civil engineering*, vol. 15, no. 1, pp. 27–34, 2001.

[3] I. Björnsson, O. L. Ivanov, D. Honfi, and J. Leander, "Decision support framework for bridge condition assessments," *Structural Safety*, vol. 81, p. 101874, 2019.

[4] D. M. Frangopol and S. Kim, *Bridge safety, maintenance and management in a life-cycle context*. CRC Press, 2022.

[5] Federal Highway Administration (FHWA), "Bridge management." https://www.fhwa.dot.gov/bridge/management/. Accessed: 2025-10-28.

[6] P. Vassie and C. Arya, "Bridge management," in *ICE Manual of Bridge Engineering: Second Edition*, pp. 591–613, ICE Publishing, 2008.

[7] D. Isailović and R. Hajdin, "Geometry as a common ground for bms and bim," in *IABSE Symposium, Prague 2022: Challenges for Existing and Oncoming Structures*, 2022.

[8] A. Jiménez Rios, V. Plevris, and M. Nogal, "Bridge management through digital twin-based anomaly detection systems: A systematic review," *Frontiers in Built Environment*, vol. 9, p. 1176621, 2023.

[9] A. C. P. Martins, J. M. Franco de Carvalho, M. C. S. Alvarenga, D. S. d. Oliveira, K. M. L. Cesar Junior, J. C. L. Ribeiro, G. S. Santos, and R. C. Verly, "Detecting, monitoring and modeling damage within the decision-making process in the context of managing bridges: a review," *Structure and Infrastructure Engineering*, pp. 1–23, 2024.

[10] R. Woodward, D. Cullington, A. Daly, P. Vassie, P. Haardt, R. Kashner, R. Astudillo, C. Velando, B. Godart, C. Cremona, *et al.*, "Bridge management in europe (brime)-deliverable d14-final report," 2001.

[11] R. McGee *et al.*, "Bridge management systems – the state of the art," 2002.

[12] B. T. Adey, L. Klatter, and J. S. Kong, "Overview of existing bridge management systems," tech. rep., ETH Zurich, 2010.

[13] P. J. Cruz, D. M. Frangopol, and L. C. Neves, *Bridge maintenance, safety, management, life-cycle performance and cost*. Taylor & Francis Group, 2006.

[14] R. Folic and D. Partov, "Some aspect of bridge management systems–inspection, evaluation and maintenance," *Eng Sci*, vol. 57, no. 4, 2020.

[15] D. Zonta, R. Zandonini, and F. Bortot, "A reliability-based bridge management concept," *Structures & Infrastructure Engineering*, vol. 3, no. 3, pp. 215–235, 2007.

[16] P. D. Thompson, E. P. Small, M. Johnson, and A. R. Marshall, "The pontis bridge management system," *Structural engineering international*, vol. 8, no. 4, pp. 303–308, 1998.

[17] H. Hawk and E. P. Small, "The bridgit bridge management system," *Structural engineering international*, vol. 8, no. 4, pp. 309–314, 1998.

[18] V. Saback de Freitas Bello, C. Popescu, T. Blanksvärd, and B. Täljsten, "Bridge management systems: Overview and framework for smart management," in *IABSE Congress 2021: Structural Engineering for Future Societal Needs, Ghent, Belgium, September 22-24, 2021*, pp. 1014–1022, International Association for Bridge and Structural Engineering (IABSE), 2021.

[19] H. S. Manual, "American association of state highway and transportation officials," *Washington, DC*, vol. 19192, 2010.

[20] IOWADOT, "Bridge maintenance manual," 2014.

[21] Massachusetts Department of Transportation, "Bridge inspection handbook – field inspection, data collecting, report writing and report review," 2014.

[22] T. Leckrone, P. D. Thompson, K. Malarich, C. Domingo, *et al.*, "Integration of aashto element inspections data into nysdot structures management system and processes," tech. rep., New York State Department of Transportation, 2021.

[23] Federal Highway Administration, "Framework for improving resilience of bridge design," 2011.

[24] R. D. Guide *et al.*, "American association of state highway and transportation officials," *Washington, DC*, 1996.

[25] A. Miyamoto and H. Asano, "Development and practical application of a lifetime management system for prestressed concrete bridges," *Civil Engineering Infrastructures Journal*, vol. 50, no. 2, pp. 395–410, 2017.

[26] R. Helmerich, E. Niederleithinger, D. Algernon, D. Streicher, and H. Wiggenhauser, "Bridge inspection and condition assessment in europe," *Transportation research record*, vol. 2044, no. 1, pp. 31–38, 2008.

[27] H.-K. Liao and N.-J. Yau, "Development of various bridge condition indices for taiwan bridge management system," *Proceedings of the 28th ISARC, Seoul, Korea*, pp. 911–916, 2011.

[28] M. Kušar and A. Srdić, "Bridge management system based on cost action tu1406 findings," in *International Conference of the European Association on Quality Control of Bridges and Structures*, pp. 481–490, Springer, 2021.

[29] G. Hearn, J. Puckett, I. Friedland, T. Everett, K. Hurst, G. Romack, G. Christian, R. Shepard, T. Thompson, and R. Young, "Bridge preservation and maintenance in europe and south africa," tech. rep., 2005.

[30] J. Lauridsen, J. Bjerrum, N. H. Andersen, and B. Lassen, "Creating a bridge management system," *Structural engineering international*, vol. 8, no. 3, pp. 216–220, 1998.

[31] C. Pellegrino, A. Pipinato, and C. Modena, "A simplified management procedure for bridge network maintenance," *Structure and Infrastructure Engineering*, vol. 7, no. 5, pp. 341–351, 2011.

[32] M. Pregnolato, "Bridge safety is not for granted–a novel approach to bridge management," *Engineering Structures*, vol. 196, p. 109193, 2019.

[33] D. Agdas, J. A. Rice, J. R. Martinez, and I. R. Lasa, "Comparison of visual inspection and structural-health monitoring as bridge condition assessment methods," *Journal of Performance of Constructed Facilities*, vol. 30, no. 3, p. 04015049, 2016.

[34] F. Furtado and D. Ribeiro, "Railway bridge management system based on visual inspections with semi-markov continuous time process," *KSCE Journal of Civil Engineering*, vol. 27, no. 1, pp. 233–250, 2023.

[35] Z. I. Turksezer, C. Iacovino, P. F. Giordano, and M. P. Limongelli, "Development and implementation of indicators to assess bridge inspection practices," *Journal of Construction Engineering and Management*, vol. 147, no. 12, p. 04021165, 2021.

[36] N. FHWA, "Bridge inspector's reference manual," 2012.

[37] G. Hearn, *Bridge inspection practices*, vol. 375. Transportation Research Board, 2007.

[38] J. Smith, C. Watters, and J. Stephenson, "Optimizing municipal structures inspections," in *2024 TAC Conference and Exhibition-Technology & TransformationTransportation Association of Canada*, 2024.

[39] Technical Standards Branch, Alberta Transportation, *Bridge Inspection and Maintenance System (BIM) Level 1 Inspection Manual*, 2020. Online.

[40] H. England, "Assessment of highway bridges and structures," *Design Manual for Roads and Bridges*, 2020.

[41] Norwegian Public Roads Administration (NPRA), *Handbook for Bridge Inspections, Part I*, 2005. Online.

[42] G. Tang, J. Li, and X. Tao, "Ministry of transport of the people's republic of china," 2008.

[43] Main Roads, *Detailed Visual Bridge Inspection Guidelines for Concrete and Steel Bridges*, 2008. Online.

[44] M. d. I. e dei Trasporti, "Consiglio superiore dei lavori pubblici," *Linee guida per la classificazione e gestione del rischio, la valutazione della sicurezza ed il monitoraggio dei ponti esistenti*, vol. 14, no. 3, 2020.

[45] MITMA, *Guía para la realización de inspecciones principales de obras de paso en la Red de Carreteras del Estado*, 2012. Online.

[46] Transport Infrastructure Ireland, *EIRSPAN Bridge Management System Principal Inspection Manual*, 2022.

[47] J. Ghosh and J. E. Padgett, "Aging considerations in the development of time-dependent seismic fragility curves," *Journal of Structural Engineering*, vol. 136, no. 12, pp. 1497–1511, 2010.

[48] N. Hallermann and G. Morgenthal, "Visual inspection strategies for large bridges using unmanned aerial vehicles (uav)," in *Proc. of 7th IABMAS, International Conference on Bridge Maintenance, Safety and Management*, pp. 661–667, 2014.

[49] S. S. Khedmatgozar Dolati, N. Caluk, A. Mehrabi, and S. S. Khedmatgozar Dolati, "Non-destructive testing applications for steel bridges," *Applied Sciences*, vol. 11, no. 20, p. 9757, 2021.

[50] D. Tonelli, F. Rossi, M. Luchetta, V. Caspani, D. Zonta, P. Migliorino, A. Selleri, E. Valeri, A. Marchiondelli, and G. Ascari, "Effectiveness of acoustic emission monitoring for in-service prestressed concrete bridges," in *Sensors and Smart Structures Technologies for Civil, Mechanical, and Aerospace Systems 2021*, vol. 11591, pp. 178–192, SPIE, 2021.

[51] V. F. Caspani, D. Tonelli, F. Poli, and D. Zonta, "Designing a structural health monitoring system accounting for temperature compensation," *Infrastructures*, vol. 7, no. 1, p. 5, 2021.

[52] N. Faris, T. Zayed, E. M. Abdelkader, and A. Fares, "Corrosion assessment using ground penetrating radar in reinforced concrete structures: Influential factors and analysis methods," *Automation in Construction*, vol. 156, p. 105130, 2023.

[53] D. Tonelli, F. Rossi, F. Brighenti, A. Verzobio, A. Bonelli, and D. Zonta, "Prestressed concrete bridge tested to failure: the alveo vecchio viaduct case study," *Journal of Civil Structural Health Monitoring*, vol. 13, no. 4, pp. 873–899, 2023.

[54] N. Bagge, M. Plos, and C. Popescu, "A multi-level strategy for successively improved structural analysis of existing concrete bridges: Examination using a prestressed concrete bridge tested to failure," *Structure and Infrastructure Engineering*, vol. 15, no. 1, pp. 27–53, 2019.

[55] C. S. Cai and M. Shahawy, "Predicted and measured performance of prestressed concrete bridges," *Journal of Bridge Engineering*, vol. 9, no. 1, pp. 4–13, 2004.

[56] J. H. Bungey and M. G. Grantham, *Testing of concrete in structures*. Crc Press, 2006.

[57] J. J. Lin, A. Ibrahim, S. Sarwade, and M. Golparvar-Fard, "Bridge inspection with aerial robots: Automating the entire pipeline of visual data capture, 3d mapping, defect detection, analysis, and reporting," *Journal of Computing in Civil Engineering*, vol. 35, no. 2, p. 04020064, 2021.

[58] A. Di Matteo, D. Fiandaca, and A. Pirrotta, "Smartphone-based bridge monitoring through vehicle–bridge interaction: analysis and experimental assessment," *Journal of Civil Structural Health Monitoring*, vol. 12, no. 6, pp. 1329–1342, 2022.

[59] S. Quqa, P. F. Giordano, and M. P. Limongelli, "Shared micromobility-driven modal identification of urban bridges," *Automation in Construction*, vol. 134, p. 104048, 2022.

[60] Y. Xu and Y. Turkan, "Brim and uas for bridge inspections and management," *Engineering, Construction and Architectural Management*, vol. 27, no. 3, pp. 785–807, 2020.

[61] L. Gigli, L. Sciullo, F. Montori, A. Marzani, and M. Di Felice, "Blockchain and web of things for structural health monitoring applications: A proof of concept," in *2022 IEEE 19th Annual Consumer Communications & Networking Conference (CCNC)*, pp. 699–702, IEEE, 2022.

[62] D. T. Nepomuceno, J. Bennetts, M. Pregnolato, T. Tryfonas, and P. J. Vardanega, "Development of a schema for the remote inspection of bridges," in *Proceedings of the Institution of Civil Engineers-Bridge Engineering*, vol. 178, pp. 36–51, Emerald Publishing Limited, 2022.

[63] M. Mandirola, C. Casarotti, S. Peloso, I. Lanese, E. Brunesi, and I. Senaldi, "Use of uas for damage inspection and assessment of bridge infrastructures," *International Journal of Disaster Risk Reduction*, vol. 72, p. 102824, 2022.

[64] A. J. Hughes, L. A. Bull, P. Gardner, N. Dervilis, and K. Worden, "On robust risk-based active-learning algorithms for enhanced decision support," *Mechanical Systems and Signal Processing*, vol. 181, p. 109502, 2022.

[65] L. Bindra, C. Lin, E. Stroulia, and O. Ardakanian, "Decentralized access control for smart buildings using metadata and smart contracts," in *2019 IEEE/ACM 5th international workshop on software engineering for smart cyber-physical systems (SEsCPS)*, pp. 32–38, IEEE, 2019.

[66] K. Achuthan, N. Hay, M. Aliyari, and Y. Z. Ayele, "A digital information model framework for uas-enabled bridge inspection," *Energies*, vol. 14, no. 19, p. 6017, 2021.

[67] "International society for structural health monitoring of intelligent infrastructure (ishmii)." https://ishmii.org/. Online; accessed 2025-11-29.

[68] "International association for experimental vibration analysis for civil engineering structures (evaces ia)." https://www.evaces-ia.com/. Online; accessed 2025-11-29.

[69] "Smar 2024 - 7th international conference on smart monitoring, assessment, and rehabilitation of civil structures (smar)." https://www.smar2024.org/. Online; accessed 2025-11-29.

[70] "Evaces 2023 - 10th international conference on experimental vibration analysis for civil engineering structures." https://www.evaces2023.polimi.it/. Online; accessed 2025-11-29.

[71] "Ewshm 2024 - 11th european workshop on structural health monitoring." https://ewshm2024.com/frontend/index.php. Online; accessed 2025-11-29.

[72] "Iwshm 2023 - 14th international workshop on structural health monitoring." https://iwshm2023.stanford.edu/. Online; accessed 2025-11-29.

[73] "Iomac 2024 - international operational modal analysis conference." https://iomac2024.com/. Online; accessed 2025-11-29.

[74] "Eurostruct 2023 - 2nd conference of the european association on quality control of bridges and structures." https://eurostruct.org/eurostruct-2023/. Online; accessed 2025-11-29.

[75] "Iabmas 2024 - international association for bridge maintenance and safety conference." https://iabmas2024.dk/. Online; accessed 2025-11-29.

[76] "Eurodyn 2023 - 12th international conference on structural dynamics." https://eurodyn2023.dryfta.com/. Online; accessed 2025-11-29.

[77] "Cost tu1402 - quantifying the value of structural health monitoring." http://www.cost-tu1402.eu/. Online; accessed 2025-11-29.

[78] W.-H. Zhang, D.-G. Lu, J. Qin, S. Thöns, and M. H. Faber, "Value of information analysis in civil and infrastructure engineering: a review," *Journal of Infrastructure Preservation and Resilience*, vol. 2, no. 1, p. 16, 2021.

[79] G. Santarsiero, A. Masi, V. Picciano, and A. Digrisolo, "The italian guidelines on risk classification and management of bridges: Applications and remarks on large scale risk assessments," *Infrastructures*, vol. 6, no. 8, p. 111, 2021.

[80] P. G. Malerba, "Bridge vulnerabilities and collapses: the italian experience," *Structure and Infrastructure Engineering*, vol. 20, no. 7-8, pp. 976–1001, 2024.

[81] ANAS, "Monitoraggi di ponti e viadotti tramite sensori." https://www.stradeanas.it/it/le-strade/

monitoraggio-di-ponti-e-viadotti-tramite-sensori. Online; accessed 2025-11-29.

[82] C. Fabre. https://www.consorziofabre.it/. Online; accessed 2025-11-29.

[83] ReLUIS, "Rete dei laboratori universitari di ingegneria sismica e strutturale (reluis)." https://www.reluis.it/. Online; accessed 2025-11-29.

[84] P. F. Giordano, S. Quqa, and M. P. Limongelli, "The value of monitoring a structural health monitoring system," *Structural safety*, vol. 100, p. 102280, 2023.

[85] B. Glisic, D. Inaudi, and N. Casanova, "Shm process as perceived through 350 projects," in *Smart Sensor Phenomena, Technology, Networks, and Systems 2010*, vol. 7648, pp. 174–187, SPIE, 2010.

[86] M. P. Limongelli, "Standardization of structural performance monitoring: existing documents and open questions," in *IABSE Symposium. Prague 2022*, pp. 1–7, 2022.

[87] C. R. Farrar and K. Worden, "An introduction to structural health monitoring," *Philosophical Transactions of the Royal Society A: Mathematical, Physical and Engineering Sciences*, vol. 365, no. 1851, pp. 303–315, 2007.

[88] M. Abdulkarem, K. Samsudin, F. Z. Rokhani, and M. F. A Rasid, "Wireless sensor network for structural health monitoring: A contemporary review of technologies, challenges, and future direction," *Structural health monitoring*, vol. 19, no. 3, pp. 693–735, 2020.

[89] Z. He, W. Li, H. Salehi, H. Zhang, H. Zhou, and P. Jiao, "Integrated structural health monitoring in bridge engineering," *Automation in construction*, vol. 136, p. 104168, 2022.

[90] F. Zanelli, N. Debattisti, M. Mauri, A. Argentino, and M. Belloli, "Development and field validation of wireless sensors for railway bridge modal identification," *Applied Sciences*, vol. 13, no. 6, p. 3620, 2023.

[91] S. Kang, Y. C. Wu, D. S. David, and S. Ham, "Rapid damage assessment of concrete bridge deck leveraging an automated double-sided bounce system," *Automation in Construction*, vol. 138, p. 104244, 2022.

[92] R. Bogue, "Recent developments in mems sensors: A review of applications, markets and technologies," *Sensor review*, vol. 33, no. 4, pp. 300–304, 2013.

[93] B. Glisic and D. Inaudi, *Fibre optic methods for structural health monitoring*. John Wiley & Sons, 2007.

[94] F. Huseynov, C. Kim, E. J. Obrien, J. Brownjohn, D. Hester, and K. Chang, "Bridge damage detection using rotation measurements–experimental validation," *Mechanical Systems and Signal Processing*, vol. 135, p. 106380, 2020.

[95] Á. Cunha, E. Caetano, F. Magalhães, and C. Moutinho, "Dynamic identification and continuous dynamic monitoring of bridges: different applications along bridges life cycle," *Structure and Infrastructure Engineering*, vol. 14, no. 4, pp. 445–467, 2018.

[96] M. Limongelli, "Frequency response function interpolation for damage detection under changing environment," *Mechanical Systems and Signal Processing*, vol. 24, no. 8, pp. 2898–2913, 2010.

[97] I. Bayane and E. Brühwiler, "Acoustic emission and ultrasonic testing for fatigue damage detection in a rc bridge deck slab," *Proceedings of the SMAR*, 2019.

[98] X. Kong, J. Li, W. Collins, C. Bennett, S. Laflamme, and H. Jo, "A large-area strain sensing technology for monitoring fatigue cracks in steel bridges," *Smart Materials and Structures*, vol. 26, no. 8, p. 085024, 2017.

[99] Y. Wang, A. Mukherjee, and A. Castel, "Ultrasonic guided waves for monitoring incipient corrosion in reinforced concrete with top-bar defect," *Cement and Concrete Composites*, vol. 141, p. 105116, 2023.

[100] R. R. Rabi, M. Vailati, and G. Monti, "Effectiveness of vibration-based techniques for damage localization and lifetime prediction in structural health monitoring of bridges: A comprehensive review," *Buildings*, vol. 14, no. 4, p. 1183, 2024.

[101] Y. Zhu, H. Sekiya, T. Okatani, M. Tai, and S. Morichika, "B-cnn: a deep learning method for accelerometer-based fatigue cracks monitoring system," *Journal of Civil Structural Health Monitoring*, vol. 13, no. 4, pp. 947–959, 2023.

[102] M. Mashayekhi, E. Santini-Bell, and S. Eftekhar Azam, "Fatigue crack detection in welded structural components of steel bridges using artificial neural network," *Journal of Civil Structural Health Monitoring*, vol. 11, no. 4, pp. 931–947, 2021.

[103] J. J. Yanez-Borjas, M. Valtierra-Rodriguez, J. M. Machorro-Lopez, D. Camarena-Martinez, and J. P. Amezquita-Sanchez, "Convolutional neural network-based methodology for detecting, locating and quantifying corrosion damage in a truss-type bridge through the autocorrelation of vibration signals," *Arabian Journal for Science and Engineering*, vol. 48, no. 2, pp. 1119–1141, 2023.

[104] Y. Ni, X. Ye, and J. Ko, "Monitoring-based fatigue reliability assessment of steel bridges: analytical model and application," *Journal of Structural Engineering*, vol. 136, no. 12, pp. 1563–1573, 2010.

[105] L. Dellenbaugh, X. Kong, H. Al-Salih, W. Collins, C. Bennett, J. Li, and E. J. Sutley, "Development of a distortion-induced fatigue crack characterization methodology using digital image correlation," *Journal of Bridge Engineering*, vol. 25, no. 9, p. 04020063, 2020.

[106] W. Collins, C. Bennett, J. Li, E. Sutley, M. Juno, H. Al-Salih, L. Dellenbaugh, *et al.*, "Automated bridge inspection using digital image correlation part ii: Application of digital image correlation techniques for in-service inspection conditions," tech. rep., University of Nebraska. Mid-America Transportation Center, 2023.

[107] K. Wardhana and F. C. Hadipriono, "Analysis of recent bridge failures in the united states," *Journal of performance of constructed facilities*, vol. 17, no. 3, pp. 144–150, 2003.

[108] L. J. Prendergast and K. Gavin, "A review of bridge scour monitoring techniques," *Journal of Rock Mechanics and Geotechnical Engineering*, vol. 6, no. 2, pp. 138–149, 2014.

[109] L. J. Prendergast, K. Gavin, and D. Hester, "Isolating the location of scour-induced stiffness loss in bridges using local modal behaviour," *Journal of Civil Structural Health Monitoring*, vol. 7, no. 4, pp. 483–503, 2017.

[110] S. Mustapha, Y. Lu, C.-T. Ng, and P. Malinowski, "Sensor networks for structures health monitoring: Placement, implementa-

tions, and challenges—a review," *Vibration*, vol. 4, no. 3, pp. 551–585, 2021.

[111] J. Ko and Y. Q. Ni, "Technology developments in structural health monitoring of large-scale bridges," *Engineering structures*, vol. 27, no. 12, pp. 1715–1725, 2005.

[112] S. Cho, C.-B. Yun, J. P. Lynch, A. T. Zimmerman, B. F. Spencer Jr, and T. Nagayama, "Smart wireless sensor technology for structural health monitoring of civil structures," *Steel structures*, vol. 8, no. 4, pp. 267–275, 2008.

[113] D. L. Mascarenas, M. D. Todd, G. Park, and C. R. Farrar, "Development of an impedance-based wireless sensor node for structural healthmonitoring," *Smart Materials and Structures*, vol. 16, no. 6, p. 2137, 2007.

[114] V. Gattulli, F. Franchi, F. Graziosi, A. Marotta, C. Rinaldi, F. Potenza, and U. D. Sabatino, "Design and evaluation of 5g-based architecture supporting data-driven digital twins updating and matching in seismic monitoring," *Bulletin of Earthquake Engineering*, vol. 20, no. 9, pp. 4345–4365, 2022.

[115] P. Paul, N. Dutta, B. A. Biswas, M. Das, S. Biswas, Z. Khalid, and H. N. Saha, "An internet of things (iot) based system to analyze real-time collapsing probability of structures," in *2018 IEEE 9th Annual Information Technology, Electronics and Mobile Communication Conference (IEMCON)*, pp. 1070–1075, IEEE, 2018.

[116] F. Zonzini, C. Aguzzi, L. Gigli, L. Sciullo, N. Testoni, L. De Marchi, M. Di Felice, T. S. Cinotti, C. Mennuti, and A. Marzani, "Structural health monitoring and prognostic of industrial plants and civil structures: A sensor to cloud architecture," *IEEE Instrumentation & Measurement Magazine*, vol. 23, no. 9, pp. 21–27, 2020.

[117] J. R. Casas and J. C. Matos, "Quality specifications for roadway bridges, standardization at a european level," in *Risk-based Bridge Engineering*, pp. 285–298, CRC Press, 2019.

[118] A. Strauss, K. Bergmeister, A. M. Ivanković, and J. C. e Matos, "Applied and research based performance indicator database for highway bridges across europe," *Life-cycle of engineering systems: Emphasis on sustainable civil infrastructure*, pp. 1503–1510, 2016.

[119] M. A. Zanini, F. Faleschini, and J. R. Casas, "State-of-research on performance indicators for bridge quality control and management," *Frontiers in built environment*, vol. 5, p. 22, 2019.

[120] C. Iacovino, Z. I. Turksezer, P. F. Giordano, and M. P. Limongelli, "A survey of bridge condition rating systems," in *International Conference of the European Association on Quality Control of Bridges and Structures*, pp. 14–22, Springer, 2021.

[121] V. Gattulli and L. Chiaramonte, "Condition assessment by visual inspection for a bridge management system," *Computer-Aided Civil and Infrastructure Engineering*, vol. 20, no. 2, pp. 95–107, 2005.

[122] M. P. Limongelli, E. Chatzi, M. Döhler, G. Lombaert, and E. Reynders, "Towards extraction of vibration-based damage indicators," in *EWSHM-8th European workshop on structural health monitoring*, 2016.

[123] D. Saydam and D. M. Frangopol, "Time-dependent performance indicators of damaged bridge superstructures," *Engineering Structures*, vol. 33, no. 9, pp. 2458–2471, 2011.

[124] B. Zhu and D. M. Frangopol, "Reliability, redundancy and risk as performance indicators of structural systems during their lifecycle," *Engineering Structures*, vol. 41, pp. 34–49, 2012.

[125] A. C. Estes and D. M. Frangopol, "Relsys: A computer program for structural system reliability," *Structural engineering and mechanics: An international journal*, vol. 6, no. 8, pp. 901–919, 1998.

[126] M. Ghosn, D. Frangopol, T. McAllister, M. Shah, S. Diniz, B. Ellingwood, L. Manuel, F. Biondini, N. Catbas, A. Strauss, *et al.*, "Reliability-based performance indicators for structural members," *Journal of Structural Engineering*, vol. 142, no. 9, p. F4016002, 2016.

[127] J. S. Kong and D. M. Frangopol, "Life-cycle reliability-based maintenance cost optimization of deteriorating structures with emphasis on bridges," *Journal of Structural Engineering*, vol. 129, no. 6, pp. 818–828, 2003.

[128] P. F. Giordano and M. P. Limongelli, "The benefit of informed risk-based management of civil infrastructures," *Infrastructures*, vol. 7, no. 12, p. 165, 2022.

[129] M. Torti, I. Venanzi, S. Laflamme, and F. Ubertini, "Life-cycle management cost analysis of transportation bridges equipped with seismic structural health monitoring systems," *Structural health monitoring*, vol. 21, no. 1, pp. 100–117, 2022.

[130] F. Biondini and D. M. Frangopol, "Life-cycle performance of deteriorating structural systems under uncertainty," *Journal of Structural Engineering*, vol. 142, no. 9, p. F4016001, 2016.

[131] D. M. Frangopol, K.-Y. Lin, and A. C. Estes, "Life-cycle cost design of deteriorating structures," *Journal of structural engineering*, vol. 123, no. 10, pp. 1390–1401, 1997.

[132] S. B. Chase, Y. Adu-Gyamfi, A. Aktan, E. Minaie, *et al.*, "Synthesis of national and international methodologies used for bridge health indices," 2016.

[133] R. B. Testa and B. S. Yanev, "Bridge maintenance level assessment," *Computer-Aided Civil and Infrastructure Engineering*, vol. 17, no. 5, pp. 358–367, 2002.

[134] R. Denysiuk, J. Fernandes, J. C. Matos, L. C. Neves, and U. Berardinelli, "A computational framework for infrastructure asset maintenance scheduling," *Structural engineering international*, vol. 26, no. 2, pp. 94–102, 2016.

[135] L. Quirk, J. Matos, J. Murphy, and V. Pakrashi, "Visual inspection and bridge management," *Structure and Infrastructure Engineering*, vol. 14, no. 3, pp. 320–332, 2018.

[136] D. Fernando, B. T. Adey, and N. Lethanh, "A model for the evaluation of intervention strategies for bridges affected by manifest and latent deterioration processes," *Structure and Infrastructure Engineering*, vol. 11, no. 11, pp. 1466–1483, 2015.

[137] S. Valenzuela, H. de Solminihac, and T. Echaveguren, "Proposal of an integrated index for prioritization of bridge maintenance," *Journal of Bridge Engineering*, vol. 15, no. 3, pp. 337–343, 2010.

[138] I. Zambon, A. Vidovic, A. Strauss, J. Matos, and J. Amado, "Comparison of stochastic prediction models based on visual inspections of bridge decks," *Journal of Civil Engineering and Management*, vol. 23, no. 5, pp. 553–561, 2017.

[139] H. Liu, X. Wang, Y. Jiao, X. He, and B. Wang, "Condition evaluation for existing reinforced concrete bridge superstructure using fuzzy clustering improved by particle swarm optimisation," *Structure and Infrastructure Engineering*, vol. 13, no. 7, pp. 955–965, 2017.

[140] A. Bolar, S. Tesfamariam, and R. Sadiq, "Condition assessment for bridges: a hierarchical evidential reasoning (her) framework," *Structure and Infrastructure Engineering*, vol. 9, no. 7, pp. 648–666, 2013.

[141] K. Kawamura, A. Miyamoto, D. M. Frangopol, and R. Kimura, "Performance evaluation of concrete slabs of existing bridges using neural networks," *Engineering Structures*, vol. 25, no. 12, pp. 1455–1477, 2003.

[142] A. Rytter, "Vibrational based inspection of civil engineering structures," 1993.

[143] J. L. Beck and S.-K. Au, "Bayesian updating of structural models and reliability using markov chain monte carlo simulation," *Journal of engineering mechanics*, vol. 128, no. 4, pp. 380–391, 2002.

[144] C. R. Farrar and K. Worden, *Structural health monitoring: a machine learning perspective*. John Wiley & Sons, 2012.

[145] E. Figueiredo and J. Brownjohn, "Three decades of statistical pattern recognition paradigm for shm of bridges," *Structural Health Monitoring*, vol. 21, no. 6, pp. 3018–3054, 2022.

[146] F. Magalhães, Á. Cunha, and E. Caetano, "Vibration based structural health monitoring of an arch bridge: From automated oma to damage detection," *Mechanical Systems and signal processing*, vol. 28, pp. 212–228, 2012.

[147] L. Ierimonti, I. Venanzi, and F. Ubertini, "Roc analysis-based optimal design of a spatio-temporal online seismic monitoring system for precast industrial buildings," *Bulletin of Earthquake Engineering*, vol. 19, no. 3, pp. 1441–1466, 2021.

[148] C. Cappello, D. Zonta, M. Pozzi, B. Glisic, and R. Zandonini, "Impact of prior perception on bridge health diagnosis," *Journal of Civil Structural Health Monitoring*, vol. 5, no. 4, pp. 509–525, 2015.

[149] D. Tonelli, A. Verzobio, C. Cappello, D. Bolognani, D. Zonta, O. S. Bursi, C. Costa, *et al.*, "Expected utility theory for monitoring-based decision support system," in *Proceedings of the 11th international workshop on structural health monitoring*, pp. 2072–2079, 2017.

[150] A. F. Shahraki, O. P. Yadav, and H. Liao, "A review on degradation modelling and its engineering applications," *International Journal of Performability Engineering*, vol. 13, no. 3, p. 299, 2017.

[151] Autonomous Province of Trento, "BMS – Manuale Modelli di Calcolo." http://www.bms.provincia.tn.it/bms, 2013. Online; accessed on April 1, 2026.

[152] D. Hallberg and G. Racutanu, "Development of the swedish bridge management system by introducing a lms concept," *Materials and structures*, vol. 40, no. 6, pp. 627–639, 2007.

[153] J. O. Sobanjo, "State transition probabilities in bridge deterioration based on weibull sojourn times," *Structure and Infrastructure Engineering*, vol. 7, no. 10, pp. 747–764, 2011.

[154] I. Srikanth and M. Arockiasamy, "Deterioration models for prediction of remaining useful life of timber and concrete bridges: A review," *Journal of traffic and transportation engineering (English edition)*, vol. 7, no. 2, pp. 152–173, 2020.

[155] M. J. Ryall, *Bridge management*. CRC Press, 2009.

[156] G. Morcous, Z. Lounis, and Y. Cho, "An integrated system for bridge management using probabilistic and mechanistic deterioration models: Application to bridge decks," *KSCE Journal of Civil Engineering*, vol. 14, no. 4, pp. 527–537, 2010.

[157] H. Mohseni, S. Setunge, G. Zhang, and R. Wakefield, "Markov process for deterioration modeling and asset management of community buildings," *Journal of Construction Engineering and Management*, vol. 143, no. 6, p. 04017003, 2017.

[158] Y. Fang and L. Sun, "Developing a semi-markov process model for bridge deterioration prediction in shanghai," *Sustainability*, vol. 11, no. 19, p. 5524, 2019.

[159] J. C. García-Marino, C. Calvo-Jurado, and E. García-Macías, "Sparse polynomial chaos expansion for universal stochastic kriging," *arXiv preprint arXiv:2402.10936*, 2024.

[160] P. Daró, I. Alovisi, G. Mancini, S. Negri, A. B.-v. Vliet, and H. van Meerveld, "Framework for proactive maintenance practices for transport infrastructures," *ce/papers*, vol. 6, no. 5, pp. 568–577, 2023.

[161] A. Strauss, A. Orcesi, A. Lampropoulos, B. Briseghella, D. M. Frangopol, H. S. Sousa, J. Casas, J. C. Matos, K. Schellenberg, M. Valenzuela, *et al.*, "Iabse survey of implemented decision-making models used by public and private owners/operators of road-and railway infrastructures," *Structural Engineering International*, vol. 34, no. 1, pp. 87–96, 2024.

[162] C. Stenström, P. Norrbin, A. Parida, and U. Kumar, "Preventive and corrective maintenance–cost comparison and cost–benefit analysis," *Structure and Infrastructure Engineering*, vol. 12, no. 5, pp. 603–617, 2016.

[163] P. Bocchini and D. M. Frangopol, "Connectivity-based optimal scheduling for maintenance of bridge networks," *Journal of Engineering Mechanics*, vol. 139, no. 6, pp. 760–769, 2013.

[164] F. Yokota and K. M. Thompson, "Value of information analysis in environmental health risk management decisions: past, present, and future," *Risk analysis: an international journal*, vol. 24, no. 3, pp. 635–650, 2004.

[165] N. H. Andersen, "Danbro—a bridge management system for many levels," in *Bridge evaluation, repair and rehabilitation*, pp. 11–21, Springer, 1990.

[166] R. Hajdin, "Bms development in switzerland," in *Advanced Technology in Structural Engineering*, pp. 1–8, 2000.

[167] G. Kabir, R. Sadiq, and S. Tesfamariam, "A review of multi-criteria decision-making methods for infrastructure management," *Structure and infrastructure engineering*, vol. 10, no. 9, pp. 1176–1210, 2014.

[168] Bundesministerium für Klimaschutz, Umwelt, Energie, Mobilität, "Lebenszykluskosten Ermittlung für Brücken RSV 13.05.11.," 2017. I. und T.

[169] R. Hajdin, "Kuba-ms: The swiss bridge management system," in *Structures 2001: A Structural Engineering Odyssey*, pp. 1–3, 2001.

[170] Z. Allah Bukhsh, I. Stipanovic, G. Klanker, A. O'Connor, and A. G. Doree, "Network level bridges maintenance planning using multi-attribute utility theory," *Structure and infrastructure engineering*, vol. 15, no. 7, pp. 872–885, 2019.

[171] F. Bortot, D. Zonta, R. Zandonini, *et al.*, "A bridge management strategy based on future reliability and semi-markov deterioration models," in *Proceedings of the 3rd International ASRANet Colloquium, Glasgow, UK*, pp. 10–12, 2006.

[172] C. Ye, L. Butler, C. Bartek, M. Iangurazov, Q. Lu, A. Gregory, M. Girolami, and C. Middleton, "A digital twin of bridges for structural health monitoring," in *12th International Workshop on Structural Health Monitoring 2019*, Stanford University, 2019.

[173] J. Vieira, J. Poças Martins, N. Marques de Almeida, H. Patrício, and J. Gomes Morgado, "Towards resilient and sustainable rail and road networks: A systematic literature review on digital twins," *Sustainability*, vol. 14, no. 12, p. 7060, 2022.

[174] M. F. Bado, D. Tonelli, F. Poli, D. Zonta, and J. R. Casas, "Digital twin for civil engineering systems: An exploratory review for distributed sensing updating," *Sensors*, vol. 22, no. 9, p. 3168, 2022.

[175] E. García-Macías, L. Ierimonti, I. Venanzi, and F. Ubertini, "An innovative methodology for online surrogate-based model updating of historic buildings using monitoring data," *International Journal of Architectural Heritage*, vol. 15, no. 1, pp. 92–112, 2021.

[176] M. Torzoni, A. Manzoni, and S. Mariani, "A multi-fidelity surrogate model for structural health monitoring exploiting model order reduction and artificial neural networks," *Mechanical Systems and Signal Processing*, vol. 197, p. 110376, 2023.

[177] T. Tong, X. Li, S. Wu, H. Wang, and D. Wu, "Surrogate modeling for the long-term behavior of pc bridges via fem analyses and long short-term neural networks," in *Structures*, vol. 63, p. 106309, Elsevier, 2024.

[178] A. Aloisio, A. Contento, R. Alaggio, and G. Quaranta, "Physics-based models, surrogate models and experimental assessment of the vehicle–bridge interaction in braking conditions," *Mechanical Systems and Signal Processing*, vol. 194, p. 110276, 2023.

[179] A. Mohammadkhorasani, K. Malek, R. Mojidra, J. Li, C. Bennett, W. Collins, and F. Moreu, "Augmented reality-computer vision combination for automatic fatigue crack detection and localization," *Computers in Industry*, vol. 149, p. 103936, 2023.

[180] C. Ferraris, G. Amprimo, and G. Pettiti, "Computer vision and image processing in structural health monitoring: Overview of recent applications," *Signals*, vol. 4, no. 3, pp. 539–574, 2023.

[181] X. Yang, E. del Rey Castillo, Y. Zou, and L. Wotherspoon, "Uav-deployed deep learning network for real-time multi-class damage detection using model quantization techniques," *Automation in Construction*, vol. 159, p. 105254, 2024.

[182] X. Peng, X. Zhong, C. Zhao, A. Chen, and T. Zhang, "A uav-based machine vision method for bridge crack recognition and width quantification through hybrid feature learning," *Construction and Building Materials*, vol. 299, p. 123896, 2021.

[183] B. Perry, Y. Guo, R. Atadero, and J. van de Lindt, "Unmanned aerial vehicle (uav)-enabled bridge inspection framework," in *Bridge Maintenance, Safety, Management, Life-Cycle Sustainability and Innovations*, pp. 158–165, CRC Press, 2021.

[184] S. Moon, S. Chung, and S. Chi, "Bridge damage recognition from inspection reports using ner based on recurrent neural network with active learning," *Journal of Performance of Constructed Facilities*, vol. 34, no. 6, p. 04020119, 2020.

[185] F. Luleci, J. Chi, C. Cruz-Neira, D. Reiners, and F. N. Catbas, "Fusing infrastructure health monitoring data in point cloud," *Automation in Construction*, vol. 165, p. 105546, 2024.

[186] F. Luleci, L. Li, J. Chi, D. Reiners, C. Cruz-Neira, and F. N. Catbas, "Structural health monitoring of a foot bridge in virtual reality environment," *Procedia Structural Integrity*, vol. 37, pp. 65–72, 2022.

[187] D. Zonta, B. Glisic, and S. Adriaenssens, "Value of information: impact of monitoring on decision-making," *Structural Control and Health Monitoring*, vol. 21, no. 7, pp. 1043–1056, 2014.

[188] V. Macchiarulo, P. Milillo, M. J. DeJong, J. Gonzalez Marti, J. Sánchez, and G. Giardina, "Integrated insar monitoring and

structural assessment of tunnelling-induced building deformations," *Structural Control and Health Monitoring*, vol. 28, no. 9, p. e2781, 2021.

[189] C. Reyes-Carmona, A. Barra, J. P. Galve, O. Monserrat, J. V. Pérez-Peña, R. M. Mateos, D. Notti, P. Ruano, A. Millares, J. López-Vinielles, *et al.*, "Sentinel-1 dinsar for monitoring active landslides in critical infrastructures: The case of the rules reservoir (southern spain)," *Remote Sensing*, vol. 12, no. 5, p. 809, 2020.

[190] D. Tonelli, V. F. Caspani, A. Valentini, A. Rocca, R. Torboli, A. Vitti, D. Perissin, and D. Zonta, "Interpretation of bridge health monitoring data from satellite insar technology," *Remote Sensing*, vol. 15, no. 21, p. 5242, 2023.

[191] S. Selvakumaran, S. Plank, C. Geiß, C. Rossi, and C. Middleton, "Remote monitoring to predict bridge scour failure using interferometric synthetic aperture radar (insar) stacking techniques," *International journal of applied earth observation and geoinformation*, vol. 73, pp. 463–470, 2018.

[192] V. Giglioni, J. Poole, I. Venanzi, F. Ubertini, and K. Worden, "A domain adaptation approach to damage classification with an application to bridge monitoring," *Mechanical Systems and Signal Processing*, vol. 209, p. 111135, 2024.

[193] I. John Samuel, O. Salem, and S. He, "Defect-oriented supportive bridge inspection system featuring building information modeling and augmented reality," *Innovative Infrastructure Solutions*, vol. 7, no. 4, p. 247, 2022.

[194] L. Iannacone, P. F. Giordano, P. Gardoni, and M. P. Limongelli, "A renewal theory formulation for the quantification of the benefits of structural health monitoring," in *International Conference of the European Association on Quality Control of Bridges and Structures*, pp. 277–284, Springer, 2021.

[195] A. Kamariotis, E. Chatzi, and D. Straub, "A framework for quantifying the value of vibration-based structural health monitoring," *Mechanical Systems and Signal Processing*, vol. 184, p. 109708, 2023.

[196] G. Costa, M. P. Limongelli, and S. Thöns, "Forecasting the value of vibration-based monitoring information in structural integrity

management," in *International Conference on Experimental Vibration Analysis for Civil Engineering Structures*, pp. 21–31, Springer, 2023.

[197] S. Sakore, D. Ghosh, P. Ashwin Kumar, and S. Shiradhonkar, "Fatigue life evaluation of corroded steel truss bridge girder," in *Symposium in Earthquake Engineering*, pp. 591–606, Springer, 2022.

[198] X. Su, Y. Ma, L. Wang, Z. Guo, and J. Zhang, "Fatigue life prediction for prestressed concrete beams under corrosion deterioration process," in *Structures*, vol. 43, pp. 1704–1715, Elsevier, 2022.

[199] M. M. Borah and A. Sil, "Service-life estimation of a reinforced concrete bridge structure exposed to chloride-contaminated environments and variable traffic loads," *ASCE-ASME Journal of Risk and Uncertainty in Engineering Systems, Part A: Civil Engineering*, vol. 9, no. 4, p. 04023028, 2023.

[200] J. Zhu, Y. Chen, J. Heng, M. Wu, Y. Zhang, and Y. Li, "Probabilistic corrosion-fatigue prognosis of rib-to-deck welded joints in coastal weathering steel bridges exposed to heavy traffics," *International Journal of Fatigue*, vol. 182, p. 108210, 2024.

[201] F. Jiang, Y. Ding, Y. Song, F. Geng, and Z. Wang, "Digital twin-driven framework for fatigue lifecycle management of steel bridges," *Structure and Infrastructure Engineering*, vol. 19, no. 12, pp. 1826–1846, 2023.

[202] C. S. Wang, Y. Z. Wang, W. De Corte, and C. Shu, "Digital simulation of distortion-induced fatigue in steel bridges with different geometrical configurations," *Journal of Constructional Steel Research*, vol. 216, p. 108613, 2024.

[203] D. Jajich and A. Schultz, "Measurement and analysis of distortion-induced fatigue in multigirder steel bridges," *Journal of Bridge Engineering*, vol. 8, no. 2, pp. 84–91, 2003.

[204] M. Aygül, M. Al-Emrani, Z. Barsoum, and J. Leander, "Investigation of distortion-induced fatigue cracked welded details using 3d crack propagation analysis," *International journal of fatigue*, vol. 64, pp. 54–66, 2014.

[205] C.-s. Wang and Y.-z. Wang, "Influence of distortion ratio on distortion-induced fatigue behavior of steel girder bridges," *Thin-Walled Structures*, vol. 188, p. 110790, 2023.

[206] O. Skoglund and J. Leander, "A numerical evaluation of new structural details for an improved fatigue strength of steel bridges," *International Journal of Fatigue*, vol. 160, p. 106866, 2022.

[207] F. Jiang, Y. Ding, Y. Song, F. Geng, and Z. Wang, "Digital twin-driven framework for fatigue life prediction of steel bridges using a probabilistic multiscale model: Application to segmental orthotropic steel deck specimen," *Engineering Structures*, vol. 241, p. 112461, 2021.

[208] A. Ghaffary and M. A. Moustafa, "Synthesis of repair materials and methods for reinforced concrete and prestressed bridge girders," *Materials*, vol. 13, no. 18, p. 4079, 2020.

[209] S. Nakamura, T. Ogata, M. Takano, and Y. Kobayashi, "New technologies in retrofitting and strengthening of ageing steel and composite bridges in japan," *Structural Engineering International*, vol. 29, no. 4, pp. 519–526, 2019.

[210] C. Miki, T. Hanji, and K. Tokunaga, "Weld repair for fatigue-cracked joints in steel bridges by applying low temperature transformation welding wire," *Welding in the World*, vol. 56, no. 3, pp. 40–50, 2012.

[211] Y. Chen, J. Saunders, I. Hodgson, and R. Sause, "Distortion-induced fatigue cracking after crack arrest hole retrofit of steel girder bridges," *Journal of Bridge Engineering*, vol. 28, no. 6, p. 04023027, 2023.

[212] L. Bridwell, W. Collins, C. Bennett, and J. Li, "Mechanical treatment of crack-arrest holes subjected to distortion-induced fatigue," *Procedia Structural Integrity*, vol. 17, pp. 674–681, 2019.

[213] Y.-z. Wang, C.-s. Wang, and L. Duan, "Bonding and bolting angle reinforcement for distortion-induced fatigue in steel girder bridges," *Thin-Walled Structures*, vol. 166, p. 108027, 2021.

[214] C.-s. Wang, M.-s. Zhai, L. Duan, and Y.-z. Wang, "Cold reinforcement and evaluation of steel bridges with fatigue cracks," *Journal of Bridge Engineering*, vol. 23, no. 4, p. 04018014, 2018.

[215] H. Unterweger and C. Derler, "Specific distortion-induced fatigue failure at main girders of a railway bridge–efficiency of different reinforcements based on strain measurements," *ce/papers*, vol. 6, no. 3-4, pp. 997–1002, 2023.

[216] H. S. Shim and S. H. Lee, "Balanced allocation of bridge deck maintenance budget through multi-objective optimization," *KSCE Journal of Civil Engineering*, vol. 21, no. 4, pp. 1039–1046, 2017.

[217] S. Kim, B. Ge, and D. M. Frangopol, "Effective optimum maintenance planning with updating based on inspection information for fatigue-sensitive structures," *Probabilistic Engineering Mechanics*, vol. 58, p. 103003, 2019.

[218] C. Gong and D. M. Frangopol, "Condition-based multiobjective maintenance decision making for highway bridges considering risk perceptions," *Journal of Structural Engineering*, vol. 146, no. 5, p. 04020051, 2020.

[219] "IM SAFE." https://im-safe-project.eu/. Accessed: 18 Dec 2025.

[220] "Bridgitise." https://www.bridgitise.polimi.it/. Accessed: 18 Dec 2025.

[221] S. A. Mitoulis, M. Domaneschi, G. P. Cimellaro, and J. R. Casas, "Bridge and transport network resilience–a perspective," in *Proceedings of the Institution of Civil Engineers-Bridge Engineering*, vol. 175, pp. 138–149, Thomas Telford Ltd, 2022.

6. Interpretation of Bridge Health Monitoring Data from Satellite InSAR Technology

This chapter contains the post-print of

> Tonelli, D., **Caspani, V. F.**, Valentini, A., Rocca, A., Torboli, R., Vitti, A., Perissin, D., Zonta, D. (2023). Interpretation of bridge health monitoring data from satellite InSAR technology. Remote Sensing, 15(21), 5242, https://doi.org/10.3390/rs15215242.

as published in the Journal *Remote Sensing*, differing only from the published article in terms of layout, formatting, and notation.

Abstract

This paper presents a study on applying satellite Interferometric Synthetic Aperture Radar (InSAR) technology for the remote monitoring of road bridges and interpreting the results from a structural standpoint. The motivation behind this study arises from the widespread deterioration observed in many road bridges worldwide, leading to the need for large-scale, economic, and effective structural health monitoring (SHM) techniques. While traditional contact-type sensors have cost sustainability limitations, remote sensing techniques, including satellite-based InSAR, offer interesting alternative solutions. The objective of this study is threefold: (i) to process InSAR data specifically for road bridges in operational conditions through the Multi-Temporal InSAR (MT-InSAR) technique and extract displacement time series of reflective targets on their decks; (ii) to interpret the observed millimetric bridge displacements to verify the consistency with expected response to environmental loads and the possibility to detect unexpected behaviours; and (iii) to investigate the correlation between bridge displacements and environmental loads as temperature and river water flow variations. The study focuses on the multi-span prestressed concrete A22 Po River Bridge in Italy, utilising a dataset of X-Band HIMAGE mode Stripmap images acquired over eight years by the satellite constellation COSMO-SkyMed. The study demonstrates the effectiveness of InSAR-based SHM in detecting temperature-induced displacements and identifying different bridge spans simply by studying the sign of the correlation between displacements and temperature variation. It also reveals an unexpected behaviour in a portion of the

bridge retrofitted to prevent scour issues a few years before the dataset start date. Furthermore, the correlation between pier displacements and river level variations underscores the importance of considering environmental factors and the geotechnical characteristics of the foundation soils in bridge monitoring. The results obtained from this study are significant with a view to using this satellite InSAR-based monitoring for early detection of anomalous bridge behaviour on a large scale.

Keywords:
structural health monitoring; interpretation; InSAR; road bridges; remote sensing; satellite; persistent scatterers; displacement time series; correlation analysis; temperature deformation.

Glossary

In this section, the authors provide a brief glossary of the notation involved in the present paper.

SHM	Structural Health Monitoring
SAR	Synthetic Aperture Radar
InSAR	Interferometric SAR
MT-InSAR	Multi-Temporal InSAR
MR&R	Maintenance, Repair, and Rehabilitation
PS	Persistent Scatterer
LoS	Line of Sight
CSK	COSMO-SkyMed
θ	incidence angle
β	heading angle
APS	Atmospheric Phase Screen
RP	Reference Point
d_{LoS}	displacements along the LoS
d_H	horizontal displacements
d_V	vertical displacements
d_L	longitudinal displacements
ζ	bridge orientation
$\gamma = \zeta - \beta$	bridge's longitudinal axis - LoS horizontal projection angle
ρ_{XY}	Pearson correlation coefficient between random variables X and Y
LSA	Least Square Analysis
ϵ	deformation
T	temperature

t	time
ϵ_0	geometric offset
v	deformation trend
α	thermal expansion coefficient
μ	mean value
σ	standard deviation

6.1 Introduction

Structural Health Monitoring (SHM) has repeatedly demonstrated its effectiveness in providing accurate and in-time information on the condition state of bridges, improving the managers' capability to optimise Maintenance, Repair, and Rehabilitation (MR&R) strategies and resource allocation [1, 2]. Contact-type sensors (e.g., strain gauges, accelerometers, load cells) permanently installed on bridges continuously acquire real-time, accurate information, increasing the knowledge of infrastructure operators on the bridges' response to traffic and environmental loads [3, 4]. However, researchers and practitioners have repeatedly highlighted issues related to the economic and environmental sustainability of traditional contact-type sensors: (i) scalability: cost of intensive instrumentation of a bridge ranges from 50k € to 500k €; therefore, SHM systems are typically installed on few strategic bridges [5]; (ii) adaptability: when a contact-type SHM system is installed on a bridge, its components can be hardly re-used for other structures; (iii) reliability: extensive faults of contact SHM system components occur during extreme events, precisely when they are expected to provide critical information on the structural health condition [6]. Furthermore, like any other monitoring system, contact-type SHM is affected by data quality issues: large amounts of data are generated and must be appropriately analysed and managed to support decision-making [7].

Several remote sensing techniques have been explored in the last few years to cope with the limits of contact-type sensors. Among them, satellite Interferometric Synthetic Aperture Radar (InSAR) technology has emerged as a solution to remotely monitor large-scale phenomena such as subsidence, uplifting, or landslides [8, 9, 10, 11]. Recently, the research community has started to investigate the possibility of applying such innovative technology for monitoring the long-term response of civil infrastructure [12, 13, 14].

Satellite InSAR exploits the Synthetic Aperture Radar (SAR) sensors carried by many satellites orbiting around our planet, which provide high-resolution weather-independent imagery of the Earth's surface. Some natural and artificial elements (e.g., rocks, light poles, house

roofs, road guardrails) strongly reflect the electromagnetic signal emitted by SAR sensors, which receive it back and generate radar images of Earth's surface: the SAR images. Through appropriate datasets and data-analysis techniques, it is possible to obtain displacement time series of some of those reflective elements—called Persistent Scatterers (PSs)—along the Line of Sight (LoS) connecting the SAR sensor to the reflective elements up to millimetric level [15]. In principle, SAR technology allows the monitoring of large territory and civil infrastructures without installing traditional sensors on-site. Moreover, it potentially gives the possibility of going back in time and studying the past behaviour of structures based on archive SAR imagery acquired by satellites in the past years. However, the use of such technology for these purposes is still in its early stages, and only a limited number of case studies have been reported in the literature.

As far as buildings are concerned, visual inspection campaigns were conducted in [16] to confirm the reliability of satellite technology in determining differential movements that would decrease serviceability, and the negative effects of the subsidence phenomenon have been observed in [17]. The reliability of structural monitoring of dams through InSAR technology was studied by [18], even though it was carried out by first-generation sensors (ENVISAT) with low spatial/temporal resolution. However, this study encouraged monitoring dams with higher spatial resolution sensors, as in the case of [19]. InSAR has also been used for monitoring ground surface movements following the construction of underground tunnels. Two applications are reported by [20]: the first emphasises the integration between InSAR monitoring and traditional monitoring; the second studies the temporal evolutions of settlements along a landslide slope hosting two tunnels using Multi-Temporal InSAR. Regarding roads and railways, the possibility of large-scale monitoring of these structures through InSAR is demonstrated in [21]. Similarly, [22] presents a completely automated monitoring solution for road networks, highlighting possible damages or unexpected displacements.

Delving into the published studies on bridge monitoring using InSAR technology, [12] extracted important information regarding the effects of bridge scour. Through the analysis of historical series, the authors observed unexpected behaviour of the pier affected by scour already one month before its collapse. In addition, [23] studied the progressive displacement of some bridges in California (USA), observing how these movements were not attributable to structural defects but were caused by subsidence phenomena resulting from the continuous water pumping from the surrounding aquifers. Also, [24] demonstrated that it was possible to measure past anomalous deformations of the Morandi

Bridge (Italy)—which collapsed in 2018—using archived InSAR images, highlighting a continuous increase in the relative deformation between the pier and the deck of this bridge since 2015. An attempt to reconstruct the two-dimensional displacement field was conducted by [25], acquiring displacement information from ascending and descending geometry for the Albiano-Magra viaduct, which collapsed in 2020. Finally, an interesting study published by [13] utilises satellite monitoring as an early warning tool for unexpected displacements.

The number of scientific publications focusing on InSAR-based SHM of civil infrastructure is increasing exponentially, as well as the special sessions on this topic in international conferences. Most current research works can be divided into two groups. Group 1 addresses the estimation of displacement time series of PSs identified on the civil infrastructure, focusing on the InSAR data processing technique and the mathematical aspects of the algorithms exploited, without giving any interpretation of data from the structural standpoint (e.g., kinematic behaviour of the structure, structural response to loads, identification of abnormal variation in extracted time series possibly related to structural damages or evolving degradation). Group 2 addresses the interpretation of the PS displacement time series, paying little or no attention to measurement accuracy or the possibility that some patterns visible in the time series were related to the interpretation model used in the data analysis.

In the given context, this paper aims to cover the gap by presenting (i) an entire MT-InSAR data processing specifically performed for road bridges in operational conditions to extract displacement time series of PSs; (ii) the engineering interpretation of the millimetric ground and bridge displacements observed while being aware of the process followed to obtain such results; and (iii) a study of the correlation between the displacements of the bridge and environmental phenomena (temperature and river water flow) to further improve the engineering interpretation of InSAR results. Specifically, our analysis is based on a real-life case study: the A22 Po River Bridge of the Italian A22 Highway, a strategic, prestressed concrete bridge along the European route E45, which crosses the wider and longer Italian river, the Po River. Our study exploits a dataset of 109 X-Band HIMAGE mode Stripmap images acquired in the descending geometry by the Italian COSMO-SkyMed mission from 2014 to 2021. We performed the MT-InSAR data processing with the software SarProZ© (https://www.sarproz.com/), version 'SARPROZ 08-September-2022 16:32:33'.

In detail, 6.2 introduces the A22 Po River Bridge, the case study area, and the dataset of SAR images. 6.3 describes the methods used to process SAR images through MT-InSAR, calculate the vertical and

horizontal components of PSs displacements from the InSAR results, and study the correlation between the bridge displacements over time and the environmental load it experienced. 6.4 reports and discusses our study's results, from the structural interpretation of the MT-InSAR displacements to the correlation analysis between bridge displacements and environmental loads. Conclusions are eventually drawn in 6.5.

6.2 Case Study

6.2.1 A22 Po River Bridge

The A22 Po River Bridge is part of the Italian A22 Highway. It is located in the Mantua province, Italy. It consists of two identical, parallel viaducts made entirely of reinforced concrete and prestressed concrete; it has 14 spans for a total length of 980 m. Each viaduct accommodates a separate highway carriageway. It was designed and built following the 1962 Italian standards for calculating loads of road bridges "Circ. Min. LL.PP. 14/02/1962, n. 384". Figure 6.1 shows a picture of the A22 Po River Bridge and a top view of the case-study area. Figure 6.2 shows the plant and prospect of the bridge.

(a) (b)

Figure 6.1: (a) Picture of the A22 Po River Bridge, Italy; (b) Top view of the case-study area.

The structural system comprises 36 m-long internally simply supported spans that lean on shear keys at the end of 14.15 m-long cantilevers, resulting in a total span length of 72.8 m between the piers. The cantilevers' deck comprises a double box girder with variable heights ranging from approximately 2.3 m to 3.5 m. The supported span girders are 2.2 m high. In 2002, a widening work involved the symmetrical widening of the carriageways from 10 m to 11.3 m, increasing the thickness of the upper slab. The original slab thickness ranged from 20–22

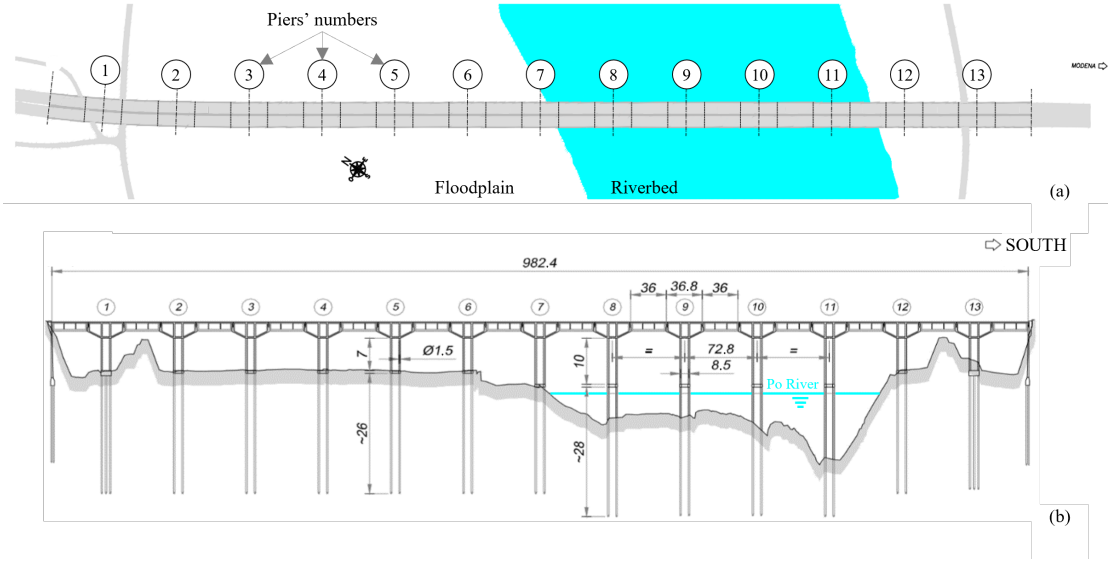

Figure 6.2: (a) Plant and (b) elevation of the A22 Po River Bridge. Dimensions in meters.

cm, which was increased to an average thickness of 35–37 cm for the suspended spans and piers. Additionally, the transverse slope of the deck was increased from the original 2% to the current 2.5%. Consequently, the widening works significantly increased the overall deck mass (approximately 6 t/m). Figure 6.3 shows longitudinal and cross sections of the bridge in the current configuration.

The suspended spans lean on monodirectional and multidirectional steel-Teflon bearings in the north direction and fixed steel bearings in the south direction. Seismic dissipators connect the suspended spans to the cantilevers at the shear keys with fixed bearings. Figure 6.4 shows a scheme of the suspended span bearings and a picture of the seismic dissipators.

The bridge has 13 piers, with 5 piers within the riverbed and 9 on the floodplain (6 on the north side towards Mantua and 2 on the south side towards Modena). Each pier consists of 6 circular column elements with a diameter of 1.5 m. At the base of the columns is a reinforced concrete collar with dimensions 2.0 m × 0.6 m. The foundation piles, also with a diameter of 1.5 m, extend below the collar and serve as natural extensions into the ground from the columns above. The piers in the riverbed have 10 m-heigh columns and approximately 28 m-long piles; the piers in the floodplain have 7 m-heigh columns and approximately 26 m-long piles.

The last bathymetric survey was performed in 2009, and backfill soil was placed around Pier 11 to decrease its free length in 2012. As a result,

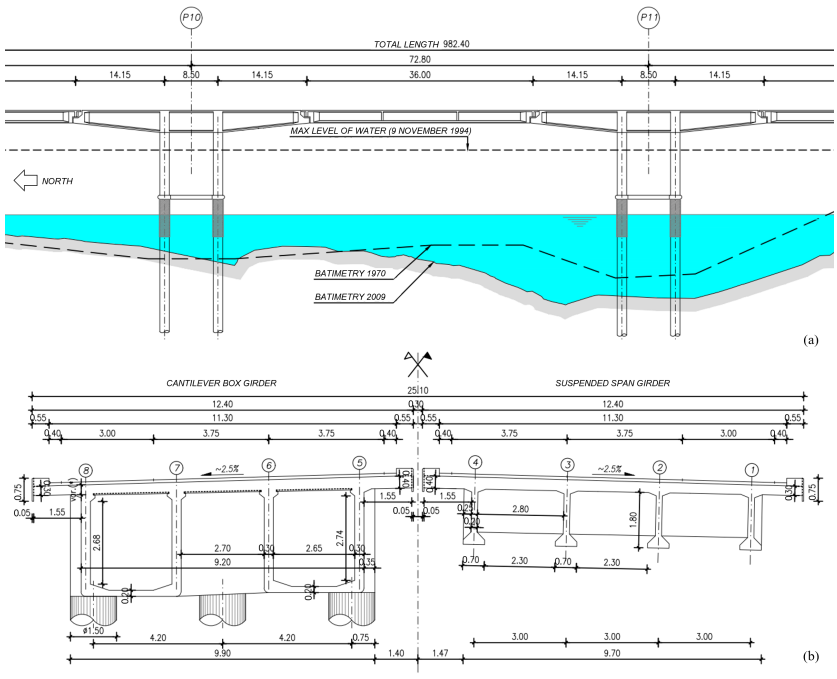

Figure 6.3: (a) Longitudinal section of Piers 10 and 11 and (b) cross sections of the A22 Po River Bridge. Dimensions in meters.

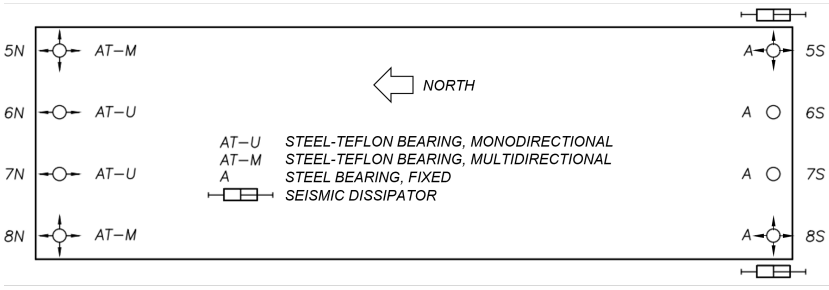

(a) (b)

Figure 6.4: (a) Scheme of the suspended span bearings; (b) picture of the seismic dissipators.

the above-ground part of the foundation poles is approximately 8 m for Piers 8, 9, and 10, approximately 11.40 m for Pier 11, and approximately 1 m for the other piers. The erosion at the base of Pier 11 was essentially caused by the increased speed of the stream and the formation of vortexes at the base of the pier; these actions generated the progressive removal of material (solid transport) in the area surrounding the base of the pier with

the consequent formation of a localised depression in the riverbed. Given this erosion phenomenon, some backfill soil might have been removed since 2012.

6.2.2 Case Study Area and Environmental Loads

The case-study area is 17.6 km2, close to Mantua in northern Italy. It includes the villages of San Nicolò Po and Portiolo and is crossed by the Po River, Italy's longest and widest river. This area is subjected to a slow progressive subsidence of around 1.0–1.5 mm/year, as visible in the vertical displacement measurement accessible from the European Ground Motion Service [26].

In the case study area, the subcontinental climate is characterised by high humidity, snowfall and fog in winter and a muggy, humid climate with little ventilation in summer. Temperatures vary between –5 °C and 40 °C throughout the year, with daily temperature variations of 10 °C to 15 °C around the average. Figure 6.5a shows the air temperature measured between UTC 5 p.m. and 5:30 p.m. from January 2014 to December 2021 by the meteorological station 5.6 km from the A22 Po River Bridge in Gorgo di San Benedetto Po (MN). As commonly known, the vertical deflection and longitudinal deformation of prestressed concrete bridges with a structural scheme similar to the A22 Po River Bridge strongly respond to temperature variation [27]. Thus, we expect to measure a periodical displacement of the A22 Po River Bridge from satellite SAR images, which is correlated to seasonal temperature variation.

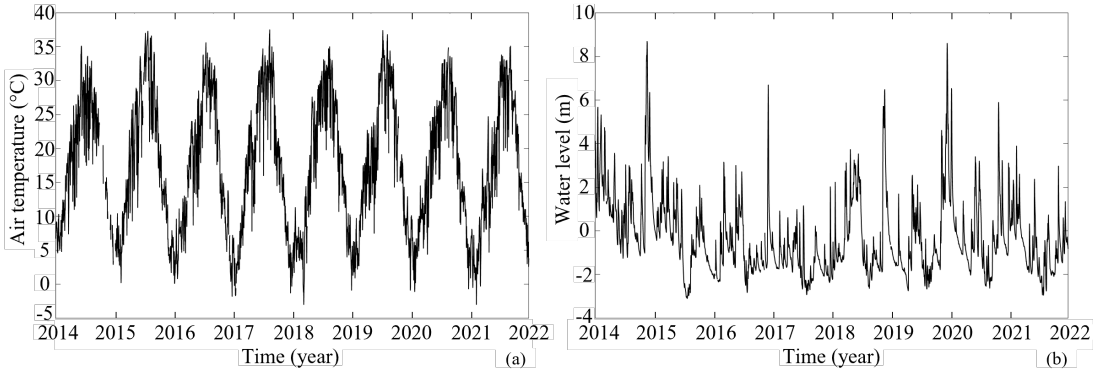

Figure 6.5: Time series from 1 May 2014 to 12 May 2021 of (a) temperature variation in the case study area and (b) water flow level of the Po River.

Significant water flow variations characterise the Po River; the water level has periodically increased up to 10 m in the period we are interested in, which caused the floodplain to fill up during heavy rains. Figure 5b

shows the water level of the Po River from 2014 to 2021 measured between UTC 5 p.m. and 5:30 p.m. by the hydrometer of the Interregional Agency for the River Po (AIPO) installed on the Borgoforte Bridge, located just 7.4 km before the A22 Po River Bridge.

The lithology of the foundation soils was deduced from the results of surveys conducted during the construction close to Pier 7 and the South Abutment. Surveys show a predominance of uniform grain size sands with traces of silt in the higher levels and peaty traces at the deeper levels ($>$15 m from ground level). The survey report indicates an average value of the soil elastic modulus of 8 MPa, constant over a depth of 15 m from ground level, and a friction angle conservatively assumed to be $\phi = 32°$ at the base of the piles and zero cohesion over the entire length of the foundation piles.

6.2.3 Dataset of SAR Images

We analysed a dataset of SAR images acquired by the Italian satellite mission COSMO-SkyMed (CSK, 1st generation), which have been granted free of charge by the Italian Space Agency (ASI) to the Department of Civil, Environmental and Mechanical Engineering at the University of Trento. CSK satellites carry X-band radar sensors with a frequency of 9.6 GHz and a wavelength of 3.1 cm. The revisit time of the CSK constellation (i.e., the number of days between two successive identical passes over the same area) is about 16 days; therefore, the temporal resolution is about 1–2 products per month for images of the same area in both ascending and descending geometry.

Our dataset includes CSK images acquired in Stripmap HIMAGE mode—a medium-resolution mode with a nominal spatial resolution of 3 m—collected over long, continuous 40 km-wide swaths. The dataset counts 109 images acquired in descending orbit at UTC 5:13 p.m. and covers 8 years, from 1 May 2014 to 12 May 2021. The CSK satellite that acquired the images of our dataset has right-side looking-angle with an incidence angle $\theta = 33.9449°$ (i.e., the angle between the LoS and the normal to the ground in our area) and a heading angle $\beta = 10.6095°$ (i.e., the angle between the satellite orbit and the North-South direction). Figure 6.6a shows the footprint of our dataset. The investigated area is a 4.2×4.2 km^2 portion of this footprint, cropped from the original SAR images and shown in Figure 6.6b. It includes the A22 Po River Bridge and the villages of San Nicolò Po and Portiolo. Villages and artificial structures in this area contribute to the successful co-registration of SAR imagery. Figure 6.7 shows the "Star Graph" connecting the dataset, highlighting the temporal and normal baselines. The master image of the descending dataset corresponds to the date 24 July 2017; it is the barycentre

of the images' graph and minimises the temporal and normal baselines, reducing the temporal and spatial decorrelation between images.

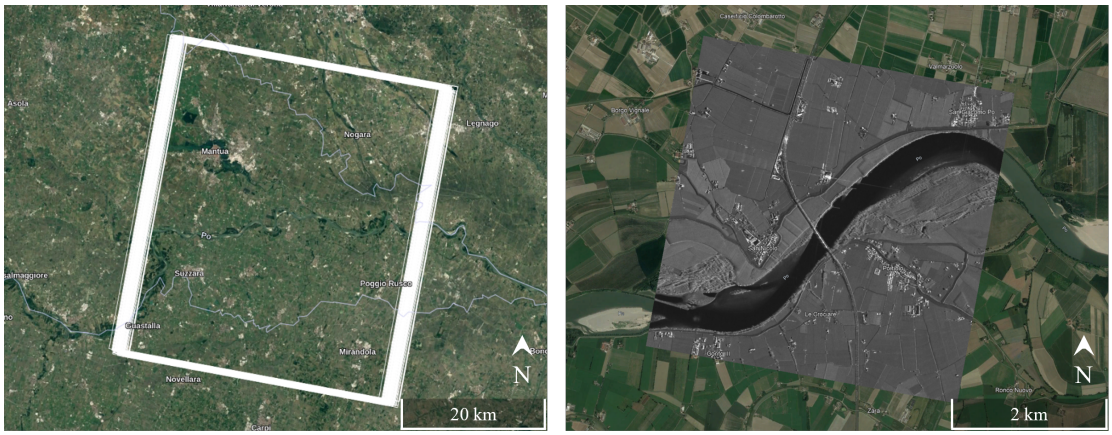

Figure 6.6: (a) Footprint of our dataset (full frame) and (b) multi-temporal reflectivity map of the investigated area, which represents a portion of the dataset footprint cropped from the original SAR images.

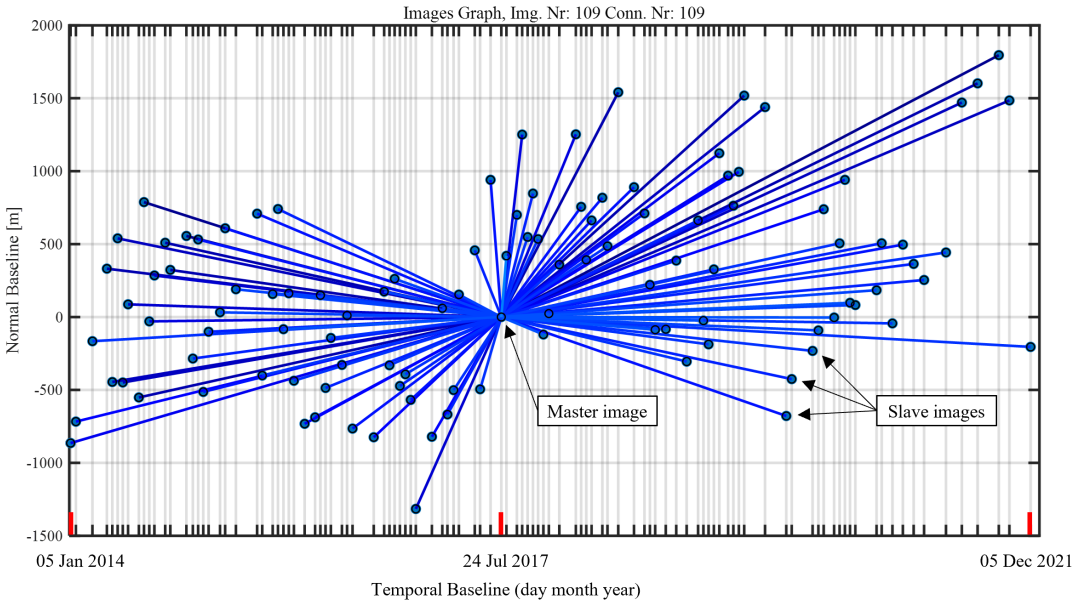

Figure 6.7: Star Graph of the dataset with red marks highlighting dates of first, master, and last images.

6.3 Method

6.3.1 Multi-Temporal InSAR for Bridge Monitoring

InSAR is a remote sensing technique that uses the phase information of radar signals emitted by Synthetic Aperture Radar (SAR) sensors mounted on satellites and backscattered by the Earth's surface to measure the displacement of reflective targets along the Line of Sight (LoS) of the satellites [28]. A SAR image is a collection of complex numbers organised in pixels over the investigated portion of the Earth's surface. The module of the complex number represents the signal amplitude and is related to the target reflectivity; the phase of the complex number is related to the distance between the radar sensor and the reflective target in the pixel. By comparing two or more SAR images of the same area taken at different times (repeat-pass interferometry), it is possible to calculate the phase differences of pixels between the images, which are related to the deformation of the Earth's surface. The phase differences can be converted into a displacement map showing the spatial distribution of the reflective targets' displacements along the LoS. Those reflective targets are called Scatterers (PSs) and are point-like targets that exhibit high reflectivity and stable phase behaviour over time).

The standard InSAR approach is affected by many different limitations, so different Multi-Temporal InSAR (MT-InSAR) techniques have been developed in the last decades [8, 9, 10, 15]. The MT-InSAR technique is a method of processing SAR images that allows for detecting small changes in the Earth's surface over long periods. This technique involves analysing a series of radar images of the same area taken over several years and comparing the phase differences between them and a reference image called master.

After the coregistration of all 109 SAR images and the preliminary analysis aimed at deriving the dataset's main statistics, we performed the actual MT-InSAR processing. The following are the main steps involved in our MT-InSAR workflow and the main choices we made during the analysis of our dataset:

(1) *Atmospheric-phase removal.* One advantage of MT-InSAR compared to standard InSAR is the possibility to estimate and remove the atmospheric phase disturbance from the SAR images. This step is critical because the atmospheric phase contribution is one of the primary sources of error in InSAR data. An initial selection of pixels related to potential candidate targets (the PSs) is processed by connecting them in a spatial graph and estimating the main parameters affecting the interferometric phase along the connections

(for our case, deformation velocity, thermal expansion, and height of the targets). After this estimation, the residual phase signal is used to estimate and remove the Atmospheric Phase Screen (APS) contribution from the original SAR images [28].

(2) *Persistent Scatterer Selection.* Once the APS phase contribution is removed from the images, a higher number of pixels can be analysed with the MT-InSAR algorithm to derive the parameters with respect to a common reference point (RP)—a specific PS used to anchor the estimated deformation time series. The RP is selected based on high temporal coherence and limited deformation over time [15, 28]. After estimating the parameters, we filtered out all PSs with a temporal coherence lower than 0.6. We recall that temporal coherence is a quality metric of the extracted displacement time series with respect to the model used and ranges from 0 (low quality) to 1 (high quality) [28]. As a result, we included 8426 PSs in our analysis, most of them located over roads and villages.

(3) *Time series analysis.* Deformation time series can be extracted for every PSs based on the filtered phase data. Displacements are relative in time and space. In time, they are relative to the date of the master image; in space, they are relative to the displacement of the common RP (the same used in the previous step of the analysis). Note that deformations mean displacements along the Line of Sight of the satellite. A negative deformation means that the PS moves away from the satellite, while a positive deformation means that the PS moves towards the satellite.

Figure 6.8 shows some results obtained during the MT-InSAR data processing of our dataset.

6.3.2 Calculation of Vertical and Horizontal Displacement

Suppose the displacements of an area of the Earth's surface along the LoS of satellites within a specific time interval are known for ascending and descending geometries. In that case, it is possible to derive the East–West and vertical displacements of the PSs in the same area using trigonometric calculations that depend solely on the incidence angles of the two geometries. More information on the assumptions and the procedure to perform this calculation can be found in [29]. In our study, we only analysed SAR images acquired in the descending geometry because the dataset of SAR images acquired in the ascending geometry is highly incomplete. Therefore, we cannot utilise the procedure mentioned above to extract the vertical and horizontal displacements of the bridge.

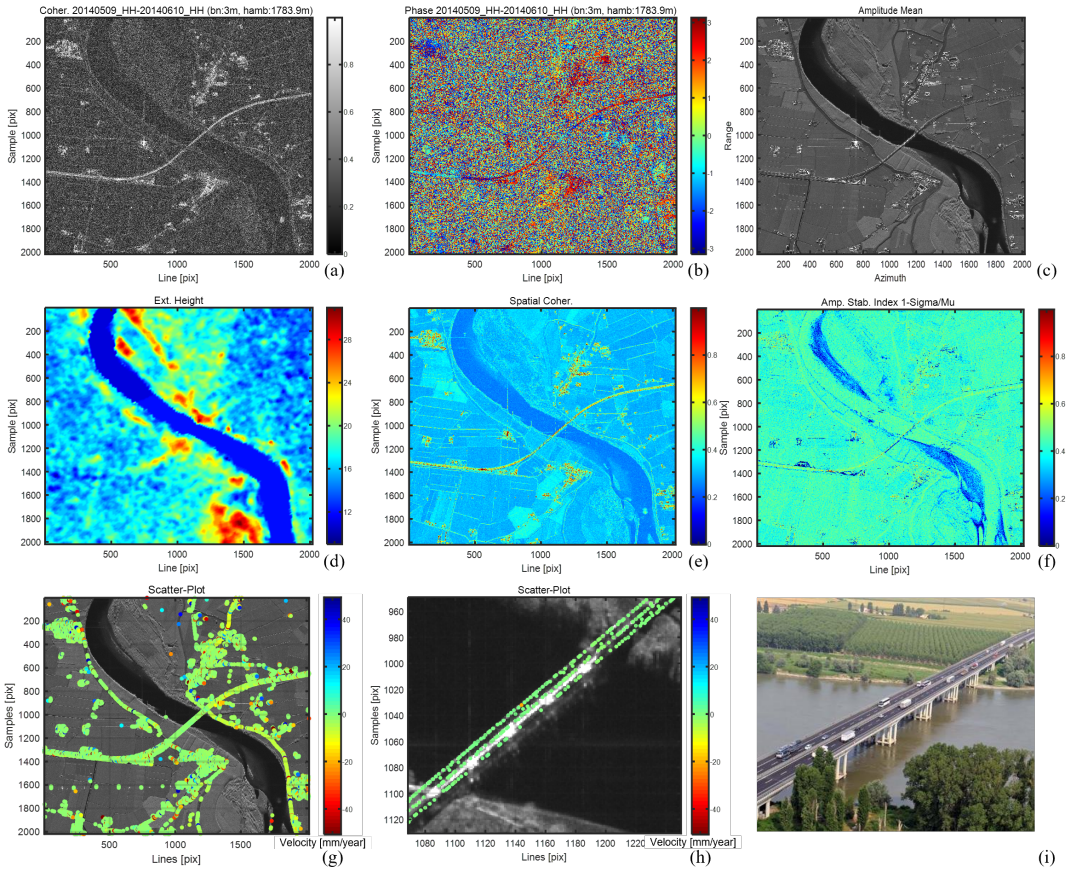

Figure 6.8: Some preliminary and final results obtained during the MT-InSAR data processing of our dataset. Example of (a) coherence and (b) phase of an interferogram of two images belonging to the dataset; (c) reflectivity map; (d) DEM in SAR coordinates; (e) average spatial coherence for all the interferograms generated—the map is related to the interferograms generated by connecting the images using the Minimum Spanning Tree (MST) graph [11]; (f) amplitude stability index; (g) map of the PSs of the case-study area (not filtered by coherence threshold); (h) detail of the PSs of the A22 Po River Bridge; (i) picture of the bridge aligned as in the (h).

However, we can study the bridge behaviour under the two extreme conditions: (i) the deck experiences exclusively vertical displacements, and (ii) the deck experiences exclusively horizontal displacements while being aware that the actual behaviour of the bridge is a combination of these two.

In the case of these two extreme conditions, it is possible to project the measured PS displacements along the LoS (d_{LoS}) onto the vertical (d_V) and horizontal (d_H) components of the LoS, given the incidence an-

gle of the LoS ($\theta = 33.9449°$) for our dataset. Furthermore, in the case of exclusively horizontal displacements along the longitudinal direction of the bridge, it is possible to project horizontal displacements d_H onto the longitudinal direction of the bridge (d_L), knowing the angle between the satellite's orbit direction and the North–South direction (heading angle, $\beta = 10.6095°$) and the angle between the bridge's direction and the North–South direction (bridge orientation, $\zeta = -33.5°$). Figure 6.9 shows these projections for displacements derived from a right-looking satellite in descending geometry and for the actual orientation of the Po River Bridge.

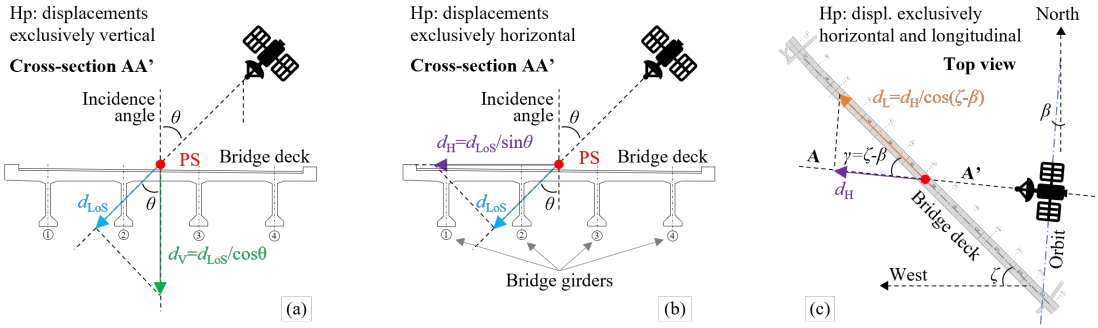

Figure 6.9: (a) Projection of displacements along the LoS (d_{LoS}) onto the vertical direction (d_V) assuming exclusively vertical displacements of the bridge; (b) projection of d_{LoS} onto the horizontal component of the LoS (d_H) assuming exclusively horizontal displacements of the bridge; (c) projection of d_H onto the longitudinal direction of the bridge (d_L) assuming exclusively horizontal longitudinal displacements of the bridge.

Although strong, the hypothesis of exclusively longitudinal horizontal displacements is plausible for the Po River Bridge portion in the floodplain, as no loads induce transversal displacements to the bridge's direction. Indeed, displacements induced by wind have a frequency and variability too high to be observed with the 16-day acquisition frequency determined by the satellite's revisit time. The only displacements induced by environmental loads observable on this bridge portion at this acquisition frequency are those resulting from seasonal temperature variations. A different scenario applies to the displacements of the bridge portion in the riverbed, which can also be influenced by the hydraulic forces of the Po River on the piers, transverse to the bridge's direction, varying with changes in the water level measured by the hydrometer located upstream of the bridge.

Regarding our dataset, the CSK satellite that acquired the SAR images moved from North to South with a right-looking angle. Considering that a negative deformation means that the PS moves away from the

satellite, while a positive deformation means that the PS moves towards the satellite, we can conclude that:

- Negative displacement along the LoS of a PS means that that portion of the bridge moves mainly vertically downward, mainly horizontally toward the West, or a combination of the two;
- Positive displacement along the LoS of a PS means that that portion of the bridge moves mainly vertically upwards or mainly horizontally toward the East, or a combination of the two.

6.3.3 Correlation between Time Series

Displacements of isostatic structures are typically linearly correlated to the loads applied (e.g., dead loads, live loads, and temperature variations). Many studies investigate the correlation between time series of environmental loads and measurements from long-term monitoring of civil structures [30]. Correlation analysis is a method of statistical evaluation used to study the strength of a relationship between continuous variables. Given two random variables, X and Y, the Pearson correlation coefficient ρ_{XY} expresses their linear correlation [31]. The Pearson coefficient ranges between -1 and +1: +1 means perfect direct correlation, and -1 means perfect inverse correlation. Investigating a potential correlation between variables employing the Pearson coefficient involves considering the hypothesis of a linear relationship between them. However, it should be acknowledged that variables can exhibit more complex relationships than simple linear ones. Remarkably, two datasets with low or no linear correlation may demonstrate a robust nonlinear relationship. Nevertheless, assessing linear correlation as a preliminary step is valuable for identifying variables that exhibit a relationship before performing further correlation analyses.

6.4 Results and Discussion

Section 6.4.1 and Section 6.4.2 report and discuss the results directly obtained from the MT-InSAR analysis of COSMO-SkyMed SAR images of the area of interest. Specifically, Section 6.4.1 interprets the displacement time series and velocity of the PSs identified on the bridge and its access lines, while Section 6.4.2 interprets their consistency with the expected response to temperature variation. On the other hand, Section 6.4.3 and Section 6.4.4 investigate and discuss the correlation between the displacement time series and environmental loads. Specifically, Section 6.4.3 focuses on the correlation of displacements with the variations in air temperature, while Section 6.4.4 focuses on the correlation of dis-

placements with the variation of the water level of the Po River measured in proximity to the bridge. They also investigate whether it is possible to identify different bridge spans based on the opposite longitudinal deformation of the bridge cantilevers in the floodplain and the effect of water level variation on the response of the bridge piers in the riverbed.

6.4.1 Structural Interpretation of PS Deformation Velocity

Using the MT-InSAR technique, we identified 8426 PSs on the bridge and in its surrounding area, and we extracted the time series of displacements along the LoS over eight years, from 2014 to 2021. Figure 6.10 shows the PSs' distribution in the case-study area, illustrated in a colour scale representing their displacement velocity along the satellite LoS. The velocity ranges from –13.21 mm/year (away from the satellite, in red) to 3.59 mm/year (toward the satellite, in blue). The velocity of PSs has been calculated during the MT-InSAR data processing by fitting a linear function over the entire time series of displacement through the least-square analysis. The standard deviations of the estimated velocity range between 0.21 and 0.56 mm/year, depending on the considered PS.

Figure 6.10: Distribution of the PSs identified in the case-study area illustrated in a colour scale representing their displacement velocity along the satellite LoS.

The PSs are mainly concentrated along the highway, within urban centres, and along local roads. As expected, the PSs are absent along

the river and cultivated fields, except for four aligned PSs in the upper left corner, corresponding to high-voltage power line towers. Most PSs are coloured in green, indicating nearly negligible deformation velocity ranging between –1.5 and +1.5 mm/year. The road accessing the bridge from the south exhibits red and orange PSs, as does the road adjacent to the southern embankment of the river. The bridge is primarily covered by green PSs, with a small yellow portion—meaning deformation velocity between –3 and –1.5 mm/year—near Piers 10 and 11. These results suggest that the bridge experiences nearly negligible deformation velocity throughout its span, except for the portion that underwent significant erosion at the base of the piers and was retrofitted with backfill soil in 2012, as indicated by the yellow colour of PSs. This result may suggest the resumption of erosion phenomena at the base of the piers, which may have eroded the backfill soil after 2012.

It is important to note that the deformation measurements obtained using the MT-InSAR technique from SAR satellite images are along the satellite LoS, i.e., from the sky to the ground and from right to left in this image. Negative values indicate displacements away from the satellite; therefore, negative velocities may result from a combination of downward and westward displacements.

We focus on the deformation velocities ranging from 0.5 to –2.5 mm/year to investigate the bridge displacements further; this allows for a better graphical representation—with greater details—of the PS displacements extracted along the bridge's LoS. Figure 6.11a shows the PSs on the bridge in a colour scale representing velocity with small ranges; Figure 6.11b shows the same PSs in a colour scale representing temporal coherence; as we can see, the temporal coherence of these PSs is mostly higher than 0.7, confirming the results' quality.

Let us focus on Figure 6.11a. In the portion of the bridge over the floodplain, the deformation velocities are mainly between –0.5 and –1 mm/year. Conversely, in the portion of the bridge over the riverbed, the deformation velocities are close to 0 mm/year towards the north bank of the river and exceed –2 mm/year near Piers 10 and 11. The velocities return to approximately –0.5 mm/year after leaving the river's south bank. This result confirms the nearly negligible deformation velocity along most of the bridge but close to Piers 10 and 11.

6.4.2 Structural Interpretation of PS Deformation Periodicity

Besides studying the deformation velocities of the different bridge sections and the surrounding territory, we are interested in investigating the periodicity of the observed displacements because we expect their cor-

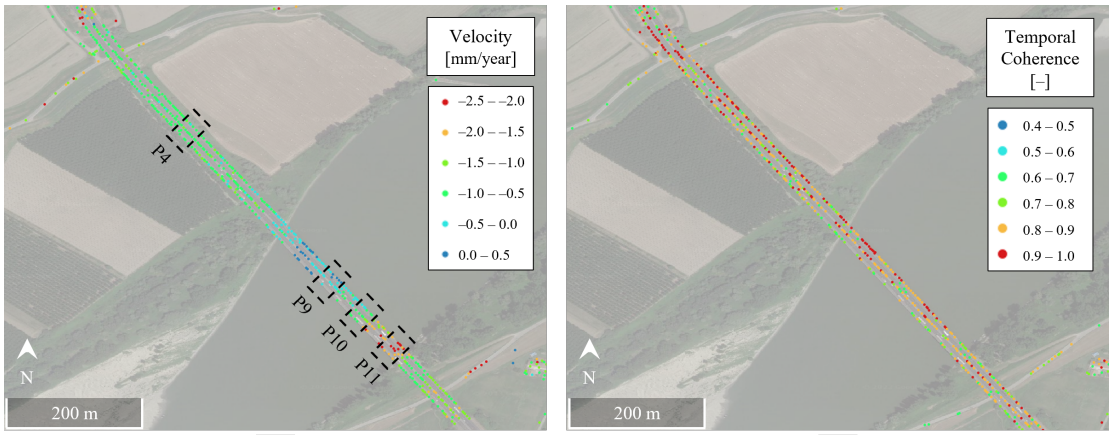

Figure 6.11: (a) Velocity along the LoS and (b) temporal coherence of the PSs identified on the A22 Po River Bridge.

relation with the seasonal air temperature variations in that area. For this purpose, in Figure 6.12 and Figure 6.13, we isolated the displacement time series of some PSs of particular interest to observe and discuss them. All the selected PSs have temporal coherence higher than 0.8.

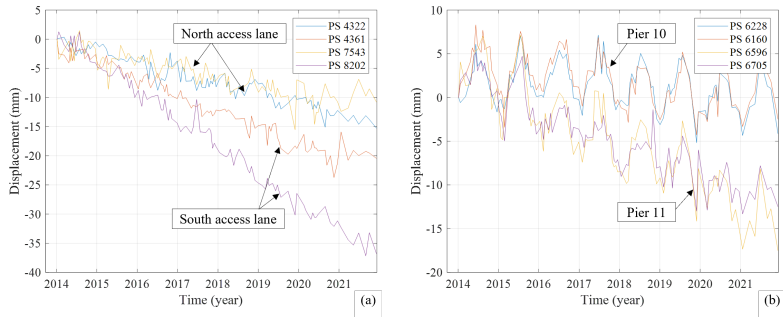

Figure 6.12: Displacement time series of PSs located on (a) the access lane to the north (PS 4322, PS 4361) and south (PS 77542, PS 8202) of the bridge; (b) the top of Pier 10 (PS 6228, PS 6160) and Pier 11 (PS 6596, PS 6705).

Let us begin with the PSs located on the access lane north and south of the viaduct, whose displacement time series are shown in Figure 6.12. We can observe that the displacement time series of a PS on the southern access lane (PS 8202) is characterised by a deformation velocity exceeding –5 mm/year along the LoS and limited seasonal periodicity. The limited periodicity aligns with the expectation since this access lane has

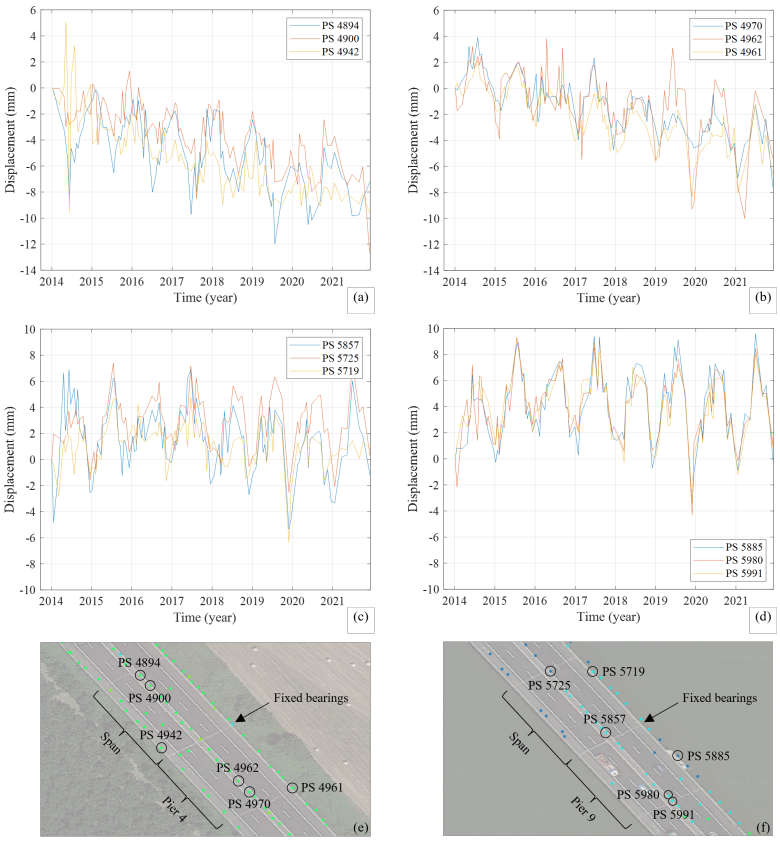

Figure 6.13: Displacements of (a) the north cantilever and (b) the south cantilever of Pier 4 in the floodplain; displacements of (c) the north cantilever and (d) the south cantilever of Pier 9 in the riverbed; (e) location of PSs on Pier 4, and (f) location of PSs on Pier 9.

been constructed with embankment soil, which is not expected to exhibit significant displacements in response to temperature variations. In contrast, the high velocity suggests abnormal displacements of the access lane. The infrastructure operator has recently detected such abnormal displacements and is already addressing this issue. A similar behaviour is observed on the northern access lane, where the periodicity is almost absent, and the deformation velocity is around –2 mm/year, indicating a less pronounced effect than the southern access lane, consistent with the results shown in Figure 6.10.

Next, we examine the displacement time series of some PSs identified along the bridge. Figure 12b illustrates the displacements of the top of Piers 10 and 11, represented by yellow PSs in Figure 10. It is

evident that the behaviour is similar for both PSs: a noticeable negative displacement trend along the LoS of approximately –2 mm/year-even though more pronounced in the PSs located at the top of Pier 11–and a more visible periodicity compared to the PSs on the access lanes.

The greater periodicity was expected since these are displacements of reinforced concrete piers with a theoretical thermal expansion coefficient of around $\alpha = 15 \cdot 10^{-6}\ ^{\circ}\mathrm{C}^{-1}$. We can estimate the actual thermal expansion coefficient α based on the observed displacements and the measured temperatures. That would allow us to qualitatively verify whether the displacements obtained through MT-InSAR applied to our dataset are consistent with the expected displacements for a structure of this type. To do this, we perform the following procedure, whose results are reported in Table 6.2:

Table 6.2: Mean value (μ) and standard deviation (σ) of the model parameters fitting PS deformation time series estimated through LSA, including deformation trend v—both in $\mu\epsilon/year$ and $mm/year$—and the thermal deformation coefficient α. $1\ \mu\epsilon = 1\ \mu m/m$

PS	Pier	$\epsilon_0\ [\mu\epsilon]$		$v\ [\mu\epsilon/Year]$		$v\ [mm/Year]$		$\alpha\ [\mu\epsilon/^{\circ}C]$	
		μ	σ	μ	σ	μ	σ	μ	σ
6228	10	23.32	15.60	−25.56	3.236	−0.3840	0.0485	19.22	0.790
6160	10	156.3	20.70	−48.76	4.293	−0.7315	0.0644	18.93	1.050
6705	11	78.06	22.91	−182.2	4.751	−2.7334	0.0713	22.54	1.162
6831	11	65.14	23.58	−150.5	4.891	−2.2583	0.0734	13.09	1.196

(1) Assume that the piers' displacements in response to thermal variations are mainly vertical;

(2) Project the observed displacements along the LoS (d_{LoS}) onto the vertical direction (d_V) according to Equation 6.1, knowing the incidence angle $\theta = 33.9449^{\circ}$:

$$d_V = d_{\mathrm{LoS}}/cos\theta \tag{6.1}$$

(3) Divide the vertical displacements by the height of the piers and the girders (approximately 15 m above the river surface) to obtain the time series of vertical deformation ϵ of Piers 10 and 11;

(4) Fit the time series of vertical displacement with Least Square Analysis (LSA) and a linear model that takes as inputs deformations ϵ, temperatures T, and the time t at which the measurements were taken and estimates a purely geometric offset ϵ_0, the deformation trend v, and the thermal deformation coefficient α. The model is described in Equation 6.2:

$$\epsilon = \epsilon_0 + v \cdot t + \alpha \cdot T \tag{6.2}$$

The velocities—v [mm/year]—are consistent with those obtained directly from the MT-InSAR analysis (see Figure 6.12b), and the thermal expansion coefficients α are consistent with those expected for prestressed concrete bridges. These results allow us to conclude that the magnitude of the periodic displacements observed through this technique is consistent with the expected temperature response for this bridge.

Now, let us focus on the part of the bridge characterised by green PSs in Figure 6.10 and Figure 6.11, indicating deformation velocities between -1.5 and 1.5 mm/year. Figure 6.13a,b show the displacements of the north and south cantilevers of Pier 4 in the floodplain, while Figure 6.13c,d show the displacements of the north and south cantilevers of Pier 9 in the riverbed. We can observe that all displacement time series exhibit a significant periodicity with an annual period, consistent with the periodicity of temperature variations. However, there is an opposite sign in the displacement variation between the PSs in opposite cantilevers of Pier 4: when the northern cantilever displacements increase, the southern cantilever displacements decrease, and vice versa. Regarding the observed displacements of the cantilever of the riverbed Pier 9, periodicity is present but less pronounced on the northern side than on the southern side. However, unlike Pier 4, where a deflection trend is clearly visible, displacements of Pier 9 seem to be affected by other phenomena in addition to temperature variation. We will discuss this in Section 6.4.4.

6.4.3 Correlation between Displacements and Temperature Variations

We start the correlation analysis by studying the linear correlation between PS displacements and temperature variations. First, we decimate the temperature dataset to one measurement per day for the days corresponding to the satellite passage over the case study area.

Figure 6.14 illustrates the map of identified PSs on the bridge, represented in a colour scale corresponding to the Pearson correlation coefficient resulting from comparing displacements time series of each PS and temperatures. In Figure 6.14a, we can immediately observe a clear difference in correlation values between the floodplain and the riverbed portions. Specifically, a positive correlation ranging from 1 to 0.7 is observed in the riverbed portion between Piers 8 and 11, while a positive but lower correlation–below 0.5–is seen between Pier 11 and the southern bank of the river. In contrast, in the floodplain portion, there is a periodic variation in the colours of the PSs, ranging from transverse groups of yellow–orange–red PSs (with a negative correlation between -1 and

-0.3) to transverse groups of green PSs (with a correlation between -0.3 and 0.1), and finally to transverse groups of blue PSs (with a correlation between 0.1 and 0.5), followed by another yellow–red PS groups (where the correlation drops down to -1 again). Figure 6.14b shows a zoom on the floodplain portion of the bridge where magenta arrows highlight the yellow–red coloured PS groups.

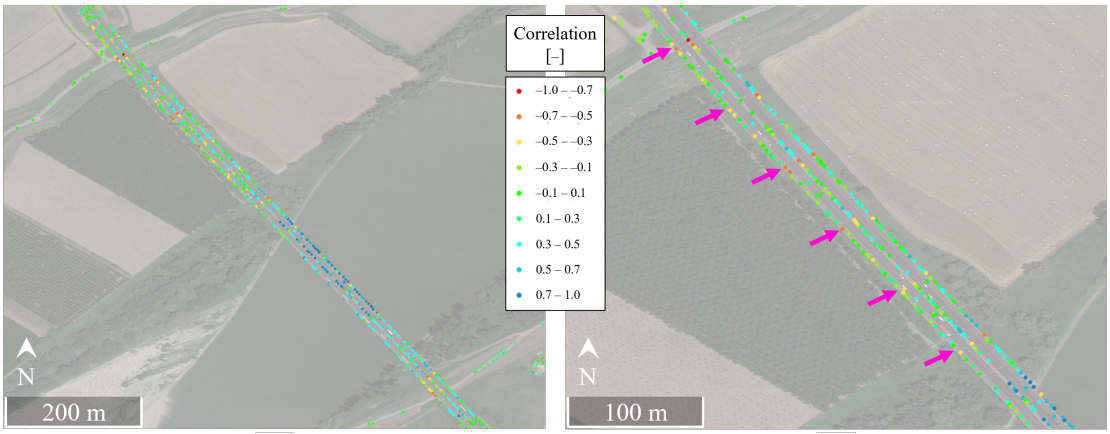

Figure 6.14: Linear correlation between air temperature variation and displacement time series of PSs identified on (a) the A22 Po River Bridge and (b) the portion of the bridge in the floodplain. Magenta arrows highlight the yellow–red coloured PS groups.

These differences in the linear correlation are also clearly visible in 6.15, which shows the scatterplot of the variables Displacements (d_{LoS}) and Temperature with the least-squares reference line—the slope of which is equal to the displayed correlation coefficient ρ—for some PSs whose displacement time series have been reported in Figure 6.13. In the riverbed, the displacements of the PSs located over the Pier 9 exhibit a positive correlation ranging from 0.7 to 0.9. In the floodplain, the displacements of the PSs located over the north cantilever of Pier 4 exhibit a negative correlation, while those located over its south cantilever exhibit a positive correlation.

This periodic variation of the linear correlation along the bridge is clearly visible in Figure 6.16, where this parameter is reported for the three lines of PSs highlighted in the figure plotted against the length of the bridge. Figure 6.16 also shows the longitudinal section of the bridge on the same scale as the PS map and the graph. Marking the negative peaks of the correlation (see the black dashed lines in Figure 6.16), we can notice that they correspond to the right (northern) joint of the suspended span—the one with monodirectional and multidirectional

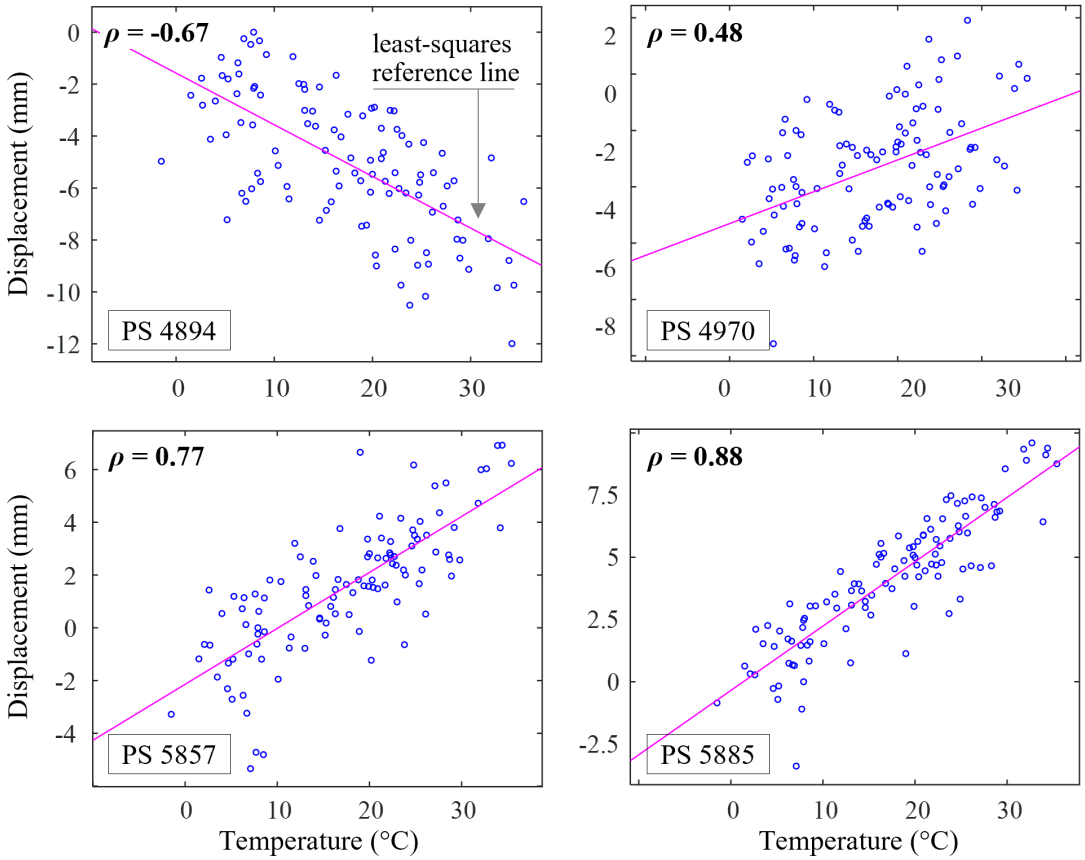

Figure 6.15: Scatterplots of the variables Displacements (d_{LoS}) and Temperature with the least-squares reference line (magenta line) and correlation coefficient (ρ) for PS 4894, PS 4970, PS 5857, PS 5885.

bearing (thus, roller supports).

To confirm the periodicity in the correlation variation along the bridge length observed in Figure 6.14 and Figure 6.16, we fitted the three PS lines highlighted in Figure 6.16 with the sine function $A \cdot \sin(\omega \cdot x + \phi)$, where A, ω, and ϕ are free parameters, and x is the longitudinal coordinate along the bridge. The estimated parameters are reported in Table 6.3, along with the estimated periodicity $T = 2\pi/\omega$. The estimated periodicity results between 72.72 m and 73.15 m, almost equal to the spacing of the spans (72.80 m, see 6.3), and thus the distance between two consecutive roller supports.

This result is in line with the expected longitudinal response of the bridge deck to temperature variation: the longitudinal displacements are zero over the piers and increase along the cantilevers until the joints as we

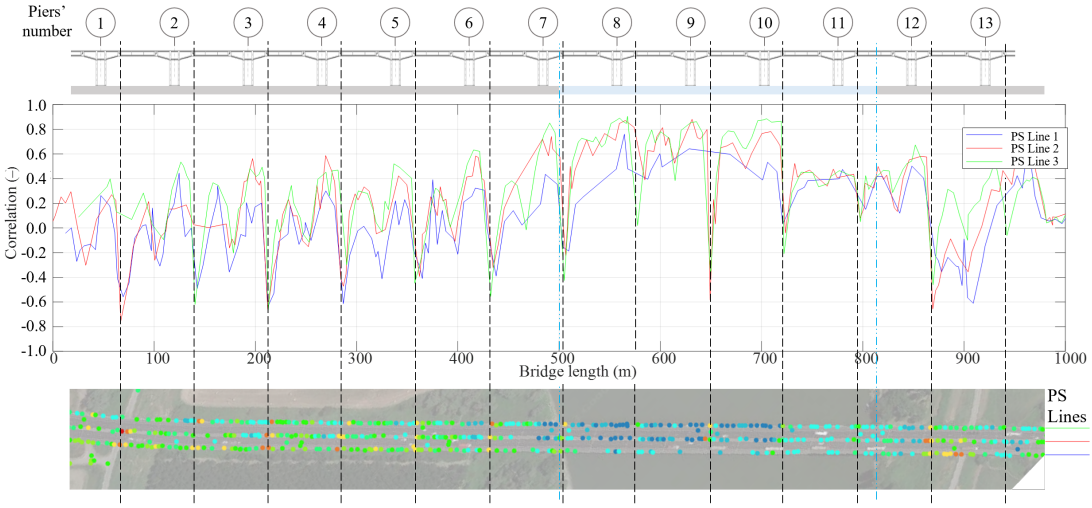

Figure 6.16: Linear correlation between PS displacement time series and temperature variation plotted against the length of the bridge. PSs are divided into three lines.

Table 6.3: Parameters A, ω, ϕ estimated by fitting the sine function $A \cdot sin(\omega \cdot x + \phi)$ to the correlation variation along the PS lines highlighted in Figure 6.16; x is the longitudinal coordinate along the bridge; T is the estimated period $T = 2\pi/\omega$.

PS Line	A **[-]**	ω **[1/m]**	ϕ **[-]**	T **[m]**
PS Line 1	0.385	0.0859	30.2	73.15
PS Line 2	0.435	0.0862	30.2	72.89
PS Line 3	0.476	0.0864	30.2	72.72

move away from the piers; the suspended spans move longitudinally in the direction of the cantilever which supports it with fixed bearings. The possibility of noticing it with such clarity from satellite measurements is quite sensational.

Let us discuss more in-depth why we can observe such periodic correlation. As shown in Figure 6.17a, the correlation is negative in the northern portion of the pier as the longitudinal displacements have an opposite sign to the temperature variation. Conversely, the correlation is positive in the southern portion of the pier as displacements and temperature variations share the same sign. Figure 6.17b illustrates this result with the correlations obtained for the A22 Po River Bridge. This result allows us to conclude that, for the A22 Po River Bridge, the horizontal longitudinal displacements in response to temperature variation can be clearly observed with satellite InSAR-based SHM. Moreover, and most

importantly, it is possible to identify different spans of the bridge simply by studying the sign of the correlation between displacement and temperature variation and its periodicity along the length of the bridge. This finding is quite important in view of using this type of monitoring to detect anomalous bridge behaviour on a large scale automatically.

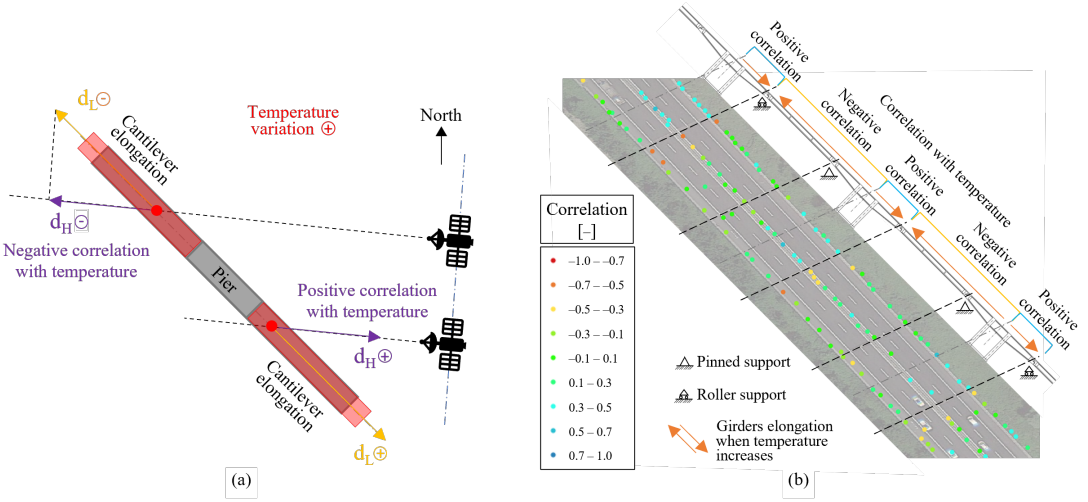

Figure 6.17: (a) Scheme explaining the negative and positive sign of the horizontal longitudinal displacements of the cantilevers obtained from satellite measurements as temperature increases; (b) application to the A22 Po River Bridge, highlighting the portions with a positive and a negative correlation between displacements time series and temperature variation.

Regarding displacements in the riverbed, a certain periodicity in the colours of the PSs is maintained, suggesting that the observations made for the floodplain portion can be extended, even though in a purely qualitative manner, to the riverbed portion.

6.4.4 Correlation between Displacements and Water Level Variations

We proceed with the correlation analysis by studying the correlation between PS displacements and water level variations of the Po River. First, we decimate the water level dataset to one measurement per day for the days corresponding to the satellite passage over the case study area.

Figure 6.18a illustrates the map of the identified PS on the bridge, represented in a colour scale corresponding to the Pearson correlation coefficient resulting from comparing displacements and water level for each PS. Figure 6.18b shows a zoom on the riverbed portion of the bridge.

As in Figure 6.14a, we can observe in Figure 6.18a a clear differ-

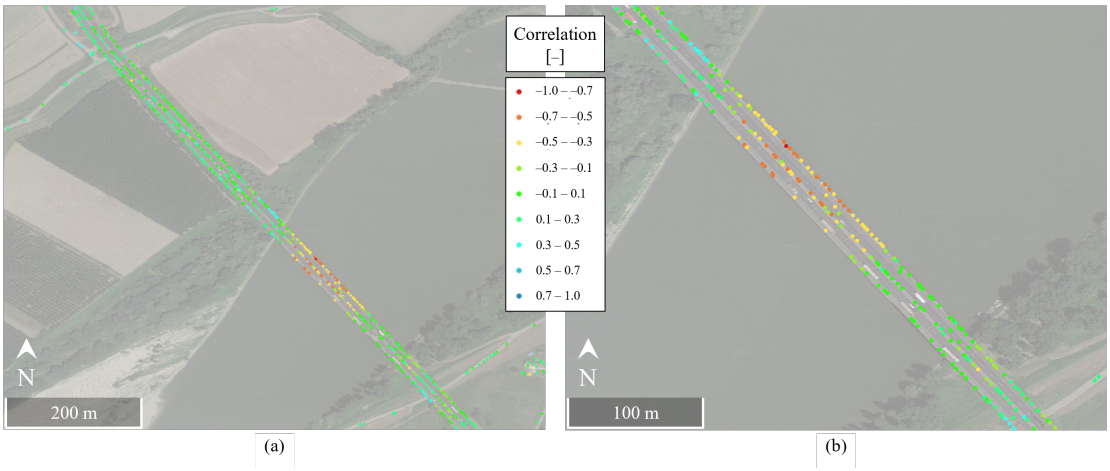

Figure 6.18: Linear correlation between water level variation of the Po River and displacement time series of PSs identified on (a) the A22 Po River Bridge and (b) the portion of the bridge in the riverbed.

ence in the correlation values between the floodplain and the riverbed portions. Specifically, we notice that the Pearson coefficient of most PSs in the floodplain portion of the bridge is almost zero, while it is negative and between -0.5 and -1 for the PSs over the riverbed portion. This difference in correlation along the bridge is also clearly visible in Figure 6.19, where this parameter is reported for the three lines of PSs highlighted in the figure plotted against the length of the bridge.

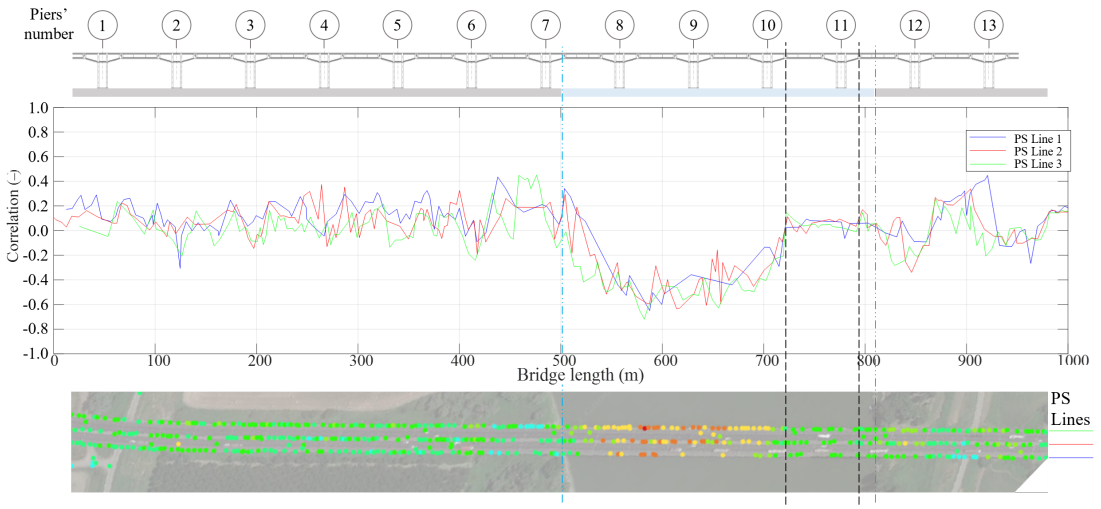

Figure 6.19: Linear correlation between PS displacement time series and water level variation plotted against the length of the bridge. PSs are divided into three lines.

The displacement periodicity of the PSs in the floodplain does not seem correlated with the seasonal water level changes. In contrast, the displacement periodicity of the PSs in the riverbed does, with downward-westward displacements occurring when the water level rises–the Po River flows from West to East. Since the soil is highly heterogeneous, these displacements may be related to ground deformations associated with seepage through soils of different permeabilities. However, further geotechnical investigations should be carried out to evaluate the pore water pressure distribution and the physical properties of the soil both below the river and in the surrounding area.

Note that the displacements of the PSs located over Pier 11 show a lower correlation with water level variation than those of PSs on other piers in the riverbed. That is probably due to the peculiar characteristics of Pier 11: greater height above the ground level, scour effects and relative maintenance works, and higher long-term displacement trend.

Similar results on the negative correlation between the PS displacements of a bridge crossing the Po River and the Po River water level were obtained and discussed by [32], who monitored through satellite InSAR three bridges not far away from our case-study area: the San Benedetto Po Road Bridge, and both the road bridge and railway bridge connecting the villages of Ostiglia and Revere. These authors observed an inverse correlation between the displacements of the PSs identified on the bridges and the water level of the Po River. They analysed SAR images acquired in C-band by the satellite constellation Sentinel 1 from 2018 to 2020 in ascending and descending geometries. They performed the MT-InSAR analysis through the open-access software SNAP&StaMPS to extract PS displacement time series. The authors concluded that the displacements were mainly vertical and seemed correlated with the seasonal changes in the water level of the Po River, with downward displacements occurring when the river rises. They added that, since those bridges lie on deep foundation piles (as the Po River Bridge), this correlation is likely not a symptom of scour phenomena.

Similar results have also been obtained in [12], in which the authors studied the anomalous deformations and the subsequent collapse in 2015 of the Tadcaster Bridge (UK). In that case study, the authors analysed a dataset of SAR images acquired from March 2014 to December 2015 in the X-band by the satellite constellation TerraSAR-X in ascending geometry. They performed the Small BAseline Subset (SBAS) technique through the software SARscape to extract displacement time series. The authors highlighted a distinct movement in the bridge portion where the collapse occurred before the event. Those movements strongly correlated to the changing water level of the Wharfe River. However, unlike

the bridges crossing the Po River, the Tadcaster Bridge lies on shallow foundations; indeed, the collapse occurred due to scour by eroding the soil at the base of the fifth pier of the bridge.

These results highlight the importance of considering environmental factors and the geotechnical characteristics of the foundation soils in bridge monitoring. Indeed, understanding the behaviour of the underlying foundation soil under fluctuations in river water levels would be crucial for accurately interpreting the structure's displacements above the ground measured by terrestrial and satellite technologies. However, this is a challenging task due to the frequent absence of persistent on-site monitoring of the movements of the foundation soil or the displacements of the piers in the riverbed. For this reason, studying the movements of the territory around the bridge by looking at the displacements of the PSs identified in the entire case-study area can give a first idea of the problems like subsidence, differential displacements, and landslides affecting the bridge.

Finally, it is important to point out that the correlation between PS displacements and temperature expresses a correlation between the response of a man-made structure and an environmental load (i.e., the temperature variation), while the correlation between PS displacements and water level expresses a possible correlation between the soil movement and an environmental load (i.e., the water level variation).

6.5 Conclusions

This paper presents an application of satellite InSAR technology for the remote monitoring of a prestressed concrete bridge–the A22 Po River Bridge in Italy–and the interpretation of results from a structural standpoint. Specifically, 109 Cosmo-SkyMed X-band SAR images covering eight years have been analysed through MT-InSAR, and the displacement time series of the PSs identified on the bridge have been (i) compared to the expected response of the bridge to temperature variation and (ii) correlated to environmental loads. All of that is to verify the effectiveness of satellite InSAR in providing reliable information on the structural behaviour of bridges and the possibility of identifying different responses in different bridge components (e.g., access lanes, piers, spans, fixed and roller bearings) and unexpected behaviour.

The MT-InSAR analysis identified 8426 PSs on the almost 1 km-long bridge, with deformation velocities along the LoS ranging from -2.5 to 0.5 mm/year, velocities' standard deviations between 0.21 and 0.56 mm/year, and temporal coherence higher than 0.7. Unexpected deformation velocities have been observed over the southern access lane,

an issue the infrastructure operator is already addressing, and over the Pier 11, which underwent significant erosion at its base in the past.

Focusing on the piers, we verified that the periodicity and magnitude of the displacements observed through satellite InSAR are consistent with this bridge's expected temperature response. Moving on to the cantilevers, we observed that their horizontal longitudinal displacements in response to temperature variation can be observed with satellite InSAR. Moreover, and most importantly, it is possible to identify different spans and piers of the bridge simply by studying the sign of the correlation between displacement and temperature variation and its periodicity along the bridge length. However, this result is strongly related to the bridge orientation. Further studies on different case studies are recommended to investigate the impact of bridge orientation on the effectiveness of satellite InSAR-based SHM performances. Finally, this study highlights the influence of river water level variations on piers displacements in the riverbed, emphasising the need to consider environmental factors and geotechnical characteristics of the foundation soils in bridge monitoring.

In conclusion, this study confirms the potential of satellite InSAR technology for the remote monitoring of road bridges and the surrounding territory without installing any sensor on site, which can foster an extensive remote SHM of civil infrastructure, potentially solve the high-cost issue of traditional contact-type sensors, and dramatically improve SHM-based bridge management. However, the performance of this remote monitoring technique should be further investigated through a direct comparison with measurements from traditional technologies.

Bibliography

[1] P. F. Giordano, L. J. Prendergast, and M. P. Limongelli, "Quantifying the value of shm information for bridges under flood-induced scour," *Structure and Infrastructure Engineering*, vol. 19, no. 11, pp. 1616–1632, 2023.

[2] A. Kamariotis, E. Chatzi, and D. Straub, "A framework for quantifying the value of vibration-based structural health monitoring," *Mechanical Systems and Signal Processing*, vol. 184, p. 109708, 2023.

[3] M. F. Bado and J. R. Casas, "A review of recent distributed optical fiber sensors applications for civil engineering structural health monitoring," *Sensors*, vol. 21, no. 5, p. 1818, 2021.

[4] F. Scozzese, L. Ragni, E. Tubaldi, and F. Gara, "Modal properties variation and collapse assessment of masonry arch bridges under scour action," *Engineering Structures*, vol. 199, p. 109665, 2019.

[5] L. Iannacone, P. Francesco Giordano, P. Gardoni, and M. Pina Limongelli, "Quantifying the value of information from inspecting and monitoring engineering systems subject to gradual and shock deterioration," *Structural health monitoring*, vol. 21, no. 1, pp. 72–89, 2022.

[6] P. F. Giordano, S. Quqa, and M. P. Limongelli, "The value of monitoring a structural health monitoring system," *Structural safety*, vol. 100, p. 102280, 2023.

[7] L. Nielsen, S. Tølbøll Glavind, J. Qin, and M. H. Faber, "Faith and fakes–dealing with critical information in decision analysis," *Civil Engineering and Environmental Systems*, vol. 36, no. 1, pp. 32–54, 2019.

[8] A. Ferretti, C. Prati, and F. Rocca, "Permanent scatterers in sar interferometry," *IEEE Transactions on geoscience and remote sensing*, vol. 39, no. 1, pp. 8–20, 2002.

[9] P. Berardino, G. Fornaro, R. Lanari, and E. Sansosti, "A new algorithm for surface deformation monitoring based on small baseline differential sar interferograms," *IEEE Transactions on geoscience and remote sensing*, vol. 40, no. 11, pp. 2375–2383, 2003.

[10] A. Ferretti, A. Fumagalli, F. Novali, C. Prati, F. Rocca, and A. Rucci, "A new algorithm for processing interferometric data-stacks: Squeesar," *IEEE transactions on geoscience and remote sensing*, vol. 49, no. 9, pp. 3460–3470, 2011.

[11] D. Perissin and T. Wang, "Repeat-pass sar interferometry with partially coherent targets," *IEEE Transactions on Geoscience and Remote Sensing*, vol. 50, no. 1, pp. 271–280, 2011.

[12] S. Selvakumaran, S. Plank, C. Geiß, C. Rossi, and C. Middleton, "Remote monitoring to predict bridge scour failure using interferometric synthetic aperture radar (insar) stacking techniques," *International journal of applied earth observation and geoinformation*, vol. 73, pp. 463–470, 2018.

[13] D. Cusson, C. Rossi, and I. F. Ozkan, "Early warning system for the detection of unexpected bridge displacements from radar satellite

data," *Journal of Civil Structural Health Monitoring*, vol. 11, no. 1, pp. 189–204, 2021.

[14] G. Della Ragione, A. Rocca, D. Perissin, and E. Bilotta, "Volume loss assessment with mt-insar during tunnel construction in the city of naples (italy)," *Remote Sensing*, vol. 15, no. 10, p. 2555, 2023.

[15] D. Perissin, "Interferometric sar multitemporal processing: Techniques and applications," in *Multitemporal Remote Sensing: Methods and Applications*, pp. 145–176, Springer, 2016.

[16] S. Bianchini, F. Pratesi, T. Nolesini, and N. Casagli, "Building deformation assessment by means of persistent scatterer interferometry analysis on a landslide-affected area: the volterra (italy) case study," *Remote sensing*, vol. 7, no. 4, pp. 4678–4701, 2015.

[17] V. Cerchiello, G. Tessari, E. Velterop, P. Riccardi, M. Defilippi, and P. Pasquali, "Building damage risk by modeling interferometric time series," *IEEE Geoscience and Remote Sensing Letters*, vol. 14, no. 4, pp. 509–513, 2017.

[18] D. Di Martire, R. Iglesias, D. Monells, G. Centolanza, S. Sica, M. Ramondini, L. Pagano, J. J. Mallorquí, and D. Calcaterra, "Comparison between differential sar interferometry and ground measurements data in the displacement monitoring of the earth-dam of conza della campania (italy)," *Remote sensing of environment*, vol. 148, pp. 58–69, 2014.

[19] P. Milillo, D. Perissin, J. T. Salzer, P. Lundgren, G. Lacava, G. Milillo, and C. Serio, "Monitoring dam structural health from space: Insights from novel insar techniques and multi-parametric modeling applied to the pertusillo dam basilicata, italy," *International journal of applied earth observation and geoinformation*, vol. 52, pp. 221–229, 2016.

[20] G. Barla, A. Tamburini, S. Del Conte, and C. Giannico, "Insar monitoring of tunnel induced ground movements," *Geomechanics and Tunnelling*, vol. 9, no. 1, pp. 15–22, 2016.

[21] L. Chang, R. P. Dollevoet, and R. F. Hanssen, "Nationwide railway monitoring using satellite sar interferometry," *IEEE Journal of Selected Topics in Applied Earth Observations and Remote Sensing*, vol. 10, no. 2, pp. 596–604, 2016.

[22] V. Macchiarulo, P. Milillo, C. Blenkinsopp, and G. Giardina, "Monitoring deformations of infrastructure networks: A fully automated gis integration and analysis of insar time-series," *Structural Health Monitoring*, vol. 21, no. 4, pp. 1849–1878, 2022.

[23] K. DePrekel, E. H. Bouali, and T. Oommen, "Monitoring the impact of groundwater pumping on infrastructure using geographic information system (gis) and persistent scatterer interferometry (psi)," *Infrastructures*, vol. 3, no. 4, p. 57, 2018.

[24] P. Milillo, G. Giardina, D. Perissin, G. Milillo, A. Coletta, and C. Terranova, "Pre-collapse space geodetic observations of critical infrastructure: The morandi bridge, genoa, italy," *Remote Sensing*, vol. 11, no. 12, p. 1403, 2019.

[25] E. Farneti, N. Cavalagli, M. Costantini, F. Trillo, F. Minati, I. Venanzi, and F. Ubertini, "A method for structural monitoring of multispan bridges using satellite insar data with uncertainty quantification and its pre-collapse application to the albiano-magra bridge in italy," *Structural Health Monitoring*, vol. 22, no. 1, pp. 353–371, 2023.

[26] Copernicus Land Monitoring Service, "European ground motion service." https://egms.land.copernicus.eu/. Accessed: 1 August 2023.

[27] H. Abdel-Jaber and B. Glisic, "Monitoring of long-term prestress losses in prestressed concrete structures using fiber optic sensors," *Structural Health Monitoring*, vol. 18, no. 1, pp. 254–269, 2019.

[28] D. Perissin, "Geometric processing: Active sensor modeling and calibration (sar)," 2018.

[29] K. Malik, D. Kumar, D. Perissin, and B. Pradhan, "Estimation of ground subsidence of new delhi, india using ps-insar technique and multi-sensor radar data," *Advances in Space Research*, vol. 69, no. 4, pp. 1863–1882, 2022.

[30] R. Ceravolo, G. Coletta, G. Miraglia, and F. Palma, "Statistical correlation between environmental time series and data from long-term monitoring of buildings," *Mechanical Systems and Signal Processing*, vol. 152, p. 107460, 2021.

[31] K. P. Murphy, *Machine learning: a probabilistic perspective*. MIT press, 2012.

[32] L. Sartorelli, "Use of sar satellite data in bridge structural health monitoring," 2019.

7. Bridge monitoring with satellite InSAR technology and clustering algorithm

This chapter contains the post-print of

> **Caspani, V.F.**, Tonelli, D., Bado, M.F., Rocca, A., Perissin, D., Zonta, D. (2025). Bridge monitoring with satellite InSAR technology and clustering algorithm. Measurement, 118939, https://doi.org/10.1016/j.measurement.2025.118939.

as published in the Journal *Measurement*, differing only from the published article in terms of layout, formatting, and notation.

Abstract

Satellite Interferometric Synthetic Aperture Radar (InSAR) technology offers a cost-effective, large-scale approach to Structural Health Monitoring (SHM). The Multi-Temporal InSAR (MT-InSAR) technique allows to detect millimetric displacements over time, providing a powerful tool for assessing the evolution of infrastructure deformation and deterioration. However, in order to extract meaningful structural information from the large amount of data generated by MT-InSAR, time-consuming analyses and careful interpretation by civil engineers are required. The present work fills this gap by presenting a clustering algorithm for the automated classification of Persistent Scatterers (PS) derived from Multi-Temporal InSAR (MT-InSAR) data, applied to the Structural Health Monitoring of bridges. Crucially, this low-input, speedy and accessible approach permits a rapid interpretation of MT-InSAR data and advances the integration of satellite information into Bridge Management System (BMS) and Decision Support System (DSS) frameworks. The proposed method accounts for both temporal and spatial domain of MT-InSAR data with a one-step analysis, enabling the identification of predominant PS time-series patterns and their association with physical entities within the study area. The algorithm was tested on two strategic bridges in Italy: the Po River Bridge and the Colle Isarco Viaduct, using COSMO-SkyMed (CSK) satellite data processed with the SarProZ® software. Results demonstrated: (i) the algorithm's ability to identify anomalies and distinct behaviours across various portions of the structures; (ii) the robustness and adaptability of the algorithm across different case studies, proving its potential for large-scale applications; and

(iii) the algorithm's effectiveness in identifying structurally relevant deformation patterns with minimal user input.

Keywords:
Structural Health Monitoring; satellite InSAR; Clustering algorithm; Persistent Scatterers; Bridge displacement.

Glossary

In this section, the authors provide a brief glossary of the notation involved in the present paper.

SHM	Structural Health Monitoring
BMS	Bridge Management System
DSS	Decision Support System
MRR	Maintenance, Repair, and Rehabilitation
GNSS	Global Navigation Satellite System
DOFS	Distributed Optical Fiber Sensors
MEMS	Micro Electro-Mechanical Systems
SAR	Synthetic Aperture Radar
InSAR	Interferometric SAR
MT-InSAR	Multi-Temporal InSAR
PCA	Principal Component Analysis
FE	Finite Element
PS	Persistent Scatterer
DBSCAN	Density-based spatial clustering of applications with noise
CSK	COSMO Sky-Med
LoS	Line of Sight
SRTM90	Shuttle Radar Topography Mission Digital Elevation Model
DEM	
WGS84	World Geodetic System 1984
GCP	Ground Control Point
LSA	Least Square Analysis
WCE	Within-Cluster Error
α	1st metric coefficient
β	2nd metric coefficient
K	Number of clusters
ρ	Pearson linear correlation coefficient
RP	Reference Point
LoS	Line of Sight
θ	incidence angle

β	heading angle
d_{LoS}	displacements along the LoS
d_H	horizontal displacements
d_V	vertical displacements
d_L	longitudinal displacements
$d_{\text{V,LoS}}$	LoS projection of vertical displacements
$d_{\text{L,LoS}}$	LoS projection of longitudinal displacements
$d_{\text{TOT,LoS}}$	LoS projection of combined displacements
ζ	bridge orientation
$\gamma = \zeta - \beta$	bridge's longitudinal axis - LoS horizontal projection angle

7.1 Introduction

Structural Health Monitoring (SHM) has increasingly demonstrated its value in accurately and timely assessing the condition of bridges, significantly enhancing the ability of infrastructure managers to optimise Maintenance, Repair, and Rehabilitation (MRR) strategies and effectively allocate resources [1, 2]. Utilising different technologies – such as DOFS [3], MEMS-based accelerometers [4], and GNSS receivers [5, 6] – which are permanently installed on bridges, SHM systems continuously gather real-time, precise, and objective data, enriching infrastructure operators' understanding of how bridges react to traffic, environmental stresses, aging and other load types or phenomena [7]. Despite their advantages, the economic and environmental sustainability of on-site permanently installed devices has been questioned due to issues of scalability, adaptability, and reliability. The cost for extensive instrumentation can range significantly, limiting SHM application to strategically important bridges [8]. Furthermore, once installed, these systems offer little flexibility for reuse on other structures, and their reliability can be compromised during extreme events when critical data is most needed [9].

In response to these limitations, the recent years have seen a surge in the exploration of device-free remote sensing techniques, such as Interferometric Synthetic Aperture Radar (InSAR) and Multi Temporal InSAR (MT-InSAR). This innovative technology utilises SAR sensors aboard satellites to produce high-resolution, weather-independent images of the Earth's surface, enabling the detection of millimetric displacements over time without the need for on-site instrumentation [10]. InSAR has emerged as a powerful tool for monitoring subsidence, uplifting, and landslides on a large scale. Among recent research contributions, Yu et al. [11] applied MT-InSAR combined with principal component analysis (PCA) to analyse long-term surface deformations in the

Liaohe oilfield. Ghaderpour et al. [12, 13] used InSAR time-series to monitor slow-moving landslides in Central Italy and to investigate the impact of river flow and climate variations on ground deformation in an industrial area of the Sacco River Valley. In recent years, the research community has also started to investigate the possibility of using InSAR technology for monitoring the response of civil infrastructure. Selvakumaran et al. [14] combined InSAR with traditional instrumentation, including total stations and sensors installed on the bridge, for the monitoring of Waterloo Bridge. Guzman-Acevedo et al. [15] proposed a risk assessment methodology that combines InSAR time-series with a calibrated Finite Element (FE) model, demonstrating its application on the El Carrizo Bridge. Lorenz et al. [16] tested the applicability of InSAR for monitoring thermal deformations of a highway bridge by comparing it to geodetic measurements and advanced structural simulations. Quqa et al. [17] developed a regional-scale methodology to detect anomalies across multiple bridges using InSAR displacements and environmental data.

Specifically, the MT-InSAR technique involves analysing a series of radar images of the same area taken over a time-span and comparing their phase differences [18]. MT-InSAR provides coordinates and displacement time-series of Persistent Scatterers (PS), which are specific objects (e.g., rocks, buildings, road guardrails) that consistently reflect the radar signal over time. When applied to infrastructure monitoring, MT-InSAR enables the identification of PS on the structure of interest as well as within the surrounding area captured in the satellite image frame. Their number can potentially be quite high (thousands of PS) depending on the size and quality of the SAR dataset imagery. The higher their number, the denser is the information on the deformation field of the area of interest. Indeed, structural displacements may be influenced by geological and environmental context, connections to other structures, and ground conditions [19]. However, the higher their number, the longer the time required by the data analyst to discriminate PS located on the structure to be monitored, analyse and compare their displacement time-series with those of the surrounding PS.

Despite the growing number of studies focusing on the interpretation of satellite-based deformation data in relation to structural and civil engineering applications, a clear research gap remains i.e., the development of automated methods that reduce the user effort to extract and interpret information from large MT-InSAR datasets. To overcome this limitation in the use of MT-InSAR for SHM, this study develops a clustering algorithm for the automated classification of PS, thus facilitating their physical interpretation and the extraction of useful information on the

structural behaviour.

In particular, such automated approach aims to simplify and speed up the process of identifying predominant temporal evolution patterns within the dataset, and associating them with physical structural components and entities in the study area. This enables a quick assessment of whether the identified patterns of displacements on the examined structure and surroundings align with expected behaviours or reveal any behaviour anomalies, thus sparing the need to individually check each PS. The proposed algorithm is applicable to various case studies and structures, encompassing different geometries, types, spatial orientations, and geographical context of the monitored structure. It demands minimal effort from the users for setting and calibration, and supports nearly immediate comprehension of crucial information extracted from processed MT-InSAR data. In such a way, the proposed algorithm will be easily exploitable by structural engineers with basic level notions about both MT-InSAR processing and data-driven clustering algorithms, enabling its utilisation by infrastructure operators within their Bridge Management Systems (BMS). Indeed, efficiently and rapidly extracting meaningful insights from interferometric analysis outputs is essential for its use in infrastructure management as an early warning and decision support system (DSS) [20, 21].

This article is organised as follows. Section 7.2 describes the proposed PS clustering method based on the information provided by MT-InSAR processed data, i.e. the displacement time-series and geographic coordinates of PS. Section 7.3 and 7.4 concern, respectively, the Po River Bridge case study and the Colle Isarco Viaduct case study. The clustering algorithm is tested on these two case studies presenting different features in terms of structural scheme, orientation, and geographical context. The obtained results are reported and discussed. Section 7.5 includes a discussion on the uncertainties involved, as well as the limitations and future developments of this research. Conclusions are eventually drawn in Section 7.6.

7.2 Methodology: Clustering algorithm for the interpretation of MT-InSAR data for structural health monitoring purpose

Data-driven algorithms are often used to perform analysis to discover patterns, information, trends and correlation in data. They are particularly useful methods when dealing with large number of data, like in the case of PS extracted from MT-InSAR data processing [22]. For instance, they can help answer questions like “is there an informative way to visu-

alize the data?", "can we discover subgroups among such observations?". Clustering is the process of grouping similar objects together and includes a broad class of methods for discovering unknown subgroups in data [23, 24]. Similarity between data points is measured with a distance metric that can vary across different approaches, the most common being squared Euclidean distance [25].

Several renowned clustering algorithms are widely employed in various fields [26]. For instance, clustering is employed in customer segmentation within marketing and retail industries [27]. In computer vision, it is used for image segmentation and processing, finding application in medical imaging and satellite image analysis [28]. In data mining, it is used for identifying patterns and segmenting large datasets into clusters based on shared characteristics [29]. It is employed for spatial data analysis in geography and urban planning, enabling tasks like crime mapping or resource allocation optimization [30]. It is applied to atmospheric science data, in particular climate and meteorological data [31]. Time-series clustering has also been widely explored with numerous applications [32].

Very recently, the research community has started to investigate the application of machine learning and clustering to InSAR time-series of displacements. Khalili et al. employed K-Medians to prepare mean deformation rate maps for landslide monitoring [33]. Roque et al. used a hierarchical clustering approach to analyse vertical and horizontal displacement time-series of PS for structure monitoring [34]. Mirmazloumi et al. proposed a supervised approach to divide time-series of displacements into 5 different deformation trend models [35]. Other authors applied K-Means approach with Euclidean distance metric for clustering time-series of PS [36, 37].

However, few authors have explored clustering algorithms that incorporate both the spatial and temporal domains of MT-InSAR data, proposing multiple steps analyses in order to account for different data types [38, 39]. This type of approach can be challenging, especially when applied to bridge monitoring and BMS, where simplicity, rapid implementation, and ease of interpretation by civil engineers are essential. Specifically, each PS carries two distinct types of information: (i) displacement time-series over the observation period, with acquisition timestamps corresponding to the satellite passes over the examined area during that time; and (ii) the geographic coordinates of the target point identified by the satellite sensor within the examined area. In our approach to PS clustering for bridge monitoring, we aim to integrate both the temporal patterns and spatial proximity of PS, leveraging all the information provided by each PS. We explain the rationale behind this choice in greater

detail.

Analysing temporal patterns enables us to identify variations, periodicities, and anomalies in the movements of PS over time. This information is valuable for understanding phenomena such as subsidence, settlements, temperature effects or other variations that may affect the structural behaviour over time. Indeed, our primary objective is to cluster PS based on their temporal movement patterns. At the same time, considering the spatial proximity of points exhibiting similar behaviour is also crucial, and should serve as an additional layer of information integrated into the clustering algorithm. This ensures that PS with similar behaviour and close spatial proximity are unequivocally grouped within the same cluster. Indeed, those points are likely to belong to the same physical entity on the ground, sharing membership in connected geological or anthropic structures, which are targets of the satellite acquisition. Conversely, PS with similar behaviours but significant spatial separation are likely assigned to different clusters, reflecting associations with distinct structures or elements within the area. The PS identified by MT-InSAR analysis, which are close in proximity and exhibit sufficiently similar temporal behaviour, likely represent the same physical entity. Therefore, neglecting this aspect omits a fundamental information for engineers seeking to employ satellite data for bridge monitoring, namely, the connection to reality. These PS are not purely 'virtual'; rather, they are reflective features on the Earth's surface, specifically on the structures under investigation.

However, in practical implementation, what type of clustering algorithm can we employ to achieve this goal? Moreover, can our method maintain computational efficiency, versatility, and user-friendliness, making it applicable in a BMS framework?

Fuzzy C-Means (FCM) clustering algorithm has demonstrated promising results in various data classification tasks [40, 41]. The current literature on data-driven clustering also offers specialized algorithms tailored to different data types; for example, K-Shape is designed for time-series data clustering, while DBSCAN is particularly effective for spatially georeferenced data [42, 43]. While these and various other clustering algorithms are available, we opt for the widely-used and versatile K-Means algorithm for several reasons.

First, the K-means algorithm may be a suitable choice for our primary objective of clustering PS based on their temporal evolution trends due to the characteristics of InSAR time-series data. SAR data is sampled at low frequency (for example, the Italian mission CSK satellite revisit time is 16 days approximately), preventing noticeability of hourly or daily delays between the behaviours of different PS (e.g. shifts due to

thermal inertia, commonly observed in structural response), and preventing the possibility to observe trends and patterns confined to a short time frame. In this scenario, we are primarily interested in clustering time-series data to identify patterns related to long-term phenomena (e.g. seasonal temperature variations, ground or structural subsidence), that can be captured effectively by centroid-based clustering. Moreover, due to MT-InSAR pre-processing requirements, PS time-series are necessarily aligned, having the same length and the same acquisition dates. Due to these features, in our case, the choice of a specific and sophisticated but more complicated time-series clustering algorithm is not convenient.

Second, K-Means algorithm computational efficiency, flexibility and adaptability to different data types (both spatial and temporal data), makes it a good option for clustering PS considering both their coordinates and displacement time-series data in a one-step analysis, keeping the process fast and straightforward even as the number of data points and clusters increases.

K-Means partitions data samples into clusters by minimizing the metric of distance between the data samples and cluster centroids. The steps involved in K-Means clustering are the following:

(1) Set a number of desired clusters K.

(2) Set initial values of the K cluster centroids randomly.

(3) Evaluate the distance between each data point and the cluster centroids.

(4) Assign data points to the nearest cluster k.

(5) Calculate the new cluster centroids as the mean of the data points assigned to each cluster.

(6) Repeat the steps 3–5 with the new cluster centroids as initial values. Convergence is reached when no point changes its cluster assignment or until the centroids no longer move.

To address the specific requirements of our study – capturing both temporal and spatial information of PS – in a one-step analysis, we developed a customised metric to be used within the K-Means algorithm instead of the Euclidean distance. Our metric is tailored to account for the shapes of displacement time-series and the spatial relationships among PS within the examined area. The algorithm assigns each PS carrying its geographic coordinates and time-series information to a cluster k by minimising the following metric:

$$\text{metric} = (1 - A) + \alpha \cdot B^{\beta} \tag{7.1}$$

$$A = \rho(t_{\text{si}},\ t_{\text{sk}}) \tag{7.2}$$

$$B = \text{dist}(c_{\text{i}},\ c_{\text{k}})/\text{L}_{\text{bridge}} \tag{7.3}$$

Where:

- A is the Pearson correlation coefficient calculated between the time-series t_{si} of the i$^{\text{th}}$ PS and the time-series t_{sk} of the cluster centre. For each iteration of the K-Means algorithm, the time-series t_{sk} is calculated as the mean of the time-series of PS belonging to cluster k. A ranges between –1 – meaning perfect anti-correlation – and 1 – meaning perfect correlation –. Positive values of A indicate similarity between time-series, and the first term of the metric $(1 - A)$ results in a number close to 0.
- B is the distance in metres between the geographic coordinates c_{i} of the i$^{\text{th}}$ PS and the geographic coordinates c_{k} of the cluster centre, normalized with respect to the length of the structure of interest. For each iteration of the K-means algorithm, the coordinates c_{k} are calculated as the mean of coordinates of PS belonging to cluster k. When the distance between coordinates is small, B results in a number close to 0.
- α coefficient is a positive number ranging between 0 and 1. It can be used as a weight of the importance of the second term of the metrics (representing the spatial proximity of PS) with respect to the first one (representing the correlation between time-series of PS).
- β coefficient is a positive number. It can be interpreted as follows: the higher is β, the more important becomes the bridge length limit in the second term of the metric. The β coefficient will regulate an increasingly distinct separation in clusters of PS far apart from each other, and an increasingly likely assignment of very close points to the same cluster. The discriminating factor between proximity and distance of PS is the distance equal to the length of the bridge. Indeed, for values of β greater than 1 and B smaller than 1 – meaning distance between PS and cluster centre shorter than the bridge length –, the second term of the metric becomes an even smaller number. Instead, for values of β greater than 1 and B greater than 1 – meaning distance between PS and cluster centre larger than the bridge length –, the second term of the metric becomes an even greater number.

This approach enables us to leverage the strengths of K-Means while enhancing its capability to discern patterns in both temporal and spatial dimensions in a simple one-step analysis. The methodology is summarized in the flowchart presented in Figure 7.1, which illustrates the main inputs, processing steps, and outputs of our proposed approach.

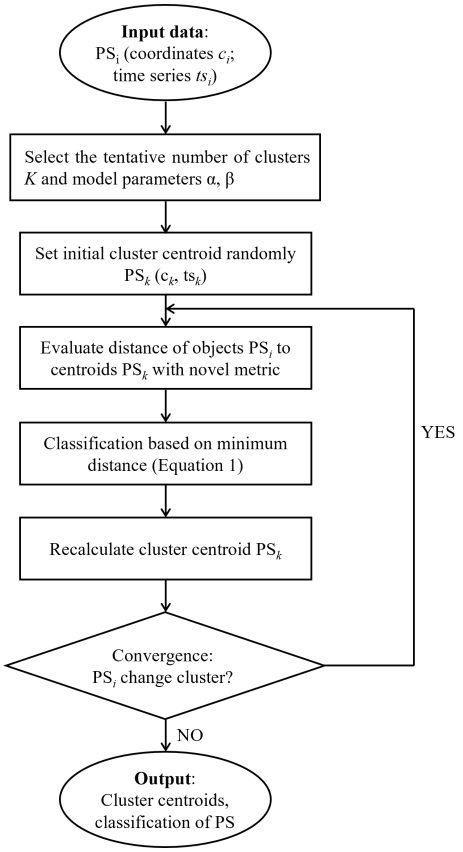

Figure 7.1: Flowchart of the methodology.

7.3 Po River bridge case study

The first case study we consider is the Po River Bridge. It crosses the Po river, and is located in a flat area (the Po Valley) between two small built-up areas (the villages of San Nicolò Po and Portiolo). The bridge and the surroundings are approximately at the same height, at an altitude of just a few metres above sea level. The case study area presents no obstacles and is reached by the radar signal. Due to the above-mentioned features of the case study area, we expect to be able to find a high number of stable high coherence PS both on the bridge and on the surrounding built-up

areas by analysing high quality imagery of the case study area.

7.3.1 Bridge structural characteristics

The Po River Bridge is part of the Italian A22 Highway. It was designed and built following the 1962 Italian standards for calculating loads of road bridges "Circ. Min. LL.PP. 14/02/1962, n. 384". It consists of two identical, parallel viaducts made entirely of reinforced concrete and prestressed concrete and 14 spans for a total length of 980 m. Figure 7.2 shows the longitudinal section of the bridge.

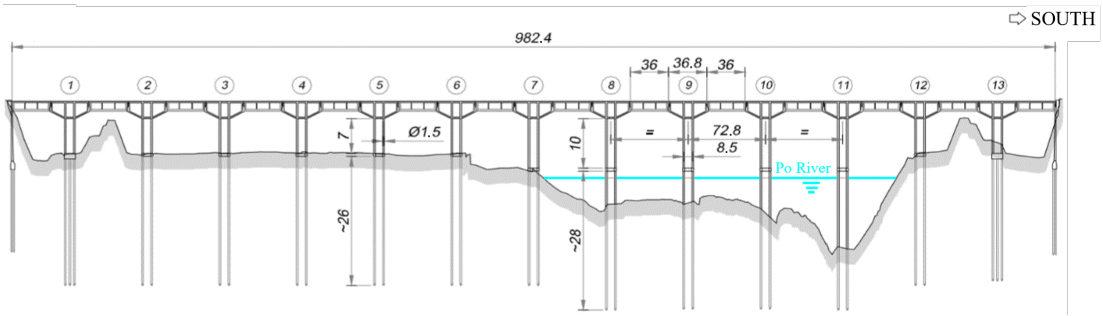

Figure 7.2: Elevation of the A22 Po River Bridge. Dimensions in metres.

The structural system consists of 36 m-long internally simply supported spans that lean on shear keys located at the end of 14.15 m-long cantilevers, resulting in a total span length of 72.8 m between the piers. Each cantilever's deck comprises a double box girder with heights ranging from approximately 3.5 m at the pier to 2.3 m at the edge. The suspended spans have a height of 2 m throughout their length, and a height of 1 m at the supports. In 2002, retrofit works were carried out, involving the symmetrical widening of the carriageways from 10 m to 11.3 m and an increase of 15 cm in the thickness of the upper slab (from 20-22 cm to 35–37 cm). Consequently, the retrofit works significantly increased the overall deck mass (approximately 6 t/m).

The suspended spans lean on unidirectional and multidirectional bearings in the north direction, and fixed bearings and multidirectional bearings in the south direction. Seismic dissipators connect the suspended spans to the cantilevers at the shear keys with fixed bearings. Figure 7.3 shows a scheme of the suspended span bearings and a picture of the seismic dissipators.

The bridge has 13 piers, with 5 piers within the riverbed and 8 on the floodplain (6 on the north side towards Mantua and 2 on the south side towards Modena). Each pier consists of 6 circular columns with a diameter of 1.5 m. At the base of the columns is a reinforced concrete

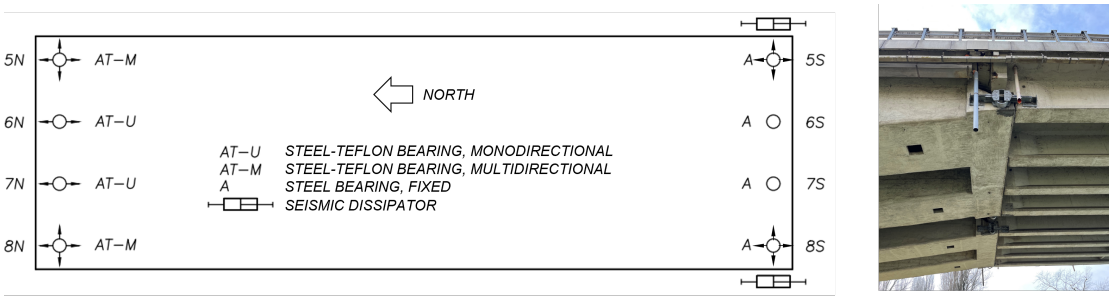

(a) (b)

Figure 7.3: (a) Scheme of the suspended span bearings; (b) picture of the seismic dissipators.

collar with dimensions 2.0 m x 0.6 m. The foundation piles, also with a diameter of 1.5 m, extend below the collar and serve as natural extensions into the ground from the columns above. The piers in the riverbed have 10 m-long columns and approximately 28 m-long piles; the piers in the floodplain have 7 m-long columns and approximately 26 m-long piles.

Before 2012, the soil at the base of Pier 11 was affected by erosion caused by the increased speed of the stream and the formation of vortexes, with the consequent formation of a localised depression in the riverbed. The last bathymetric survey was performed in 2009, and backfill soil was placed around Pier 11 to decrease its free length in 2012 (Figure 7.4). As a result, the length of the above-ground part of the foundation poles is approximately 8 m for Piers 8, 9, and 10; 11.5 m for Pier 11; and 1 m for the other piers. Thus, the effective total length of the above-ground part of the piers counting both poles and columns is, approximately, 18 m for Piers 8, 9, and 10; 21.5 m for Pier 11; 11 m for Pier 7; and 8 m for the other piers.

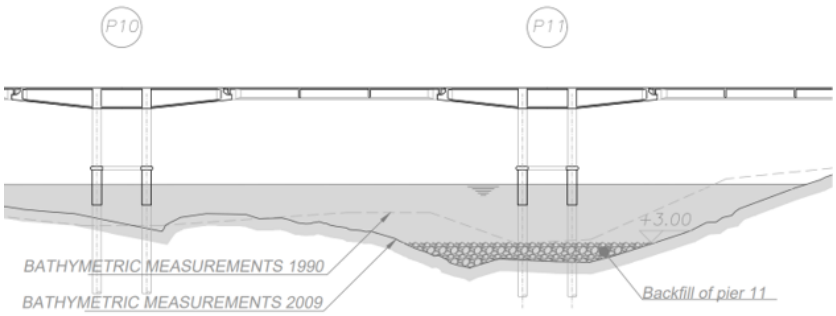

Figure 7.4: Longitudinal section of Piers 10 and 11. Dimensions in metres.

7.3.2 Case study area

Figure 7.5 shows a picture of the A22 Po River Bridge and a top view of the case-study area.

(a) (b)

Figure 7.5: (a) Picture of the A22 Po River Bridge; (b) Top view of the case-study area.

The case-study area is 17.6 km^2, close to Mantua in northern Italy. It includes the villages of San Nicolò Po and Portiolo and is crossed by the Po River. This area is subjected to a slow progressive subsidence, as visible in the vertical displacement measurement accessible from the European Ground Motion Service (https://egms.land.copernicus.eu/), reported in Figure 7.6.

In the case-study area, the subcontinental climate is marked by high humidity, snowfall, and fog during winter, while summers are characterized by a muggy, humid atmosphere with minimal ventilation. Air temperatures vary between -5°C and 40 °C throughout the year. Figure 7.7a shows the air temperature measured between UTC 5p.m. and 5:30p.m. from January 2014 to December 2021 by the meteorological station located 5.6 km from the A22 Po River Bridge in Gorgo di San Benedetto Po (MN). As commonly known, the deformations and deflections of prestressed concrete bridges strongly respond to temperature variation [44, 45]. Thus, we expect to observe periodic displacements related to seasonal temperature variation over the A22 Po River Bridge.

The Po River is characterized by significant flow variations, with water levels rising up to 10 m during the period of interest, leading to the floodplain filling during heavy rainfall events. Figure 7.7b illustrates the Po River's water levels from 2014 to 2021, recorded between 5:00p.m. and 5:30p.m. UTC by the hydrometer of the Interregional Agency for the River Po (AIPO) installed on the Borgoforte Bridge, located just 7.4 km upstream of the A22 Po River Bridge. Other bridges in the same area

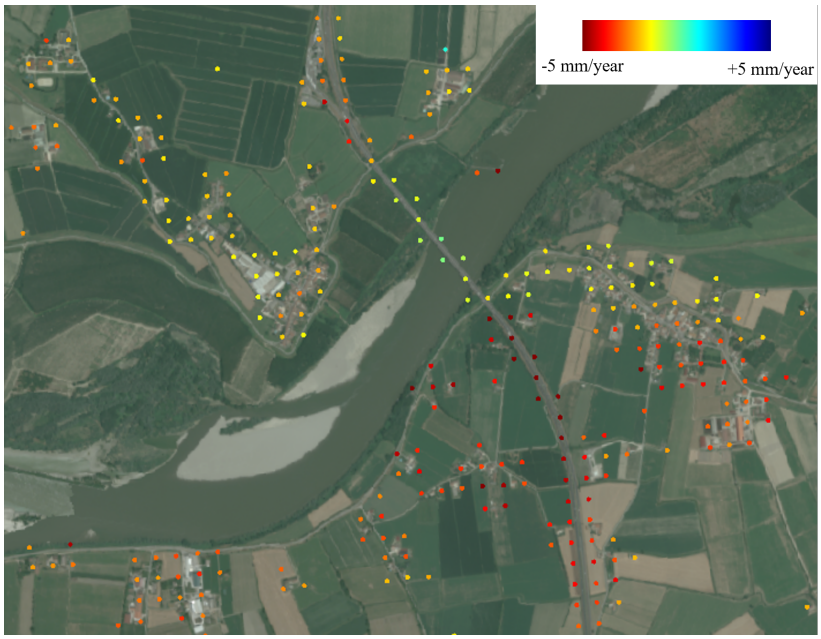

Figure 7.6: Vertical displacement measurements in the case study area from EGMS (https://egms.land.copernicus.eu/)

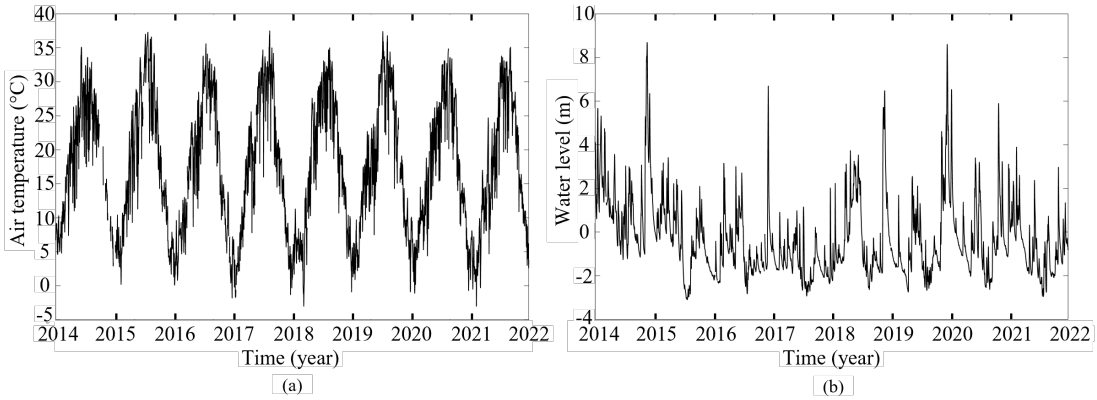

Figure 7.7: Time-series from 05/01/2014 to 05/12/2021 of (a) temperature variation in the case-study area, and (b) water flow level of the Po River.

have been studied to investigate the possible influence of the Po River on their structural behaviour [46].

7.3.3 Dataset and MT-InSAR analysis

Several satellite missions are available providing SAR imagery datasets at different wavelengths, spatial resolutions, and revisit time. In general, the use of small wavelength SAR sensors and short revisit times guarantees better displacements sensitivity and temporal coherence [47]. Given the range of displacements typically observed in civil infrastructure, the most accurate results in SHM application are usually obtained with X-band SAR sensors operating with a wavelength of 3.1 cm. X-band sensors are employed in the TerraSAR-X mission, COSMO-SkyMed (CSK) mission, ICEYE mission, and Capella Space mission. Among the alternatives, we opt for satellite images acquired by the X-band Italian satellite mission CSK in the Stripmap HIMAGE mode, with a spatial resolution of 3 m, covering large regions of 40x40 km within a single satellite scene. Indeed, this high-resolution imagery is provided free of charge to the scientific community for research purposes upon submission of a scientific proposal.

For the Po River Bridge case study, we consider a dataset of 109 images acquired in descending geometry. The images were acquired from 5 January 2014 to 5 December 2021 at UTC 5:13p.m., covering an 8-year period.

We performed the MT-InSAR data processing with the software SarProZ© (https://www.sarproz.com/), version 'SARPROZ 08-September-2022 16:32:33'. The master image of the dataset corresponds to the date 24 July 2017. We analysed only SAR images acquired in descending geometry due to the incompleteness of the dataset for ascending geometry acquisitions. Specifically, the revisit time of the CSK satellite in the ascending orbit during the considered time frame was insufficient to ensure accurate and reliable results. Only approximately 50 images acquired in the ascending orbit were available between 2014 and 2021, less than half the number of images acquired in the descending orbit during the same time frame.

The CSK satellite that acquired the images of our dataset has right-side looking-angle with an incidence angle $\theta = 33.9449°$ – i.e., the angle between the Line of Sight of the satellite (LoS) and the normal to the ground in our area – and a heading angle $\beta = 10.6095°$ – i.e., the angle between the satellite orbit and the North-South direction –. The investigated area includes the A22 Po River Bridge and the villages of San Nicolò Po and Portiolo. Villages and artificial structures in this area contribute to the successful co-registration of SAR imagery.

For the generation of differential interferograms, we employed the SRTM90 DEM and georeferenced the radar images to WGS84 coordi-

nates using a streetlamp close to the A22 Po River Bridge as Reference Point (RP). The atmospheric phase noise was estimated and removed from the SAR images. Finally, in the Persistent Scatterer (PS) selection step, we excluded all PS with a temporal coherence lower than 0.6 to ensure the accuracy of MT-InSAR results. Temporal coherence, ranging from 0 (low quality) to 1 (high quality), is a metric that reflects the quality of the extracted displacement time-series [48].

As a result, we included 8426 PS in our analysis, most of them located over roads and villages. Displacement time-series were extracted for every PS based on the filtered phase data. The extracted displacements are relative in time and space. They are measured along the LoS. A negative deformation means that the PS moves away from the satellite, while a positive deformation means that the PS moves towards the satellite. More detailed information about the single steps performed in this MT-InSAR analysis and the main choices that were taken can be found in [49].

7.3.4 MT-InSAR results

We illustrate and discuss the results of the MT-InSAR analysis of the Po River bridge case study. Figure 7.8 reports the temporal coherence and the deformation velocity of the PS identified over the case-study area. The velocity of PS has been calculated during the MT-InSAR data processing by fitting a linear function over the entire time-series of displacement through the least-square analysis. The standard deviations of the estimated velocity range between 0.21 and 0.56 mm/year, depending on the considered PS. The velocity ranges from -13.21 mm/year (away from the satellite) to 3.59 mm/year (toward the satellite).

The PS are mainly concentrated along the highway, within urban centres, and along local roads. As visible from Figure 7.8a, the PS all have temporal coherence higher than 0.6, which is the limit set during the PS selection in the MT-InSAR analysis. Most PS on the bridge have coherence higher than 0.8, confirming the results' reliability.

On the other hand, Figure 7.8b shows that the bridge is primarily covered by green PS, indicating nearly negligible deformation velocity ranging between -1.0 and +1.0 mm/year. A yellow portion is present over Piers 11, 12 and 13 at the southern end of the bridge, close to the floodplain, meaning deformation velocity between -3.0 and -1.0 mm/year. The highway road accessing the bridge from the south and the local road adjacent to the southern embankment of the river both exhibit red and orange PS, meaning deformation velocity ranging between -3.0 and -10.0 mm/year. The highway road accessing the bridge from the north also has some red and orange PS, among the yellow ones.

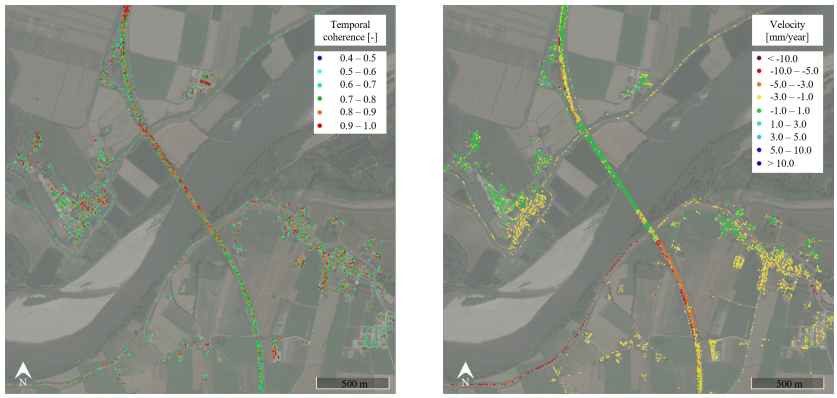

Figure 7.8: Distribution of the PS identified in the case-study area illustrated in a colour scale representing (a) their temporal coherence, and (b) their displacement velocity along the satellite LoS, over the full observation period.

In order to demonstrate the need and advantages of adopting a novel metric accounting for both the displacement time-series and spatial coordinates of PS, we first apply the standard K-Means clustering algorithm with Euclidean distance metric for the classification of the PS time-series in the Po River bridge case study area. Specifically, the standard steps for the application of K-Means – previously described in Section 7.2 – are followed, considering only PS time-series as input data and neglecting the PS coordinate data. As a result, PS are classified solely based on the sum of squared differences between the PS time-series vectors and the centroid.

Figure 7.9 reports the results obtained considering three clusters. Specifically, Figure 7.9a shows the PS map in a colour scale representing their cluster membership. Figure 7.9b shows the PS time-series grouped in the different clusters with matching colours to the map, and their centroids in black. The centroid of Cluster 1 has mean velocity of -0.77 mm/year; the centroid of Cluster 2 has mean velocity of -1.72 mm/year; the centroid of Cluster 3 has mean velocity of -5.07 mm/year. The colours of the clusters are set based on the mean velocity of their centroids, according to the displacement velocity colour scale adopted in Figure 7.8b (green for lower, yellow for medium, and red for higher mean velocities of PS).

The map of PS time-series clusters reported in Figure 7.9a appears very similar to the map of PS displacement velocity reported in Figure 7.8b. Indeed, this result does not provide significant additional insights beyond what is directly derived from MT-InSAR analysis. The reason is

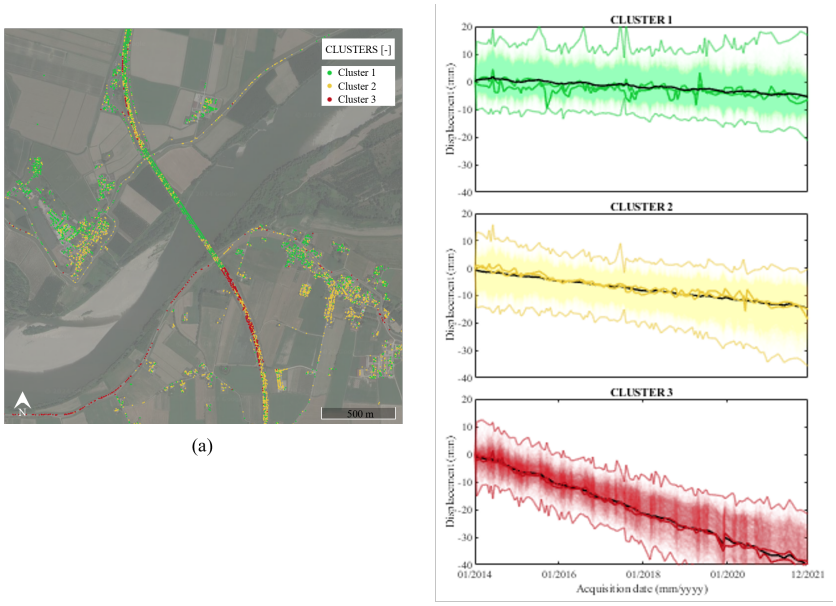

Figure 7.9: (a) Distribution of PS in the case-study area illustrated with colours representing their cluster; (b) Clusters of the PS time-series of displacement, represented with the same colours used in the map 8a.

that K-Means clustering of PS displacement time-series with Euclidean distance metric leads to classifying PS mainly based on their mean linear trend over the whole period of observation, simply confirming the differences in PS velocity across the study area. This analysis performs a kinematic evaluation of PS, but is not helpful for the physical interpretation of results. For example, a PS located over the Portiolo village and a PS located over the bridge may be assigned to the same Cluster because they have similar velocities, however they clearly belong to different physical entities, and their behaviour is not necessarily related to the same phenomena. From a civil engineer standpoint, it is important to distinguish PS that show the same type of displacement pattern because they belong to the same structural element and are influenced by the same phenomena, and PS that may simply have similar kinematic but do not have physically meaningful relations.

Additional clusters in the application of standard K-Means for time-series clustering yield a more fragmented velocity map, producing finer divisions still mainly based on the mean linear trend of the PS time-series. This results confirm the need for a novel metric for extracting meaningful information about different PS time-series patterns and their

association with physical entities within the study area.

7.3.5 Expected behaviours

To identify expected patterns or anomalies, civil engineers must understand how to correctly read displacement data measured by the satellite and extracted through MT-InSAR. It is necessary to account for the position and orientation of the structure of interest in relation to the satellite's orbit direction. The operator must also have a general idea of what to expect to observe on the structure of interest in the normal exercise of such structure, based on simple civil engineering considerations.

Regarding the dataset, the CSK satellite that acquired the SAR images moved from North to South with a right-looking angle. Considering that a negative deformation means that the PS moves away from the satellite, while a positive deformation means that the PS moves towards the satellite, we can conclude that:

- Negative displacement along the LoS of a PS means that that target moves mainly vertically downward, mainly horizontally toward the West, or a combination of the two;
- Positive displacement along the LoS of a PS means that that target moves mainly vertically upwards or mainly horizontally toward the East, or a combination of the two.

The angle between the longitudinal axis of the bridge and the North-South direction (bridge orientation) is $\zeta = -33.5°$. The heading angle of the satellite is $\beta = 10.6095°$, so that the bridge's longitudinal axis is inclined $44.1°$ with respect to the satellite orbit direction. The angle between the bridge's longitudinal axis and the LoS horizontal projection results $\gamma = 45.89°$. Due to the orientation of the bridge, the displacements of the extracted PS on the bridge along the LoS are a combination of both horizontal and vertical displacements.

The bridge's static scheme is described in Section 7.3.1. It consists of suspended spans that lean on symmetric cantilever piers. The suspended spans are free to move longitudinally in the north direction and fixed in the south direction. Regarding the expected displacements of the case study, in normal exercise conditions of the bridge we should expect only vertical and longitudinal horizontal displacements induced by environmental loads resulting from the seasonal temperature variations. Indeed, other loads like traffic loads and wind have a frequency and variability too high to be observed with the minimum 16-day acquisition frequency determined by the satellite's revisit time.

Figure 7.10 shows the expected horizontal longitudinal displacements of the cantilever piers of the bridge measured by the satellite when there

is a positive temperature variation: both cantilever elongate, but the northern cantilever elongation results in a negative variation of longitudinal displacement measured by the satellite (displacement variation inversely proportional to the temperature variation), while the southern cantilever elongation results in a positive variation of longitudinal displacement measured by the satellite (displacement variation directly proportional to the temperature variation). The same logic applies to the suspended span, in this case also depending on the longitudinal supports and their deterioration level: with positive temperature variation, the suspended span tends to elongate, meaning negative variation of longitudinal displacement of the northern joint (free to move longitudinally) and zero or slightly positive variation of longitudinal displacement of the southern joint (fixed). Regarding the vertical displacements measured by the satellite when there is a positive seasonal temperature variation, we expect elongation of the columns of the piers supporting the superstructure, meaning positive vertical displacements variation (displacement variation directly proportional to the temperature variation).

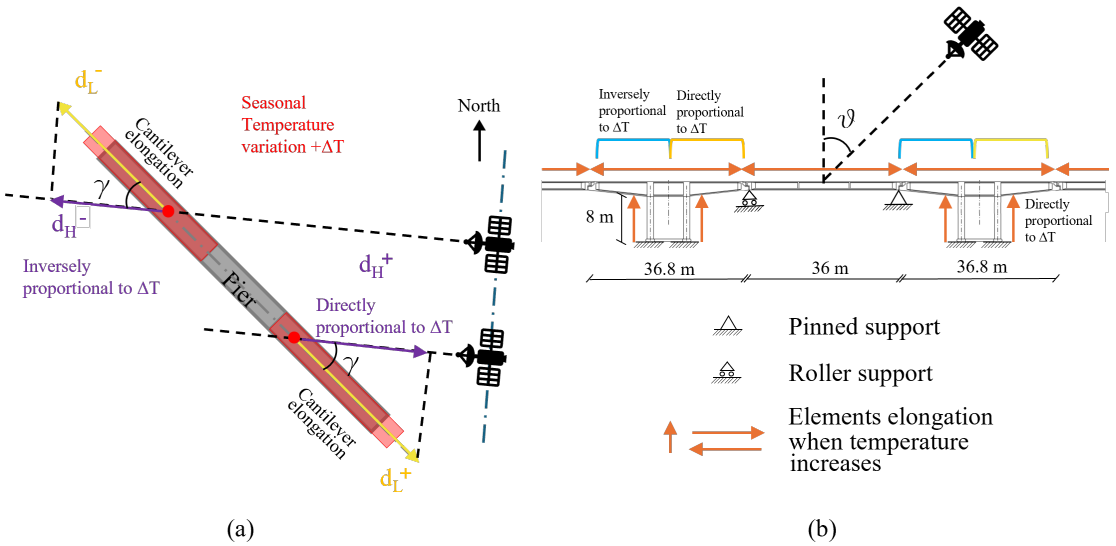

Figure 7.10: Schemes explaining the negative and positive sign of the expected horizontal longitudinal and vertical displacements of the cantilevers obtained from satellite measurements as temperature increases. (a) Plan view showing displacements of one cantilever pier of the bridge and the angle γ; (b) longitudinal profile showing displacements of cantilever piers and suspended spans and incidence angle θ.

Based on the static scheme and geometry of the structural elements shown in Figure 7.10, we can estimate the projection of the expected displacements – caused by uniform temperature variation across all struc-

tural elements – onto the satellite LoS.

First, the annual mean temperature variation in San Nicolò Po was determined using data from https://it.climate-data.org, yielding $\Delta T = 22.2°C$. Let us assume that the seasonal temperature variation induces a periodic displacement component in the structural elements. Then, the expected amplitude of these periodic displacements, projected along the LoS, can be calculated using Equations 7.4 and 7.5.

$$d_{\text{V,LoS}} = d_{\text{V}} \cdot cos(\theta) = \alpha \cdot L \cdot \Delta T/2 \cdot cos(\theta) \tag{7.4}$$

$$d_{\text{L,LoS}} = d_{\text{L}} \cdot cos(\gamma) \cdot sin(\theta) = \alpha \cdot L \cdot \Delta T/2 \cdot cos(\gamma) \cdot sin(\theta) \tag{7.5}$$

Where:

- d_{V} is the amplitude of the periodic vertical displacement of the structural element and $d_{\text{V,LoS}}$ is its projection along the LoS;
- d_{L} is the amplitude of the periodic longitudinal displacement of the structural elements, and $d_{\text{L,LoS}}$ is its projection along the LoS;
- θ is the incidence angle of the satellite;
- γ is the angle between the bridge's longitudinal axis and the LoS horizontal projection;
- L is the length of the structural element;
- α is the thermal expansion coefficient of the material, assumed as $10^{-5}\ °C^{-1}$ for all structural elements.

The resulting displacements at key structural points are summarized in Table 1. For the calculation of the vertical displacement component, the height of the floodplain piers – approximately 8 m above ground level – was taken into account. Indeed, predicting the thermal response of riverbed piers partially submerged in water with varying level would be particularly challenging. The results are based on the idealized behaviour of the static scheme shown in Figure 7.10, assuming no relative displacement between the cantilever and the suspended span at the southern joint, and full thermal elongation of the suspended span accommodated by the northern sliding joint.

The results presented in Table 7.2 indicate the following expected displacement patterns visible along the satellite LoS: (i) a displacement variation directly proportional to seasonal temperature, with amplitude of 1.53 mm at the cantilever southern free end; (ii) a displacement variation directly proportional to seasonal temperature, with amplitude of 0.74 mm at the center of the pier; (iii) a displacement variation with low correlation to seasonal temperature at the cantilever northern free end and at the suspended span southern joint; (iv) a displacement variation

Table 7.2: Quantitative evaluation of the expected amplitude of periodic structural displacements along the LoS caused by seasonal temperature variation.

	$\boldsymbol{d}_{\mathbf{V,LoS}}$ (mm)	$\boldsymbol{d}_{\mathbf{L,LoS}}$ (mm)	$\boldsymbol{d}_{\mathbf{TOT,LoS}}$ (mm)
cantilever south free end	0.74	0.79	1.53
pier center	0.74	0	0.74
cantilever north free end – suspended span southern joint (fixed)	0.74	-0.79	-0.06
suspended span northern joint (sliding)	0.74	-2.35	-1.61

inversely proportional to seasonal temperature, with amplitude of -1.61 at the suspended span northern joint.

7.3.6 Application and results of the proposed clustering algorithm

We apply the clustering algorithm presented in Section 7.2 to the PS extracted by means of MT-InSAR in the case study area. Practically, it consists of a K-Means clustering algorithm with a tailored metric accounting for both the time-series of displacement and the geographical position of the extracted PS. Out of the 8426 PS resulting from the MT-InSAR analysis, 3504 PS that fall inside an area of approximately 2x2 km with centre on the bridge are considered for the clustering analysis.

The number of clusters must be chosen and the metrics used in the algorithm must be calibrated by selecting suitable values for α and β.

First, we address the selection of the number of clusters. We do this by assessing, a priori, how many clusters we might reasonably expect to identify in the case study area. On the bridge itself, we can hypothesize the presence of at least two distinct clusters, based on the expected displacement patterns discussed in Section 7.3.5 – one exhibiting direct seasonal proportionality and the other exhibiting inverse seasonal proportionality. Additional clusters are expected to represent the highway lanes on the embankments, both north and south of the bridge, as well as the surrounding urban areas (namely, Portiolo village, San Nicolò village, and the north-eastern urban complex). Possibly, an additional separate cluster may be assumed to include eventual outliers. Based on these a priori considerations, a preliminary estimate for the number of clusters is approximately 8.

However, this estimate based on a priori considerations may not correspond to the number of clusters that would result from a posteriori analysis, i.e., by examining the PS behaviour point-by-point. Indeed, additional or unforeseen behaviours might emerge. In such a case, choos-

ing more clusters than truly necessary would merely result in separate groups of PS that could have been merged, while choosing too few could lead to a more problematic outcome: the mixing of PS related to different physical phenomena into a single cluster, thereby causing confusion in the interpretation and possibly failing to capture all distinct behavioural patterns in the case study area. For this reason, we conservatively select 12 clusters for our analysis.

At this point, the metrics used in the clustering algorithm must be calibrated. In order to choose appropriate values for coefficients α and β, we should iterate the algorithm until we can easily distinguish in the clusters representation (both time-series of displacements and distribution of PS) some expected patterns like those described in the previous Section or, on the contrary, detect anomaly in the data. We proceed to show and discuss the results of the clustering algorithm application on the case study area, including tentative calibration parameters and the final selected metric. For each application attempt, Figure a) displays the distribution of PS in the case-study area, illustrated in a colour scale representing their clustering membership; Figure b) displays the PS time-series of displacement grouped in the different clusters, with matching colours to the PS distribution map. The cluster centre is coloured in black.

The initial calibration attempt with coefficient $\alpha = 0$, i.e. neglecting the second term of the metric formula, produces PS clusters based solely on the correlation between the PS time-series of displacement, with no consideration given to their positions. As a result, the map of PS coloured according to the identified clusters reported in Figure 7.11a makes it challenging to associate any set of PS grouped in a cluster with a specific physical entity within the study area, and to distinguish clusters on the bridge from the surroundings: the clusters appear blended and spatially dispersed. By looking at the time-series clusters in Figure 7.11b, we can observe a downward trend of varying magnitude present in many clusters, and a seasonal periodicity trend present in some clusters – more evident in Clusters 2 (cyan), 5 (orange) and 7 (magenta). Many PS on the northern and southern sections of the bridge over the floodplain belong to Cluster 2 (cyan), showing a downward trend and a direct proportionality to seasonal temperature changes. In contrast, PS in the central part over the riverbed belong to Cluster 5 (orange), with almost no trend but similar temperature-related behaviour. On the other hand, PS in Cluster 7 (magenta) show a downward trend but inverse temperature proportionality.

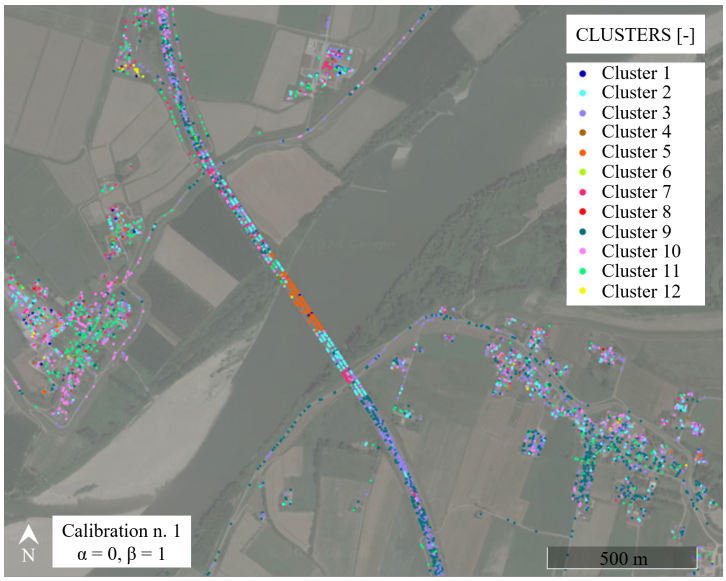

(a)

Figure 7.11: (a) Map of PS in the case-study area illustrated with 12 different colours representing their cluster.

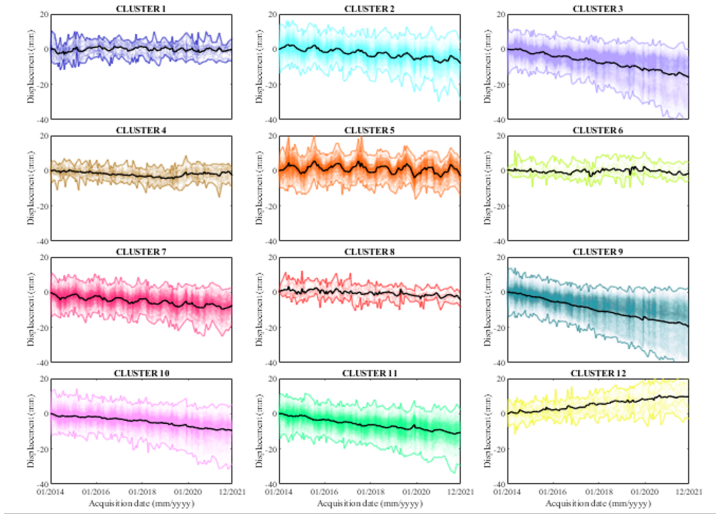

(b)

Figure 7.11: (b) Clusters of the PS time-series of displacement along the LoS, represented with the same colours used in the map.

Oppositely to the first calibration attempt, the second calibration attempt with the coefficient $\alpha = 0.5$ and the coefficient $\beta = 1$ results in a

quite neat separation of clusters from a geographical point of view, giving the impression that the clusters are built around the PS centroid based mainly on its coordinates. The clusters segment the territory into defined zones: the section of the bridge over the river and southern floodplain area and the one over the northern floodplain area, the highway lanes leading to the bridge, and portions of the villages of Portiolo and San Nicolò Po. The results are shown in Figure 7.12.

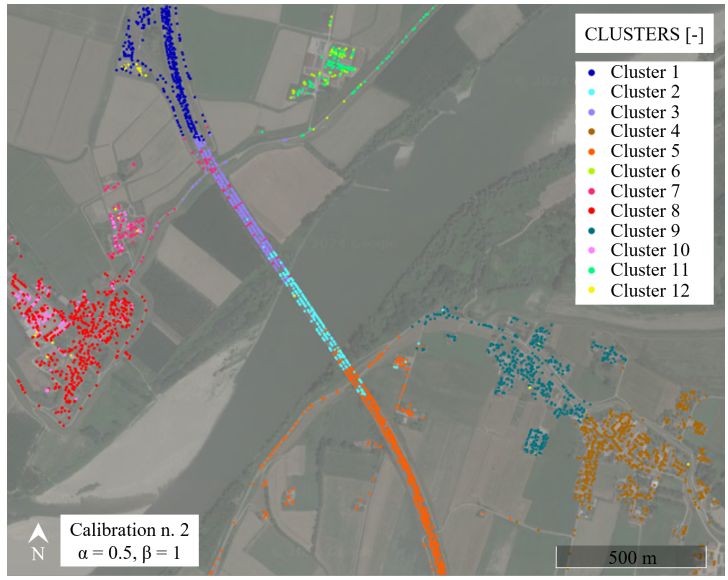

(a)

Figure 7.12: (a) Map of PS in the case-study area illustrated with 12 different colours representing their cluster.

Similarly to the first calibration attempt, we can observe a downward trend of varying magnitude present in most clusters. Moreover, a few different patterns of displacements are noticeable on the bridge. In the northern portion of the bridge, the majority of PS belong to Cluster 3 (lilac), with a linear downward trend, but a few PS fall into Cluster 7 (magenta), with an inverse proportionality to the seasonal temperature variation. In the southern portion of the bridge most PS fall in Cluster 2 (cyan) with direct proportionality to the seasonal temperature and slight downward trend, while few PS fall in Cluster 5 (orange), with a significant linear downward trend. With respect to the first calibration attempt, the difference in downward trend magnitude between different parts of the bridge is less noticeable. Moreover, in the northern section of the bridge, the proportionality of PS time-series of displacement to the temperature variation appears smoothened.

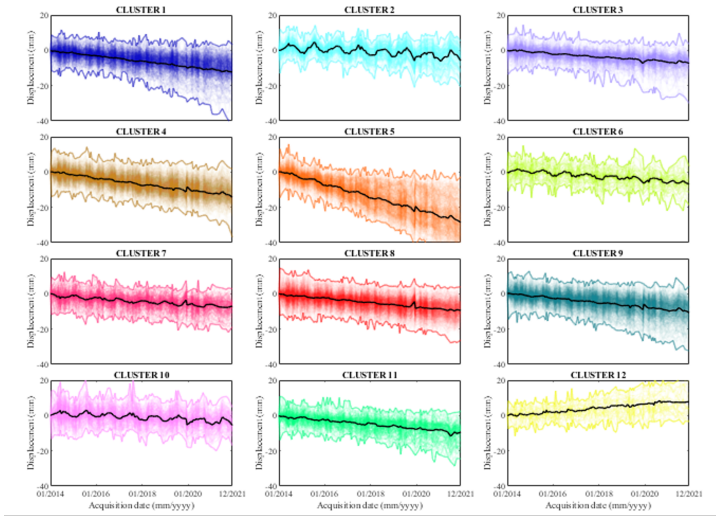

(b)

Figure 7.12: (b) Clusters of the PS time-series of displacement along the LoS, represented with the same colours used in the map.

Finally, the third and last calibration attempt is with coefficient $\alpha = 0.5$ and coefficient $\beta = 2$. The results are reported in Figure 7.13.

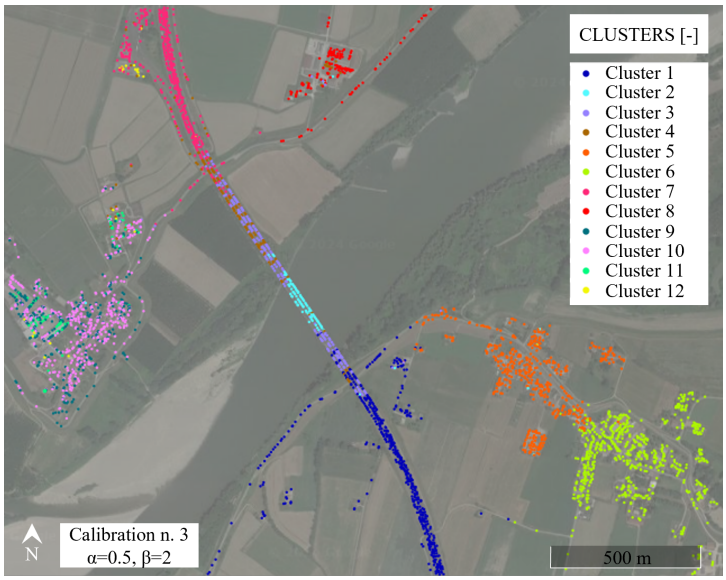

(a)

Figure 7.13: (a) Map of PS in the case-study area illustrated with 12 different colours representing their cluster.

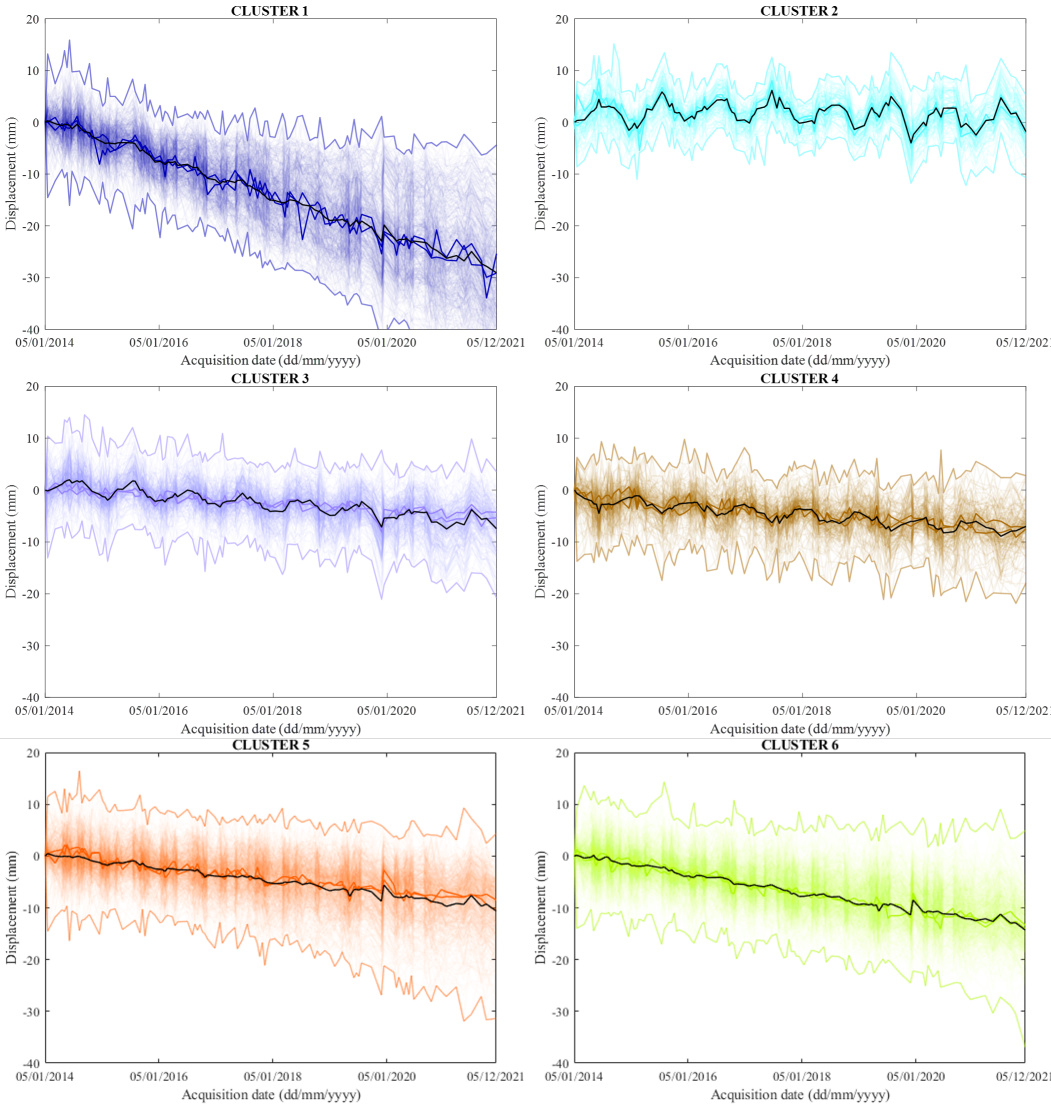

To aid in the reading and understanding of the results, a fitting of the cluster centroids' time-series is performed. Cluster centroids are fitted using Least Squares Analysis (LSA) with the model function reported in Equation 7.6.

$$\mathbf{y} = q + m \cdot \mathbf{x} - a \cdot cos(2\pi \cdot \mathbf{x} + \phi) \tag{7.6}$$

The dependent variable y is the centroid's time-series, while the independent variable x is the acquisition dates vector expressed in years. The model function has a linear component and a periodic component.

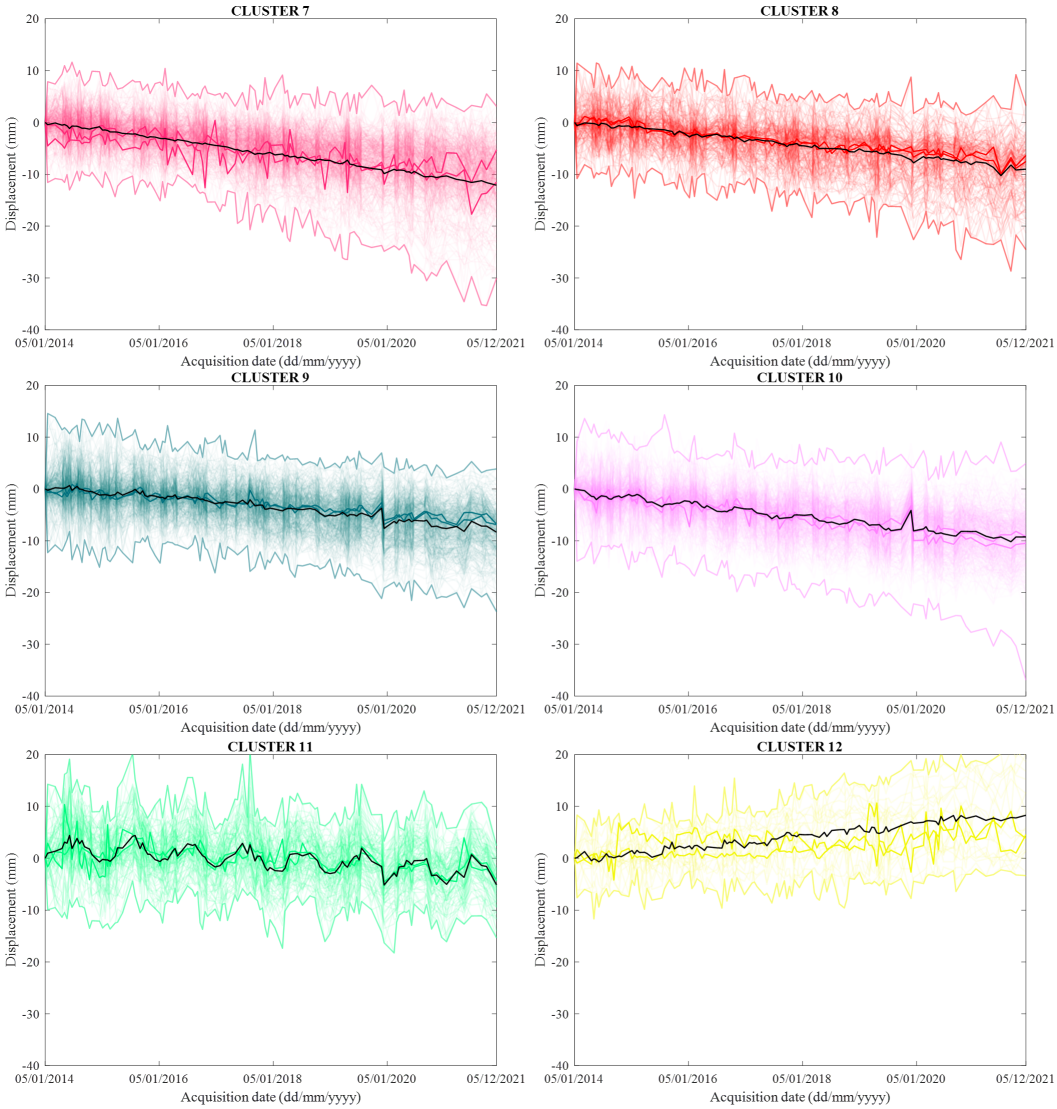

Figure 7.13: (b) Clusters of the PS time-series of displacement along the LoS, represented with the same colours used in the map.

The periodic component is represented by a negative cosine function, starting with its minimum value. This periodic function fits the air temperature measurements within the time-frame of our dataset, beginning on 5 January, close to when annual temperatures reach their lowest point.

The model function comprises 4 parameters. Parameter q is an offset; parameter m represents the linear velocity; parameter a is the amplitude of the periodic function; parameter ϕ is the phase of the periodic

function. In cases where the periodic component is not present in the cluster centroids' time-series, the model function is simplified to a linear function by neglecting the periodic term.

By looking at Table 7.3, we can note a general downward trend in almost all clusters, and a seasonal periodicity trend in some clusters.

Table 7.3: Clusters centroids' fitting parameters and their standard deviation obtained with LSA.

Cluster centroid	**Number of PS for each cluster [%]**	**velocity m [mm/year]**	**amplitude a [mm]**	**phase ϕ [years]**
CLUSTER 1	475 (13.6%)	-3.69 ± 0.02	–	–
CLUSTER 2	94 (2.7%)	-0.19 ± 0.04	2.23 ± 0.14	-0.08 ± 0.18
CLUSTER 3	237 (6.8%)	-0.96 ± 0.02	1.34 ± 0.06	-0.06 ± 0.08
CLUSTER 4	152 (4.3%)	-0.79 ± 0.02	-1.17 ± 0.06	-0.09 ± 0.08
CLUSTER 5	486 (13.9%)	-1.30 ± 0.02	–	–
CLUSTER 6	654 (18.7%)	-1.75 ± 0.02	–	–
CLUSTER 7	404 (11.5%)	-1.52 ± 0.01	–	–
CLUSTER 8	145 (4.1%)	-1.16 ± 0.06	–	–
CLUSTER 9	295 (8.4%)	-1.06 ± 0.02	–	–
CLUSTER 10	446 (12.7%)	-1.17 ± 0.06	–	–
CLUSTER 11	92 (2.6%)	-0.66 ± 0.03	1.96 ± 0.10	-0.12 ± 0.13
CLUSTER 12	24 (0.7%)	1.13 ± 0.02	–	–

As already mentioned in this Section, the global downward trend in descending orbit displacement data over the area can be interpreted as a vertical component of displacement affecting the whole study area. Indeed, the Po Valley is gradually subsiding over the years, as visible from Figure 7.6. An exception is represented by Cluster 12 (yellow), counting only 24 PS time-series, some are in a very localised part of the study area near a parking lot and storage/deposit, while a few are sparse in the San Nicolò Po village; they can be considered outliers. Other clusters all show subsidence trends with varying magnitude in mm/year.

On the southern side of the river, Cluster 1 (blue) shows the highest magnitude of downward trend of displacement, with a cluster centroid's linear displacement trend value of -3.69 mm/year; this cluster contains PS located on the southern access lane to the bridge and the local road adjacent to the southern embankment of the river. The high velocity suggests abnormal displacements of the access lane. The infrastructure operator has recently detected such abnormal displacements and is already addressing this issue. The Clusters 5 and 6 (orange and lime green), with PS located over the urban area of Portiolo, also have quite marked downward trends of linear displacements.

On the northern side of the river, Cluster 7 (magenta) on the northern access lane to the bridge and Clusters 8, 9 and 10 (red, dark green and pink) over San Nicolò Po urban area also show downward trends of lin-

ear displacements, but their magnitude is lower than in the southern area. Those clusters all have limited periodicity; that aligns with the expectation for the behaviour of the PS over the access lanes to the bridge and the local roads, since they have been constructed over embankment soil, which is not expected to exhibit significant displacements in response to temperature variations. Moreover, the PS located over the rural areas of Portiolo and San Nicolò Po mainly represent simple concrete residential constructions with red tile roofs, not particularly sensitive to thermal seasonal variations in terms of deformations.

Cluster 11 (light green) contains some PS located mainly on metallic constructions, such as a high-voltage power line tower and warehouses in an industrial area of San Nicolò Po. PS belonging to this cluster have a similar trend to the seasonal temperature variations; this is expected since both steel lattice towers and warehouses' metal roofs are sensitive to temperature and usually have a significant component of deformation due to thermal variation.

The Clusters 2, 3 and 4 (cyan, lilac and brown), containing PS located on the bridge, all show a marked seasonal periodicity. While Cluster 2 and 3 (cyan and lilac) both show direct proportionality to seasonal temperature variations, Cluster 4 (brown) shows inverse proportionality to seasonal temperature variations. On the other hand, Cluster 3 and 4 have a similar magnitude of linear downward trend component with velocity of -0.96 and -0.79 mm/year respectively, while Cluster 2 has lower velocity (-0.19 mm/year). This phenomenon can be better understood by zooming in on the bridge and investigating the correspondence between the PS of those 3 clusters and the different parts of the structure (Figure 7.14).

In the northern section of the bridge, on the north side of the river, there is a clear noticeable pattern.

Cluster 3 (lilac) collects PS located at intervals corresponding to the southern end of the cantilever piers, the piers center, and the southern end of the suspended span. These PS show a variation of displacement with direct seasonal periodicity, with mean amplitude represented by the centroid's fitting parameter $a = 1.34\ mm$ (Table 7.3).

Cluster 4 (brown) collects PS located at intervals corresponding to the northern end of the suspended span and the northern end of the cantilever piers. These PS show a variation of displacement with inverse seasonal periodicity, with mean amplitude represented by the centroid's fitting parameter $a = -1.17\ mm$ (Table 7.3)).

A few PS belong to Cluster 7 (magenta), indicating that the downward trend starts to prevail as we are approaching the northern access lane of the bridge on the soil embankment.

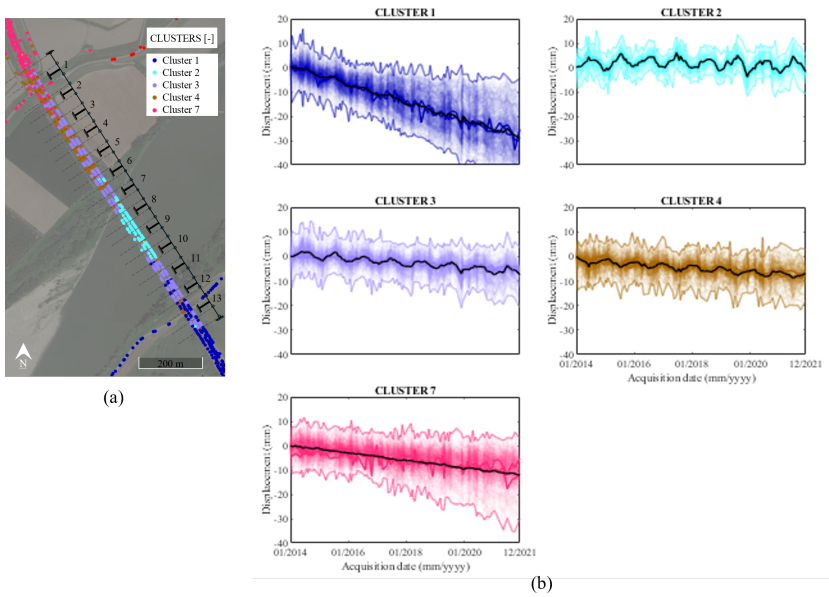

(a) (b)

Figure 7.14: Focus on the PS clusters on the bridge: (a) Distribution of PS over the bridge and schematic representation of the junctions and piers positions; (b) Clusters of the PS time-series of displacement, represented with the same colours used in the map.

This result is in line with the expected longitudinal and vertical deformation response of the bridge, previously explained in Figure 7.10 and in Table 7.2. The longitudinal displacements are zero over the piers and increase along the cantilevers until the joints as we move away from the piers; the suspended span can elongate longitudinally, mainly in the direction of the cantilever which supports it with sliding bearings; while the vertical deformation is due to the piers seasonal elongation and contraction. The theoretical amplitudes of the periodic displacements calculated in Table 7.2 are: 1.53 mm at the cantilever southern end; 0.74 mm at the piers; close to zero at the southern end of the suspended span and at the northern end of the cantilever; and -1.61 mm at the suspended span northern joint. The differing seasonal correlation observed from the satellite between the PS located at the cantilever's northern end and those at the suspended span's southern end – belonging to Clusters 4 and 3, respectively –, suggests the presence of small relative movements at the joint.

In the southern section of the bridge, the clustering algorithm detects a different behaviour. On part of the riverbed portion of the bridge, including piers 8-9-10, most PS belong to Cluster 2 (cyan). The pattern of

Cluster 4 (brown) indicating the horizontal longitudinal displacements of the northern joints of the suspended span and the northern cantilever of the piers is less delineated, with only very few PS belonging to it. On the remaining part of the bridge, including pier 11 in the riverbed and piers 12–13 on the floodplain, most PS belong to Cluster 3 (lilac). Few PS also belong to Cluster 4 (brown) at the northern cantilever of pier 13 and the northern joint of its suspended span, and few belong to Cluster 1 (blue), indicating that the downward trend starts to prevail as we are approaching the access lane of the bridge on the soil embankment. We remind the Reader that both Clusters 2 and 3 are directly proportional to the seasonal temperature variations, however they have different velocity, Cluster 2 being more stable.

The reduced detectability of the pattern of Cluster 4 (brown) in the southern section of the bridge, where most PS belong to Clusters 2 (cyan) and 3 (lilac) with direct proportionality to seasonal temperature variation, can indicate the prevalence of vertical deformation response to temperature effects in this part of the structure. Indeed, the columns of piers 8, 9, 10 and 11 have length above the ground spacing between 18 and 21.50 m, – more than double the above-ground lengths of other pier columns – meaning that their vertical elongation and contraction due to seasonal temperature variations can be significantly more pronounced than those of other piers. However, predicting the thermal response of piers partially submerged by water is not trivial. The difference in velocities between clusters 2 and 3 may indicate that PS of piers 8, 9 and 10 on deep foundation poles over the riverbed are more stable than PS of piers 11, 12 and 13 close to the floodplain ground, which is notably subjected to subsidence.

Another hypothesis for the change of PS displacements pattern on the riverbed portion of the bridge is that the hydraulic forces of the river might interfere with the behaviour of the bridge, generating an horizontal transverse component of displacement in the bridge, and making it more difficult to discern the expected patterns of the structural behaviour in normal exercise conditions [49].

7.4 Colle Isarco viaduct case study

The second case study focuses on the Colle Isarco Viaduct, located in a mountainous and sparsely populated area. This setting poses challenges for image co-registration and Reference Point (RP) determination. The viaduct is surrounded by rural areas and forests, which poorly reflect SAR signals, hindering the identification of PS in the MT-InSAR analysis. In ascending geometry, part of the bridge is obscured by a mountain,

preventing the radar signal from reaching it. Additionally, the viaduct and the highway are elevated about 100 m above the valley. This height disparity, combined with the low reflectivity of rural surroundings, further complicates image processing.

7.4.1 Bridge structural characteristics

The Colle Isarco Viaduct is part of the Italian A22 Highway. It was erected in 1968 and opened to traffic in 1971. It consists of two structurally independent parallel viaducts made of reinforced concrete and prestressed concrete with 13 spans, for a total length of 1028.2 m. The piers have variable heights, reaching 70 m. Figure 7.15 shows longitudinal section of the viaduct.

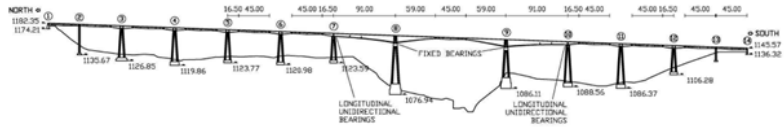

Figure 7.15: Elevation of the A22 Colle Isarco Viaduct. Dimensions in metres.

The static scheme of the viaduct consists of suspended spans that lean on simple cantilever piers, and a central Niagara section. The Niagara section of the bridge, between pier 7 and 10, is 345 m long and comprises two symmetric prestressed concrete box girders, which support a suspended beam 45 m long. Each box girder ends with a 59 m long cantilever, counterbalanced by a back arm with a length of 91 m. Each box girder is composed of 33 box-girder cast-in-place segments with a height varying from 10.93 m at the pier to 2.57 m at the edge. The thickness of the top slab is constant at 0.29 m, while the bottom slab varies from 0.99 m to 0.12 m.

The Colle Isarco Viaduct has experienced a progressive abnormal deflection since its construction, mainly evident at the edge of the 59-m long cantilever, even after many decades. The cause of such behaviour is the combination of different factors: the creep and shrinkage phenomena, the tension loss in precompression cables, the difference in the concrete thickness of the top and bottom slabs, and the load history during the construction and the maintenance works. Just after 2 years from its opening to traffic, level measurements showed a deflection trend with an apparent velocity of over 8 mm/year, which resulted in a 200 mm deflection in 1984, as opposed to a design prediction of fewer than 20 mm [50]. These observations prompted the owner to undertake, between 1988 and 1989, a radical retrofit of the Niagara section to prevent further deflection of

the bridge, consisting in a reduction of the load by replacing the original pavement with a thinner layer of lightweight asphalt. The effect was an evident immediate 70 mm deflection recovery and the disappearance of the deflection drift. However, the deflection drift resumed the following years at an apparent rate of over 2 mm/year. In 2014, the owner of the viaduct performed another critical retrofit intervention, which involved installing an external post-tensioning system within the four main box girders between piers 7 and 10. This intervention led to a recovery of 80 mm deflection and a change from the negative to a positive deflection drift. It is important to highlight that these high displacement gradients can lead to phase ambiguity errors in the MT-InSAR analysis, affecting the results.

Since 2014, two topographic total stations Leica Nova TM50 collimate 72 optical prisms GPR112: 60 anchored along the main spans as measurement points, 12 located in the surrounding area as benchmarks (Figure 7.16). In addition, 82 PT100 platinum resistance thermometers measure the temperature field measurement in the concrete of the main spans to compensate for the displacement data provided by the topographic network [51].

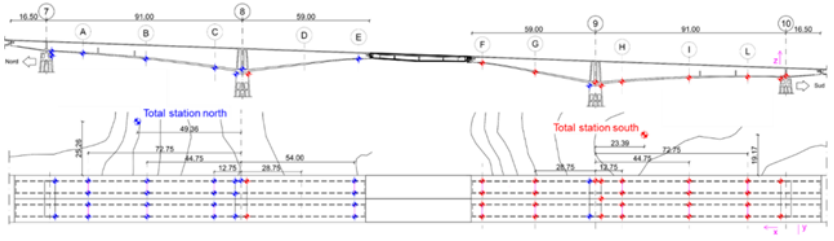

Figure 7.16: Distribution of the optical prisms along the main span of the Colle Isarco Viaduct. Blue prisms are monitored by the total station north, red prisms by the total station south. (For interpretation of the references to colour in this figure legend, the reader is referred to the web version of this article.)

7.4.2 Case study area

Figure 7.17 shows a picture of the A22 Colle Isarco Viaduct and a top view of the case-study area.

The case-study area is close to the Brenner Pass at the border between Italy and Austria. This area is stable as it is not subjected to any significant subsidence phenomena, as visible in the vertical displacement measurement accessible from the European Ground Motion Service (https://egms.land.copernicus.eu/), reported in Figure 7.18.

The viaduct lies in a valley at an altitude of approximately 900 m

(a) (b)

Figure 7.17: (a) Picture of the A22 Colle Isarco Viaduct; (b) Top view of the case-study area, with the viaduct marked with a red rectangle.

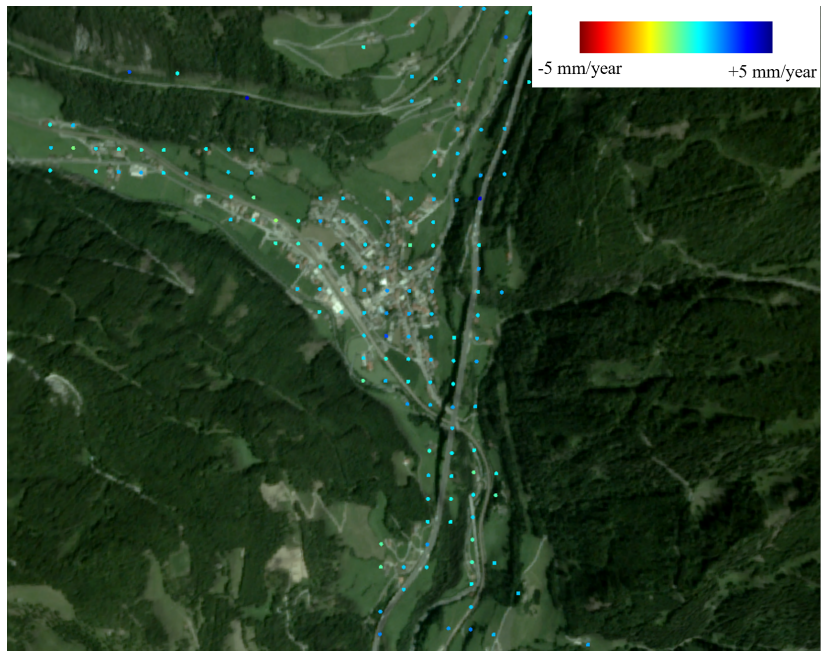

Figure 7.18: Vertical displacement measurements in the case study area from EGMS (https://egms.land.copernicus.eu/).

above sea level, and it is surrounded by mountainous terrain, with steep slopes and rugged topography, and mountain peaks that reach over 2000 m. It is a sparsely populated area, with constructions located at a very different height level with respect to the viaduct and the highway. The region of the case study area with the highest density of man-made structures corresponds to the village of Colle Isarco, which lies on the valley floor, more than 100 m below the viaduct deck. The vegetation covering

the surroundings does not reflect the SAR signal and does not allow the identification of PS. Moreover, the area is prone to seasonal changes, including snow coverage and vegetation growth. These factors can affect InSAR measurement's accuracy and reliability, generating difficulties in image co-registration and Ground Control Point determination, leading to signal decorrelation and shadowing effects, distorting the interferometric phase and reducing the coherence of the extracted PS. To sum up, the location of the bridge makes the analysis of SAR images particularly challenging.

In the case-study area, the alpine climate is characterised by significant seasonal temperature variations, with cold winters and moderately warm summers. Air temperatures vary between $-15°C$ and $30°C$ throughout the year; the concrete temperature has a lower variability range due to thermal inertia, between $-10°C$ and $25°C$, especially in the parts of the structure not directly exposed to irradiation of the sun. Figure 7.19a and 7.19b show, respectively, the measurements acquired by a temperature sensor and an optical prism of the Colle Isarco viaduct monitoring system between UTC 5p.m. and 5:30p.m. from 5 July 2016 to 25 June 2020. The temperature sensor measures the concrete temperature on the lower slab of the eastern box girder over pier 8; the optical prism measures the vertical deflections of the same point. As visible from Figure 7.19, the deformations and deflections of prestressed concrete bridges with a structural scheme similar to the Colle Isarco viaduct strongly respond to temperature variation. Thus, we expect to measure a periodical displacement of the Colle Isarco viaduct from satellite SAR images, which is correlated to seasonal temperature variation. An in-depth study regarding the impact of temperature variations on the deformation of concrete in the main structural elements of the Colle Isarco viaduct was conducted by Caspani et al. in [44].

7.4.3 Dataset and MT-InSAR analysis

Based on the considerations outlined in Section 7.3.3, X-band Stripmap HIMAGE mode CSK imagery was likewise employed in the Colle Isarco Viaduct case study.

For the Colle Isarco Viaduct case study, we consider a dataset of 62 images acquired in descending geometry. The images were acquired from 5 July 2016 to 25 June 2020 at UTC 5:13p.m., covering a 4 year period. The period of analysis was chosen to limit issues of phase ambiguity in MT-InSAR results due to the elastic response experienced by the bridge during the retrofit intervention, performed between 2014–2015. We performed the MT-InSAR data processing with the software SarProZ© (https://www.sarproz.com/), version 'SARPROZ 08-September-2022 16:32:33'.

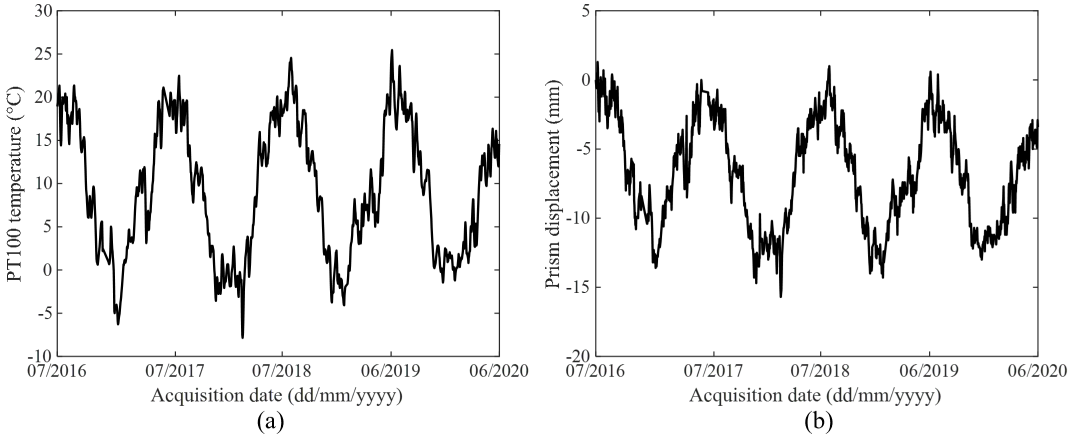

Figure 7.19: Time-series from 05/07/2016 to 15/06/2020 of (a) temperature variation recorded by a PT100 temperature sensor located on the lower slab of the eastern box girder (north lane deck) over pier 8, and (b) vertical displacements of a prism in the same position.

The master image of the dataset corresponds to the date 9 June 2018. Due to the complex topography surrounding Colle Isarco Viaduct, only the images acquired by the descending orbit of the satellite were exploited for this analysis; indeed, in the ascending geometry the bridge is partially covered by the mountains. This is a typical issue affecting bridges and other infrastructures (e.g., dams, bridges, tunnels) in the Alpine Region, and also structures in urbanised areas with high buildings.

The CSK satellite that acquired the images of our dataset has right-side looking-angle with an incidence angle $\theta = 33.9449°$ (i.e., the angle between the LoS and the normal to the ground in our area) and a heading angle $\beta = 10.6095°$ (i.e., the angle between the satellite orbit and the North South direction). The investigated area includes the Colle Isarco Viaduct, and the continuation of the highway infrastructure north of the viaduct. The Colle Isarco village on the valley floor, rural area in the surroundings and mountain slopes are not considered. The reason for this choice is that the surroundings of the Colle Isarco Viaduct are a limit for the success of the MT-InSAR analysis. This is further explained in the following paragraphs about the MT-InSAR analysis steps.

For the differential interferograms generation, we employed the DEM SRTM90 and georeferenced the radar images in coordinates WGS84 using a point located on the highway guard-rail, above the northern abutment of the viaduct, as Reference Point (RP).

The atmospheric-phase noise was estimated and removed from the SAR images. Due to the sparseness and the elevation difference of the

PS candidate targets in the area surrounding the Colle Isarco Viaduct with respect to those on the viaduct itself and on the highway, PS in the surroundings over the valley or mountain slopes must be discarded. Indeed, otherwise, the connections between the candidate PS in the spatial graph appear distant and sparse and the estimation of the parameters affecting the interferometric phase along the connections (i.e., deformation velocity, thermal expansion, and height of the targets) is inaccurate.

Only PS candidate targets on the highway and the viaduct are selected in order to obtain an accurate atmospheric-phase removal.

In the Persistent Scatterer selection step, we don't apply any filter based on the PS temporal coherence. The reason is that we want to include most possible PS in this analysis, since many were excluded in the atmospheric-phase removal step. As a result, we included 639 PS in our analysis. Deformation time-series are extracted for every PS based on the filtered phase data.

7.4.4 MT-InSAR results

We illustrate and discuss the results of the Colle Isarco viaduct case study analysis. Figure 7.20 shows the outputs of the MT-InSAR data processing of our dataset: the temporal coherence of PS and the deformation velocity of PS. The PS are concentrated on the infrastructure, isolated from the surrounding area.

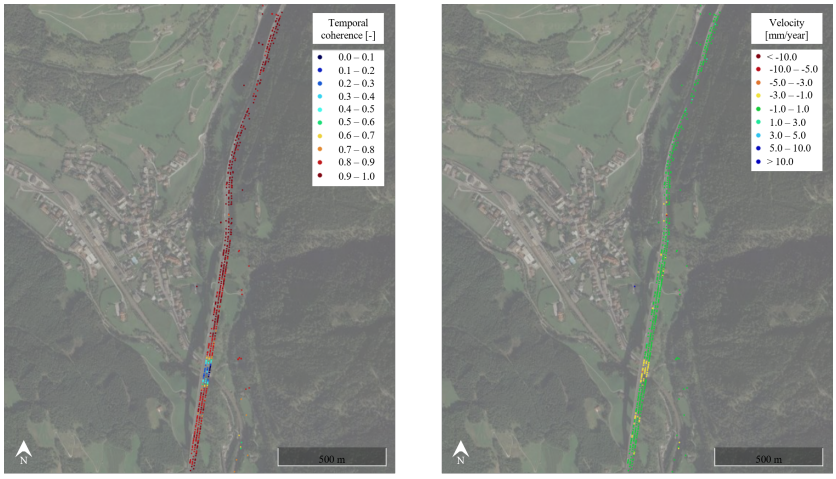

(a) (b)

Figure 7.20: Distribution of the PS identified in the case-study area illustrated in a colour scale representing (a) their temporal coherence, and (b) their displacement velocity along the satellite LoS.

The first thing that immediately stands out by looking at Fig. 7.20a is

the fact that not all the PS are characterised by the same quality. The PS' colours show that the temporal coherence is small (lower than 0.6) over the central span of the viaduct, between piers 8 and 9, while it is higher than 0.8 for all the other PS. That is a symptom of the high displacements experienced by the viaduct's main span throughout the years.

Fig. 7.20b shows most PS coloured in green, indicating nearly negligible deformation velocity ranging between -1.0 and +1.0 mm/year. The only exception is represented by the yellow PS located over the central span of the viaduct, indicating deformation velocity between -3.0 and -1.0 mm/year. This result confirms again the higher deflections experienced by this portion of the viaduct during the time-span of the MT-InSAR analysis. Moreover, it confirms the absence of any long-term subsidence phenomena in the mountainous area where the infrastructure lies, as previously observed from Fig. 7.18.

7.4.5 Expected behaviours

The CSK satellite that acquired the SAR images moved from North to South with a right-looking angle. As a consequence, the sign conventions of PS displacements measured along the LoS are consistent with those previously described in Section 7.3.5, for the Po River Case Study.

The bridge's orientation is nearly parallel to the descending satellite orbit – indeed, the longitudinal axis of the bridge is approximately north–south oriented, like the satellite orbit direction. Specifically, the bridge orientation is $\zeta = 9°$, while the heading angle of the satellite is $\beta = 10.6095°$, so that the viaduct's longitudinal axis orientation is inclined only $1.6°$ with respect to the satellite orbit direction. Due to this orientation, it is impossible to extract horizontal longitudinal displacements of the viaduct from the satellite data.

The static scheme of the viaduct consists of suspended spans that lean on simple cantilever piers, and a central Niagara section. Regarding the expected displacements of the case study, in normal exercise conditions of the bridge we should expect only vertical and longitudinal horizontal displacements induced by environmental loads resulting from the seasonal temperature variations, as previously observed for the Po River Bridge case study.

By combining the considerations regarding the orientation of the bridge relative to the satellite orbit with those concerning its static scheme and expected structural response, we can conclude that the displacements of PS over the bridge measured by the satellite along the LoS are mainly vertical. Specifically, when there is a positive seasonal temperature variation, we expect elongation of the piers supporting the superstructure of the viaduct, meaning positive vertical displacements variation mea-

sured by the satellite (displacement variation directly proportional to the temperature variation). Given the dimensions of the piers, we expect significant vertical displacements induced by environmental loads resulting from seasonal temperature variations. The topographic measurements of the Colle Isarco Viaduct confirm this hypothesis, as visible in Figure 7.19, which shows that the vertical displacements measured by the total station in correspondence of the top of pier 8 reaches maximum total variations of approximately 15 mm.

The expected displacements, possibly observable by satellite measurements, are schematically illustrated in Figure 7.21.

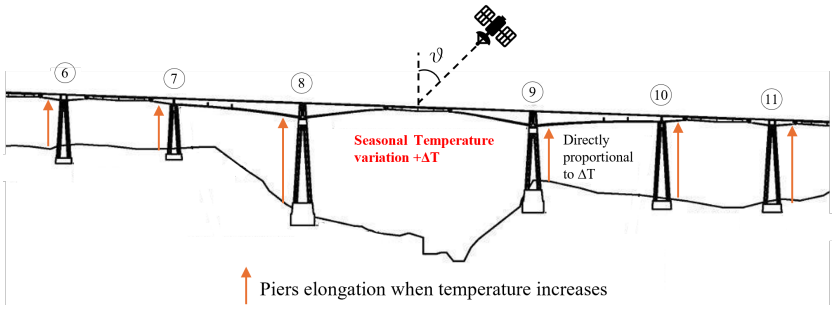

Figure 7.21: Schemes explaining the expected vertical displacements of the piers as seasonal temperature increases.

Based on the static scheme and geometry of the structural elements shown in Figure 7.21, we can estimate the projection of the expected vertical displacements – caused by uniform temperature variation across all piers – onto the satellite LoS. The same procedure reported in Section 7.3.5 is followed, considering only the expected vertical displacements of the piers of the Colle Isarco viaduct.

The annual mean temperature variation in Colle Isarco was determined using data from https://it.climate-data.org, yielding $\Delta T = 20.4°C$. Assuming that the seasonal temperature variation induces a periodic vertical displacement in the piers, the expected amplitude of such displacement projected along the LoS can be calculated using Equation 7.4 (Section 7.3.5). The results varying for different above-ground heights of the piers of the Colle Isarco viaduct are reported in Table 7.4. The mean value is 3.19 mm.

7.4.6 Application and results of the proposed clustering algorithm

Finally, we apply the data driven clustering algorithm presented in Section 7.2 to the PS extracted by means of MT-InSAR in the case study

Table 7.4: Quantitative evaluation of the expected amplitude of periodic structural displacements along the LoS caused by seasonal temperature variation.

	$\boldsymbol{d}_{\mathbf{V,LoS}}\ (mm) = \boldsymbol{d}_{\mathbf{TOT,LoS}}\ (mm)$
Pier 2 (29.08 m)	2.46
Pier 3 (37.68 m)	3.19
Pier 4 (42.44 m)	3.59
Pier 5 (36.17 m)	3.06
Pier 6 (31.39 m)	2.70
Pier 7 (30.44 m)	2.58
Pier 8 (59.19 m)	5.01
Pier 9 (44.19 m)	3.74
Pier 10 (53.15 m)	4.50
Pier 11 (53.34 m)	4.51
Pier 12 (28.18 m)	2.38
Pier 13 (7 m)	0.59
Mean value	3.19

area.

The number of clusters is set to 4 for this analysis, considering the smaller size of the Colle Isarco dataset compared to the Po River bridge case, and the expectation that only one type of structural displacement of the viaduct (direct proportionality to seasonal temperature) is detectable from the satellite data.

The calibration for coefficients α and β yields the same values as those used in the first case study, namely, $\alpha = 0.5$ and $\beta = 2$.

We show and discuss the results of the clustering algorithm application on the case study area. Figure 7.22a displays the PS' distribution in the case-study area, illustrated in a colour scale representing their clustering of belonging; Figure 7.22b displays the PS time-series of displacement grouped in the different clusters, with matching colours to the PS distribution map. The cluster centre is coloured in black.

To aid in the reading and understanding of the results, a fitting of the cluster centroids' time-series is performed. Cluster centroids are fitted using Least Squares Analysis (LSA) with the model function reported in Equation 7.7.

$$\mathbf{y} = q + m \cdot \mathbf{x} + a \cdot cos(2\pi \cdot \mathbf{x} + \phi) \tag{7.7}$$

The model function is similar to the one employed in Section 7.3.6, with the only difference that the periodic component is represented by a positive cosine function, starting with its maximum value. This periodic function fits the air temperature measurements within the time-frame of our dataset, beginning on 5 July, close to when annual temperatures reach their highest point. Similarly as in Section 7.3.6, in cases where the

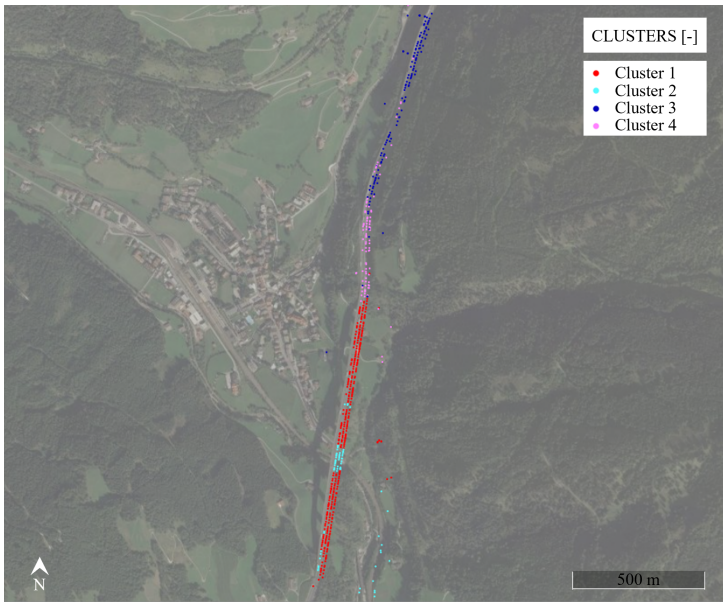

(a)

Figure 7.22: (a) Map of PS in the case-study area illustrated with 4 different colours representing their cluster.

periodic component is not present in the cluster centroids' time-series, the model function is simplified to a linear function by neglecting the periodic term.

The mean displacement velocities (in mm/year) are quite low across the identified clusters, confirming that the area is not affected by any significant subsidence trend, as also illustrated in Figure 7.18. Two clusters (Cluster 1 and Cluster 3) display a clear seasonal periodicity, which is directly proportional to seasonal temperature variations. In contrast, Cluster 2 exhibits distinct characteristics, differing from the others both in mean velocity and periodicity. The reasons for this are discussed below in this Section.

Cluster 1 (red) includes all the PS located on the bridge, except for those on the central span between pier 8 and pier 9, which are part of Cluster 2 (cyan). The two clusters exhibit distinctly different behaviours.

Cluster 1 (red) shows a marked seasonal periodicity, with displacements directly proportional to the seasonal temperature variations, with mean amplitude represented by the centroid's fitting parameter $a = 3.23mm$ (Table 7.5). This behaviour aligns with the expected vertical deformations of the viaduct, which are primarily due to the seasonal elongation and contraction of the piers. Indeed, the theoretical amplitude of the

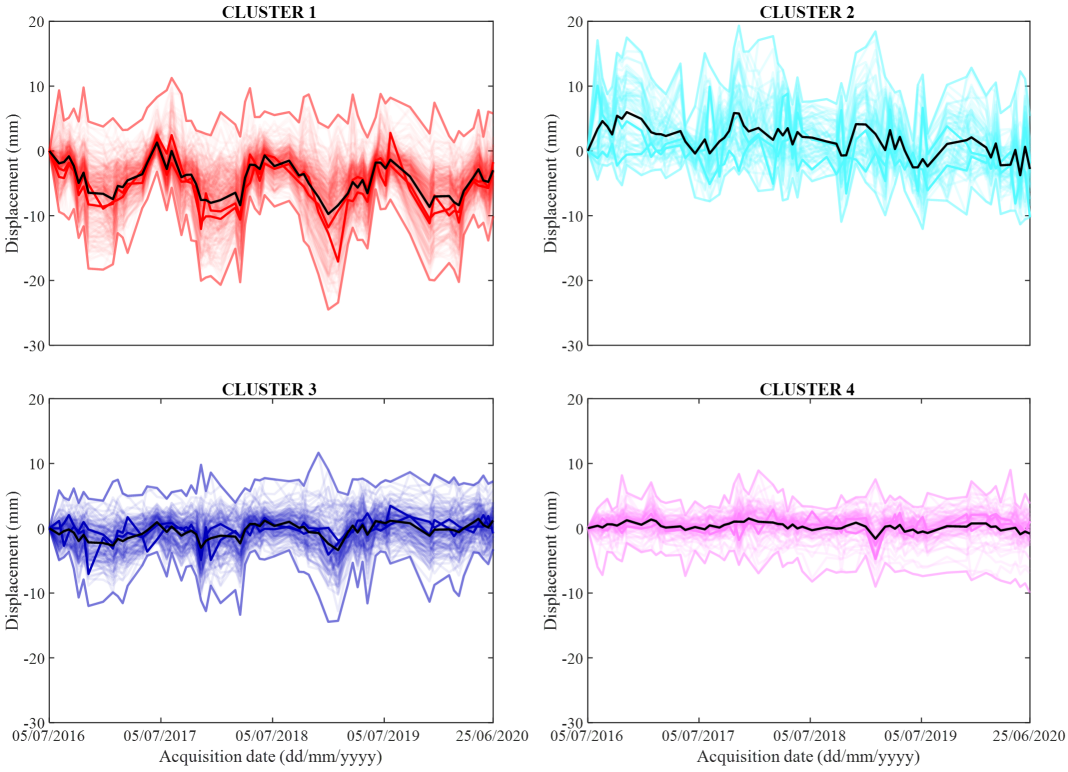

(b)

Figure 7.22: (b) Clusters of the PS time-series of displacement along the LoS, represented with the same colours used in the map.

periodic displacements calculated in Table 7.4 is 3.19 mm, obtained as a mean value considering all different pier heights above ground level. It is important to remember that in this case study, the horizontal longitudinal displacements caused by seasonal temperature variations cannot be detected using the SAR data. As a result, all PS on the bridge are grouped into the same cluster, reflecting consistent behaviour with the expected vertical displacements. This demonstrates the effective performance of the clustering algorithm across different case studies, with varying orientations and geometries.

Cluster 2 (cyan) shows an abnormal behaviour, clearly different from Cluster 1, apparently not following any clear recognizable expected pattern. Indeed, the PS belonging to Cluster 2 match with those with temporal coherence values lower than 0.6, located at the edge of the 59-m long cantilevers of the Niagara section and over the central span (Fig.

*Table 7.5: Clusters centroids' fitting parameters and their standard deviation obtained with LSA.*The fitting parameters found for Cluster 2 do not have interpretable physical meaning due to low temporal coherence of PS in Cluster 2.*

Cluster centroid	**Number of PS for each cluster [%]**	**velocity m [mm/year]**	**amplitude a [mm]**	**phase ϕ [years]**
CLUSTER 1	351 (54.9%)	-0.53 ± 0.13	3.23 ± 0.21	-0.10 ± 0.29
CLUSTER 2	67 (10.5%)	$-1.16 \pm 0.17^{*}$	$-1.51 \pm 0.28^{*}$	$0.17 \pm 0.38^{*}$
CLUSTER 3	133 (20.8%)	0.46 ± 0.08	1.18 ± 0.13	-0.10 ± 0.17
CLUSTER 4	88 (13.8%)	-0.21 ± 0.05	–	–

7.20a). Notably, this span is subjected to higher displacement gradients than the rest of the viaduct, as explained in Section 7.4.1. These high displacement gradients cause phase ambiguity in the MT-InSAR phase unwrapping process, a condition in which the measured interferometric phase becomes uncertain because the actual displacement causes phase shifts beyond half of the radar wavelength. As a consequence, the displacements time-series of PS belonging to Cluster 2 cannot be considered reliable results of the MT-InSAR analysis, and do not reflect the actual displacements of those points. The fitting parameters reported in Table 4 for Cluster 2 do not have interpretable physical meaning, and phase ambiguity should be resolved before attempting interpretation of these PS [52]. This serves as an example of how the algorithm effectively identifies anomalies or differing behaviours in MT-InSAR results across specific sections of the structure.

Above the northern end of the viaduct, two clusters are identified: Cluster 3 (blue) and Cluster 4 (pink). Cluster 3 exhibits a seasonal periodicity, with displacements directly proportional to seasonal temperature variations. Specifically, Cluster 3 detects another highway viaduct located just north of the Colle Isarco viaduct: parts 4–5 and 6 of the Ponticolo viaducts. These are six consecutive prestressed concrete viaducts with similar structural elements and static schemes, consisting of beams simply supported by piers. The height of the piers along Ponticolo viaducts 4–5 and 6 ranges from 15 to 30 m.

The Ponticolo viaducts have a similar orientation to the Colle Isarco viaduct. As a consequence, the horizontal longitudinal displacements of the beams cannot be extracted, and the behaviour of Cluster 3 aligns with the expected vertical deformations caused by the seasonal elongation and contraction of the piers. The displacements range of Cluster 2 is smaller compared to that of Cluster 4, reflecting the shorter height of the Ponticolo viaduct piers relative to those of the Colle Isarco viaduct. This is another interesting result of this case study: with the clustering algorithm, it is possible to identify different viaducts within the same image

without having to define the coordinates of these structures beforehand.

Finally, Cluster 4 (pink) has nearly zero trend and no seasonal periodicity. It includes PS located along the highway on the mountain slope, connecting the Colle Isarco viaduct and the Ponticolo viaducts. The algorithm has allowed us to automatically distinguish between PS belonging to viaducts and those belonging to road sections. This avoids the need to manually identify which PS are part of a bridge, or to define the start and end coordinates of the bridge.

7.5 Discussion

In this Section, critical aspects of the study are discussed. First, we focus on the uncertainties involved in MT-InSAR pre-processing and in the clustering approach. Then, we report an alternative application of the clustering approach to the Po River Bridge case study, in order to analyse the influence of the number of clusters and the choice of metric coefficients. Finally, we outline the limitations of the current research and suggest directions for future development, also considering insights from related studies.

7.5.1 MT-InSAR uncertainties

The input data for the application of our method are PS derived from MT-InSAR analysis. Despite careful processing of SAR datasets for both case studies (7.3.3, 7.4.3), the accuracy of MT-InSAR results is inherently affected by several sources of uncertainty related to both the SAR data and the MT-InSAR processing chain.

In particular, the accuracy of displacement rates is influenced by SAR system parameters such as radar wavelength, spatial resolution, the number and temporal distribution of SAR acquisitions, and the overall observation time span. The density of measurable PS targets on the ground is mainly influenced by the spatial resolution. Specifically, short-wavelength, high-resolution datasets – such as CSK X-band data with 3 x 3 m resolution – enable more accurate detection of infrastructure displacements, allowing capturing variations in the order of a few millimetres between satellite acquisitions [47, 48].

Primary sources of error that arise in the MT-InSAR processing chain, which may lead to noisy or biased results, include:

- phase ambiguity, when the phase unwrapping process does not occur correctly due to displacements larger than half the wavelength of the radar signal between successive satellite passes;
- atmospheric phase delay, where uncorrected atmospheric signals

introduce phase shifts unrelated to ground motion;

- topographic phase removal, where inaccuracies in the DEM can introduce biases in both displacement estimates and geolocation;
- temporal decorrelation, caused by changes in surface properties between acquisitions, which can degrade coherence and reduce the number of reliable PS;
- baseline estimation, where incorrect estimation of the baseline between image pairs can affect phase computation and PS selection.

Several authors have assessed the accuracy of X-band MT-InSAR measurements by comparing them with data obtained from topographic monitoring systems, GNSS observations, or through the use of corner reflectors. These studies report that the accuracy of X-band MT-InSAR displacement measurements is typically in the order of 1–2 mm [10, 52, 53].

7.5.2 Clustering error and number of clusters selection

An assessment of the robustness of the proposed clustering method reliability can be performed using the elbow method, a commonly adopted technique in unsupervised learning.

This technique involves computing the total Within-Cluster Error (WCE) for different values of the number of clusters K. In standard K-Means clustering, the WCE for a cluster k is typically computed as the sum of squared Euclidean distances between each data point assigned to cluster k and its corresponding centroid. In our case, the WCE is calculated using the novel similarity metric applied in the case studies (Equation 7.1, with $\alpha = 0.5$ and $\beta = 2$) [54].

Each value of WCE is listed in a graph were the Y-axis label is the value of WCE and X-axis label is the value of K. When the curve exhibits a distinct “elbow” –that is, a point beyond which the error reduction becomes marginal– this point is considered indicative of the optimal number of clusters. However, identifying this point is often subjective and not always clearly defined, as the curve may show a gradual decrease without a sharp bend, making the ”elbow” less evident.

Figure 7.23 displays the elbow plots obtained for (a) the Po River Bridge case study and (b) the Colle Isarco Viaduct case study, based on the proposed novel metric.

We observe that the WCE decreases as the number of clusters increases, confirming the robustness of the proposed metric. However, no distinct ”elbow” is evident in the curves, particularly for the Po River Bridge case study.

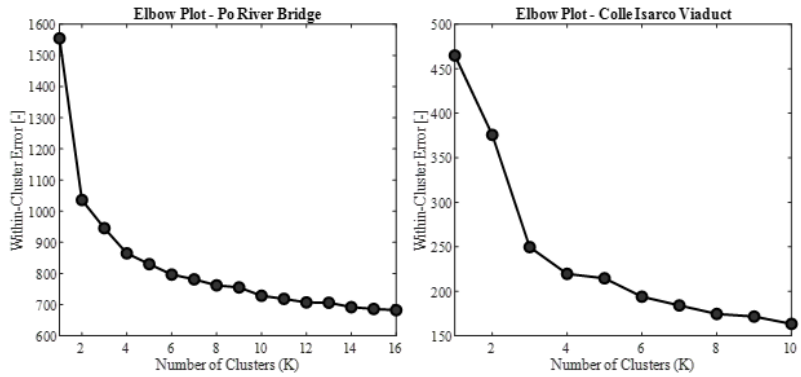

Figure 7.23: Elbow plot for (a) Po River Bridge case study and (b) Colle Isarco Viaduct case study.

It is important to emphasize that the elbow method and other internal validation indices do not account for the interpretative value of clusters or the specific requirements of a given application. These methods are not specifically designed for the novel metric proposed in this study, nor for its SHM-focused context. However, they can serve as a preliminary evaluation tool for assessing the quality of clustering results in relation to the number of clusters.

For the Colle Isarco Viaduct case study, 4 clusters were selected, taking into account both the elbow plot results and the expected behaviours, as discussed in Section 7.4.6.

In the case of the Po River Bridge case study, 12 clusters were chosen, despite a smaller number of clusters could have been selected based solely on the elbow plot.

This choice is justified by the large spatial extent of the dataset, and the numerous different behaviours expected in the case study area based on a priori evaluation, as discussed in Section 7.3.6. A large number of clusters is necessary to capture the full range of behaviours of different physical entities in this case study, enabling effective interpretation of results, and allowing association of similar patterns with their underlying causes.

7.5.3 Impact of the metric coefficients and the number of clusters

To further evaluate the impact of the number of clusters on the proposed clustering algorithm, as well as the influence of the metric coefficients and their relationship with the number of clusters, we present an alternative application of the clustering approach to the Po River Bridge

case study.

In this analysis, the number of clusters was set to 8 (as opposed to 12 used in Section 7.3.6 for the same case study), and the metric coefficients were calibrated to $\alpha = 0.4$ and $\beta = 4$ (instead of $\alpha = 0.5$ and $\beta = 2$ in Section 7.3.6).

The metric required recalibration to ensure that the clustering could still distinguish all different behavioural patterns of the bridge, despite the reduced number of clusters applied to the same area and number of PS. In this calibration, the coefficient β plays a particularly important role. High values of β exponentially increase the metric's term B (related to the spatial proximity of PS, as defined in Equation 7.1 for PS located far apart ($B > 1$), reducing the chances of geographically distant PS being grouped into the same cluster. Conversely, when PS are spatially close ($B < 1$), high values of β exponentially reduce the values of term B, giving greater weight to term A (related to the time-series correlation of PS) in Equation 7.1.

This mechanism enables finer fragmentation of clusters within a fixed distance (specifically, $\mathrm{L}_{\mathrm{bridge}} = 1000\ m$ m), rather than across the entire area, thus enhancing the ability to identify different temporal behaviours within this spatial range.

Figure 7.24 shows the resulting distribution map and displacements time-series clusters. The results are consistent with those shown in Figure 7.13 of Section 7.3.6. Different behaviours identified on the bridge include: Cluster 2 (characterized by direct seasonal periodicity), Cluster 3 (direct seasonal periodicity with a downward trend), and Cluster 4 (inverse seasonal periodicity with a downward trend). However, the separation between clusters representing PS on the bridge and those in the surrounding environment is less distinct.

For example, among PS located on the northern section of the bridge, those exhibiting lower seasonal periodicity are assigned to Cluster 5 – associated with the highway lanes over the northern embankment – making it more difficult to clearly interpret the behavioural pattern of the bridge in this area.

Additionally, several PS over the San Nicolò village – in particular, those with strong correlation to temperature variations – are assigned to Cluster 3, which also includes PS of the bridge. As a result, displacement time-series of PS of the village are blended with those of the bridge exhibiting similar periodicity.

Moreover, the urban complex at north-east and the nearby local road are not assigned to a separate, dedicated cluster, due to the reduced number of total clusters. Consequently, the PS in this region are absorbed into the nearest available clusters, namely Cluster 5 (highway) and Cluster 4

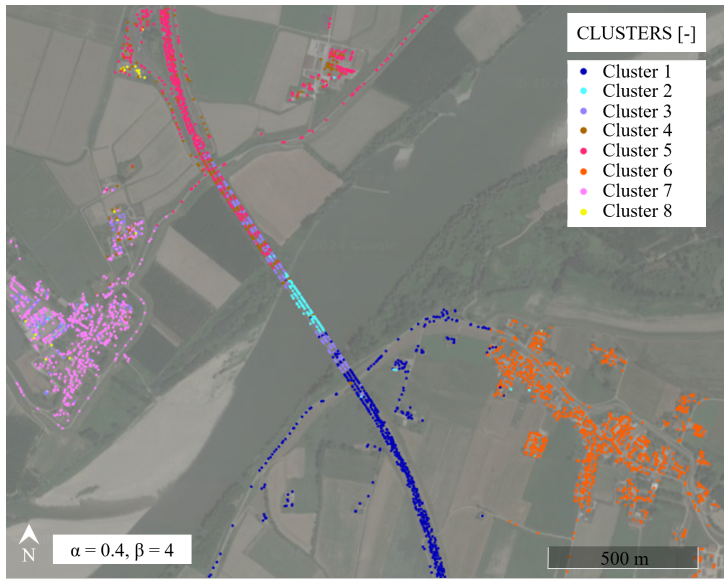

(a)

Figure 7.24: (a) Map of PS in the case-study area illustrated with 8 different colours representing their cluster.

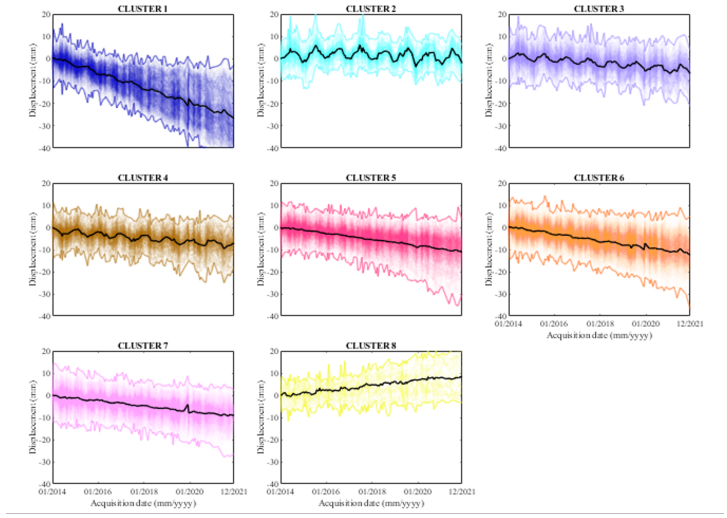

(b)

Figure 7.24: (b) Clusters of the PS time-series of displacement along the LoS, represented with the same colours used in the map.

(bridge).

In conclusion, while the results obtained using a reduced number

of clusters and a recalibrated metric are still satisfactory, employing a higher number of clusters allows for a clearer spatial distinction between different physical entities and facilitates interpretation of the temporal patterns of the bridge and its surroundings.

7.5.4 Limitations and future developments

Despite the novelty and potential of the proposed approach, some limitations must be highlighted:

- The proposed procedure for automated classification of PS still requires calibration and some user inputs. Specifically, the user must define for each case study: (i) the number of clusters; (ii) the values of coefficients α and β.
- The unsupervised nature of the proposed approach makes it inherently challenging to rigorously assess the accuracy of the assigned cluster labels. Ideally, accuracy should be assessed by comparing the clustering results against a reliable ground truth, when available. Alternatively, a time-demanding point-by-point analysis could be performed, assigning labels to each PS based on engineering judgment and comparing them with those produced by the clustering algorithm.
- The algorithm is currently applied to descending orbit datasets, limiting the ability to distinguishing between vertical and horizontal (longitudinal and transverse) displacements of the investigated structures.

To enhance the findings of this study and expand its applicability, future developments should aim to address the following aspects:

- Designing a tailored method to determine the optimal number of clusters, taking into account the geographical extent, PS density, and the expected structural behaviours in the study area. Additional case studies will help refine this aspect and improve scalability.
- Developing a systematic procedure for selecting the coefficients α and β, in relation to the chosen number of clusters and the specific features of each case study.
- Incorporating both ascending and descending datasets in the analysis, to allow the separation of vertical and horizontal displacement components.
- Testing the proposed approach on different datasets, to improve accessibility and replicability. For instance, the open-access Sentinel-

1 mission datasets may offer broader applicability despite lower resolution.

- Linking the observed displacements to structural performance by using FE models to determine displacement thresholds corresponding to service or failure stress states, enabling risk evaluation in terms of limit states. This idea is aligned with the approach proposed by Guzman-Acevedo et al. [15].
- Identifying trend turning points and their directions in PS displacement time-series, as a means to characterize changes driven by climate events and human activity. This approach, applied by Ghaderpour et al. [13], could be particularly relevant for the Po River Bridge case study, where ground movements are influenced by river flow variations. Turning points could also serve as an alternative similarity metric for clustering PS time-series.

7.6 Conclusions

The proposed clustering algorithm has the following features:

- the algorithm enables the rapid and automatic identification of clusters of PS with distinct behaviours such as periodic trends, subsidence, uplift, and stationary zones. It allows the visualization and interpretation of results by means of both time-series and spatial distribution of PS for each cluster representing a predominant behaviour.
- The algorithm takes into account not only the PS time-series of displacements, but also their geographic coordinates. Indeed, the primary objective is to sort PS into clusters based on their temporal movement patterns – identifying periodicities, trends, anomalies, and variations over time. Simultaneously, the spatial proximity of PS exhibiting similar behaviour is considered. This approach allows identifying the behaviours exhibited by PS of the dataset and their association with physical objects in the examined area.
- The algorithm is applicable to various case studies and structures, encompassing different geometries and materials, structural schemes, spatial orientations, geographical position and surrounding environment of the monitored structure.

The data-driven clustering algorithm was tested by applying it to two different case studies: the Po River Bridge case study and the Colle Isarco Viaduct case study. The obtained results were analysed and discussed. It was found that:

- The algorithm allowed distinguishing different structures and separating them from their surroundings. It was possible to observe expected patterns over the bridge and to differentiate the local structural response from global phenomena affecting the whole area. Different types of response across different portions of the same structure were detected, as well as PS showing unreliable behaviour due to low temporal coherence values.
- The algorithm demands minimal calibration efforts and does not require to specify bridges coordinates or technical InSAR data parameters, enabling its utilisation by civil engineers with little expertise in data science techniques and MT-InSAR data processing. However, the user must still specify the number of clusters and calibrate the values for the coefficients α and β accordingly.
- The algorithm fosters rapid and accessible interpretation of MT-InSAR data. It can be integrated into BMS frameworks to quickly assess bridge displacements and their surroundings, enabling infrastructure operators to decide whether to delve deeper into the analysis of any apparent anomaly, or not to investigate further in case that the observed data aligns with the expected structural behaviours, thus speeding up their work.
- The consistency of results obtained in both case studies proves one of the main strengths of the clustering algorithm, which is its adaptability to different case studies conditions and different choices made in the MT-InSAR satellite data processing.

Bibliography

[1] A. Kamariotis, E. Chatzi, and D. Straub, "A framework for quantifying the value of vibration-based structural health monitoring," *Mechanical Systems and Signal Processing*, vol. 184, p. 109708, 2023.

[2] F. Brighenti, V. F. Caspani, G. Costa, P. F. Giordano, M. P. Limongelli, and D. Zonta, "Bridge management systems: A review on current practice in a digitizing world," *Engineering structures*, vol. 321, p. 118971, 2024.

[3] M. F. Bado and J. R. Casas, "A review of recent distributed optical fiber sensors applications for civil engineering structural health monitoring," *Sensors*, vol. 21, no. 5, p. 1818, 2021.

[4] S. Kavitha, R. J. Daniel, and K. Sumangala, "Design and analysis

of mems comb drive capacitive accelerometer for shm and seismic applications," *Measurement*, vol. 93, pp. 327–339, 2016.

[5] M. R. Kaloop and H. Li, "Monitoring of bridge deformation using gps technique," *KSCE Journal of Civil Engineering*, vol. 13, no. 6, pp. 423–431, 2009.

[6] R. Xi, W. Jiang, X. Meng, H. Chen, and Q. Chen, "Bridge monitoring using bds-rtk and gps-rtk techniques," *Measurement*, vol. 120, pp. 128–139, 2018.

[7] F. Scozzese, L. Ragni, E. Tubaldi, and F. Gara, "Modal properties variation and collapse assessment of masonry arch bridges under scour action," *Engineering Structures*, vol. 199, p. 109665, 2019.

[8] L. Iannacone, P. Francesco Giordano, P. Gardoni, and M. Pina Limongelli, "Quantifying the value of information from inspecting and monitoring engineering systems subject to gradual and shock deterioration," *Structural health monitoring*, vol. 21, no. 1, pp. 72–89, 2022.

[9] D. M. Frangopol and S. Kim, *Bridge safety, maintenance and management in a life-cycle context*. CRC Press, 2022.

[10] A. Ferretti, G. Savio, R. Barzaghi, A. Borghi, S. Musazzi, F. Novali, C. Prati, and F. Rocca, "Submillimeter accuracy of insar time series: Experimental validation," *IEEE Transactions on Geoscience and Remote Sensing*, vol. 45, no. 5, pp. 1142–1153, 2007.

[11] B. Yu, T. Niu, J. Zhao, D. Ma, G. Liu, X. Wang, K. Dai, and Y. Gu, "Deformation monitoring and primary driving factor analysis in the coastal area of liaohe oilfield utilizing mt-insar and pca," *PFG–Journal of Photogrammetry, Remote Sensing and Geoinformation Science*, vol. 92, no. 3, pp. 213–234, 2024.

[12] E. Ghaderpour, C. Masciulli, M. Zocchi, F. Bozzano, G. Scarascia Mugnozza, and P. Mazzanti, "Estimating reactivation times and velocities of slow-moving landslides via ps-insar and their relationship with precipitation in central italy," *Remote Sensing*, vol. 16, no. 16, p. 3055, 2024.

[13] E. Ghaderpour, P. Mazzanti, F. Bozzano, and G. S. Mugnozza, "Ground deformation monitoring via ps-insar time series: An industrial zone in sacco river valley, central italy," *Remote Sensing Applications: Society and Environment*, vol. 34, p. 101191, 2024.

[14] S. Selvakumaran, C. Rossi, A. Marinoni, G. Webb, J. Bennetts, E. Barton, S. Plank, and C. Middleton, "Combined insar and terrestrial structural monitoring of bridges," *IEEE Transactions on Geoscience and Remote Sensing*, vol. 58, no. 10, pp. 7141–7153, 2020.

[15] G. M. Guzman-Acevedo, G. E. Vazquez-Becerra, J. A. Quintana-Rodriguez, J. R. Gaxiola-Camacho, M. Anaya-Diaz, J. C. Mediano-Martinez, and F. J. C. Viramontes, "Structural health monitoring and risk assessment of bridges integrating insar and a calibrated fe model," in *Structures*, vol. 63, p. 106353, Elsevier, 2024.

[16] R. Lorenz, Y. Petryna, C. Lubitz, O. Lang, and V. Wegener, "Thermal deformation monitoring of a highway bridge: Combined analysis of geodetic and satellite-based insar measurements with structural simulations," *Journal of Civil Structural Health Monitoring*, vol. 14, no. 5, pp. 1237–1255, 2024.

[17] S. Quqa, A. Palermo, F. Ubertini, and A. Marzani, "Regional-scale bridge condition monitoring using insar displacements and environmental data," *Structural Health Monitoring*, vol. 24, no. 4, pp. 2271–2291, 2025.

[18] D. Perissin, "Interferometric sar multitemporal processing: Techniques and applications," in *Multitemporal Remote Sensing: Methods and Applications*, pp. 145–176, Springer, 2016.

[19] V. Macchiarulo, P. Milillo, C. Blenkinsopp, and G. Giardina, "Monitoring deformations of infrastructure networks: A fully automated gis integration and analysis of insar time-series," *Structural Health Monitoring*, vol. 21, no. 4, pp. 1849–1878, 2022.

[20] D. Cusson, C. Rossi, and I. F. Ozkan, "Early warning system for the detection of unexpected bridge displacements from radar satellite data," *Journal of Civil Structural Health Monitoring*, vol. 11, no. 1, pp. 189–204, 2021.

[21] F. Brighenti, M. F. Bado, F. Romeo, and D. Zonta, "Forecasting bridge damage within a predictive structural reliability-based dss," *Automation in Construction*, vol. 168, p. 105740, 2024.

[22] A. Montisci and M. C. Porcu, "A satellite data mining approach based on self-organized maps for the early warning of ground settlements in urban areas," *Applied Sciences*, vol. 12, no. 5, p. 2679, 2022.

[23] C. M. Bishop, *Pattern recognition and machine learning by Christopher M. Bishop*, vol. 400. Springer Science+ Business Media, LLC Berlin, Germany:, 2006.

[24] G. James, D. Witten, T. Hastie, and R. Tibshirani, *An introduction to statistical learning: with applications in R*, vol. 103. Springer, 2013.

[25] K. P. Murphy, *Machine learning: a probabilistic perspective*. MIT press, 2012.

[26] A. Saxena, M. Prasad, A. Gupta, N. Bharill, O. P. Patel, A. Tiwari, M. J. Er, W. Ding, and C.-T. Lin, "A review of clustering techniques and developments," *Neurocomputing*, vol. 267, pp. 664–681, 2017.

[27] K. Tabianan, S. Velu, and V. Ravi, "K-means clustering approach for intelligent customer segmentation using customer purchase behavior data," *Sustainability*, vol. 14, no. 12, p. 7243, 2022.

[28] X. Zheng, Q. Lei, R. Yao, Y. Gong, and Q. Yin, "Image segmentation based on adaptive k-means algorithm," *EURASIP Journal on Image and Video Processing*, vol. 2018, no. 1, pp. 1–10, 2018.

[29] M. Z. Hossain, M. N. Akhtar, R. B. Ahmad, and M. Rahman, "A dynamic k-means clustering for data mining," *Indonesian Journal of Electrical engineering and computer science*, vol. 13, no. 2, pp. 521–526, 2019.

[30] V. Prasannakumar, H. Vijith, R. Charutha, and N. Geetha, "Spatio-temporal clustering of road accidents: Gis based analysis and assessment," *Procedia-social and behavioral sciences*, vol. 21, pp. 317–325, 2011.

[31] P. Govender and V. Sivakumar, "Application of k-means and hierarchical clustering techniques for analysis of air pollution: A review (1980–2019)," *Atmospheric pollution research*, vol. 11, no. 1, pp. 40–56, 2020.

[32] S. Aghabozorgi, A. S. Shirkhorshidi, and T. Y. Wah, "Time-series clustering–a decade review," *Information systems*, vol. 53, pp. 16–38, 2015.

[33] M. A. Khalili, L. Guerriero, S. Coda, C. Sellers, D. Calcaterra, and D. Di Martire, "Assessment of mt-insar processing techniques for slow-moving landslides monitoring in cuenca (ecuador) through

double-band sar satellite," *Italian journal of engineering geology and environment*, pp. 81–88, 2023.

[34] D. Roque, A. P. Falcão, D. Perissin, C. Amado, J. V. Lemos, and A. Fonseca, "Sarclust—a new tool to analyze insar displacement time series for structure monitoring," *Sustainability*, vol. 15, no. 4, p. 3728, 2023.

[35] S. M. Mirmazloumi, A. F. Gambin, R. Palamà, M. Crosetto, Y. Wassie, J. A. Navarro, A. Barra, and O. Monserrat, "Supervised machine learning algorithms for ground motion time series classification from insar data," *Remote Sensing*, vol. 14, no. 15, p. 3821, 2022.

[36] V. Gagliardi, F. Tosti, L. B. Ciampoli, F. D'Amico, A. M. Alani, M. L. Battagliere, and A. Benedetto, "Monitoring of bridges by mt-insar and unsupervised machine learning clustering techniques," in *Earth Resources and Environmental Remote Sensing/GIS Applications XII*, vol. 11863, pp. 132–140, SPIE, 2021.

[37] W. Zhu, F. Hu, and F. Xu, "Post-processing of insar deformation time series using clustering-based pattern identification," *Journal of Beijing Institute of Technology*, vol. 32, no. 6, pp. 704–716, 2023.

[38] A. Tiwari and M. Shirzaei, "A novel machine learning and deep learning semi-supervised approach for automatic detection of insar-based deformation hotspots," *International Journal of Applied Earth Observation and Geoinformation*, vol. 126, p. 103611, 2024.

[39] G. Martin, A. Hooper, T. J. Wright, and S. Selvakumaran, "Blind source separation for mt-insar analysis with structural health monitoring applications," *IEEE Journal of Selected Topics in Applied Earth Observations and Remote Sensing*, vol. 15, pp. 7605–7618, 2022.

[40] S. Ghosh and S. K. Dubey, "Comparative analysis of k-means and fuzzy c-means algorithms," *International Journal of Advanced Computer Science and Applications*, vol. 4, no. 4, 2013.

[41] S. Askari, "Fuzzy c-means clustering algorithm for data with unequal cluster sizes and contaminated with noise and outliers: Review and development," *Expert Systems with Applications*, vol. 165, p. 113856, 2021.

[42] J. Paparrizos and L. Gravano, "k-shape: Efficient and accurate clustering of time series," in *Proceedings of the 2015 ACM SIGMOD international conference on management of data*, pp. 1855–1870, 2015.

[43] E. Schubert, J. Sander, M. Ester, H. P. Kriegel, and X. Xu, "Dbscan revisited, revisited: why and how you should (still) use dbscan," *ACM Transactions on Database Systems (TODS)*, vol. 42, no. 3, pp. 1–21, 2017.

[44] V. F. Caspani, D. Tonelli, F. Poli, and D. Zonta, "Designing a structural health monitoring system accounting for temperature compensation," *Infrastructures*, vol. 7, no. 1, p. 5, 2021.

[45] H. Abdel-Jaber and B. Glisic, "Monitoring of long-term prestress losses in prestressed concrete structures using fiber optic sensors," *Structural Health Monitoring*, vol. 18, no. 1, pp. 254–269, 2019.

[46] G. Crotti and A. Cigada, "Scour at river bridge piers: real-time vulnerability assessment through the continuous monitoring of a bridge over the river po, italy," *Journal of Civil Structural Health Monitoring*, vol. 9, no. 4, pp. 513–528, 2019.

[47] F. Bovenga, A. Belmonte, A. Refice, G. Pasquariello, R. Nutricato, D. O. Nitti, and M. T. Chiaradia, "Performance analysis of satellite missions for multi-temporal sar interferometry," *Sensors*, vol. 18, no. 5, p. 1359, 2018.

[48] D. Perissin, "Geometric processing: Active sensor modeling and calibration (sar)," 2018.

[49] D. Tonelli, V. F. Caspani, A. Valentini, A. Rocca, R. Torboli, A. Vitti, D. Perissin, and D. Zonta, "Interpretation of bridge health monitoring data from satellite insar technology," *Remote Sensing*, vol. 15, no. 21, p. 5242, 2023.

[50] D. Tonelli, A. Beltempo, C. Cappello, O. S. Bursi, and D. Zonta, "Reliability analysis of complex structures based on bayesian inference," *Structural Health Monitoring*, vol. 22, no. 5, pp. 3481–3497, 2023.

[51] C. Cappello, A. Beltempo, A. Bonelli, C. Costa, D. Bolognani, O. S. Bursi, D. Zonta, *et al.*, "Advanced monitoring system applied to colle isarco viaduct," in *8th European Workshop on Structural Health Monitoring, EWSHM 2016*, vol. 1, pp. 327–336, 2016.

[52] D. Tonelli, A. Valentini, A. Rocca, S. Zorzi, A. Lotti, and D. Zonta, "Uncertainty quantification of satellite insar-monitoring of bridges: a case study," *ce/papers*, vol. 6, no. 5, pp. 900–906, 2023.

[53] A. Alonso-Díaz, D. Roque, M. Solla, and J. N. Lima, "Comparative analysis of mt-insar algorithms supported by gnss data and corner reflectors: Assessing performance and accuracy," *Procedia Computer Science*, vol. 239, pp. 1460–1466, 2024.

[54] M. Raeisi and A. B. Sesay, "A distance metric for uneven clusters of unsupervised k-means clustering algorithm," *IEEE Access*, vol. 10, pp. 86286–86297, 2022.

8. Designing a Structural Health Monitoring System Accounting for Temperature Compensation

This chapter contains the post-print of

> **Caspani, V. F.**, Tonelli, D., Poli, F., Zonta, D. (2021). Designing a structural health monitoring system accounting for temperature compensation. Infrastructures, 7(1), 5, https://doi.org/10.3390/infrastructures7010005.

as published in the Journal *Infrastructures*, differing only from the published article in terms of layout, formatting, and notation.

Abstract

Structural health monitoring is effective if it allows us to identify the state of a structure with an appropriate level of confidence. The estimation of the uncertainty of the state parameter is relatively straightforward a posteriori, i.e., when monitoring data are available. However, monitoring observations are not available when designing a monitoring system; therefore, the expected uncertainty must be estimated beforehand. This paper proposes a framework to evaluate the effectiveness of a monitoring system accounting for temperature compensation. This method is applied to the design process of a structural health monitoring system for civil infrastructure. In particular, the focus is on the key state parameters representing the structural long-term response trend, e.g., due to creep and shrinkage effects, and the tension losses in prestressed concrete bridges. The result is a simple-to-use equation that estimates the expected uncertainty of a long-term response trend of temperature-compensated response measurements in the design phase. The equation shows that the state parameter uncertainty is affected by the measurement and model uncertainties, the start date and duration of the monitoring activity, and the sampling frequency. We validated our approach on a real-life case study: the Colle Isarco viaduct. We verified whether the pre-posterior estimation of expected uncertainty, performed with the experimented approach, is consistent with the real uncertainty estimated a posteriori based on the monitoring data.

Keywords:
structural health monitoring; temperature compensation; monitoring system design; monitoring capacity; pre-posterior analysis; long-term struc-

tural response; parameter estimation; uncertainty quantification; Bayesian data analysis; prestressed concrete bridge.

Glossary

In this section, the authors provide a brief glossary of the notation involved in the present paper.

DI	Damage Indicator
N	total number of samples
$\boldsymbol{y}$	response vector
$\boldsymbol{T}$	temperature vector
$\boldsymbol{t}$	timestamp vector
$\boldsymbol{z}$	residuals vector
T_0	reference temperature value
t_0	reference time value
y_0	offset
m	trend of response variation
α	thermal expansion coefficient
$\boldsymbol{\theta}$	parameters vector
$\boldsymbol{D}$	Jacobian matrix
μ_m	prior mean of parameter m
μ_α	prior mean of parameter α
$\boldsymbol{\mu_\theta}$	a priori parameters mean value
σ_m	prior uncertainty of parameter m
σ_α	prior uncertainty of parameter α
$\boldsymbol{\Sigma_\theta}$	a priori parameters covariance matrix
σ^2_{LH}	residuals variance (likelihood variance)
$\rho_{\boldsymbol{tT}}$	Pearson correlation between time and temperature vectors
$\sigma_{m,\text{pp}}$	pre-posterior uncertainty of parameter m
f_s	acquisition frequency
σ_{model}	model uncertainty
σ_y	response measurements uncertainty
σ_T	temperature measurements uncertainty
$n_i(\sigma^2)$	zero-mean normal noise with variance σ^2
$\sigma_{m\|\boldsymbol{y}}$	posterior uncertainty of parameter m, given the measured response $\boldsymbol{y}$
$\mu_{m\|\boldsymbol{y}}$	posterior mean value of parameter m, given the measured response $\boldsymbol{y}$
η_{exp}	expected (preposterior) effectiveness of the monitoring system

η_{real}	real (posterior) effectiveness of the monitoring system
$\boldsymbol{e}_{m,\text{pp}}$	error in the pre-posterior estimation of the uncertainty of parameter m

8.1 Introduction

When monitoring a civil structure, the purpose is to identify a number of key state parameters–including modal frequencies, long-term strain trends and damage indicators (DIs) [1, 2]–which are representative of its health state. The monitoring is successful if these parameters can be identified with an appropriate level of confidence, keeping their uncertainty below an acceptable target value [3]. Acceptable uncertainty normally depends on the nature of the physical problem that is being investigated and could be required by the user of the monitoring information within the management framework of the infrastructure [4, 5]. In any case, controlling parameter uncertainty is as important as the identification of the parameter values themselves.

Estimating the uncertainty of key state parameters is relatively straightforward a posteriori, i.e., when monitoring data are available. Data analysis methods for the estimation of the posterior uncertainty of parameters range from plain least squares [6] to more sophisticated Markov-chain Monte Carlo sampling [7, 8] and to other probabilistic machine learning techniques [9]. However, monitoring observations are not yet available when designing a monitoring system; therefore, in order to understand whether a monitoring strategy (the choice of sensors, sensor placement and acquisition protocols) is suitable, it is necessary to estimate an expected uncertainty of the key state parameters beforehand. This expected uncertainty is indeed an a priori estimation (i.e., before acquiring any data) of posterior uncertainty: it is sometimes referred to, in short, as pre-posterior uncertainty, and the estimation process of this value is known as pre-posterior analysis [3].

The optimal sensor placement is a typical instance of bridge monitoring problems solved through pre-posterior analysis: the problem is the choice of the optimal configuration of a fixed number of sensors to maximize the acquired information. Papadimitriou et al. [10] proposed a method based on the minimization of information entropy, defined as the parameter that quantifies the uncertainty of a random variable; Udwadia [11] proposed a method based on the maximization of the Fisher information matrix norm; Fedorov and Hackl proposed the individuation of the optimal sensor configuration in the one that minimizes the coefficients of the variance and covariance matrix [12]. In all of these

problems, the choice of the configuration and technical specifications of sensors is based on the minimization of a value representing the expected uncertainty of the key state parameters.

This paper focuses on a different typology of bridge monitoring problems, where the key state parameters to be identified are long-term response trends, e.g., strain ($\mu\epsilon/year$), deflection ($mm/year$) or rotation ($\mu rad/year$) trends. Long-term response drifts are very useful to predict the future behaviour of a structure, and to understand ahead of time whether the bridge may transit towards a damaged state (e.g., cracking) or exceed the value for the serviceability limit (e.g., excessive deflection). Sudden changes in the response trends are also typical symptoms of the occurrence of damage (e.g., the failure of one or more prestressing tendons) [13].

Long-term deflection trends are particularly evident in prestressed concrete bridges [14, 15, 16]. Hubler et al. [17] analysed the vertical deflection of 63 bridges with different structural types, ages, and deterioration states. They pointed out that all of the bridges experienced a long-term deflection trend and exceeded the design predictions. They also developed a predictive model of creep and shrinkage, named Model B3 [18], for a more realistic assessment of long-term concrete phenomena, which significantly affect the durability and life-long functionality of bridges. This model better predicts the experimental evidence than older ones commonly used in bridge design, such as ACI 209 [19], CEB [20], and EN1992 [21]. In particular, it clearly explains the excessive deformation and deflection of prestressed reinforced concrete bridges with box girder sections (e. g., Colle Isarco Viaduct [22] and Koror-Babeldaob Bridge [23]). Another frequent parameter is the trend in the loss of prestressing force [24].

Usually, the long-term response trends of bridges have a small entity, and their typical values are lower than 30 $\mu\epsilon/year$ for strains, 0.50 $mm/year$ for deflections, and 10 $\mu rad/year$ for rotations [17, 25]. Hence, these trends are difficult to recognize in a data record that is strongly affected by traffic loads and temperature variation. The use of indirect measurement produces additional uncertainty and noise. For example, the loss of prestress in the tendons is commonly estimated indirectly using strain sensors embedded in the concrete [25, 26], as direct measurement methods (e.g., using load cells) are often unfeasible.

Among the different sources of uncertainty, temperature is usually the most important by far [27]. Indeed, besides the complex phenomena that can occur at elevated temperatures [28, 29], daily and seasonal temperature variations also have a relevant effect on structural responses. For example, the value of the permanent contraction drift in a concrete

member due to creep or shrinkage typically ranges around a few $\mu\epsilon$ per year, while the sole daily thermal variation is in the order of 100–200 $\mu\epsilon$ per day [30]. Extracting that drift requires us to perform a thermal compensation on a signal dominated by the thermal effect, and this will inevitably introduce some errors that must be controlled. When data are available, thermal compensation can be performed by fitting monitoring data with a model that considers the effects of temperature [31]. By fitting the monitoring data with a probabilistic method [6], the posterior uncertainty introduced by the thermal compensation can be quantified as well, in order to evaluate whether its magnitude is acceptable or not.

However, at the design stage, no monitoring system is installed and no recording is available. As such, how is it possible to predict the error introduced by the thermal compensation? How can we design a proper monitoring system to keep the uncertainty below the limit values?

This paper aims to answer these questions by introducing a logical approach for a pre-posterior estimation of the expected uncertainty of a long-term structural response trend. The proposed formulation considers the errors related to temperature compensation, sensor performance, and the interpretation model. It allows the estimation of the expected uncertainty before monitoring data are available, thus helping monitoring system designers to answer the following design questions: (i) What sensor technology and measurement accuracy are required? (ii) What should be the duration of the monitoring, in order to verify the target uncertainty? (iii) What is the minimum sampling frequency to satisfy the target uncertainty, given a certain monitoring duration?

This paper is organized as follows. Section 8.2 outlines the underlying assumptions of the approach, and the development of the formulation for the evaluation of the uncertainty of the trend parameters. Section 8.3 contains the analysis of the variation of the expected uncertainty of the trend parameters according to the sensor performance, model uncertainty, sampling frequency, monitoring duration and start date of the monitoring acquisition. Section 8.4 introduces the Colle Isarco Viaduct case study [32] and describes the monitoring system that is currently installed on it. The Colle Isarco Viaduct is one of the longest statically determinate, prestressed concrete highway bridges in the European Alpine region. An abnormal progressive deflection of the main span has been observed on it, due to a combination of creep effects and the loss in prestressing force; recently, a drastic retrofit intervention was performed on the structure [22]. In Section 8.5, the approach for the estimation of the pre-posterior uncertainty of the long-term local-strain trend is applied on the concrete box girders of the Colle Isarco Viaduct. Furthermore, a pre-posterior calculation is performed by the analysis of different ap-

proaches: (1) in the first, the temperature is modelled as a sine function; (2) in the second, the temperature is modelled as a sine function with the addition of Gaussian noise. The uncertainty of the trend parameter is calculated a posteriori based on the monitoring data, then the pre-posterior and posterior results are compared in order to validate the approach used. Finally, in Section 6, some conclusions are drawn.

8.2 Problem Statement and Formulation

Assume that we are monitoring the response y (e.g., displacement, deflection, rotation, stress, strain, modal frequency) of a structural element, and that this response is strongly affected by temperature T. Assume that the monitoring consists of a total number of N samples, and indicate with y_i and T_i the response and temperature sample simultaneously recorded at time t_i, with index $i = 1, \ldots, N$. Let us indicate with N x 1 vectors $\boldsymbol{y}$, $\boldsymbol{T}$, and $\boldsymbol{t}$, respectively. Assume that the measurements are independent, and that a daily thermal compensation has been performed, while the measurements are not compensated for the seasonal thermal variations.

It is often convenient to express time and temperature in relative terms: label $\Delta t = t_i - t_0$ and $\Delta T = T_i - T_0$ where t_0 and T_0 are an arbitrary reference time and temperature. For instance, t_0 could be the starting time of the monitoring, and $T0$ could be equal to $0\ ^\circ C$.

Let m be the permanent trend of variation over the time of the response $y(t)$ (e.g., the deflection trend of a cantilever bridge, the local contraction or expansion trend of concrete), purged from the seasonal temperature effect. The goal is to identify the most probable value of m and its uncertainty σ, given the monitoring observations. For this purpose, we define a probabilistic interpretation model, stating the relationship between measurements y_i, temperature T_i and time t_i.

(1) Assume a linear interpretation model, in the form:

$$y_i = y_0 + m \cdot \Delta t_i + \alpha \cdot \Delta T_i + z_i \tag{8.1}$$

where

- y_0 is an offset parameter representing the ideal strain at time t_0 and temperature T_0.
- α is the apparent thermal expansion coefficient. Because the thermal expansion coefficients of common building materials do not show significant variations within the range of temperatures where they are designed to be used [21], α is assumed to be a constant value regardless of the temperature changes.

- m is the variation trend over time, which is the object of the estimation. It is the gradient of the linear model with respect to time. It expresses the linear trend over time of $y(t)$ purged from temperature effects, and includes all long-term effects. We model the long-term effects with a linear trend because we consider the measurements acquired during a relatively short time interval (one–two years of monitoring) [7].
- z_i is the residual, the difference between the statistically independent observation y_i and the nominal value of the model, $y_0 + m \cdot \Delta t_i + \alpha \cdot \Delta T_i$.
- In practice, the interpretation model that connects the temperature, time, and response measurements is controlled by three unknown parameters, clustered into the vector $\boldsymbol{\theta} = \{y_0,\ m,\ \alpha\}$.
- Let us label $\boldsymbol{D}$ the Jacobian matrix of the interpretation model with respect to the parameters:

$$\boldsymbol{D} = \begin{bmatrix} \dfrac{\partial y}{\partial y_0} & \dfrac{\partial y}{\partial m} & \dfrac{\partial y}{\partial \alpha} \end{bmatrix} = \begin{bmatrix} 1 & \Delta t_1 & \Delta T_1 \\ \vdots & \vdots & \vdots \\ 1 & \Delta t_N & \Delta T_N \end{bmatrix} = \begin{bmatrix} \mathbf{1} & \boldsymbol{\Delta t} & \boldsymbol{\Delta T} \end{bmatrix} \tag{8.2}$$

  As a result, Equation 8.1 can be written in a matrix form:

$$\boldsymbol{y} = \boldsymbol{D} \cdot \boldsymbol{\theta} + \boldsymbol{z} \tag{8.3}$$

(2) A priori model parameters are Gaussian independent random variables with a mean value $\boldsymbol{\mu_\theta}$ and covariance $\boldsymbol{\Sigma_\theta}$ equal to

$$\boldsymbol{\Sigma_\theta} = \begin{bmatrix} \sigma_{y_0}^2 & 0 & 0 \\ 0 & \sigma_\alpha^2 & 0 \\ 0 & 0 & \sigma_m^2 \end{bmatrix} \tag{8.4}$$

(3) Residuals vector $\boldsymbol{z}$ is distributed as zero-mean Gaussian noise with known variance σ_{LH}^2.

The goal is to estimate the most probable value of parameter m and its uncertainty $\sigma_{m|\boldsymbol{y}}$ based on monitoring observation $\boldsymbol{y}$; to do so, the prior distribution of the model parameter $p(\boldsymbol{\theta})$ is updated into the posterior distribution $p(\boldsymbol{\theta}|\boldsymbol{y})$ through Bayes' rule [33]:

$$p(\boldsymbol{\theta}|\boldsymbol{y}) = \frac{p(\boldsymbol{y}|\boldsymbol{\theta}) \cdot p(\boldsymbol{\theta})}{p(\boldsymbol{y})} \tag{8.5}$$

where $p(\boldsymbol{y}|\boldsymbol{\theta})$ is the likelihood function, i.e., the probability of observing measurement $\boldsymbol{y}$ given the interpretation model and the parameters vector $\boldsymbol{\theta}$; $p(\boldsymbol{y})$ is a normalization constant referred to as evidence.

According to Hp. (2) and Hp. (3) (linear Gaussian model), the joint probability distribution $p(\boldsymbol{y}|\boldsymbol{\theta}) \cdot p(\boldsymbol{\theta})$ over parameters vector $\boldsymbol{\theta}$ is Gaussian [33]. The aim is to estimate the mean values of the model parameters that maximize the posterior probability distribution $p(\boldsymbol{\theta}|\boldsymbol{y})$, $\boldsymbol{\theta}_{\text{MAP}}$, and their covariance matrix $\boldsymbol{\Sigma}_{\boldsymbol{\theta}|\boldsymbol{y}}$.

$$\boldsymbol{\theta}_{\text{MAP}} = \arg\max_{\theta} p(\boldsymbol{\theta}|\boldsymbol{y}) = \arg\max_{\theta} \{p(\boldsymbol{y}|\boldsymbol{\theta}) \cdot p(\boldsymbol{\theta})\} \tag{8.6}$$

In practice, it is more convenient to maximize the log of a Gaussian posterior distribution $p(\boldsymbol{\theta}|\boldsymbol{y})$ than the Gaussian distribution itself. Indeed, the logarithm is a monotonically increasing function of its argument, and the maximization of the log of a function is equivalent to the maximization of the function itself [33]. As a result, Equation 8.6 becomes:

$$\begin{aligned} \boldsymbol{\theta}_{\text{MAP}} &= \arg\max_{\theta} \{\log p(\boldsymbol{y}|\boldsymbol{\theta}) + \log p(\boldsymbol{\theta})\} \\ &= \arg\min_{\theta} \left\{ \frac{1}{2 \cdot \sigma_{\text{LH}}^2} \boldsymbol{z}^T \boldsymbol{z} + \frac{1}{2} (\boldsymbol{\theta} - \boldsymbol{\mu}_{\boldsymbol{\theta}})^{\text{T}} \boldsymbol{\Sigma}_{\boldsymbol{\theta}}^{-1} (\boldsymbol{\theta} - \boldsymbol{\mu}_{\boldsymbol{\theta}}) \right\} \end{aligned} \tag{8.7}$$

The value of $\boldsymbol{\theta}$ that maximizes $p(\boldsymbol{\theta}|\boldsymbol{y})$ can be calculated by setting as equal to zero the derivative of the log-posterior with respect to $\boldsymbol{\theta}$, while the inverse of the a posteriori covariance matrix can be calculated as the second-order derivative of the log-posterior with respect to $\boldsymbol{\theta}$. As a result, by combining Equations 8.2 and 8.7, we arrive at

$$\begin{cases} \boldsymbol{\theta}_{\text{MAP}} &= \boldsymbol{\mu}_{\boldsymbol{\theta}} + \dfrac{1}{\sigma_{\text{LH}}^2} \boldsymbol{\Sigma}_{\boldsymbol{\theta}|\boldsymbol{y}} \boldsymbol{D}^{\text{T}} \left(\boldsymbol{y} - \boldsymbol{D} \cdot \boldsymbol{\mu}_{\boldsymbol{\theta}} \right) \\ \boldsymbol{\Sigma}_{\boldsymbol{\theta}|\boldsymbol{y}}^{-1} &= \dfrac{1}{\sigma_{\text{LH}}^2} \boldsymbol{D}^{\text{T}} \boldsymbol{D} + \boldsymbol{\Sigma}_{\boldsymbol{\theta}}^{-1} \end{cases} \tag{8.8}$$

We can explicitly compute matrix $\boldsymbol{\Sigma}_{\boldsymbol{\theta}|\boldsymbol{y}}^{-1}$ in Equation 8.8 with the matrices $\boldsymbol{D}$ and $\boldsymbol{\Sigma}_{\boldsymbol{\theta}}$ defined in Equations 8.2 and 8.4:

$$\boldsymbol{\Sigma}_{\boldsymbol{\theta}|\boldsymbol{y}}^{-1} = \frac{1}{\sigma_{\text{LH}}^2} \begin{bmatrix} \mathbf{1}^{\text{T}}\mathbf{1} & \mathbf{1}^{\text{T}}\Delta\boldsymbol{T} & \mathbf{1}^{\text{T}}\Delta\boldsymbol{t} \\ \mathbf{1}^{\text{T}}\Delta\boldsymbol{T} & |\Delta\boldsymbol{T}|^2 & \Delta\boldsymbol{T}^{\text{T}}\Delta\boldsymbol{t} \\ \mathbf{1}^{\text{T}}\Delta\boldsymbol{T} & \Delta\boldsymbol{T}^{\text{T}}\Delta\boldsymbol{t} & |\Delta\boldsymbol{t}|^2 \end{bmatrix} + \begin{bmatrix} \dfrac{1}{\sigma_{y_0}^2} & 0 & 0 \\ 0 & \dfrac{1}{\sigma_{\alpha}^2} & 0 \\ 0 & 0 & \dfrac{1}{\sigma_{m}^2} \end{bmatrix} \tag{8.9}$$

where $|\Delta \boldsymbol{v}| = \Delta \boldsymbol{v}^{\mathrm{T}} \Delta \boldsymbol{v}$ indicates the Eulerian norm of the generic vector $\boldsymbol{v}$. It is convenient to express the relative time and temperature $\Delta \boldsymbol{t}$ and $\Delta \boldsymbol{T}$ with respect to the mean values $\bar{\boldsymbol{t}} = \mathbf{1}^{\mathrm{T}} \Delta \boldsymbol{t}/N$ and $\bar{\boldsymbol{T}} = \mathbf{1}^{\mathrm{T}} \Delta \boldsymbol{T}/N$ of the vectors time $\boldsymbol{t}$ and temperature $\boldsymbol{T}$:

$$\begin{cases} \Delta \boldsymbol{t} = \boldsymbol{t} - \bar{\boldsymbol{t}} \\ \Delta \boldsymbol{T} = \boldsymbol{T} - \bar{\boldsymbol{T}} \end{cases} \tag{8.10}$$

As a result, Equation 8.9 becomes

$$\begin{aligned} \boldsymbol{\Sigma}_{\boldsymbol{\theta}|\boldsymbol{y}}^{-1} &= \boldsymbol{D}^{\mathrm{T}} \boldsymbol{\Sigma}_{\boldsymbol{y}|\boldsymbol{\theta}}^{-1} \boldsymbol{D} + \boldsymbol{\Sigma}_{\boldsymbol{\theta}} \\ &= \frac{1}{\sigma_{\mathrm{LH}}^2} \begin{bmatrix} N & 0 & 0 \\ 0 & |\Delta \boldsymbol{T}|^2 & \Delta \boldsymbol{T}^{\mathrm{T}} \Delta \boldsymbol{t} \\ 0 & \Delta \boldsymbol{T}^{\mathrm{T}} \Delta \boldsymbol{t} & |\Delta \boldsymbol{t}|^2 \end{bmatrix} + \begin{bmatrix} \frac{1}{\sigma_{y0}^2} & 0 & 0 \\ 0 & \frac{1}{\sigma_{\alpha}^2} & 0 \\ 0 & 0 & \frac{1}{\sigma_m^2} \end{bmatrix} \end{aligned} \tag{8.11}$$

The posterior uncertainty $\sigma_{m|\boldsymbol{y}}$ of the trend-parameter m is the third diagonal element of the posterior covariance matrix $\boldsymbol{\Sigma}_{\boldsymbol{\theta}|\boldsymbol{y}}$. After a simple mathematical manipulation of Equation 8.11, the posterior uncertainty can be expressed as:

$$\sigma_{m|\boldsymbol{y}}(\boldsymbol{T}, \boldsymbol{t}) = \sigma_{\mathrm{LH}} \cdot \frac{1}{\sqrt{\frac{\sigma_{\mathrm{LH}}^2}{\sigma_m^2} + |\Delta \boldsymbol{t}|^2}} \cdot \frac{1}{\sqrt{1 - \left(\frac{|\Delta \boldsymbol{t}|^2}{\frac{\sigma_{\mathrm{LH}}^2}{\sigma_m^2} + |\Delta \boldsymbol{t}|^2} \right) \left(\frac{|\Delta \boldsymbol{T}|^2}{\frac{\sigma_{\mathrm{LH}}^2}{\sigma_{\alpha}^2} + |\Delta \boldsymbol{T}|^2} \right) \rho_{\boldsymbol{tT}}^2}} \tag{8.12}$$

where $\rho_{\boldsymbol{tT}}$ is the Pearson correlation coefficient [34] between the time and temperature, i.e., the ratio between the covariance of the two variables and the product of their standard deviations:

$$\rho_{\boldsymbol{tT}} = \frac{\Delta \boldsymbol{t} \cdot \Delta \boldsymbol{T}}{\sqrt{|\Delta \boldsymbol{t}|^2 |\Delta \boldsymbol{T}|^2}} = \frac{\sum_{t=1}^{N} (t_i - \bar{\boldsymbol{t}})(T_i - \bar{\boldsymbol{T}})}{\sqrt{\sum_{t=1}^{N} (t_i - \bar{\boldsymbol{t}})^2} \sqrt{\sum_{t=1}^{N} (T_i - \bar{\boldsymbol{T}})^2}} \tag{8.13}$$

The Pearson correlation coefficient ranges between -1 and +1, with +1 meaning perfect direct correlation, -1 being perfect inverse correlation, and 0 being independency between the two data records. In this specific case, $\rho_{\boldsymbol{tT}}$ is close to 1 if the temperature history can be approximated to a straight line, and it is close to 0 if the temperature and time are far from a linear relationship.

Equation 8.12 provides an explicit expression of the posterior uncertainty of a linear trend m, which depends on the prior uncertainty σ_m^2 of

m, monitoring noise, the extension of time sampling $|\Delta \boldsymbol{t}|$, and the correlation between temperature and time $\rho_{\boldsymbol{tT}}$, although the dependence on these quantities is not exactly intuitive.

When the prior parameters are highly uncertain ($\sigma_m \to \infty$ and $\sigma_\alpha \to \infty$), or the prior information is negligible, Equation 8.12 is particularly simple and easy to read:

$$\sigma_{m|\boldsymbol{y}}(\boldsymbol{T}, \boldsymbol{t}) = \sigma_{\text{LH}} \cdot \frac{1}{|\Delta \boldsymbol{t}|} \cdot \frac{1}{\sqrt{1 - \rho_{\boldsymbol{tT}}^2}} \tag{8.14}$$

This equation clearly shows that the posterior uncertainty of parameter m is the combination of three different factors:

- The monitoring noise σ_{LH}, accounting for the measurement of the noise and the uncertainty of the hypothesized linear model.
- The term $1/|\Delta \boldsymbol{t}|$, which effectively depends on the monitoring duration and the sampling rate.
- The term $1/\sqrt{1 - \rho_{\boldsymbol{tT}}^2}$, which depends on the extent to which the temperature history is close to a straight line.

8.3 Application to Monitoring System Design

Equations (12) and (14) allow the calculation of the uncertainty $\sigma_{m|\boldsymbol{y}}$ of a linear fit a posteriori, i.e., after monitoring data are acquired. In the design stage of the monitoring system, the goal is to predict the uncertainty of m that is expected in the monitoring, even if no data are currently available. Let $\sigma_{m,\text{pp}}$ be the a priori estimate (i.e., before data is acquired) of the posterior uncertainty of parameter m. This quantity is also referred to as pre-posterior uncertainty (hence the "pp" in the symbol), in order to distinguish it both from the prior uncertainty σ_m (the uncertainty of the parameter if no monitoring is carried out) and the posterior uncertainty $\sigma_{m|\boldsymbol{y}}$ (the uncertainty after monitoring data are acquired).

A notable feature of both Equations 8.12 and 8.14 is that the posterior uncertainty is completely independent from the response recording $\boldsymbol{y}$. Therefore, it is possible to estimate the pre-posterior uncertainty $\sigma_{m,\text{pp}}$ by making reasonable assumptions on the time sampling vector $\boldsymbol{t}$, the expected temperature record $\boldsymbol{T}$, and the value of the residual's noise σ_{LH}.

8.3.1 Pre-Posterior Estimate of Time and Temperature Vectors

Assuming that the monitoring sampling is uniform, the time vector only depends on the total monitoring time t_{tot} and the design sampling fre-

quency f_s. The total number of measurements N acquired during the monitoring is

$$N = t_{tot} \cdot f_s + 1 \tag{8.15}$$

and the timestamps of the measurements are defined as

$$t_i = \frac{1}{f_s}(i-1),\ i = 1, 2, 3, ..., N \tag{8.16}$$

For design purposes, the expected temperature measurements T_i can be expressed through a sine function with a period $\tau = 365.25\ days$, or 1 year [24]:

$$T_i = a \cdot sin\left(\frac{2\pi}{\tau}t_i + b\right),\ i = 1, 2, 3, ..., N \tag{8.17}$$

where a is the amplitude of the temperature sinusoidal function, b is the phase, and c is an offset corresponding to the temperature's seasonal mean value.

8.3.2 Pre-Posterior Estimate of the Residual Noise $\Sigma_{\mathbf{LH}}$

Assume that sensor measurements y_i and T_i are approximations of the corresponding true physical values $\hat{y}(t_i)$ and $\hat{T}(t_i)$, and that the scatter between the two is zero-mean random noise $n_j(\sigma^2)$. Let the variances of the measurements be σ_y^2 and σ_T^2, depending on sensor accuracy:

$$\begin{cases} y_i = \hat{y}(t_i) + n_i\sigma_y^2 \\ \Delta T_i = \Delta\hat{T}(t_i) + n_i\sigma_T^2 \end{cases} \tag{8.18}$$

Given the linear interpretation model defined, we assume that the true values satisfy

$$\hat{y}(t_i) = y_0 + m \cdot \Delta t_i + \alpha \cdot \Delta\hat{T}(t_i) + n_i(\sigma_{model}^2) \tag{8.19}$$

where $n_i(\sigma_{model}^2)$ is zero-mean normal noise with variance σ_{model}^2 that represents the difference between the true physical quantity and the model prediction. The model uncertainty σ_{model}^2 derives from approximations and idealizations made in the formulation of the interpretation model, as well as in the choice of the probability distribution of the model parameters.

Then, Equations 8.18 and 8.19 can be merged into a single equation:

$$y_i - n_i(\sigma_y^2) = y_0 + m \cdot \Delta t_i + \alpha \cdot (T_i - n_i(\sigma_T^2)) + n_i(\sigma_{model}^2) \tag{8.20}$$

and all of the zero-mean Gaussian errors can be merged into one zero-mean Gaussian error $n_i(\sigma^2_{\text{LH}})$, which corresponds precisely to the residual z_i between the observation y_i and the nominal value of the model:

$$n_i(\sigma^2_{\text{LH}}) = n_i(\sigma^2_y) + \alpha \cdot n_i(\sigma^2_T) + n_i(\sigma^2_{model}) \tag{8.21}$$

As a result, variance σ^2_{LH} includes both the noise of the sensors and the uncertainty of the model, combined with the propagation of uncertainty through the square root of the sum of squares, assuming statistically uncorrelated errors [34]:

$$\sigma^2_{\text{LH}} = \sigma^2_y + \alpha \cdot \sigma^2_T + \sigma^2_{model} \tag{8.22}$$

8.3.3 Impact of the Time–Temperature Correlation

The term $1/\sqrt{1-\rho^2_{\boldsymbol{tT}}}$ in Equation 8.14 depends on the linear correlation coefficient $\rho_{\boldsymbol{tT}}$ between the time and temperature vectors. Given the definition of $T_i(a,b,c)$ in Equation 8.17, the coefficient $\rho_{\boldsymbol{tT}}$, in turn, depends on the phase-parameter b. In practice, this parameter allows the setting of the start date of the monitoring period. On the other hand, both the parameters amplitude a and offset c do not have any influence on $\rho_{\boldsymbol{tT}}$; therefore, they can be set arbitrarily.

Given two sine temperature functions like Equation 8.17, if their differences with regard to phase-parameter b are equal to π, e.g., $\boldsymbol{T}(b=0)$ and $\boldsymbol{T}(b=\pi)$, the results in terms of $\sigma_{m,\text{pp}}$ are the same. This is due to the presence of the square value of $\rho_{\boldsymbol{tT}}$ in $1/\sqrt{1-\rho^2_{\boldsymbol{tT}}}$, which makes it irrelevant whether the time and temperature vectors are directly or inversely correlated:

$$\sigma_{m,\text{pp}}(\boldsymbol{T}_{b=0}) = \sigma_{m,\text{pp}}(\boldsymbol{T}_{b=\pi}) \tag{8.23}$$

In contrast, if the difference in the phase-parameter b is equal to $\pi/2$, e.g., $\boldsymbol{T}(b=0)$ and $\boldsymbol{T}(b=\pi/2)$, the result is the maximum difference Δ_{max} between the values of $\sigma_{m,\text{pp}}$ estimated with those two temperature vectors:

$$\sigma_{m,\text{pp}}(\boldsymbol{T}_{b=0}) - \sigma_{m,\text{pp}}(\boldsymbol{T}_{b=\pi/2}) = \Delta_{\text{max}} \tag{8.24}$$

Because the sinusoidal function T has a period of $\tau = 365\ days$, a difference in b equal to π corresponds approximately to 6 months ($\tau/2 = 182.5\ days \approx 6\ months$); in contrast, a difference in b equal to $\pi/2$ approximately corresponds to 3 months ($\tau/4 = 91.25\ days \approx 3\ months$).

Figure 8.1 shows the impact of the time–temperature correlation on $\sigma_{m,\mathrm{pp}}$; specifically, it shows the comparison between the two limit cases, $b = 0$ and $b = \pi/2$, in terms of $\rho_{\boldsymbol{tT}}$, $1/\sqrt{1-\rho_{\boldsymbol{tT}}^2}$, and $\sigma_{m,\mathrm{pp}}$.

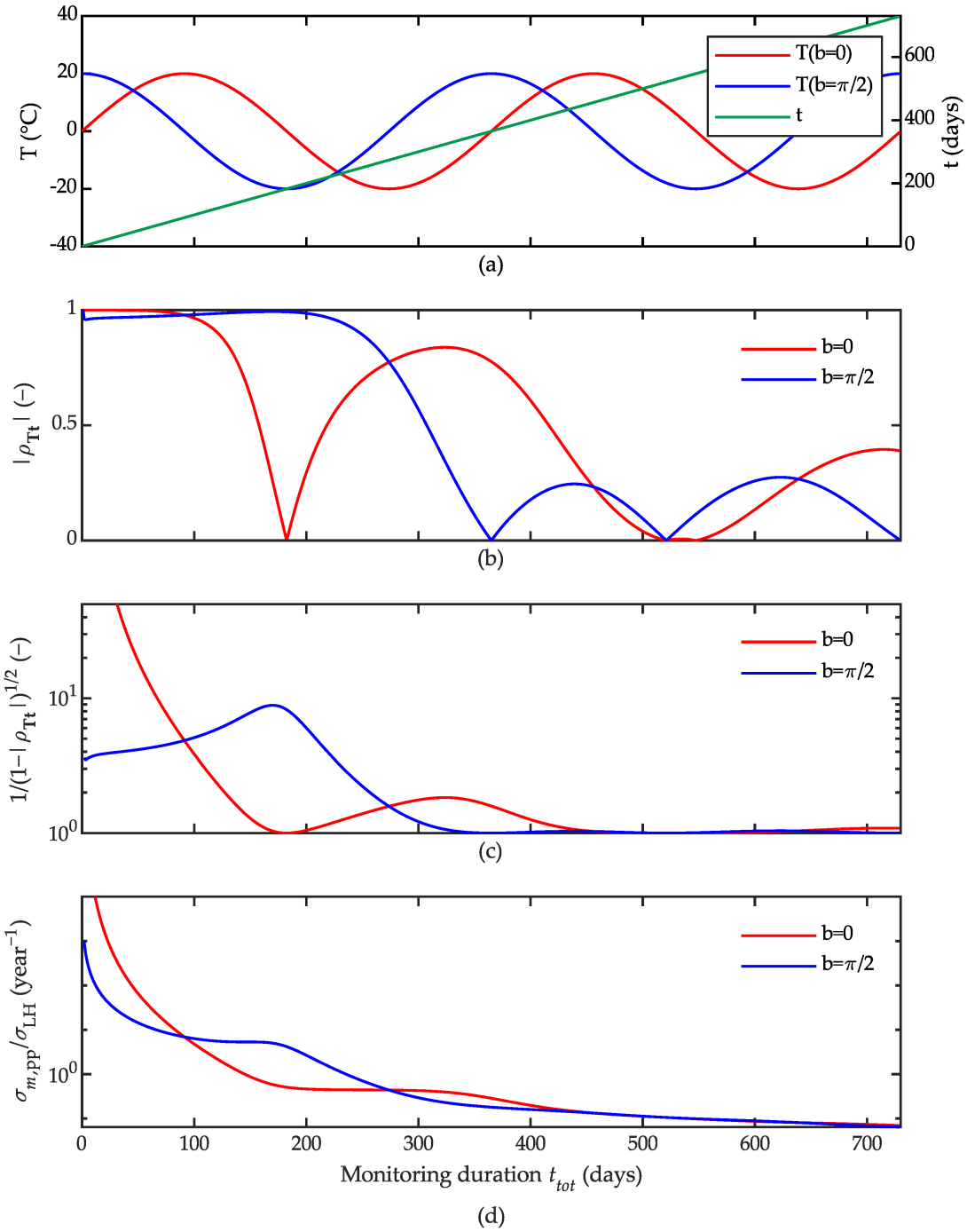

Figure 8.1: Impact of the time–temperature correlation on the pre-posterior uncertainty as the monitoring duration t_{tot} increases from 1 to 730 days in the limit cases $b = 0$ (red lines) and $b = \pi/2$ (blue lines). (a) Time $\boldsymbol{t}$ with $N = 730$ and $f_s = 1/day$, and temperature $\boldsymbol{T}$ with $a = 20°C$ and $c = 0°C$; (b) the absolute value of the linear correlation coefficient $\rho_{\boldsymbol{tT}}$ between $\boldsymbol{t}$ and $\boldsymbol{T}$; (c) term $1/\sqrt{1-\rho_{\boldsymbol{tT}}^2}$ of Equation 8.14; (d) the ratio between the pre-posterior uncertainty $\sigma_{m,pp}$ and the likelihood uncertainty σ_{LH}.

Figure 8.1b shows the absolute value of $\rho_{\boldsymbol{tT}}$ as the monitoring duration increases, while Figure 8.1c,d show the effect of $|\rho_{\boldsymbol{tT}}|$ on $1/\sqrt{1-\rho^2_{\boldsymbol{tT}}}$ and $\sigma_{m,\text{pp}}$; different values of the phase parameter b in the temperature function $\boldsymbol{T}(b)$ determine different outcomes.

When $b = 0$ (red curves), the absolute value of the correlation coefficient $\rho_{\boldsymbol{tT}}$ decreases to 0 after approximately 183 days from the monitoring start date. Then, it increases until 320 days, when it decreases again; it reaches 0 for the second time after around 540 days from the monitoring start date. In contrast, when $b = \pi/2$ (blue curves), $|\rho_{\boldsymbol{tT}}|$ increases until 180 days from the monitoring start date. Then, from 180 to 360 days, $|\rho_{\boldsymbol{tT}}|$ decreases monotonically. It is interesting to highlight that for longer monitoring durations, the linear correlation between the time and temperature increases and decreases periodically, without zeroing permanently. However, such variations in $|\rho_{\boldsymbol{tT}}|$ do not have a great influence on $1/\sqrt{1-\rho^2_{\boldsymbol{tT}}}$, or consequently on $\sigma_{m,\text{pp}}$. Indeed, after approximately 450 days of monitoring, $5\tau/4 \approx 457\ days \approx 15\ months$, the term $1/\sqrt{1-\rho^2_{\boldsymbol{tT}}}$ is approximately equal to 1. Therefore, the impact of the time–temperature correlation on $\sigma_{m,\text{pp}}$ is negligible for long monitoring periods (more than 15 months).

Figure 8.1d shows that the difference between the two limit cases $\sigma_{m,\text{pp}}(\boldsymbol{T}_{b=0})$ and $\sigma_{m,\text{pp}}(\boldsymbol{T}_{b=\pi/2})$ also becomes negligible after around 15 months of monitoring; therefore, the start date of the monitoring does not influence the monitoring effectiveness.

From Figure 8.1d, it can also be noted that the red curve $\sigma_{m,\text{pp}}(\boldsymbol{T}_{b=0})/\sigma_{\text{LH}}$ has a constant plateau from day 183 to day 320; the expected uncertainty remains constant without decreasing for a long interval of the monitoring period due to the increasing linear correlation $\rho^2_{\boldsymbol{tT}}$ during such an interval. The practical meaning of this observation is that increases in the monitoring period within this interval will not produce an improved knowledge of the structural state in terms of the measurement trend, due to the effect of temperature.

It may be observed that a theoretical sinusoidal function like $T(t_i, a, b, c)$ in Equation 8.17 might not be representative of experimental temperature measurements. Real temperature measurements can be better simulated by adding Gaussian noise $n_i(\sigma_{\text{noise}})$ to the sinusoidal temperature, which represents the observed variation in real temperature between one day and the following one:

$$T_{i,\text{noise}} = T_i + n_i(\sigma_{\text{noise}}) \tag{8.25}$$

where σ_{noise} can be set, for instance, as 5% of the temperature range

of the sine function. Figure 8.2 shows the impact of temperature variation simulated as Gaussian noise $n_i(\sigma_{\text{noise}})$ on the pre-posterior uncertainty $\sigma_{m,\text{pp}}$.

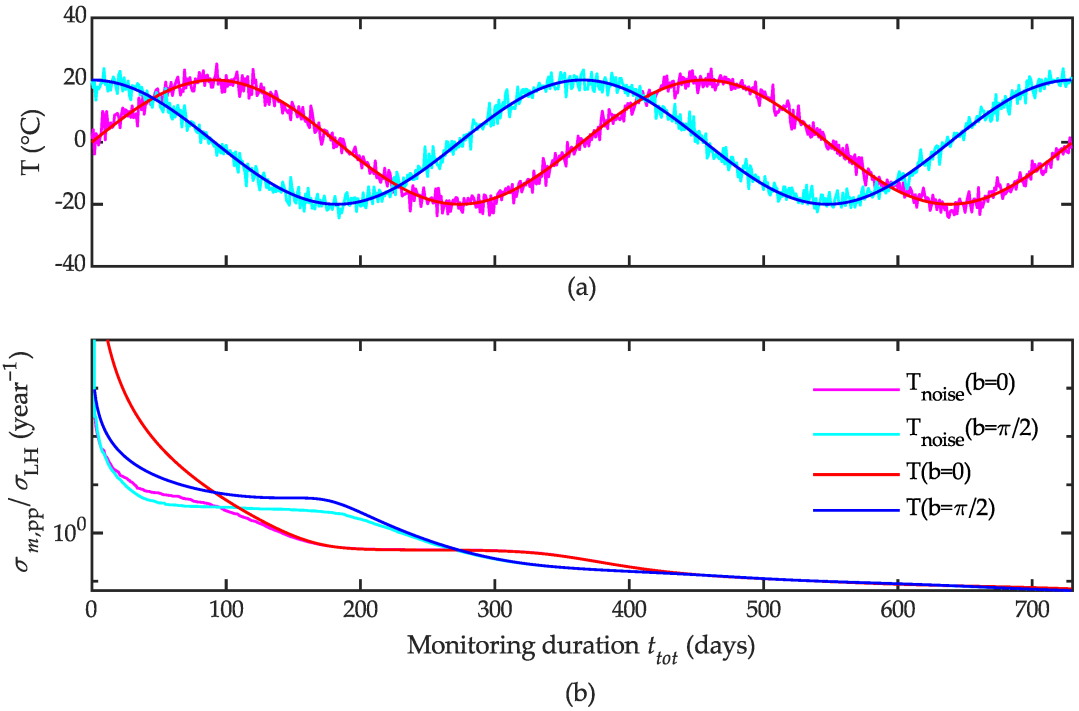

Figure 8.2: Impact of the day-by-day variation in temperature simulated as Gaussian noise $n_i(\sigma_{noise})$ on the pre-posterior uncertainty as the monitoring duration ttot increases from 1 to 730 days in the limit cases $b = 0$ and $b = \pi/2$. (a) Comparison between $\boldsymbol{T}_{noise}$ and $\boldsymbol{T}$; (b) comparison between $\sigma_{m,pp}(\boldsymbol{T}, \boldsymbol{t})/\sigma_{LH}$ and $\sigma_{m,pp}(\boldsymbol{T}_{noise}, \boldsymbol{t})/\sigma_{LH}$. Temperatures with $a = 20°C$, $a = 0°C$, and $\sigma_{noise} = 2°C$.

Figure 8.2b shows that the pre-posterior uncertainty calculated with the simulated experimental temperature function $\boldsymbol{T}_{\text{noise}}$ is smaller than the pre-posterior uncertainty calculated with the theoretical temperature function $\boldsymbol{T}$. Indeed, the random variability $n_i(\sigma_{\text{noise}})$ in $\boldsymbol{T}_{\text{noise}}$ reduces the linear correlation between the temperature and time. As a result, the evaluation of $\sigma_{m,\text{pp}}/\sigma_{\text{LH}}$ based on the theoretical temperature $\boldsymbol{T}$ provides safer results compared to the scenario where it is based on some real temperature data affected by day-by-day variability.

8.3.4 Impact of the Sampling Frequency

Term $1/|\Delta \boldsymbol{t}|$ in Equation 8.14 is the reciprocal of the absolute value of vector $\Delta \boldsymbol{t}$, i.e., the reciprocal of the standard deviation of vector $\boldsymbol{t}$. We

can express $1/|\Delta \boldsymbol{t}|$ as

$$\frac{1}{|\Delta \boldsymbol{t}|} = \frac{1}{\sqrt{\sum_{i=1}^{N} \left(\frac{1}{f_s}(i-1) - \frac{t_{tot}}{2} \right)^2}} = \frac{1}{\frac{1}{f_s}\sqrt{\frac{N}{12}(N^2-1)}} \tag{8.26}$$

The term $1/|\Delta \boldsymbol{t}|$ depends on both the number of samples N and the sampling frequency f_s, and behaves as the inverse of an inertial factor: as the monitoring duration and sampling frequency increase, $1/|\Delta \boldsymbol{t}|$ and $\sigma_{m,\text{pp}}$ decrease. Figure 8.3 shows the impact of the monitoring duration and sampling frequency on $1/\sqrt{1-\rho^2_{\boldsymbol{tT}}}$, $1/|\Delta \boldsymbol{t}|$ and $\sigma_{m,\text{pp}}$; it clearly shows that $1/\sqrt{1-\rho^2_{\boldsymbol{tT}}}$ does not depend on f_s, unlike $1/|\Delta \boldsymbol{t}|$.

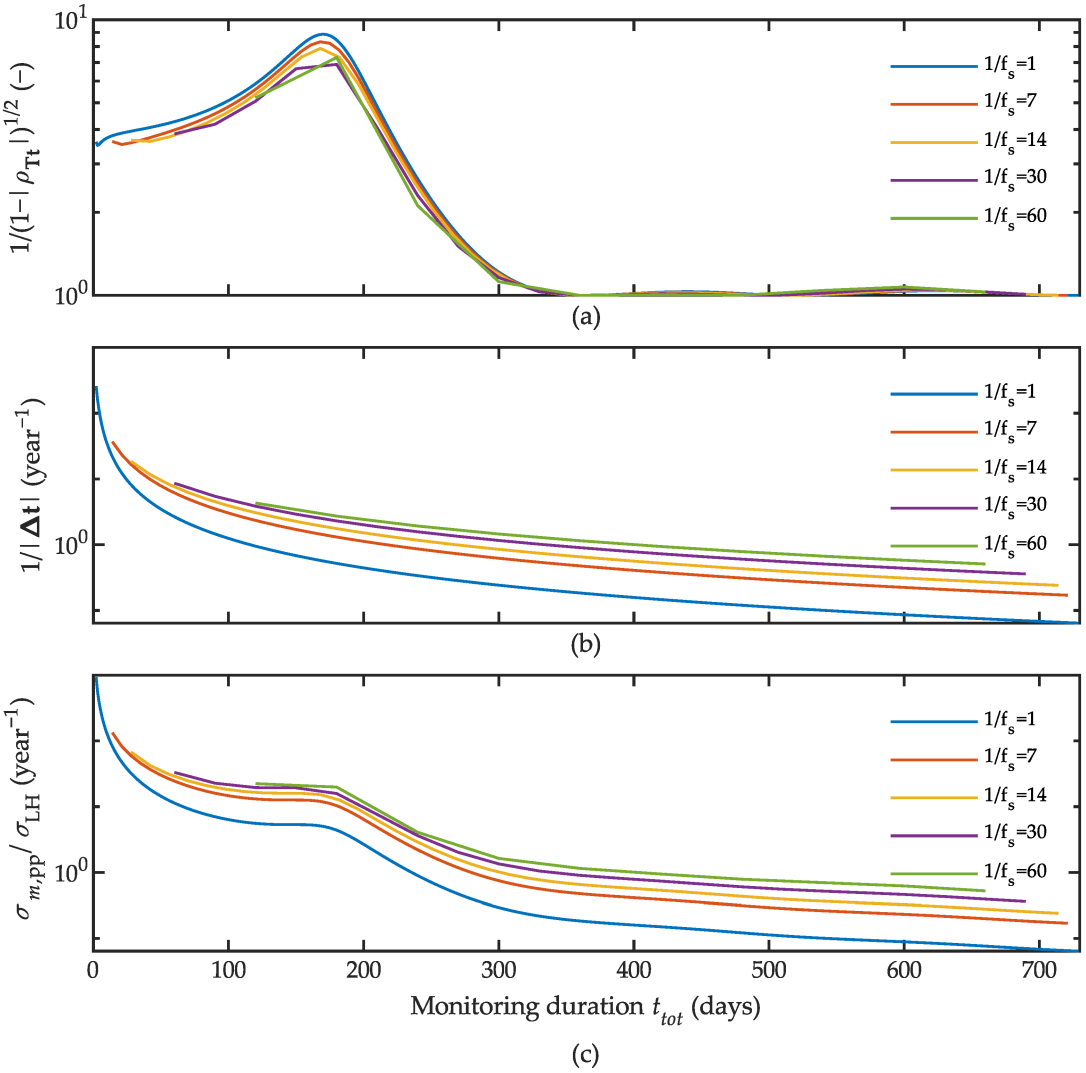

Figure 8.3: Impact of the sampling frequency f_s on pre-posterior uncertainty $\sigma_{m,pp}$. The graphs are plotted against the monitoring duration ttot from 1 to 730 days, for different time intervals $1/f_s$ between measurements, from 1 to 60 days. (a) Impact on term $1/\sqrt{1-\rho^2_{\boldsymbol{tT}}}$; (b) impact on term $1/|\Delta \boldsymbol{t}|$, where b is set equal to $\pi/2$; (c) impact on $\sigma_{m,pp}/\sigma_{LH}$.

8.3.5 Impact of the Residual's Noise σ_{LH}

The residual's noise σ_{LH} works as an amplification coefficient on $\sigma_{m,\mathrm{pp}}$: as it decreases, $\sigma_{m,\mathrm{pp}}$ decreases. In order to reduce σ_{LH}, and thus to obtain a more accurate estimation of m, we can choose high-performance sensors; in particular, the sensors' accuracy (i.e., the small random noise σ_ϵ and σ_T) is critical when the model uncertainty σ_{model} is small. How-

ever, under the assumption of statistically uncorrelated errors, the sensor accuracy can be less critical: high model uncertainties σ_{model} strongly reduce the influence of sensor noise σ_y and σ_T on σ_{LH}; therefore, using very accurate and expensive instrumentation does not drastically improve the monitoring effectiveness in the estimation of the trend parameter.

8.3.6 Impact of Prior Distributions

Finally, we can analyse the difference between Equations 8.12 and 8.14. Figure 8.4 shows a comparison between $\sigma_{m,\text{pp}}$ with Gaussian prior parameter distributions (Equation 8.12), and $\sigma_{m,\text{pp}}$ neglecting prior parameter distributions (Equation 8.14).

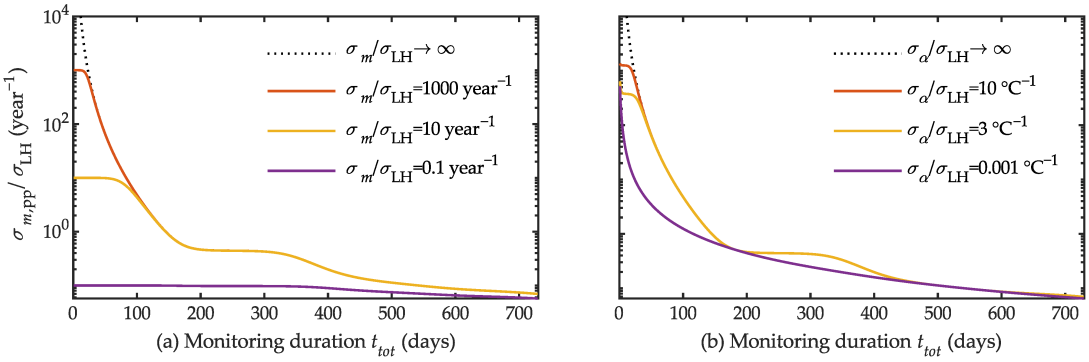

Figure 8.4: Impact of the prior distributions of parameters α and m on the pre-posterior uncertainty. The graphs are plotted against the monitoring duration t_{tot} from 1 to 730 days, $b = 0$, $f_s = 1$. (a) $\sigma_m/\sigma_{LH} \to \infty$, $\sigma_\alpha/\sigma_{LH}$ varies from 10 to 0.001 $°C^{-1}$; (b) $\sigma_\alpha/\sigma_{LH} \to \infty$, σ_m/σ_{LH} varies from 1000 to 0.1 $year^{-1}$.

In Figure 8.4a, Equation 8.12 is plotted assuming different possible prior Gaussian distributions of parameter m while the prior distribution of the thermal coefficient α is neglected ($\sigma_\alpha/\sigma_{\text{LH}} \to \infty$). In Figure 8.4b, Equation 8.12 is plotted assuming different possible prior Gaussian distributions of α while the prior distribution of m is neglected ($\sigma_m/\sigma_{\text{LH}} \to \infty$). The standard deviations of the prior distributions range from highly uncertain to very accurate values: from $\sigma_m/\sigma_{\text{LH}} = 1000\ year^{-1}$ to $\sigma_m/\sigma_{\text{LH}} = 0.1\ year^{-1}$ in Figure 8.4a, and from $\sigma_\alpha/\sigma_{\text{LH}} = 10\ °C^{-1}$ to $\sigma_\alpha/\sigma_{\text{LH}} = 0.001\ °C^{-1}$ in Figure 8.4b.

When the prior distribution of the model parameters is highly uncertain (orange solid lines), Equation 8.12 provides the same results as Equation 8.14 (black dashed lines), apart from very short monitoring durations. In contrast, when the prior distribution of m is very accurate (the purple solid line in Figure 8.4a), $\sigma_{m,\text{pp}}$ stays almost constant and slightly

decreases as the monitoring duration increases. Therefore, if the trend parameter m is accurately known a priori, structural health monitoring is not necessary. When $\sigma_m/\sigma_{\text{LH}} \to 0$, Equation 8.12 becomes

$$\sigma_{m,\text{pp}}(\boldsymbol{T},\boldsymbol{t}) = 0 \;\forall\; N \tag{8.27}$$

On the other hand, when the prior distribution of α is very accurate (the purple solid line in Figure 8.4b), $\sigma_{m,\text{pp}}$ is completely independent from the linear correlation between the time and temperature. Indeed, if the thermal coefficient α is accurately known a priori, we can compensate the temperature effects deterministically. When $\sigma_\alpha/\sigma_{\text{LH}} \to 0$, Equation 8.12 becomes

$$\sigma_{m,\text{pp}}(\boldsymbol{T},\boldsymbol{t}) = \sigma_{\text{LH}} \frac{1}{\sqrt{\dfrac{\sigma_{\text{LH}}^2}{\sigma_m^2} + |\Delta \boldsymbol{t}|^2}} \tag{8.28}$$

Generally, for typical values of the prior uncertainty of the parameters, the prior Gaussian distributions affect the results of $\sigma_{m,\text{pp}}$ only for short monitoring periods. Consequently, as the monitoring duration increases, the prior distributions become less influential, and Equation 8.12 resembles Equation 8.14.

8.4 Colle Isarco Viaduct Case Study

The Colle Isarco Viaduct [32] is an Italian prestressed concrete highway bridge. It was erected in 1968, and opened to traffic in 1971. The viaduct consists of two structurally independent decks, both with 13 spans, for a total length of 1028 m. The main span is 163 m long, and is made of two symmetric reinforced concrete Niagara box girders, which support a 45 m-long suspended beam. At the end of each box girder is a 59 m-long cantilever, counterbalanced by a back arm with a length of 91 m. Each box girder is composed of 33 cast-in-place segments with a depth varying from 10.93 m at the pier to 2.57 m at the edge. The thickness of the top slab is constant, at 0.29 m, while the bottom slab varies from 0.99 m to 0.12 m. A concrete with nominal class $R_{ck} = 450\ kg/cm^2$ was used for all of the cast-in-place elements of thepiers and girders. The initial prestressing was applied through 32 mm diameter Dywidag ST 85/105 threaded bars, with an initial jacking tension of 720 MPa. For each 59m-long cantilever, the longitudinal force above the pier was about 120 MN, and was provided by a total of 266 cables. Figure 8.5a shows a picture of the viaduct from pier 7 to 9. Figure 8.5b shows a longitudinal section of the viaduct between piers 7 and 10, as well as two cross-sections of the box girders.

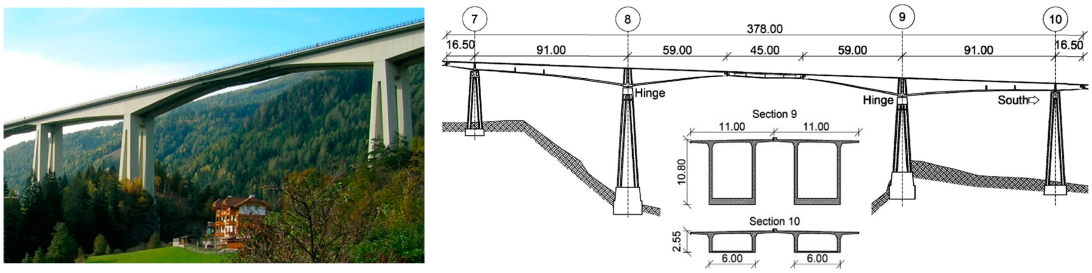

(a) (b)

Figure 8.5: (a) The main span and northernmost cantilever of Colle Isarco Viaduct; (b) a longitudinal section of the viaduct between piers 7 and 10, and cross-sections of the box girders, with dimensions in meters.

The Colle Isarco Viaduct has been subjected to excessive creep and shrinkage phenomena since its construction. It has experienced a progressive abnormal deformation of the top and bottom slab, resulting in an abnormal deflection of the cantilever beams, which are mostly evident at the edge of the 59 m-long cantilever even several decades after its construction. This high sensitivity to creep and shrinkage phenomena is experienced by many other bridges of the same type, and has been investigated by several authors [23, 35, 36]. They suggest that the cause of such behaviour is the combination of creep phenomena, prestress tension losses, the huge difference between the top and the bottom slab in terms of thickness, the variation of the load condition during the construction phase, and maintenance works. Just a few years after its construction, the main span showed an excessive deflection trend, which resulted in a deflection of 100 mm in 1976 and 200 mm in 1984, while the design prediction was less than 20 mm. In 2014, through a retrofit work, the four box girders were equipped with an external post-tensioning system, which provides additional prestress through 212 0.6” diameter compact strands, with a jacking load of 213 kN. The additional longitudinal force produced above the piers was about 45 MN, which is almost 40% of the original prestress. The thickness of the top slab of the box girder was increased from 260 mm to 290 mm, to compensate for the additional post-tensioning force. This retrofit work reduced the deflection by 80 mm and changed the deflection drift from negative to positive. Details of the retrofit work can be found in the relevant design documentation [37].

The Colle Isarco Viaduct is currently monitored by three different technologies [22]. First, a topographic network measures the 3D displacements of the decks between pier 7 and pier 10. It consists of two stations, Leica Nova TM50, which collimate GPR112 prisms: 60 mea-

surement points and 12 benchmarks. The topographic system was installed in 2014 before the retrofit works. Second, a network of 82 resistance temperature detectors (RTDs), TH-PT100, provided by Nova Metrix measures the local concrete temperature of the top and bottom slabs of the four cantilevers. The RTD network was installed in 2016. Third, 56 long-gauge fibre optic sensors (FOSs) measure the concrete local strain in the middle of the top and bottom slab. They are 12.1010 MuST deformation sensors, provided by Smartec SA. The FOSs network was installed in 2016 to monitor the long-term effects of the 2014 post-tensioning intervention. In the present study, the focus is on strain and temperature measurements: Figure 8.6 shows the positions of the RTDs and FOSs on the northernmost cantilever of the northbound carriageway. The strain and temperature sensors are placed next to each other, and take one measurement every 15 min simultaneously. The local strain measured in the concrete slabs allows the effective calculation of the curvature of the girders, and the investigation of the causes of possible excessive long-term deformation trends. Conversely, the curvature calculated from the displacements provided by the topographic systems would be affected by severe errors due to the propagation of uncertainty. The local temperature of the concrete allows the compensation of the total strain measurements, which are severely affected by the response of the structure to daily and seasonal temperature variations.

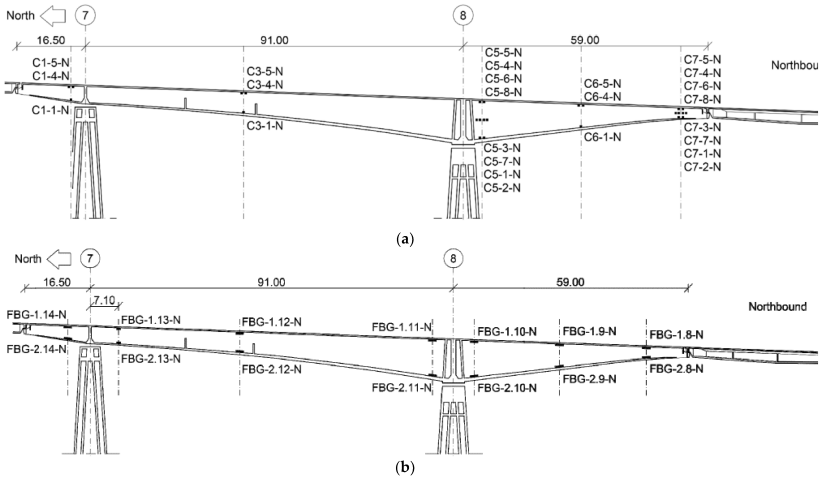

Figure 8.6: Positions of (a) the RTDs and (b) the FOSs on the northernmost cantilever of the northbound carriageway. The dimensions are given in meters.

8.5 Application to the Case Study

In this Section, we apply our approach to the Colle Isarco Viaduct case study; our aim is the evaluation of the expected uncertainty of the long-term strain trend of concrete, as compensated from temperature effects. In particular, we consider the strain and temperature monitoring system currently installed on the structure. First, we play the role of monitoring system designers, who chose the strain and temperature sensors and their location on the concrete box girders in 2016; our goal is the pre-posterior estimation of the expected uncertainty of the strain trend through Equation 8.12. Then, we play the role of monitoring data analysts, and we analyse the local strain and temperature recorded by the monitoring system; here, the goal is to infer a posteriori the posterior uncertainty based on the monitoring data acquired from the structure from April 2017 to February 2019. Finally, we validate the proposed approach by comparing the expected uncertainty with the posterior uncertainty, and we discuss the impact of the monitoring duration, monitoring start date, and temperature simulation.

8.5.1 Pre-Posterior Analysis: Expected Uncertainty in the Design Phase

Let us play the role of the monitoring system designer. It is the year 2016, and we are designing a local-strain monitoring system for the concrete box girders of the Colle Isarco Viaduct. It must provide the local-strain linear trend m, as compensated from the seasonal temperature changes. We have already chosen the tentative strain and temperature sensors: their random noise is a zero-mean Gaussian variable with standard deviations σ_ϵ and σ_T, respectively. In addition, we have already defined the sensor placement, see Figure 8.6, and the linear interpretation model, see Equation 8.1. Our goal is the pre-posterior estimation of the expected uncertainty $\sigma_{m,\text{pp}}$ of the local strain linear trend m, in order to verify whether it is lower than a target value set by the viaduct manager, who oversees the infrastructure operation. We assume that once the monitoring system is up and running, it will acquire one local strain ϵ_i and one temperature measurement T_i per day, for N days.

Simulation of the Expected Time and Temperature

First, we must define the elements within the time ti and temperature T_i vectors. We simulate time through Equation 8.16, and we set the sampling frequency as one measurement per day, $f_s = 1\ day^{-1}$. We obtain the same vector t in Figure 8.1a. We wish to study how $\sigma_{m,\text{pp}}$ changes with the monitoring duration t_{tot} varying from 3 to 600 days.

Then, we simulate the expected seasonal temperature variation in

two different ways: a sine function $\boldsymbol{T}$, defined as Equation 8.17, and a sine function with Gaussian noise Tnoise, defined as Equation 8.25. In order to represent two different start dates of the monitoring, we set two cases of the phase-parameter: $b = \pi/2$ and $b = 0$. In the first case, the monitoring period starts when the seasonal temperature reaches approximately its maximum stationarity point (during the summer season); in the second case, it starts in proximity to its point of inflection (during the spring season).

Estimation of the Measurements and Model Uncertainties

We must calculate the likelihood-function uncertainty σ_{LH} through Equation 8.22, where the measurement uncertainty σ_y is represented by the standard deviation σ_ϵ of the strain-sensors' zero-mean Gaussian random noise:

$$\sigma_{\text{LH}} = \sqrt{\sigma_\epsilon^2 + \alpha \cdot \sigma_T^2 + \sigma_{model}^2} = 21\mu\epsilon \tag{8.29}$$

where:

- $\alpha = 10\ \mu\epsilon/^\circ C$ is the local-concrete thermal-expansion coefficient at 20 $^\circ C$ [21].
- $\sigma_\epsilon = 2\ \mu\epsilon$ is the accuracy of the strain sensors.
- $\sigma_T = 0.5\ ^\circ C$ is the accuracy of the temperature sensors.
- $\sigma_{\text{model}} = 20\ \mu\epsilon$, based on similar case studies [7, 22].

Expected Uncertainty

We perform the pre-posterior estimation of the expected uncertainty $\sigma_{m,\text{pp}}$ of the local strain linear trend m through Equation 8.12. We use the likelihood-function uncertainty σ_{LH} defined in Equation 8.29 and the time and temperature vectors defined in Section 8.5.1. In particular, we calculate $\sigma_{m,\text{pp}}$ with the two simulated temperature vectors, $\boldsymbol{T}$ and $\boldsymbol{T}_{\text{noise}}$, and we study how $\sigma_{m,\text{pp}}$ changes as the monitoring duration N increases from 3 to 600 days. Figure 8.7 shows the results, which we will discuss in Section 8.5.3, along with the results on the real uncertainty $\sigma_{m|\boldsymbol{\epsilon}}$ inferred a posteriori based on the monitoring observations.

8.5.2 Posterior Analysis: Real Uncertainty Based on the Monitoring Data

Let us play the role of the monitoring data analyst. The structural health monitoring system has been running for 4 years. We analyse the measurements of local-strain ϵ and the temperature acquired from April 2017 to February 2019 from the bottom slab of the northernmost box girder C5-N by strain sensor FBG-2.10-N and temperature sensors C5-1-N and C5-2-N (see Figure 8.6). We analyse the mean value of the temperature

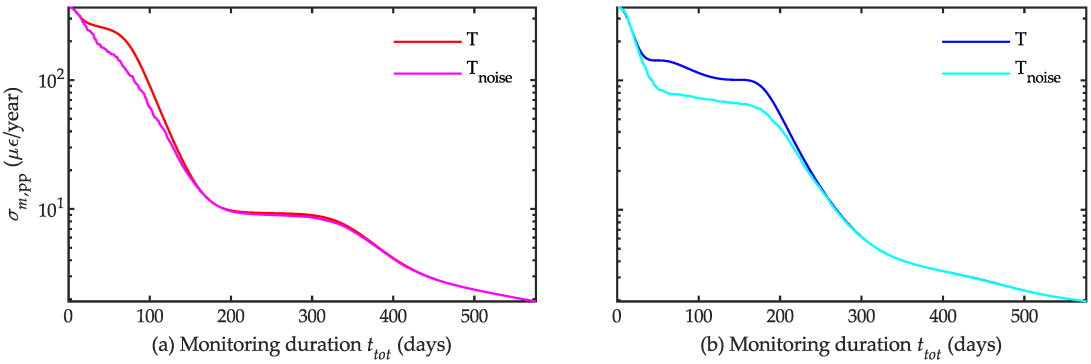

Figure 8.7: Expected uncertainty $\sigma_{m,pp}$ of the linear-trend parameter m estimated in the design phase. Phase parameter b is set as (a) $b = 0$ and (b) $b = \pi/2$. The monitoring duration t_{tot} varies from 3 to 600 days.

data recorded by the two sensors, which we label $\boldsymbol{T}_{\text{str}}$. Our goal is now to infer a posteriori the posterior uncertainty $\sigma_{m|\boldsymbol{\epsilon}}$ of the local strain linear trend m, based on these monitoring data, and to study how it changes when the monitoring duration N increases from 3 to 600 days.

Under the hypotheses Hp. 1 and Hp. 2 (linear-Gaussian model), we define the prior Gaussian probability distribution of model parameters m and α: parameter m has prior mean value $\mu_m = 0$ and prior standard deviation $\sigma_m = 365\ \mu\epsilon/year$; parameter α has prior mean value $\mu_\alpha = 10$ and prior standard deviation $\sigma_\alpha = 3\ \mu\epsilon/^\circ C$. Moreover, we consider σ_{LH} as an additional model parameter to be estimated a posteriori, and we assume its prior probability distribution to be uniform. Then, we perform a Bayesian parameter estimation through a Markov chain Monte Carlo method based on the Metropolis Hasting algorithm [38]. Through an iterative process, this method estimates the posterior probability distribution of parameters $p(m|\boldsymbol{\epsilon})$ and $p(\alpha|\boldsymbol{\epsilon})$, as well as the distribution of the residual $p(z|\boldsymbol{\epsilon})$, for any chosen monitoring duration. Finally, we perform temperature compensation on the total strain measurements by removing the thermal-strain component of the model, $\alpha \cdot \boldsymbol{T}_{\text{str}}$, and isolating the strain trend due to long-term effects $m \cdot \boldsymbol{t}$. Figure 8.8a,b show the strain and temperature measurements recorded from 20 July 2017 to 17 February 2019, respectively; Figure 8.8c shows the temperature-compensated strain-data $\epsilon - \alpha \cdot \boldsymbol{T}_{\text{str}}$, as well as the linear strain trend $m \cdot \boldsymbol{t}$.

We are interested in studying the ways in which the model parameter m, its uncertainty $\sigma_{m|\boldsymbol{\epsilon}}$, and the uncertainty of the likelihood function $\sigma_{\text{LH}|\boldsymbol{\epsilon}}$ a posteriori change as the monitoring duration increases from 3

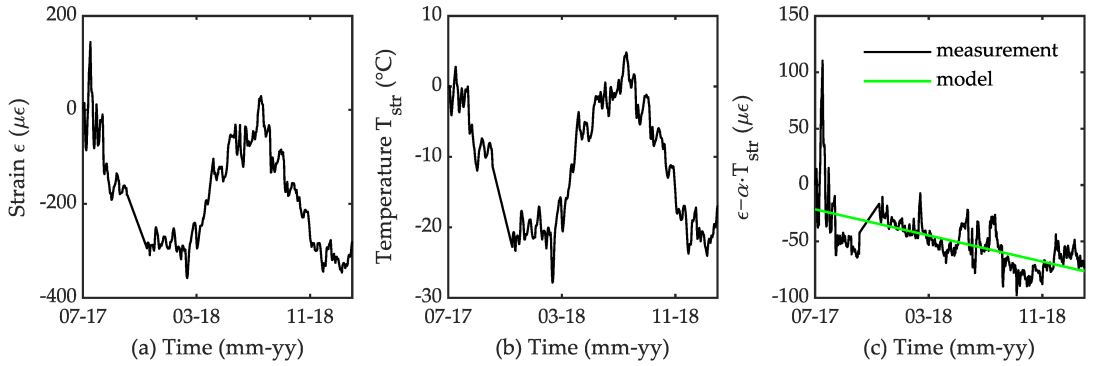

Figure 8.8: (a) 600 days of strain measurements from sensor FBG-2.10-N; (b) mean values of 600 days of temperature measurements from sensors C5-1-N and C5-2-N; (c) temperature-compensated strain measurements and the posterior local-strain linear-trend $m \cdot \boldsymbol{t}$ over 600 days. Measurements of each sensor are plotted subtracting the first value.

to 600 days. In order to obtain the same initial conditions as in the design phase (Section 8.5.1) in terms of the monitoring start date, we fit $\boldsymbol{T}_{\text{str}}$ with a sinusoidal function defined as Equation 8.17, and we identify the timestamps corresponding to the maximum stationarity point and the inflection point: the first corresponds approximately to 20 July, and the second corresponds to 20 April. Therefore, we perform parameter estimation and temperature compensation with two sets of monitoring data: the first starts on 20 April 2017, corresponding to setting $b = 0$ in the design simulated temperature function, while the second starts on 20 July 2017, corresponding to setting $b = \pi/2$ in the design simulated temperature function. We repeat the analysis multiple times, changing monitoring duration t_{tot} from 3 to 600 days. Figure 8.9a,b show the results in terms of m and $\sigma_{\text{LH}|\boldsymbol{\epsilon}}$, with monitoring data starting on 20 July 2017. They are plotted along with their 0.01 and 0.99 percentile to highlight the interval of confidence.

Figure 8.9a shows the posterior mean value of m, $\mu_{m|\boldsymbol{\epsilon}}$, as the monitoring duration increases. It varies as the monitoring duration increases during the first year of monitoring; for longer monitoring durations, it settles around a constant value. The reason is that m is affected by a higher uncertainty due to the time-temperature correlation during the first period of monitoring, while this correlation decreases and becomes uninfluential for longer monitoring durations, as we observed in Section 8.3.3.

Figure 8.9b shows the posterior mean value of the likelihood-function uncertainty $\mu_{\sigma_{\text{LH}|\boldsymbol{\epsilon}}}$ as the monitoring duration increases. Like the trend parameter m, σ_{LH} stabilizes at an approximately constant value after

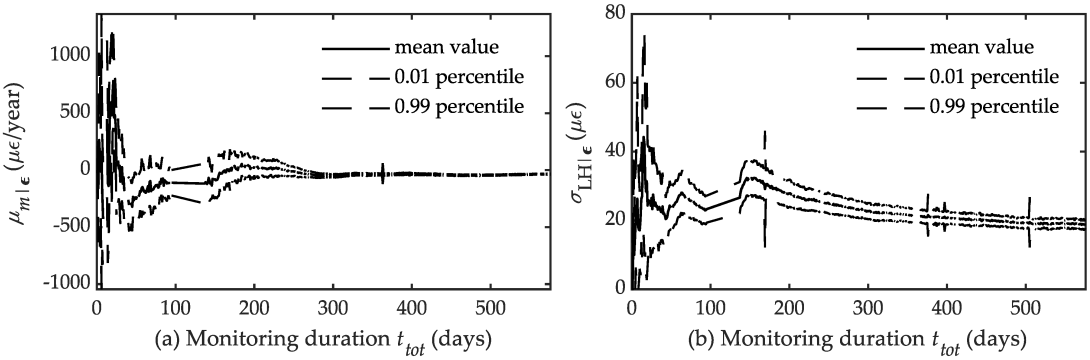

Figure 8.9: (a) Mean value and percentiles 0.01 and 0.99 of parameter m a posteriori; (b) mean value and percentiles 0.01 and 0.99 of the likelihood-function uncertainty $\sigma_{LH|\epsilon}$ a posteriori.

around one year of monitoring; this indicates that the linear interpretation model defined in Equation 8.1 is appropriate to approximate the long-term structural response.

Figure 8.10 shows the posterior uncertainty $\sigma_{m|\epsilon}$ as the monitoring duration increases for the two limit cases of the monitoring start date.

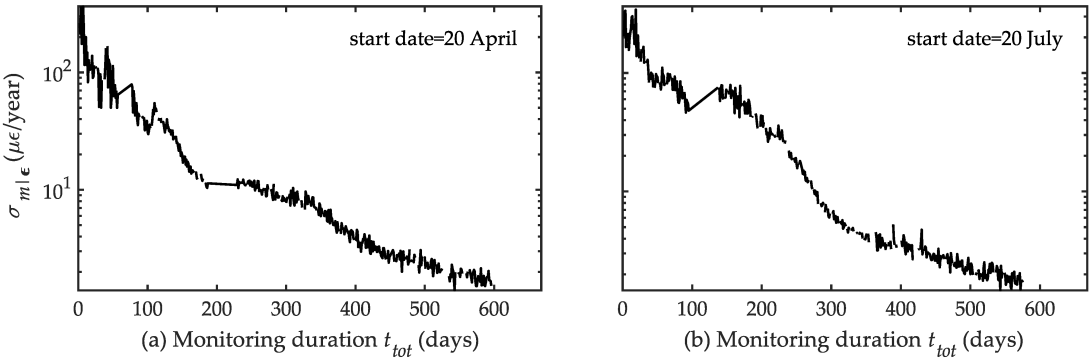

Figure 8.10: Real uncertainty $\sigma_{m|\epsilon}$ of the linear-trend parameter m, estimated a posteriori based on the monitoring data. The monitoring start dates are (a) 20 April and (b) 20 July.

8.5.3 Discussion of the Results

Here, we validate the proposed approach by comparing the expected uncertainty with the posterior uncertainty, and discuss the impact of the monitoring duration, the monitoring start date, and the temperature simulation. Finally, we compare our approach.

Expected vs. Real Uncertainty

Based on the case study results, we aim to validate the proposed approach for the estimation of the pre-posterior uncertainty of the structural long-term linear response trend. Therefore, we compare the expected uncertainty $\sigma_{m,\text{pp}}$ with the posterior uncertainty $\sigma_{m|\boldsymbol{\epsilon}}$, and we discuss their difference as we change the monitoring duration, monitoring start date, and temperature simulation.

Figure 8.11 shows the comparison between the pre-posterior linear trend uncertainty $\sigma_{m,\text{pp}}$ estimated with $\boldsymbol{T}$ and $\boldsymbol{T}_{\text{noise}}$, and the linear trend uncertainty calculated a posteriori, $\sigma_{m|\boldsymbol{\epsilon}}$. They are plotted against monitoring duration t_{tot}; we reported both the limit scenarios of monitoring start date: 20 April, corresponding to $b = 0$ in the design simulated temperature function, and 20 July, corresponding to $b = \pi/2$ in the design simulated temperature function. Here, σ_m is 1 $\mu\epsilon/day = 365$ $\mu\epsilon/year$, which is the value used in the Bayesian parameter estimation described in Section 8.5.3.

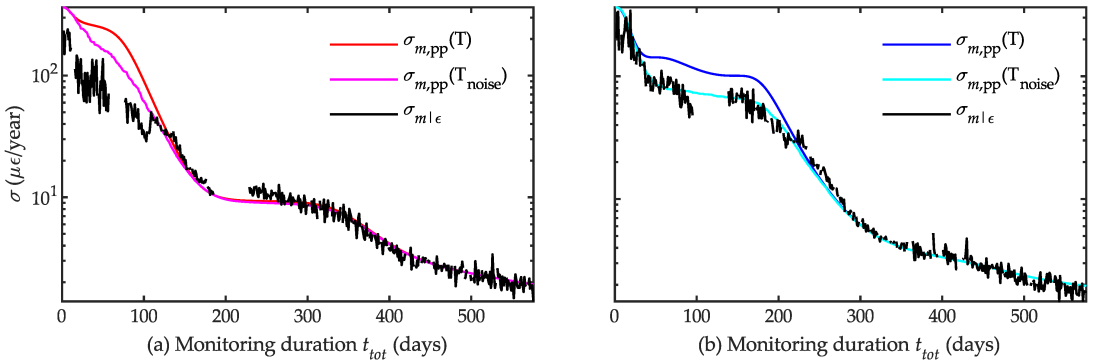

Figure 8.11: Pre-posterior $\sigma_{m,pp}$ and posterior $\sigma_{m|\boldsymbol{\epsilon}}$ linear trend uncertainty plotted against the monitoring duration t_{tot}. The monitoring start dates are (a) 20 April, $b = 0$, and (b) 20 July, $b = \pi/2$. The monitoring duration t_{tot} varies from 3 to 600 days.

We note that the expected–pre-posterior–uncertainty estimated with $\boldsymbol{T}$ tends to overestimate the real–posterior–uncertainty for short monitoring durations, while they become qualitatively similar for longer monitoring durations. In contrast, the expected uncertainties estimated with both $\boldsymbol{T}_{\text{noise}}$ is closer to the real uncertainty even for short monitoring durations. Such results confirm what we observed in Section 8.3.3: the expected uncertainty is smaller when calculated with $\boldsymbol{T}_{\text{noise}}$ for short monitoring durations, because the random variability $n_i(\sigma_{\text{noise}})$ in $\boldsymbol{T}_{\text{noise}}$ reduces the correlation between the temperature and time. As a result, within the calculation of the expected uncertainty $\sigma_{m,\text{pp}}$ with $\boldsymbol{T}_{\text{noise}}$, the

posterior uncertainty of the trend-parameter $\sigma_{m|\epsilon}$ might be underestimated, depending on the chosen value of σ_{noise}. In contrast, the expected uncertainty $\sigma_{m,\text{pp}}$ calculated with $\boldsymbol{T}$ always slightly overestimates the posterior one, so that its use is safe for the design purpose.

In order to quantify the difference between the expected and real uncertainty of a model parameter, and to validate the proposed approach, we use the concept of monitoring system effectiveness [3] in the estimation of the model parameter m. The monitoring effectiveness, η, expresses the extent to which the monitoring observations improve the knowledge of the structure behaviour; in other words, the extent to which the parameter uncertainty a posteriori is lower than a priori. We define the expected effectiveness of the monitoring system, η_{exp}, as the ratio between the prior uncertainty σ_m and the pre-posterior uncertainty $\sigma_{m,\text{pp}}$. We define the real effectiveness of the monitoring system, η_{real}, as the ratio between the prior uncertainty σ_m and the posterior uncertainty $\sigma_{m|\epsilon}$.

$$\eta_{\text{exp}} = \sigma_m / \sigma_{m,\text{pp}} \tag{8.30}$$

$$\eta_{\text{exp}} = \sigma_m / \sigma_{m|\epsilon} \tag{8.31}$$

The inverse of the monitoring effectiveness, $1/\eta$, expresses the ineffectiveness of the monitoring system: the closer $1/\eta$ is to zero, the higher the reduction in the parameter uncertainty thanks to the monitoring data; the closer $1/\eta$ is to 1, the lower the reduction in the parameter uncertainty thanks to the monitoring data. Figure 8.12 shows the expected and real ineffectiveness of the monitoring system, $1/\eta_{\text{exp}}$ and $1/\eta_{\text{real}}$, respectively.

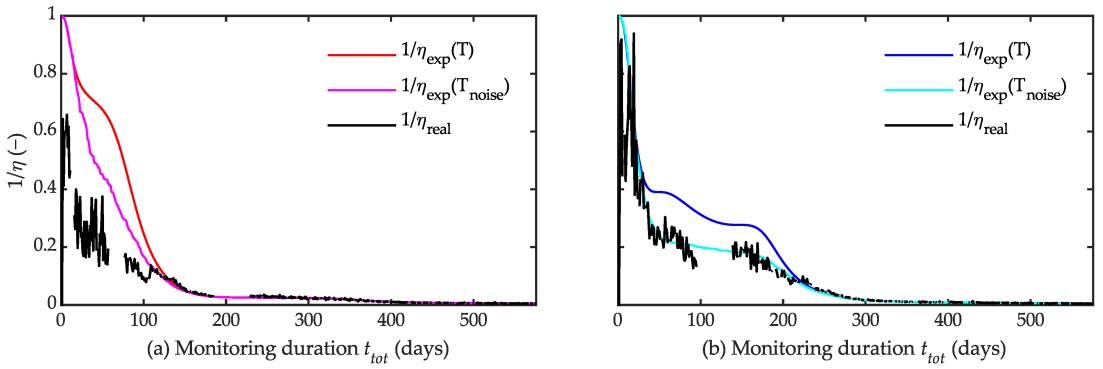

Figure 8.12: Expected $1/\eta_{exp}$ and real $1/\eta_{real}$ ineffectiveness of the monitoring system. The $1/\eta_{exp}$ is calculated with $\boldsymbol{T}$ and $\boldsymbol{T}_{noise}$. The monitoring start dates are (a) 20 April, $b = 0$, and (b) 20 July, $b = \pi/2$. The monitoring duration t_{tot} varies from 3 to 600 days.

As the monitoring duration increases, both the expected and the real monitoring ineffectiveness $1/\eta$ decrease. The monitoring start date influences the monitoring duration required before $1/\eta$ stabilizes around zero. In particular, a monitoring system that starts measuring in summer reaches $1/\eta \approx 0$ after around 250 days; in contrast, a monitoring system that starts measuring in spring reaches $1/\eta \approx 0$ after around 150 days. A few days' variations depend on the simulated temperature used.

Finally, we quantify the error $\boldsymbol{e}_{m,\text{pp}}$ in the pre-posterior estimation of the linear trend uncertainty $\sigma_{m,\text{pp}}$ as the difference between the expected and real ineffectiveness of the monitoring system.

$$\boldsymbol{e}_{m,\text{pp}} = 1/\eta_{\text{exp}} - 1/\eta_{\text{real}} \tag{8.32}$$

Figure 8.13 shows how the error $\boldsymbol{e}_{m,\text{pp}}$ changes as the monitoring duration increases.

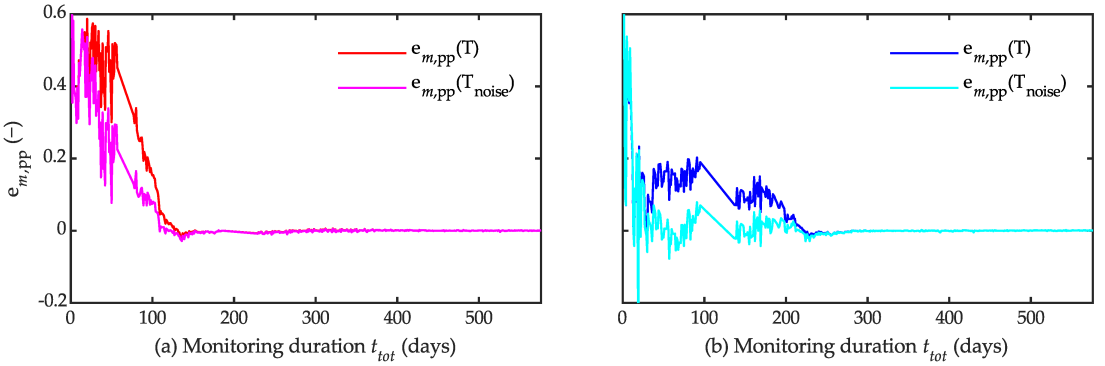

Figure 8.13: Error $\boldsymbol{e}_{m,pp}$ between the expected and the real uncertainty of the parameter m. The expected uncertainty is calculated with $\boldsymbol{T}$ and $\boldsymbol{T}_{noise}$. The monitoring start dates are (a) 20 April and (b) 20 July. $\sigma_m = 1\ \mu\epsilon/day = 365\ \mu\epsilon/year$.

The error $\boldsymbol{e}_{m,\text{pp}}$ may have negative values according to the simulated temperature function used in the estimation of $\sigma_{m,\text{pp}}$ [39]; for positive values of $\boldsymbol{e}_{m,\text{pp}}$, the posterior uncertainty $\sigma_{m|\boldsymbol{\epsilon}}$ is overestimated, while for negative values of $\boldsymbol{e}_{m,\text{pp}}$, the posterior uncertainty $\sigma_{m|\boldsymbol{\epsilon}}$ is underestimated. In our case, when the monitoring starts in the spring, $\boldsymbol{e}_{m,\text{pp}}$ is mostly positive with any simulated temperature function; it progressively decreases and zeroes after around 150 days. On the other hand, when the monitoring starts during summer, $\boldsymbol{e}_{m,\text{pp}}$ has some negative values in the evaluation with $\boldsymbol{T}_{\text{noise}}$; the value of $\boldsymbol{e}_{m,\text{pp}}$ remains constantly equal to zero after a longer monitoring period of around 250 days.

We note that the expected uncertainty estimated with $\boldsymbol{T}$ is less accurate than the one with $\boldsymbol{T}_{\text{noise}}$, but it is always positive; the expected un-

certainty estimated with our approach and with $\boldsymbol{T}$ always overestimates the real uncertainty. In this case, we may look at $\boldsymbol{e}_{m,\text{pp}}$ as a safety factor: the monitoring system will never provide the key parameter with posterior uncertainty higher than what is expected. In contrast, the expected uncertainty estimated with $\boldsymbol{T}_{\text{noise}}$ is more accurate, but can underestimate the real uncertainty; this confirms again that the day-by-day variation of $\boldsymbol{T}_{\text{noise}}$ reduces the time–temperature correlation.

Proposed Approach vs. Previous Studies

Our approach is in line with many previous studies in the literature regarding the use of a linear interpretation model to combine the mechanical response with the temperature effects. Such a model can be used to effectively perform the temperature compensation of monitoring data: the effectiveness of this choice has been validated for mechanical responses such as strain measurements [40], ultrasonic measurements [41], vibrational measurements [27, 31], and cracks opening [31]. The linear temperature compensation of the monitoring data has proven to be necessary to detect whether damage is present or not based on the measured dynamic or static characteristics of a monitored system [13]. Moreover, our approach is similar to that which is currently used for the temperature compensation of the sensor response [39, 42, 43, 44], rather than the structural response. Indeed, the response of sensors is also sensible to temperature variation; therefore, sensor measurements must compensate for temperature effects before being used for structural assessment.

As far as the design of a structural health monitoring system is concerned, there are many previous studies regarding the optimal sensor placement based on the maximisation of the information acquired or on the maximisation of the value of information acquired for structural management purposes. However, to our best knowledge there aren't any previous studies regarding the estimation of the expected uncertainty of structural response trends accounting for temperature compensation for monitoring system design purposes.

Concerning the design of structural health monitoring systems, there are many previous studies regarding the optimal sensor placement based on the maximisation of the information acquired or on the maximisation of the value of information acquired for structural management purposes. However, to our best knowledge there aren't any previous studies on the estimation of the expected uncertainty of structural response trends accounting for temperature compensation for design purposes.

The main advantage of our approach is its ease of use by the majority of civil engineers, who typically have a solid background in structural design but not necessarily in statistics and probability. They can apply our

algorithm to predict the performance of a tentative monitoring system in the design phase, even without being familiar with Bayesian probability. This is an important step forward for the extension of structural health monitoring to a higher number of bridges. Indeed, the effectiveness of a tentative monitoring system can be practically evaluated by comparing the expected uncertainty (the monitoring system capacity) resulting from the proposed algorithm with a target value required by the infrastructure operator (monitoring system demand). This corresponds to the comparison between the structural capacity and structural demand in structural design.

On the other hand, the main disadvantage of the proposed algorithm is its tendency to overestimate the real uncertainty of the trend-parameter for short monitoring periods, which might require a stronger performance of the sensors than is really necessary. This issue can be mitigated by choosing the simulated temperature $\boldsymbol{T}_{\text{noise}}$, which models the observed variation in the real temperature between two consecutive days, rather than the sinusoidal temperature $\boldsymbol{T}$. However, the use of $\boldsymbol{T}_{\text{noise}}$ requires the statistical estimation of an appropriate value of σ_{noise} based on the values of the local temperature. Finally, the uncertainty of the linear model σ_{model} should also be statistically estimated. It depends on the trend parameter to be identified (e.g., the strain trend, displacement trend, frequency trend, crack amplitude trend) and on the structure to be monitored (e.g., prestressed concrete bridge, cable-stayed bridge, arch bridge). Concerning prestressed concrete highway bridges and long-term concrete strain trends, a value of $\sigma_{\text{model}} = 20\ \mu\epsilon$ is generally acceptable.

8.6 Conclusions

When designing a monitoring system, we need to predict beforehand the uncertainty of the key performance parameters we expect to achieve after the monitoring is performed. In this paper, we derived a simple-to-use formulation that allows us to calculate the expected uncertainty of a long-term structural response trend based on monitoring data compensated from temperature effects. This formulation does not depend on the response measurements; therefore, it can be used by the designer to validate the performances of a tentative monitoring strategy before the measurements are actually available. The formulation only requires us to make reasonable assumptions on the sampling timestamp vector, the expected temperature variation and the residual noise. The timestamp vector depends on the sampling frequency chosen by the designers. The temperature can be roughly, but effectively, simulated with a sine function with a period of 1 year. The residual error can be predicted by

combining sensor noise and the approximation error of the interpretation model. According to the formulation, the uncertainty of a linear drift depends essentially on these factors:

- sensor accuracy, usually provided in the technical datasheets of the sensors;
- the correctness of the interpretation model, i.e., how well the model fits the actual structural response;
- the monitoring duration, and, to a minor extent, the sampling frequency;
- the degree of correlation between the time and temperature records, i.e., the extent to which the temperature record confuses with a straight line.

The formulation predicts that, for monitoring periods of a few months, the uncertainty is particularly sensitive to the linear correlation between the time and temperature, as temperature can be approximated to a linear trend. In particular, the fitting quality changes significantly depending on whether the monitoring start date is a solstice or an equinox. Beyond the first year of monitoring, the confusion between the time and temperature is negligible, and the quality of the monitoring primarily depends on the monitoring duration.

We validated our approach by applying the formulation to a real-life case study, the Colle Isarco Viaduct. This is one of the longest prestressed concrete bridges in the European Alpine region, and it is currently equipped with an optical fibre sensor network and resistance temperature detectors. We focused on a cross-section of the box girder of the bridge, and we estimated the expected uncertainty of the long-term strain trend, purged of seasonal temperature effects, with our approach. Then, we verified whether the pre-posterior estimation of uncertainty is consistent with its posterior estimation, based on the actual monitoring data.

We observed that the expected uncertainty accurately predicts the posterior uncertainty after 150–250 days of monitoring data. For shorter monitoring durations, the prediction accuracy depends on the way in which the expected temperature record was been simulated. In particular, the pre-posterior uncertainty estimated assuming an ideal sinusoidal temperature record always slightly overestimates the actual posterior uncertainty; therefore, its use is appropriate for the design purpose. Adding Gaussian noise to the simulated sine temperature allows the prediction of the posterior uncertainty with a smaller error, but it may underestimate it; therefore, its use could be less appropriate for the design purpose.

The proposed approach is an important step forward for the extension of structural health monitoring to a higher number of bridges. Indeed, it can easily be used by civil engineers to quantify the expected performance of a monitoring solution in its design phase, and it does not require a solid background in statistics and probability. It allows the verification beforehand of the effectiveness of a monitoring solution with the consolidated logical approach for structural design: capacity $>$ demand.

Its validation for other types of structural response trends (e.g., displacement, rotation, frequency variation, crack propagation) will be further investigated in future research studies. Moreover, future research will address the estimation of the expected uncertainty, accounting for temperature compensation with a number of temperature sensors.

Bibliography

[1] U. E. I. di Normazione, "Uni/tr 11634:2016. guidelines for structural health monitoring," tech. rep., Ente Italiano di Normazione (UNI), Milano, Italy, 2016. Technical Report.

[2] C. Cappello, D. Zonta, and B. Glišić, "Expected utility theory for monitoring-based decision-making," *Proceedings of the IEEE*, vol. 104, no. 8, pp. 1647–1661, 2016.

[3] D. Tonelli, C. Cappello, and D. Zonta, "Performance-based design of structural health monitoring systems," in *European Workshop on Structural Health Monitoring*, pp. 238–247, Springer, 2020.

[4] D. Bolognani, A. Verzobio, D. Tonelli, C. Cappello, B. Glisic, D. Zonta, and J. Quigley, "Iwshm 2017: Quantifying the benefit of structural health monitoring: what if the manager is not the owner?," *Structural Health Monitoring*, vol. 17, no. 6, pp. 1393–1409, 2018.

[5] A. Verzobio, D. Bolognani, J. Quigley, and D. Zonta, "Consequences of representativeness bias on shm-based decision-making," *Structure and Infrastructure Engineering*, vol. 18, no. 6, pp. 851–863, 2022.

[6] W. M. Bolstad and J. M. Curran, *Introduction to Bayesian statistics*. John Wiley & Sons, 2016.

[7] C. Cappello, D. Zonta, M. Pozzi, B. Glisic, and R. Zandonini, "Impact of prior perception on bridge health diagnosis," *Journal of Civil Structural Health Monitoring*, vol. 5, no. 4, pp. 509–525, 2015.

[8] W. M. Bolstad, *Understanding computational Bayesian statistics*. John Wiley & Sons, 2009.

[9] J.-A. Goulet, *Probabilistic machine learning for civil engineers*. MIT press, 2020.

[10] C. Papadimitriou, J. L. Beck, and S.-K. Au, "Entropy-based optimal sensor location for structural model updating," *Journal of Vibration and Control*, vol. 6, no. 5, pp. 781–800, 2000.

[11] F. E. Udwadia, "Methodology for optimum sensor locations for parameter identification in dynamic systems," *Journal of engineering mechanics*, vol. 120, no. 2, pp. 368–390, 1994.

[12] V. V. Fedorov and P. Hackl, "Optimal experimental design: spatial sampling," *Calcutta Statistical Association Bulletin*, vol. 44, no. 1-2, pp. 57–82, 1994.

[13] H. Sohn, "Effects of environmental and operational variability on structural health monitoring," *Philosophical Transactions of the Royal Society A: Mathematical, Physical and Engineering Sciences*, vol. 365, no. 1851, pp. 539–560, 2007.

[14] V. Křístek, Z. Bažant, M. Zich, and A. Kohoutková, "Box girder bridge deflections," *Concrete international*, vol. 28, no. 01, pp. 55–63, 2006.

[15] R. Wendner, M. H. Hubler, and Z. P. Bažant, "Optimization method, choice of form and uncertainty quantification of model b4 using laboratory and multi-decade bridge databases," *Materials and Structures*, vol. 48, no. 4, pp. 771–796, 2015.

[16] G. F. Giaccu, D. Solinas, B. Briseghella, and L. Fenu, "Time-dependent analysis of precast segmental bridges," *International Journal of Concrete Structures and Materials*, vol. 15, no. 1, p. 13, 2021.

[17] M. H. Hubler, R. Wendner, and Z. P. Bazant, "Comprehensive database for concrete creep and shrinkage: analysis and recommendations for testing and recording," *ACI Materials Journal*, vol. 112, no. 4, p. 547, 2015.

[18] Z. P. Bazant and S. Baweja, "Creep and shrinkage prediction model for analysis and design of concrete structures: Model b3," *ACI Special Publications*, vol. 194, pp. 1–84, 2000.

[19] C. Videla, D. J. Carreira, N. Garner, *et al.*, "Guide for modeling and calculating shrinkage and creep in hardened concrete," *ACI report*, vol. 209, p. 76, 2008.

[20] M. C. Ceb-Fip, "Design code," *Comite Euro International du Beton*, pp. 51–59, 1990.

[21] C. Européen, "Eurocode 2: Design of concrete structures—part 1-1: General rules and rules for buildings," *London: British Standard Institution*, p. 37, 2004.

[22] D. Zonta, C. Cappello, A. Beltempo, A. Bonelli, D. Bolognani, O. S. Bursi, C. Costa, W. Pardatscher, *et al.*, "Structural retrofit and health monitoring of colle isarco viaduct," in *Structural faults & repair 2016: 16th International conference and exhibition, venue: Radisson Blu Edinburgh 17th-19th May 2016*, Edinburgh: Engineering Technics Press [2016], 2016.

[23] Z. P. Bazant, Q. Yu, and G.-H. Li, "Excessive long-time deflections of prestressed box girders. i: Record-span bridge in palau and other paradigms," *JOURNAL OF STRUCTURAL ENGINEERING-ASCE*, vol. 138, no. 6, pp. 676–686, 2012.

[24] H. Abdel-Jaber and B. Glisic, "Monitoring of prestressing forces in prestressed concrete structures—an overview," *Structural Control and Health Monitoring*, vol. 26, no. 8, p. e2374, 2019.

[25] H. Abdel-Jaber and B. Glisic, "Monitoring of long-term prestress losses in prestressed concrete structures using fiber optic sensors," *Structural Health Monitoring*, vol. 18, no. 1, pp. 254–269, 2019.

[26] B. Glisic and D. Inaudi, *Fibre optic methods for structural health monitoring*. John Wiley & Sons, 2007.

[27] E. Cross, K. Koo, J. Brownjohn, and K. Worden, "Long-term monitoring and data analysis of the tamar bridge," *Mechanical Systems and Signal Processing*, vol. 35, no. 1-2, pp. 16–34, 2013.

[28] L. Possidente, N. Tondini, and J.-M. Battini, "Branch-switching procedure for post-buckling analysis of thin-walled steel members at elevated temperature," *Thin-Walled Structures*, vol. 136, pp. 90–98, 2019.

[29] L. Possidente, N. Tondini, and J.-M. Battini, "3d beam element for the analysis of torsional problems of steel-structures in fire,"

Journal of Structural Engineering, vol. 146, no. 7, p. 04020125, 2020.

[30] C. Rodrigues, C. Félix, A. Lage, and J. Figueiras, "Development of a long-term monitoring system based on fbg sensors applied to concrete bridges," *Engineering Structures*, vol. 32, no. 8, pp. 1993–2002, 2010.

[31] A. Kita, N. Cavalagli, F. Ubertini, *et al.*, "Temperature effects on static and dynamic behavior of consoli palace in gubbio, italy," *Mechanical Systems and Signal Processing*, vol. 120, pp. 180–202, 2019.

[32] B. Gentilini and L. Gentilini, "Il viadotto di colle isarco per l'autostrada del brennero," *L'Industria Italiana del Cemento*, vol. 5, pp. 318–334, 1972.

[33] C. M. Bishop and N. M. Nasrabadi, *Pattern recognition and machine learning*, vol. 4. Springer, 2006.

[34] I. ISO. and B. OIML, *Guide to the Expression of Uncertainty in Measurement*. Aenor Madrid, Spain, 1993.

[35] M. F. Bado and J. R. Casas, "A review of recent distributed optical fiber sensors applications for civil engineering structural health monitoring," *Sensors*, vol. 21, no. 5, p. 1818, 2021.

[36] M. F. Bado, J. R. Casas, A. Dey, C. G. Berrocal, G. Kaklauskas, I. Fernandez, and R. Rempling, "Characterization of concrete shrinkage induced strains in internally-restrained rc structures by distributed optical fiber sensing," *Cement and Concrete Composites*, vol. 120, p. 104058, 2021.

[37] S. Autostrada del Brennero, "Consolidamento strutturale dell impalcato del viadotto colle isarco, a progressiva km 8+ 957," tech. rep., Technical report (in Italian), Trento, 2013.

[38] W. K. Hastings, "Monte carlo sampling methods using markov chains and their applications," 1970.

[39] P. Moyo, J. M. Brownjohn, R. Suresh, and S. Tjin, "Development of fiber bragg grating sensors for monitoring civil infrastructure," *Engineering structures*, vol. 27, no. 12, pp. 1828–1834, 2005.

[40] D. Sigurdardottir and B. Glisic, "On-site validation of fiber-optic methods for structural health monitoring: Streicker bridge," *Journal of Civil Structural Health Monitoring*, vol. 5, no. 4, pp. 529–549, 2015.

[41] A. J. Croxford, J. Moll, P. D. Wilcox, and J. E. Michaels, "Efficient temperature compensation strategies for guided wave structural health monitoring," *Ultrasonics*, vol. 50, no. 4-5, pp. 517–528, 2010.

[42] R. Li, Y. Tan, Y. Chen, L. Hong, and Z. Zhou, "Investigation of sensitivity enhancing and temperature compensation for fiber bragg grating (fbg)-based strain sensor," *Optical Fiber Technology*, vol. 48, pp. 199–206, 2019.

[43] H.-P. Wang, J.-G. Dai, and X.-Z. Wang, "Improved temperature compensation of fiber bragg grating-based sensors applied to structures under different loading conditions," *Optical Fiber Technology*, vol. 63, p. 102506, 2021.

[44] Y. Kuang, Y. Guo, L. Xiong, and W. Liu, "Packaging and temperature compensation of fiber bragg grating for strain sensing: a survey," *Photonic Sensors*, vol. 8, no. 4, pp. 320–331, 2018.

9. Conclusions

9.1 Summary and research contribution

Due to the progressive aging of bridges, tragic collapses, and the increasing frequency of extreme events, interest in permanent SHM of critical infrastructure has rapidly grown. Significant research efforts and technological advancements in this field have generated widespread optimism regarding the adoption of SHM technologies and methods in engineering practice, further supported by national funding initiatives and new guidelines. Nowadays, there is a common understanding –or at least a general awareness– among practitioners of the role of SHM as a tool capable of improving knowledge of structural condition through the observation of structural behaviour, and ultimately of identifying damage or deterioration. This information can then be exploited by infrastructure managers to support decision-making within a BMS framework.

Despite this optimistic context, several challenges still hinder the widespread adoption of SHM in real-world applications, mainly due to the high costs associated with the installation, maintenance, and data management of SHM systems. Traditional on-site monitoring systems usually require the installation of several expensive components and a complex architecture (e.g. sensors, cabling systems, acquisition modules, uninterruptible power supplies, centralized computers, etc.). Moreover, there is currently no standardized regulation for the design of such systems based on the different needs and objectives of the monitoring, meaning that some systems may prove ineffective and may even result in a waste of resources and financial investments.

This thesis presents practical solutions to some of the main challenges previously identified as limiting the widespread adoption of SHM for bridge management. These solutions leverage satellite SAR monitoring to explore a remote, device-free approach to bridge monitoring, and also address the design of monitoring systems and the evaluation of their effectiveness.

First of all, this thesis includes a comprehensive state-of-the-art on BMS practices, current trends, and main challenges. This contribution provides an organized and in-depth overview of the field in which SHM developments are grounded, considering that the ultimate goal of SHM is bridge condition assessment and support for effective bridge management. This work lays the foundation for the main operational research of the thesis.

Subsequently, this thesis explores the potential of satellite SAR tech-

nology for bridge monitoring without the need to install any sensors on site. It advances this growing field of research by introducing a framework for bridge deformation analysis based on satellite MT-InSAR data processing, demonstrated through the A22 Po River bridge case study. Moreover, it presents a novel data-driven approach for the automated post-processing and interpretation of results extracted by means of MT-InSAR analysis, promoting the integration of SAR data into BMS frameworks. This approach was tested on the A22 Po River bridge and the A22 Colle Isarco Viaduct case studies. The key findings from this work are:

- MT-InSAR is a promising tool for the SHM of bridges. In the analysed case studies, the high number of identified PS points, together with the high temporal coherence values, confirm the high reliability of satellite InSAR for long-term bridge monitoring.
- Periodic displacement patterns consistent with the expected thermo-structural response of the bridges were observed through MT-InSAR results, validating the sensitivity of InSAR to temperature-induced movements.
- Unexpected deformation patterns were also detected in the MT-InSAR results, highlighting localized abnormal deformation rates within the analysed areas.
- A relationship between river water level fluctuations and the displacement behaviour of bridge piers was identified, emphasizing the relevance of environmental and geotechnical factors.
- A customized data-driven clustering algorithm was developed to enable the rapid and automatic classification of MT-InSAR results, i.e. the extracted PS.
- The algorithm accounts not only for the displacement time-series of PS, but also for their geographic coordinates. This approach allows the identification of differing temporal patterns exhibited by the PS –such as periodic trends, subsidence, uplift, and stationary behaviour– and their association with physical objects in the examined area.
- The proposed algorithm is applicable to a wide range of case studies and structures, encompassing different geometries and materials, structural schemes, spatial orientations, geographical locations, and surrounding environments of the monitored structure.
- The proposed algorithm allowed the identification of both expected and unexpected deformation patterns, the characterization of the behaviour of individual structural components, and the distinction

between the structures of interest and surrounding elements within the study area.

- The proposed algorithm requires minimal calibration effort and does not require prior specification of bridge coordinates or technical InSAR parameters, enabling its use by civil engineers with limited expertise in data science techniques and MT-InSAR data processing.
- The proposed algorithm advances the integration of MT-InSAR data into BMS frameworks by providing an effective method for the rapid analysis of large volumes of satellite data.

On the other hand, this thesis advances the field of monitoring system design by proposing a formulation for evaluating the performance of a monitoring solution during the design phase, when observations are not yet available. This approach was validated using the A22 Colle Isarco Viaduct case study, considering its existing SHM system, by comparing the results of a pre-posteriori performance evaluation obtained through the proposed formulation–without exploiting any monitoring data from the system itself–with the actual a posteriori performance evaluated using the monitoring data acquired by the system. The key findings from this research are:

- A simple formulation was derived to predict the expected uncertainty of a long-term structural response trend–i.e. the monitoring capacity–after temperature compensation.
- The proposed formulation does not require actual response measurements as inputs, making it suitable for evaluating the performance of a monitoring strategy during the design phase.
- It was found that the uncertainty of a structural response trend essentially depends on:
  - sensor accuracy;
  - monitoring duration;
  - sampling frequency;
  - the degree of correlation between time and temperature.

  For short monitoring periods, the expected uncertainty is highly sensitive to temperature variations. After the first year of monitoring, the confusion between time and temperature becomes negligible.
- The proposed method represents a significant step toward extending SHM to a larger number of bridges, providing a simple tool for engineers to assess monitoring performance without requiring

advanced statistical knowledge. It can be used by practitioners to design effective monitoring systems for the evaluation of long-term structural response trends.

9.2 Limitations and future perspectives

It is important to acknowledge the limitations of this research. These limitations provide context for interpreting the results and highlight areas for future refinement and improvement:

- The effectiveness of InSAR monitoring is strongly influenced by the orientation of the analyzed bridge with respect to the satellite LoS, which constrains the sensitivity to specific displacement components. For example, when a bridge is oriented in the north–south direction with its longitudinal axis parallel to the satellite orbit, longitudinal movements of the bridge structural elements cannot be observed.
- Satellite InSAR technique measures displacements along the LoS direction, which may complicate the interpretation of complex, multi-directional structural movements. To achieve a better understanding of the different displacement components, ascending and descending satellite orbit datasets should be combined. However, the analyses presented in this thesis are based solely on descending-orbit datasets, limiting the ability to distinguish between vertical and horizontal (longitudinal and transverse) displacements of the investigated structures.
- The proposed algorithm for the automated classification of PS requires calibration and some user-defined inputs. Specifically, for each case study the user must define: (i) the number of clusters; and (ii) the values of the coefficients α and β, regulating the weights of the clustering metric components.
- The proposed formulation for monitoring system design relies on the a priori definition of a timestamp vector, a simulated temperature function, and residual noise. Inaccurate estimation or high uncertainty in these quantities during the design phase may lead to errors in the prediction of the monitoring performance.
- The proposed formulation for monitoring system design allows the evaluation of the expected uncertainty for a specific, yet essential, class of monitoring state parameters, namely structural response trends. Other types of monitoring state parameters remain unexplored.

In light of the limitations discussed above, and in order to strengthen the findings of this thesis and expand their applicability, future research should aim to address the following aspects:

- Incorporating both ascending and descending orbit satellite datasets into the analysis, to enable the separation of vertical and horizontal displacement components, whenever the monitored structure can be adequately observed from both satellite geometries. A comparative analysis with the results obtained using single-orbit datasets in this thesis, together with additional case studies, would further improve the understanding of the actual applicability of SAR technology for SHM.
- Designing a tailored methodology to determine the optimal number of clusters when applying the proposed PS clustering algorithm, by accounting for the geographical extent of the study area, PS density, and the expected deformation patterns. In addition, developing a systematic procedure for selecting the coefficients α and β as a function of the chosen number of clusters and the specific characteristics of each case study. The analysis of additional case studies would support the refinement of these aspects and improve the scalability of the proposed approach.
- Developing new formulations to evaluate the expected uncertainty of different classes of key structural state parameters–such as vibrational parameters–thereby enabling the prediction of the performance of various types of monitoring systems in the design phase.
- Further research is required on the estimation of the monitoring demand, with the aim of integrating it into design codes, similarly to what is done in structural design practice. In this context, a VoI-based analysis conducted on a comprehensive dataset covering different structure types and key monitoring state parameters is recommended, in line with the principles of performance-based monitoring system design.
- Finally, the different findings and methodologies developed in this thesis should be integrated into a comprehensive BMS framework. Such a framework should jointly exploit on-site instrumental monitoring data and satellite-based monitoring data to assess the condition state of bridges and support informed decision-making for maintenance and management actions.

Annex

A. Comparison of monitoring systems performance

In Chapter 4, the Performance-based Monitoring System Design approach was illustrated. This methodology, adopted by the Italian guidelines for Structural Health Monitoring [1], includes a series of steps for estimating the performance of a monitoring solution in the design phase: the identification of a monitoring objective, and thus of the key state parameters of the monitoring; the evaluation of the monitoring demand; the identification of a tentative solution for measuring the physical quantities; the selection of an interpretation model, stating the relation between such quantities and the key state parameters; the evaluation of the monitoring capacity; and finally, the comparison between demand and capacity, to evaluate the effectiveness of the tentative system.

The evaluation of the monitoring capacity requires calculating the expected uncertainty of the key state parameters in a pre-posteriori framework. This process is not always straightforward, depending on the objective of the monitoring, the involved observations, and the chosen interpretation model. In Chapter 8, a closed-form expression for the evaluation of the pre-posterior uncertainty of long-term response trends was developed and discussed. The proposed formulation was validated through the Colle Isarco viaduct case study.

This Chapter includes an additional discussion that provides further insight into the application of the proposed formulation for monitoring system design. Specifically, the performance of two monitoring solutions is evaluated and compared, demonstrating how the proposed approach can be applied to address a practical monitoring system design problem. The first solution is based on a traditional topographic monitoring system, while the second relies on satellite SAR technology. Both technologies are used to measure displacements, and the extracted monitoring state parameter is the long-term displacement trend.

A.1 Monitoring system design problem

Let's take into account a monitoring system design problem, and wear the hat of the monitoring system designer: a highway concessionaire manager wants to monitor the long-term displacements trend of one of their bridges, and thus ask us to suggest a monitoring solution.

As the system designers, our aim is the evaluation of the monitoring capacity, i.e. the expected uncertainty of the long-term displacements trend of the bridge compensated from temperature effects. Accordingly, the measured quantities will include the displacements of the bridge's

structural elements and the temperature of those elements (or, alternatively, the air temperature, if it can be assumed to exhibit similar variations). We take into account two specific technologies for measuring structural displacements:

(a) **A topographic on-site system** that allows measuring the position of optical prisms installed on the bridge at each reading of the automatic total stations located near the bridge. Specifically, a latest generation automatic total station will be taken into account. Specifics and datasheet of such system can be found in [2].

(b) **SAR sensors mounted on satellites**, which provide SAR imagery at each pass of the satellite over the bridge, that must be processed through MT-InSAR technique in order to extract the bridge displacements. Specifically, high-resolution X-band COSMO-SkyMed (CSK) Stripmap HIMAGE datasets will be taken into account. The specifics of such system can be found in [3].

The choice of one out of the two above described technologies has an impact both on the monitoring performance –in terms of pre-posterior uncertainty– and on the monitoring costs. Our aim is to verify what is the most cost-effective technology to solve the monitoring design problem and suggest a monitoring solution to the infrastructure manager, or alternatively to provide comprehensive information regarding the two options different performance levels and costs, enabling the manager to make an informed decision.

According to the monitoring system design procedure (Section 4.1), first we must define the monitoring demand $\bar{\sigma}_m$ in terms of maximum acceptable uncertainty in the estimation of the displacement trend m (the displacement trend m is the key state parameter in this monitoring problem). Then, we must define the interpretation model, stating the relation between model parameters and observed quantities. Finally, we can proceed to calculate the monitoring capacity $\sigma_{m,\text{pp}}$ in terms of pre-posterior uncertainty of the displacement trend, for both the proposed tentative monitoring solutions, and verify their effectiveness.

A.2 Monitoring demand

Let us define the value of the monitoring demand $\bar{\sigma}_m$. This value represents the accuracy requirement set by the infrastructure manager for the evaluation of the key monitoring state parameter, allowing us to establish a benchmark for comparing the two solutions performance. Let us assume that the manager of the bridge needs to know the state of

the structure, here represented by the long-term displacement trend m of the structural elements, with an uncertainty not higher than $\bar{\sigma}_m = 1\ mm/year$. Moreover, as the monitoring system designers, we also may want to push the request further, and evaluate the tentative systems performance with a demand of $\bar{\sigma}_{m,\text{strict}} = 0.1\ mm/year$.

A.3 Interpretation model

The interpretation model is represented by Equation A.1, where the observed structural response $\boldsymbol{y}$ are the structural elements displacements in mm.

$$y_i = y_0 + m \cdot \Delta t_i + \alpha_y \cdot \Delta T_i + z_i \tag{A.1}$$

Where:

- y_0 is an offset parameter representing the displacement at time t_0 and temperature T_0.
- α_y $[mm/°C]$ represents the apparent thermal component of displacement measurements. α_y depends on the concrete thermal expansion coefficient α_ϵ $[\mu\epsilon/°C]$, but also on the geometry of the considered structural element, and the temperature distribution in the structural element. Specifically, for a uniform temperature distribution and a structural element of length L, parameter α_y can be calculated as:

$$\alpha_y = \alpha_\epsilon \cdot L \tag{A.2}$$

- m $[mm/year]$ is the variation trend over time, which is the object of the estimation. It is the gradient of the linear model with respect to time. It expresses the linear trend over time of $y(t)$ purged from temperature effects, and includes all long-term effects.
- z_i is the residual, i.e. the difference between the statistically independent observation y_i and the nominal value of the model.
- t_i is the timestamp;
- T_i is the temperature measurement.

A.4 Monitoring capacity

For the sake of simplicity, let us assume that the manager does not have any prior knowledge of the value of the key state parameter m, so that $\sigma_m \to \infty$. Then, we can refer to the simplified version of the formulation proposed in Chapter 8 for the calculation of the pre-posterior uncertainty of the displacement trend parameter $\sigma_{m,\text{pp}}$:

$$\sigma_{m,\text{pp}} = \sigma_{\text{LH}} \cdot \frac{1}{|\Delta \boldsymbol{t}|} \cdot \frac{1}{\sqrt{1 - \rho^2_{\boldsymbol{tT}}}} \tag{A.3}$$

In order to calculate $\sigma_{m,\text{pp}}$, we must evaluate the following quantities for each considered solution:

(1) the likelihood uncertainty σ_{LH}, depending on measurements and model uncertainty;

(2) the time-dependent term $1/|\Delta \boldsymbol{t}|$, depending on the sampling frequency f_s;

(3) the time-temperature correlation term $1/\sqrt{1 - \rho^2_{\boldsymbol{tT}}}$, depending on a simulated temperature function $\boldsymbol{T}$.

A.4.1 Likelihood uncertainty evaluation

The likelihood uncertainty σ_{LH} can be estimated using the following Equation:

$$\sigma_{\text{LH}} = \sqrt{\sigma_y^2 + \alpha_y^2 \cdot \sigma_T^2 + \sigma^2_{\text{model}}} \tag{A.4}$$

where:

- σ_{model} is the model uncertainty;
- σ_y is the uncertainty of the displacement measurements;
- σ_T is the uncertainty of the temperature measurements;
- α_y is the thermal component of the displacement.

The model uncertainty can be assumed to be $\sigma_{\text{model}} = 1\ mm$, referring to previous literature case studies [4].

The measurement uncertainty for the topographic monitoring system is assumed to be $\sigma_y = 1\ mm$, based on the measurement error reported in the datasheets of the latest-generation commercial total station instrumentation [2].

The evaluation of measurement uncertainty when using SAR satellite technology is less straightforward. Several studies in the literature have estimated the accuracy of SAR-derived displacement measurements by comparison with measurements collected in controlled field tests, as well as with measurements collected on real bridges under operating conditions (see Section 3.4). For high-resolution X-band SAR sensors, the standard deviation between SAR measurements and on-site measurements has been reported to range from less than 1 mm up to approximately 3 mm.

It is important to note that assuming these values as the SAR sensor's accuracy relies on the implicit assumption that on-site measurements represent the true displacement of the structure; however, this assumption is not necessarily valid. Furthermore, the accuracy of satellite-based displacement measurements strongly depends on the direction of the displacement. Indeed, SAR satellites measure displacements of PS along the LoS, whereas real structural displacements generally occur along multiple directions. In the ideal case, where structural displacements occur only along a single known direction, the displacement can be obtained by projecting the LoS measurements onto that direction, and the measurement accuracy corresponds to the accuracy of the SAR sensor.

In real-world scenarios, however, structural displacements often have components along different directions. In such cases, multiple acquisition geometries must be combined to retrieve the individual displacement components. This combination introduces additional sources of uncertainty related to the temporal and spatial resampling of PS. Giordano et al. [5] investigated the magnitude of these errors as a function of the selected grid layout.

In the present discussion, it is assumed that only a single acquisition geometry is employed in order to limit the uncertainty in displacement measurements, and that the direction of the dominant displacement component is known (e.g., vertical displacements only). Based on these assumptions, the displacement measurement uncertainty for SAR satellite sensors is set to $\sigma_y = 2\ mm$, consistent with the typical error range reported for X-band SAR sensors when displacement measurements are extracted using MT-InSAR processing applied to long image time-series (more than 20 acquisitions) [6].

The measurement uncertainty for the temperature sensors is assumed to be $\sigma_T = 0.2\ ^\circ C$, based on the measurement error reported in the datasheets of high-precision commercial thermometers [7]. Values of α_y for structural elements with varying length ranging from 1 m to 100 m are calculated in Table A.1, assuming that the thermal expansion coefficient of concrete is $\alpha_\epsilon = 10\ \mu\epsilon/^\circ C$. Then, the values of the thermal component of the likelihood uncertainty are calculated, based on the values of α_y and σ_T.

Table A.1: Thermal component of the likelihood uncertainty

Measured quantity	$L\ [m]$	$\alpha_y\ [mm/^\circ C]$	$\sigma_T[^\circ C]$	$\alpha^2 \cdot \sigma_T^2\ [mm^2]$
Structural element elongation (Simple support span elongation; cantilever elongation; pier elongation)	$1 \div 100$	$0.01 \div 1$	0.2	$4 \cdot 10^{-6} \div 4 \cdot 10^{-2}$

Finally, Table A.2 reports the calculated values of the likelihood un-

certainty for the two considered monitoring solutions.

Table A.2: Likelihood uncertainty.

Technology	$\sigma_y^2\ [mm^2]$	$\alpha^2 \cdot \sigma_T^2\ [mm^2]$	$\sigma_{\text{model}}^2\ [mm^2]$	$\sigma_{\text{LH}}\ [mm]$
Topographic system	1	$4 \cdot 10^{-6} \div 4 \cdot 10^{-2}$	1	1.42
SAR satellite sensors	4	$4 \cdot 10^{-6} \div 4 \cdot 10^{-2}$	1	2.24

As visible from Table A.2, the thermal contribution of the likelihood uncertainty is negligible compared to the other components. In fact, the thermal contribution is on the order of $10^{-2} \div 10^{-6}\ mm$, whereas the other terms (values of σ_y^2 and σ_{model}^2) are on the order of $10^0 \div 10^1\ mm$.

A.4.2 Acquisition frequency evaluation

The minimum sampling frequency for each of the two considered monitoring technologies is evaluated as follows:

- The topographic system acquires multiple measurements per day for each prism. However, to account for and purge the effects of daily temperature variations, only one measurement per day is considered as the effective sampling frequency. Therefore, for the topographic system, $1/f_s = 1\ day$.
- The sampling frequency of SAR measurements is determined by the revisit time of the satellite over the bridge area. In this study, we consider datasets from the COSMO-SkyMed mission, which has a revisit time of approximately 16 days for the same area. Consequently, for the SAR solution, $1/f_s = 16\ days$.

A.4.3 Simulated temperature evaluation

The expected seasonal temperature variation can be simulated as a sine function $\boldsymbol{T}$, defined as Equation A.5:

$$T_i = a \cdot sin\left(\frac{2\pi}{\tau} t_i + b\right),\ i = 1, 2, 3, ..., N \tag{A.5}$$

In order to represent two different start dates of the monitoring, we set two cases of the phase-parameter: $b = \pi/2$ and $b = 0$. In the first case, the monitoring period starts when the seasonal temperature reaches approximately its maximum stationarity point (during the summer season); in the second case, it starts in proximity to its point of inflection (during the spring season).

A.4.4 Pre-posterior uncertainty evaluation

As a result, the pre-posterior uncertainty of the displacement trend parameter $\sigma_{m,\text{pp}}$ obtained using the two different monitoring solutions

can be estimated and compared. Figure A.1 presents $\sigma_{m,\text{pp}}$ as a function of the monitoring duration, t_{tot}, for both technologies, along with the target values $\bar{\sigma}_m$ (shown in magenta) and $\bar{\sigma}_{m,\text{strict}}$ (shown in red). The upper horizontal axis indicates the number of SAR images corresponding to each monitoring duration t_{tot}, based on the satellite revisit time of 16 days.

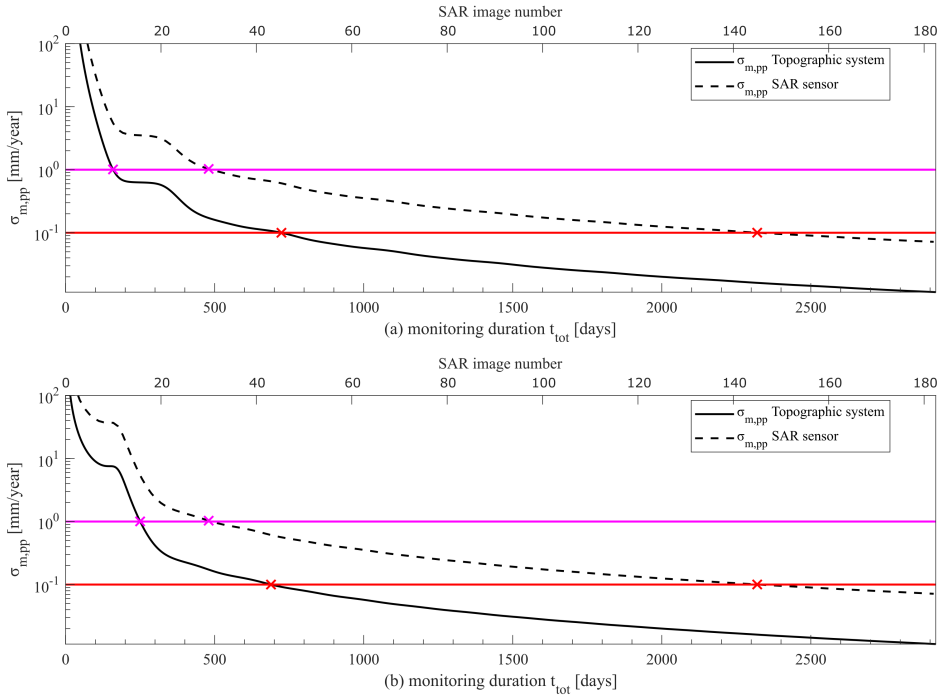

Figure A.1: Expected uncertainty $\sigma_{m,pp}$ of the linear-trend parameter m estimated in the design phase. Phase parameter b is set as (a) $b = 0$ and (b) $b = \pi/2$. The monitoring duration t_{tot} varies from 3 to 2920 days (8 years).

A.5 Discussion of results

By examining Figure A.1, it can be observed that, in all cases, after a sufficiently long monitoring period, the pre-posterior uncertainty $\sigma_{m,\text{pp}}$ becomes lower than both the standard demand $\bar{\sigma}_m$ (shown in magenta) and the stricter demand $\bar{\sigma}_{m,\text{strict}}$ (shown in red). Consequently, both technologies can be considered suitable monitoring solutions for this monitoring design problem. However, their performance clearly differs in terms of the monitoring duration required to achieve pre-posterior uncertainty values below the prescribed demand. Table A.3 reports the

required monitoring durations as a function of the selected technology and the monitoring start date, represented by the phase parameter b.

Table A.3: Monitoring durations necessary to have the pre-posterior uncertainty lower than the design target.

Demand: $\bar{\sigma}_m = 1\ mm/year$		
Technology	$b = 0$	$b = \pi/2$
Topographic system	160 days	251 days
SAR satellite sensors	480 days	480 days
Demand: $\bar{\sigma}_m = 0.1\ mm/year$		
Technology	$b = 0$	$b = \pi/2$
Topographic system	725 days	690 days
SAR satellite sensors	2320 days	2320 days

The topographic system is characterized by higher accuracy and a higher sampling frequency. As a result, it consistently satisfies the monitoring demand within a shorter monitoring duration compared to the SAR sensor technology. Specifically, for $\bar{\sigma}_m = 1\ mm/year$, the demand is met within 8 months of monitoring when using the topographic system, whereas it requires one year and four months when using SAR sensors. Conversely, for $\bar{\sigma}_m = 0.1\ mm/year$, the demand is achieved within two years of monitoring with the topographic system and within six years and a half with SAR sensors.

The SAR sensor technology demonstrates good performance for moderately strict monitoring demands, as it requires only about twice the monitoring duration needed by the topographic system to meet the design requirements in the first case ($\bar{\sigma}_m = 1\ mm/year$). However, its performance is less satisfactory for very strict monitoring demands, such as in the second case ($\bar{\sigma}_m = 0.1\ mm/year$), where SAR sensors require more than three times the monitoring duration needed by the topographic system to satisfy the requirement.

Finally, the costs associated with each monitoring solution can be considered.

For the cost of the topographic system solution, reference can be made to the recent tender notice published by the highway concessionaire *Autostrada del Brennero SpA* for the supply and installation of monitoring systems for highway bridges and viaducts [8]. Specifically, the indicated price for a high-precision automatic total station is €56,352.70 (including supply and installation), while the cost of an optical prism is €117.07 (including supply and installation).

For a multi-span bridge with moderate total length (e.g. 0.5–1 km), multiple total stations are typically installed to be able to survey the entire structure–for example, one total station covering the southern part of the bridge and another covering the northern part. The required number

depends on factors such as the measurement range of the total stations, the presence of obstacles, and the distance between the bridge and the installation locations.

For an indicative cost estimate, a configuration consisting of two total stations and 100 optical prisms is assumed, consistent with the layout adopted for the Colle Isarco viaduct. Moreover, for the sake of simplicity in this discussion, the costs of additional system components–such as the UPS system, electrical power supply, industrial PC, and shelter–are not considered. As a result, the total cost of this monitoring solution amounts to €124,412.40.

The cost of a single high-resolution satellite image can range from a few hundred to several thousand euros, depending on the product type, sensor, and image size. Specifically, COSMO-SkyMed Stripmap images are provided free of charge for research purposes and are priced at €300.00 per image for commercial use [9]. As a result, the cost of a satellite-based monitoring solution depends on the number of images purchased, and therefore on both the monitoring duration and the acquisition frequency.

For the investigated monitoring solution, assuming an acquisition frequency of 16 days, the number of images required to cover the monitoring durations of 480 days and 2320 days reported in Table A.3 is 30 images (€9,000.00) and 145 images (€43,500.00), respectively.

The costs associated with each investigated monitoring solution, for the different monitoring durations required to meet the design requirements (see Table A.3), are summarized in Table A.4.

Table A.4: Monitoring costs related to different monitoring solutions.

Demand: $\bar{\sigma}_m = 1\ mm/year$		
Technology	$b = 0$	$b = \pi/2$
Topographic system	124,412.40€ (160 days)	124,412.40€ (251 days)
SAR satellite sensors	9000.00€ (480 days)	9000.00€ (480 days)
Demand: $\bar{\sigma}_m = 0.1\ mm/year$		
Technology	$b = 0$	$b = \pi/2$
Topographic system	124,412.40€ (725 days)	124,412.40€ (690 days)
SAR satellite sensors	43,500.00€ (2320 days)	43,500.00€ (2320 days)

The SAR monitoring solution is consistently more cost-effective than the topographic monitoring solution. This is particularly evident for short monitoring periods, for which the cost of SAR satellite monitoring is less than 10% of that of the topographic system solution. At this point, having completed the performance and cost analyses and gathered all the necessary information, the monitoring system designer can present the results obtained for the two monitoring solutions to the infrastructure manager, thereby enabling an informed decision on the design of

the long-term displacement monitoring system.

Regarding the cost-effectiveness of the SAR monitoring solution, a few more observations can be made.

First, the SAR solution can become even more economically advantageous when multiple bridges are monitored using a single set of images. Different types of SAR images cover different area swaths. Specifically, COSMO-SkyMed images acquired in Stripmap HIMAGE mode cover areas of approximately 40×40 km, with the exact footprint location and orientation depending on the satellite orbit. Owing to the considerable width of SAR image swaths, it is not uncommon for a single image to capture more than one bridge.

Second, it should be noted that the prices for SAR satellite images reported in Table A.4 refer to archive imagery. If new, custom, or timely acquisitions are required, the costs reported in Table A.4 may no longer apply. As a result, SAR monitoring does not inherently allow for real-time monitoring of the structure, unlike on-site monitoring systems. SAR monitoring is affected by the time lag between image acquisition and the availability of the imagery to users. This time frame depends on the specific satellite mission; for the COSMO-SkyMed mission, imagery is classified as archive and made available up to a maximum of 30 days after acquisition [9].

Finally, an important observation concerns the impact of the sampling frequency and the total monitoring period on the performance of the SAR-based monitoring solution. When a complete archive of satellite images is available from the satellite launch onward (e.g., for COSMO-SkyMed, from approximately 2007 for the first generation and from 2019 for the second generation), it is in principle possible to exploit the long temporal extent of the archive to achieve improved accuracy at reduced costs. This could theoretically be accomplished by selecting a more temporally sparse dataset, consisting of a limited number of images distributed over a longer observation period. Indeed, as discussed in Chapter 8, the formulation adopted for estimating monitoring performance is more sensitive to the total monitoring duration than to the sampling frequency. From a purely theoretical standpoint, this would suggest that a longer observation window with fewer acquisitions could be sufficient to achieve the desired performance.

In practice, however, this approach is often not feasible due to technical constraints associated with MT-InSAR processing. In particular, the revisit time is a key factor governing the quality and reliability of MT-InSAR results. Large temporal gaps or excessively long revisit intervals can lead to temporal and spatial decorrelation effects, which in turn reduce the number of detectable PS, degrade the accuracy of the displace-

ment time-series, and lower the overall temporal coherence of the measurements. As a result, despite the theoretical advantages of long-term archives, practical MT-InSAR applications require sufficiently dense and regular acquisition sequences to ensure robust displacement estimates.

Bibliography

[1] U. E. I. di Normazione, "Uni/tr 11634:2016. guidelines for structural health monitoring," tech. rep., Ente Italiano di Normazione (UNI), Milano, Italy, 2016. Technical Report.

[2] "Trimble s9 / s9 hp – technical datasheet." Online PDF datasheet, Spektra. https://www.spektra.it/Sites/441/WebExplorer/Ecommerce/SPEKTRA/Stazioni%20Totali/Stazioni%20Robotiche%20e%20Autolock/Trimble%20S9_Datasheet.pdf; accessed 2025-11-30.

[3] European Space Agency, "Cosmo-skymed mission," 2025. Accessed: 2025-12-15.

[4] D. Zonta, C. Cappello, A. Beltempo, A. Bonelli, D. Bolognani, O. S. Bursi, C. Costa, W. Pardatscher, *et al.*, "Structural retrofit and health monitoring of colle isarco viaduct," in *Structural faults & repair 2016: 16th International conference and exhibition, venue: Radisson Blu Edinburgh 17th-19th May 2016*, Edinburgh: Engineering Technics Press [2016], 2016.

[5] P. F. Giordano, A. Kamariotis, G. Giardina, E. Chatzi, and M. P. Limongelli, "Uncertainty propagation in satellite insar data analysis for structural health monitoring," *Automation in Construction*, vol. 177, p. 106371, 2025.

[6] D. Tonelli, A. Valentini, A. Rocca, S. Zorzi, A. Lotti, and D. Zonta, "Uncertainty quantification of satellite insar-monitoring of bridges: a case study," *ce/papers*, vol. 6, no. 5, pp. 900–906, 2023.

[7] "Tem-500 / 550 / 600 sensore di temperatura immergibile – data sheet." Online PDF datasheet, Gestecno. https://www.gestecno.it/wp-content/uploads/2024/09/TEM-500-550-600-sensore-di-temperatura-immergibile.pdf; accessed 2025-11-30.

[8] "Tenders – id 115." https://autobrennero.acquistitelematici.it/tender/115. Consultato il 30 novembre 2025.

[9] e-GEOS S.p.A., "Official price list — february 22nd 2021 (gd-com-21-003)," 2021.

Credits of the cover image belong to the University of Trento

University of Trento
Doctoral School in Civil, Environmental and Mechanical Engineering
http://web.unitn.it/en/dricam
Via Mesiano 77, I-38123 Trento
Tel. +39 0461 282670 / 2611 - *dicamphd@unitn.it*